PhD-FSTM-2024-106

The Faculty of Science, Technology and Medicine

DISSERTATION

Defence held on 03/12/2024 in Luxembourg

to obtain the degree of

DOCTEUR DE L'UNIVERSITÉ DU LUXEMBOURG
EN INFORMATIQUE

by

Robin AMAR

Born on 25 September 1985 in Mohali (India)

WAVEFORM DESIGN WITH POLYNOMIAL PHASE IN MODERN RADAR SYSTEMS

Dissertation Defence Committee:

Prof. Dr. Björn Ottersten, Chair
Professor, SnT, University of Luxembourg, Luxembourg

Dr. Mohammad Alaee-Kerahroodi, Vice-Chair
Research Scientist, SnT, University of Luxembourg, Luxembourg

Prof. Dr. Bhavani Shankar Mysore Rama Rao, Supervisor
Assistant Professor, SnT, University of Luxembourg, Luxembourg

Prof. Dr. Abdelhak Zoubir
Full Professor, TU Darmstadt, Darmstadt, Germany

Dr. Ashish Pandharipande
R&D System Architect, NXP Semiconductors, Eindhoven, Netherlands

Affidavit

I hereby confirm that the PhD thesis entitled “Waveform Design with Polynomial Phase in Modern Radar Systems” has been written independently and without any other sources than cited.

Luxembourg, _____ _____

Robin Amar

Abstract

This research explores several key aspects of radar waveform design, interference mitigation, and performance optimization in modern radar systems, particularly focusing on multi-sensor environments and dynamic target detection.

High-resolution mmWave radar sensors are critical for applications such as driver safety in automotive applications collectively called Advanced Driver Assistance Systems (ADAS), and in-cabin sensing. However, the use of multiple radar sensors often leads to interference, which can degrade system performance. The study was initiated by investigating different types of radar interference in the state-of-the-art frequency modulated continuous wave (FMCW) radars, including "Same slope," "Similar slope," and "Sweeping slope," using simulations and real-world measurements to analyze the impact on the signal-to-interference-plus-noise ratio (SINR). These results help enhance radar performance in crowded frequency environments.

In addition, the mutual interference (MI) was analyzed inside a car cabin by recording data for multiple frames. Results showed the presence of similar-slope and sweeping-slope interference amongst radar sensors operating with similar sensor specifications. The understanding gained from these experiments laid the foundation for a deeper research to find a solution of this issue by leveraging the waveform diversity of FMCW and Phase Modulated Continuous Wave (PMCW) waveforms.

A significant challenge arises in dynamic target detection, where linear frequency modulation (LFM) waveforms experience performance degradation due to interference. To address this, the research introduces a waveform design framework called Polynomial phase Estimate of Coefficients for unimodular Sequences (PECS) which minimizes peak and integrated sidelobe levels (PSL/ISL) while ensuring Doppler-tolerant properties. The proposed optimization framework consists of a unique polynomial phase constraint for designing sub-sequences/sequences. A sequence is broken down into multiple sub-sequences, where the phase characteristics of every sub-sequence can be optimally derived while minimizing the ISL/PSL. The diversity of multiple sub-sequences in a sequence yields superior interference-immune characteristics. It provides robust solutions for applications where high Doppler tolerance is essential by setting the degree of the polynomial phase constraint to two (i.e. quadratic phase behavior).

Further, as a derivative of the previous study, we proposed a sub-pulse design approach for PMCW radars, by empowering them to operate with low sampling rates. This apporach integrated quadratic phase variations while minimizing sidelobe levels to improve radar detection performance. The experiments were conducted on a hardware setup consisting of Universal Serial Radio Peripheral (USRP) and other measurement devices. The SINR of the signal was evaluated for different interfering waveform categories. By evaluating SINR in different radar configurations, the proposed solution shows effectiveness in both indoor and outdoor environments. This study concluded that the PMCW waveforms can be implemented using low-sampling rate ADCs by employing stretch processing within every sub-pulse. Thus, the challenge of high sampling rate requirement for the implementation of PMCW radars is addressed and MI immunity is achieved.

As a next step, we generalized the problem of sequence design and presented a comprehensive framework for designing interference-immune waveforms/ sequence sets in FMCW and PMCW MIMO radar systems, respectively. By employing advanced optimization techniques like majorization-minimization (MM) and Block Coordinate Descent (BCD), the framework generates waveform sequences that minimize sidelobe levels and improve spatial beam shaping. Case studies demonstrate the application of these waveforms in scenarios such as tunnel-based environments and dynamic target detection, where sub-pulse based Doppler-tolerant waveform design significantly improve radar performance.

Another aspect of the research also explored radar waveform optimization for cognitive MIMO systems coexisting with communication systems. By solving a bi-objective optimization problem, the study developed waveforms that balance spectrum compatibility and minimize ISL. This approach enhances the coexistence of radar and communication systems by providing spectrally efficient, interference-resistant MIMO waveforms.

Finally in the last phase, the research study extends to environmental sensing through Wireless Sensor Networks (WSNs), where the waveform optimization techniques were used for integrated sensing and communication (ISAC) application. The proposed Doppler-tolerant waveforms embeds communication symbols within each sub-pulse, while minimizing ISL for the sensing sub-pulse. The solution involves the fusion of three optimization techniques, namely: BCD, MM, Sum of Squares (SoS) in a multi-layered iterative manner leading to objective convergence. This optimization is crucial for reliable target detection in dynamic environments where MI from other sensors is inevitable, further proving the versatility and effectiveness of our proposed waveform designs techniques.

This comprehensive investigation into radar waveform design for mutual interference mitigation, using optimization techniques exhibit significant improvement in reliability, detection accuracy, and coexistence of modern radar systems.

Acknowledgements

My journey as a *Doctoral Researcher* at the Interdisciplinary Centre for Security, Reliability, and Trust (SnT) at the University of Luxembourg has been an incredible experience, equipping me with valuable skills for my professional and personal life. I am deeply grateful to the many individuals whose support made completing this Ph.D. thesis possible.

First, I would like to express my gratitude to my supervisor, Prof. Dr. Bhavani Shankar, for his continuous support and understanding throughout my PhD studies which was crucial in making this thesis a reality. His belief in my research capabilities from the first day of interaction has been instrumental in my research. I admire his personality, and his capability to handle complex situations with a joyful spirit and open-minded reception. I am grateful to him for providing me with the opportunity to pursue my PhD studies at the University of Luxembourg.

I extend my heartfelt thanks to my co-supervisor, Dr. Mohammad Alaee-Kerahroodi, whose unwavering guidance and positive attitude were pivotal to the successful completion of this thesis. His dedicated mentorship, evident in our countless discussions on both research challenges and everyday matters, provided invaluable support throughout my PhD journey. I deeply appreciate his approachable and friendly nature; beyond being an exceptional mentor, he often took on the roles of a big brother and a trusted friend, offering personal support in times of need.

Moreover, I would like to thank my thesis supervision committee member, Prof. Dr. Björn Ottersten. His extensive knowledge and experience helped me to be on the right track with my research. In addition, I would also like to thank Prof. Dr. Prabhu Babu and Prof. Dr. Mojtaba Soltanalian for their valuable suggestions in setting up my preliminary research goals. I am grateful to Prof. Dr. Abdelhak Zoubir and Dr. Ashish Pandharipande for accepting to be in my defense committee.

I would also like to extend my thanks to the (current and past) colleagues of the SPARC group of SnT for creating an enjoyable working environment. Specially, I would like to thank Dr. Ehsan Raei, Dr. Gabriel Beltrao, Dr. Saeid Sedighi, Dr. Linlong Wu, Dr. Ahmed Murtada, Dr. Moien Ahmadi, Tong Wei, Dr. Nazilla Karimian, Johann Fuchs, and Marcel Follmann for the insightful discussions and support at various stages in my research.

Finally, I would like to acknowledge the unwavering love and support of my family. To my

wife, Prachi, thank you for your constant encouragement, understanding, and sacrifices. Your belief in me has been a source of inspiration. To my children, Kabeer and Juhi, thank you for your love and patience. Your presence in my life has brought me immense joy, motivation and maturity. My family taught me how to love and always be there when the going gets tough. And to my parents, Sarvender and Manju, thank you for your love and support. Your sacrifices and guidance have shaped me into the person I am today.

Preface

Support

This research was supported by FNR (Luxembourg) through the CORE projects “SPRINGER: Signal Processing for Next Generation Radar” under grant C18/IS/12734677/SPRINGER, FNR CORE INTER project “SENCOM: SENsing and COmmunication in Networks with High Mobility and High Directivity” under grant C20/IS/14799710/SENCOM, and “METSA: Metacognitive Radar For Emerging Sensing Applications (METSA)” under grant C22/IS/17391632.

Collaboration

A part of this work was made possible thanks to the collaboration with the industrial partner IEE S.A.

"There are nether worlds beneath nether worlds, and hundreds of thousands of heavenly worlds above. The Vedas say that you can search for them all, until you grow weary. The scriptures say that there are $18,000$ worlds, but in reality, there is only One Universe. If you try to write an account of this, you will surely finish yourself before you finish writing it. O Nanak, call Him Great! He himself knows Himself."

Guru Nanak Dev Ji

"The moving finger writes; and, having writ, moves on: nor all thy piety nor wit shall lure it back to cancel half a line, nor all thy tears wash out a word of it."

Omar Khayyam

Contents

List of Figures

List of Tables

Acronyms

A | B | C | D | F | G | I | L | M | O | P | R | S | T | U | W | X

A

ACC Adaptive Cruise Control

ADAS Advanced Driver Assistance System

ADC analog-to-digital converter

ADMM Alternating Direction Method of Multipliers

AEB automatic emergency braking

AF Ambiguity Function

B

BCD Block Coordinate Descent

BCGD Block Coordinate Gradient Descent

BPM Binary Phase Modulation

BSD Blind Spot Detection

BSUM Block Successive Upper-bound Minimization

BSW blind spot warning

C

CAN Cyclic Algorithm New

CD Coordinate Descent

CDM Code Division Multiplexing

CFAR constant false alarm rate

CISL Complementary Integrated Sidelobe Level

COTS commercial-off-the-shelf

CPI Coherent Pulse Interval

CS4MR Cognitive Spectral shaping for MIMO Radars

CW Continuous Wave

D

DDM Doppler Division Multiplexing

DFT Discrete Fourier Transform

F

FC Fusion Center

FCW forward collision warning

FDM frequency division multiplexing

FFT Fast Fourier Transform

FMCW Frequency Modulated Continuous Wave

FoV field of view

FT-CDMA fast time - code division multiple access

FTDC fast Time Doppler Compensation

G

GPS global positioning system

GUI graphical user interface

I

ICCL Integrated Cross-Correlation Level

INR Interference to Noise Ratio

ISAC Integrated Sensing and Communication

ISL Integrated Sidelobe Level

ISLR Integrated Sidelobe Level Ratio

L

LDW lane departure warning

LFM Linear Frequency Modulation

LKA lane keep assist

LMI Linear Matrix Inequality

LNA low-noise amplifier

LoS Line of Sight

LS Least Squares

M

MF Merit Factor

MI mutual interference

MIMO Multiple Input Multiple Output

MISL monotonic minimizer for integrated sidelobe level

MM Majorization-Minimization

MM-PSL Monotonic Minimizer for the ℓ_p-norm of autocorrelation sidelobes

MMIC Monolithic microwave integrated circuit

MTI Moving Target Indicator

O

OOP object oriented programming

P

PECS Polynomial phase Estimate of Coefficients for unimodular Sequences

PMCW Phase Modulated Continuous Wave

PN pseudo-noise

PRF pulse repetition frequency

PRT pulse repetition time

PSL Peak Sidelobe Level

PSLR Peak Sidelobe Level Ratio

R

RN Residual Network

RNN Recurrent Neural Network

RoC Radar-on-Chip

Rx Receiver

S

SINR Signal to Interference plus Noise Ratio

SIR Signal-to-Interference Ratio

SISO Single Input Single Output

SNR Signal to Noise Ratio

SoS Sum-of-Squares

SRR Short Range Radar

ST-CDMA slow time - code division multiple access

T

TBP time bandwidth product

TDM time division multiplexing

TI Texas Instrument

Tx Transmitter

U

URA Uniform Rectangular Array

USRP Universal Software Radio Peripheral

W

WSN Wireless Sensor Network

X

XO Crystal Oscillators

Part I

Introduction and Motivation

Chapter 1

Introduction

The global mortality rate due to traffic accidents has surged to an alarming 1.35 million fatalities annually [1]. Additionally, tens of millions more sustain injuries or disabilities each year, resulting in life-altering consequences with enduring repercussions. Road casualties now rank as the eighth leading cause of death across all age groups.

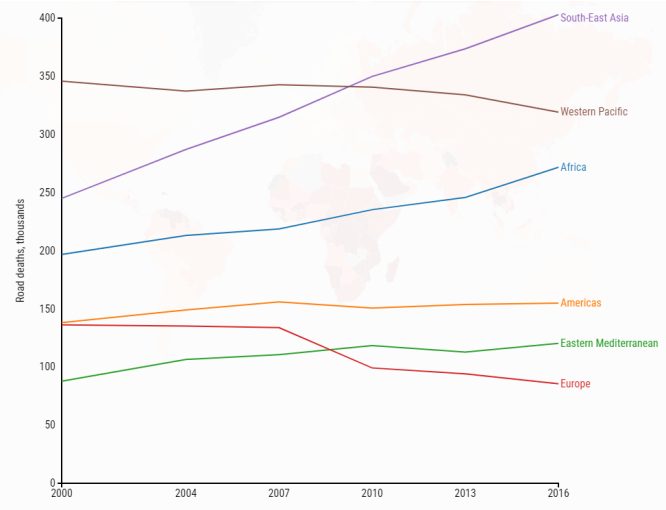

Figure 1.1: Deaths due to road accidents in the WHO regions (worldwide) [1]

Advanced Driver Assistance System (ADAS) are engineered to enhance vehicular safety by aiding drivers in maintaining control and mitigating or preventing specific types of collisions. These systems utilize sophisticated sensors, including radar, cameras, LiDAR, and ultrasonic devices, each operating on distinct principles [8]. Contemporary vehicle designs integrate features such as forward collision warning (FCW), automatic emergency braking (AEB), lane departure warning (LDW), lane keep assist (LKA) and blind spot warning (BSW).

1.1 Role of Radar Sensors in ADAS and Challenges

Radar sensors serve as a crucial component within this framework, offering superior resilience compared to cameras in adverse weather conditions. They are also more cost-effective than LiDAR and provide enhanced velocity and distance resolution. However, radar systems typically exhibit lower angular or cross-range resolution relative to camera or LiDAR technologies. To address these limitations, advanced solutions such as sparse arrays, super-resolution algorithms, and techniques to bolster radar sensitivity are being developed. These improvements enable better differentiation of smaller targets from larger ones in close proximity, such as cyclists or pedestrians near large trucks or buildings. Beyond these challenges, automotive radar sensors must also enhance their robustness against interference from other radar systems.

When multiple radars use the same allocated frequency band, there is a possibility that they could transmit simultaneously on the same frequency with similar waveform characteristics. If these radars are positioned along a common line of sight, e.g. a front-facing radar and a rear-facing radar on a vehicle ahead, they can cause interference with one another. While radar interference is a known issue, it currently isn't a major concern due to its low likelihood given the current market usage. However, as more vehicles are equipped with radar sensors, the risk of interference will inevitably rise. It is crucial for the radar industry to tackle this issue proactively, ensuring that robust radar technology can be deployed widely without being seen as a limitation by users, thereby enhancing road safety for all.

The primary question that needs to be addressed is whether radar interference poses a significant issue. While interference is certainly possible, it is critical to quantify its frequency of occurrence and assess the severity of its impact when it does occur. The European project MOSARIM [9] represents one of the first comprehensive efforts to evaluate the extent of radar interference. Building on this, an NHTSA study [10] incorporates a variety of traffic scenarios to determine the conditions under which interference arises and how often it happens. A typical case involves vehicles equipped with long-range, front-facing radars with a relatively narrow field of view (FOV) approaching each other. Interference occurs when the FOVs of these sensors overlap, and the radars are simultaneously transmitting within the same frequency spectrum.

According to a simulation study conducted by NXP Semiconductor [2], the interference probability for a highway traffic scenario given in the Figure 1.2 was calculated. The probability of receiving perceivable interference power was correlated to the radar penetration rate (RPR). The interference power results in increment of noise floor (NF) above the theoretical NF level of (-159dBm/Hz). As expected, the probability of having interference increases with the increased number of vehicles that have radar on the highway Figure 1.3. Even with 50 percent radar penetration rate (RPR), the probability of interference is as high as 0.6 for the semi-blind sub

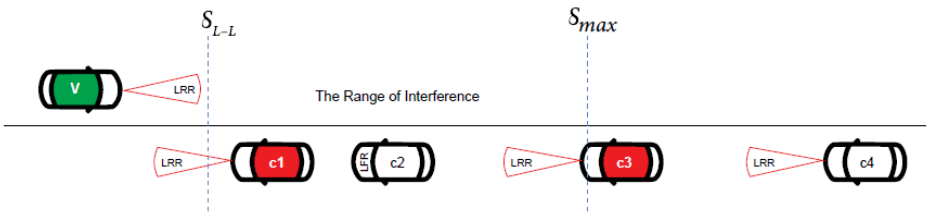

Figure 1.2: Simple highway traffic scenario - Interference at the victim radar (green) is calculated while it is generated by other vehicles (red) [2]

band jump category which highlights the seriousness of this issue in the near future.

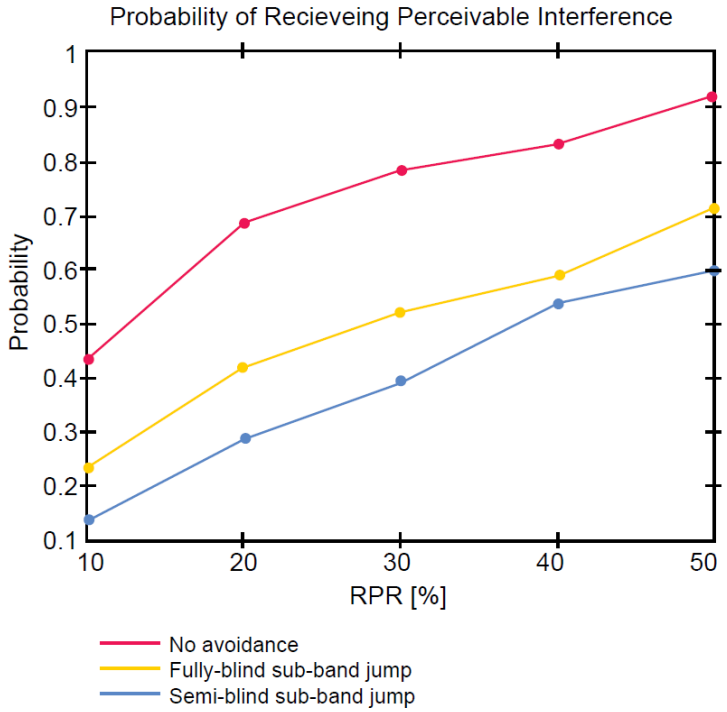

Figure 1.3: Likelihood of interference depends on the radar penetration rate (RPR) in a highway setup where vehicles use long-range, forward-looking radar for cruise control. Interference can be reduced by randomly switching resources (yellow curve) or by sensing interference first before switching to a different time or frequency resource (blue curve) [2].

1.2 Strategies to address the challenge: Radar Interference

There are several strategies to mitigate and prevent the impact of radar interference on system performance, which can be categorized into three solution types [11]. The first set of solutions prevents front-end saturation, which occurs when a radar sensor encounters a strong interference source. The second approach addresses digital interference by detecting and eliminating

it within the digital domain [12]. The third method reduces the likelihood of interference by adjusting the radar waveform, minimizing the chances of conflicting with other radars.

In this research, the third method was used to conquer the interference from other sensors in the victim sensor field of view (FoV) and mitigate the deterioration of the back-scattered received signal from the target in order to enhance the reliability of radar sensing in all practical scenarios. Radar waveform design includes multiple fundamental constructs as shown in Figure 1.4. In order to minimize the correlation of a certain transmitted waveform with the wave-

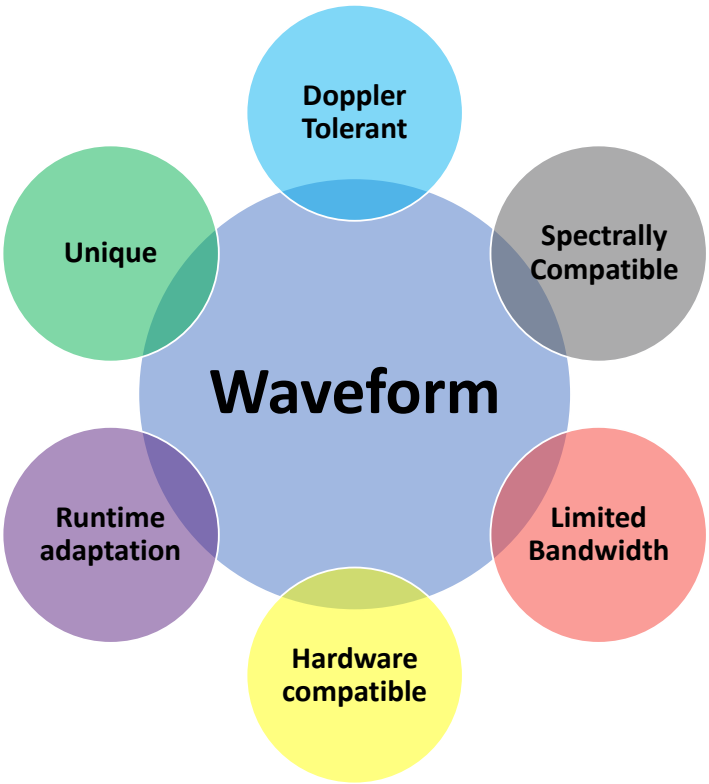

Figure 1.4: Waveform design principles considered in this research

forms transmitted from the other sensors in the environment, the uniqueness of the waveform (in terms of its phase behavior over the entire transmit duration) is a necessary feature. Additionally, the dynamic targets being sensed in the case of automotive radars require the waveform to have Doppler tolerance properties. The OEMs further dictate the cost and faster throughput of these sensors. Thus, the hardware compatibility and runtime adaptation becomes vital in the design process. Further, the spectral compatibility because of limited spectrum availability and large bandwidth for fine range resolution are two essential constraints that make the overall waveform design problem challenging in nature.

1.3 Contributions of this thesis

Despite the few recent research papers investigating the problem of radar-to-radar interference/mutual interference (MI) and its mitigation in automotive scenarios (in-cabin and outdoor sensing), most of the research focuses on the second methodology (mentioned in 1.2). In the other cases, where the third methodology is used, the efforts are made to design a waveform such that the Interference to Noise Ratio (INR) of the interferer is decreased and the Signal to Interference plus Noise Ratio (SINR) of the target is increased. However, the idea of minimizing the INR when the dynamics (location and velocity) of the interferer is known to the victim sensor is hypothetical and has little practical significance in automotive scenarios. Generally, the driving scenario is unknown and it is the radar sensor's responsibility to detect the targets reliably in the absence of the complementary input from other sensors (e.g. Camera, LiDAR and ultrasonics) mounted on the automobile.

Throughout our literature review, we observed these gaps in the existing literature. The study of interference in automotive radars is dependent on the type of waveforms used in majority of the radars i.e. Frequency Modulated Continuous Wave (FMCW) or Phase Modulated Continuous Wave (PMCW) waveforms. The technique used in FMCW waveforms employ a clever yet intelligent receiver "Stretch processing" which reduces the sampling requirements. On the other hand, it renders the designers with few degrees of freedom to choose the characteristics of the waveform in every transmitted pulse or over an entire Coherent Pulse Interval (CPI).

Broadly, we can categorize the challenges and formulate the following research questions:

- **Question 1**: MI in radar sensors is a legitimate issue or not in an in-cabin or outdoor automotive sensing setup?
- **Question 2**: How to mitigate the effect of interference on detection capability and increase the reliability of radar sensors for detecting static/dynamic targets while mounted on dynamic platforms?
- **Question 3**: Develop a reliable technique/algorithm or mathematical formulation to derive a new waveform capable of handling interference?
- **Question 4**: Verify whether the new waveform is easy to deploy on the existing state-of-the-art hardware or upcoming hardwares?
- **Question 5**: Ease of adaptability of the proposed waveforms to accommodate advanced requirements and features (e.g. Integrated Sensing and Communication (ISAC) for IoT, WSN networks) in the near-future?

In an effort to better understand and eventually answer these questions, the main contributions of this thesis are as follows:

- **Contribution 1**: Performed experiments under controlled environment to analyze the type and effects of MI amongst radar sensors.
- **Contribution 2**: Proposed a novel waveform design scheme using sub-sequences/ sub-pulse processing to minimize the auto/cross-correlation sidelobes with itself and other waveforms, respectively.
- **Contribution 3**: Proposed an optimization framework to obtain a waveform with minimal Integrated Sidelobe Level (ISL)/Peak Sidelobe Level (PSL).
- **Contribution 4**: Verified the deployability of the proposed waveforms and validated the results for SISO configuration.
- **Contribution 5**: Adapted the waveform design scheme and adapted the framework to accommodate a novel ISAC application for Wireless Sensor Network (WSN).

These contributions were tested under different design considerations and simulation scenarios ranging from ideal simulation settings to practical hardware implementations and the results are discussed.

1.4 List of Publications

The work presented in this thesis has resulted in two peer-reviewed journals and a number of conference papers, currently published or under revision. The publications related to this thesis are listed below:

Journals

- $J1$: **Robin Amar** et al, "Designing Interference-Immune Doppler-Tolerant Waveforms for Radar Systems", *IEEE Transactions on Aerospace and Electronic Systems,* vol. 59, no. 3, pp. 2402-2421, June 2023, doi: 10.1109/TAES.2022.3215116.
- $J2$: **Robin Amar** et al, "Polynomial Phase Constrained Waveforms for mmWave MIMO Radars", under revision process in *IEEE Transactions on Aerospace and Electronic Systems,*, submitted on 6 June 2024.

Conferences

- $C1$: **Robin Amar** et al, "FMCW-FMCW Interference Analysis in mm-Wave Radars; An indoor case study and validation by measurements", 2021 21st International Radar Symposium (IRS), Berlin, Germany, 2021, pp. 1-11, doi: 10.23919/IRS51887.2021.9466178.
- $C2$: **Robin Amar** et al, "Radar Waveform Design for Sensing and Communications Coexistence", 2023 20th European Radar Conference (EuRAD), Berlin, Germany, 2023, pp. 407-410, doi: 10.23919/EuRAD58043.2023.10289167.
- $C3$: **Robin Amar** et al, "USRP based Implementation of Interference Immune PMCW Radars with Low Sampling rate ADCs", 2024 21st European Radar Conference (EuRAD), Paris, France. 2024.
- $C4$: **Robin Amar** et al, "Dual-Function Waveform Design in Wireless Sensor Networks via SoS Optimization", submitted to ICASSP 2025 - 2025 IEEE International Conference on Acoustics, Speech and Signal Processing (ICASSP), Hyderabad, India.

Book Chapter

- B: Artech House Book - Mathematical Techniques for Signal Design in Modern Radar Systems. Chapter 10: Doppler Tolerant Waveform Design.

Omitted Publications

- $C5$: **Robin Amar** et al, "Optimized-Slope FMCW Waveform for Automotive Radars", 2022 23rd International Radar Symposium (IRS), Gdansk, Poland, 2022, pp. 110-115, doi: 10.23919/IRS54158.2022.9905044.
- $C6$: **Robin Amar** et al, "Doppler-Tolerant Waveform Design and Signal Processing for Interference Immune Radar Systems," 2023 31st European Signal Processing Conference (EUSIPCO), Helsinki, Finland, 2023, pp. 715-719, doi:10.23919 / EUSIPCO58844.2023.10290099.

1.5 Thesis Organization

This thesis is a "cumulative thesis". It includes six manuscripts reproduced in their entirety. While the first one ($C1$) along with an in-cabin radar measurement experimental setup in a passenger car is part of our motivation to work in this research area, the other five manuscripts ($J1$, $C3$, $J2$, $C2$, and $C4$) present our contributions to improve the state of the art. Despite

describing complete signal model, algorithm design, simulation and implementation in each one of them, the major contribution in each manuscript is related to a particular stage of the overall design flow of our research as described in Figure 1.5.

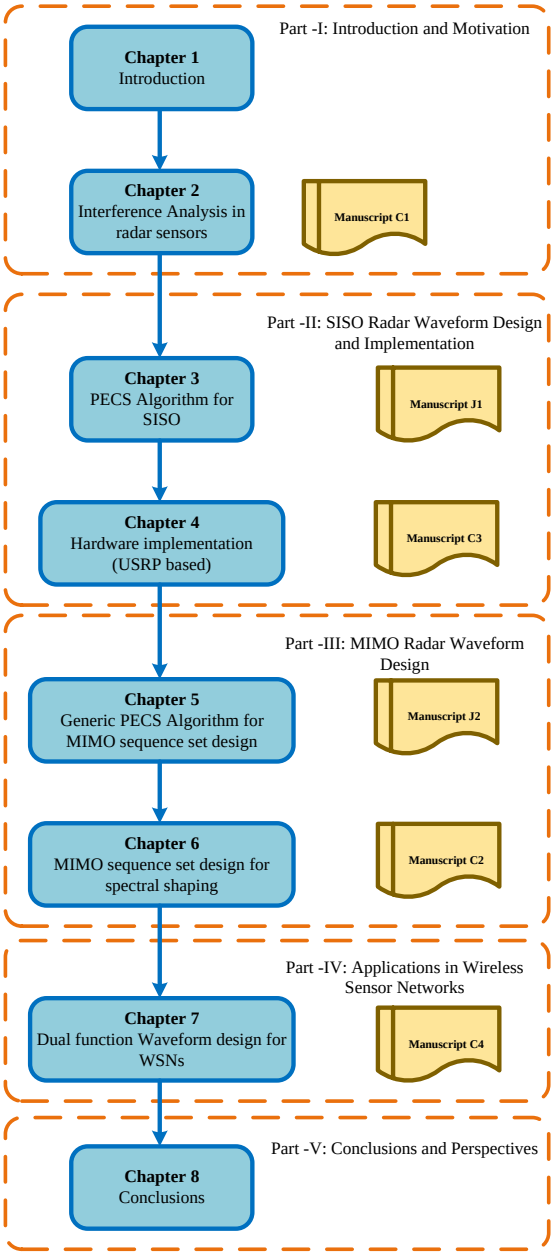

Figure 1.5: Thesis organization

Each chapter with a manuscript also contains a preamble. It aims to guide the reader along the thesis, by introducing the general topic and establishing a smooth connection between the current chapter and the rest of the thesis. The manuscripts included in each chapter are presented

as published or submitted for consideration. A few formatting aspects have been adjusted to match the rest of the thesis. All pages, tables, equations, and figures have been numbered consecutively throughout the thesis for continuity. All references were consolidated into a single reference list, presented at the end of this thesis. Please note that each manuscript presents its own notation and the used terms may differ in each chapter.

Chapter 2

Interference Analysis in Multi-sensor setup

2.1 Introduction

Radar sensing has various inherent advantages in different scenarios and its usage in civilian applications has been proliferating in addition to the traditional defence applications. Some of these applications include automotive, indoor sensing, airport, harbor and highway traffic control, wave forecast and marine climatology to name a few [13]. With different applications and dearth of standardization, presence of multiple radar systems with uncoordinated transmissions has become a reality. Considering an example of automotive application, radar sensors are used for cruise control and collision avoidance systems in cars. In the absence of coordination among different cars, scarcity of spectrum and the need for high bandwidth to enable high resolution sensing, it is inevitable that different cars use identical bands simultaneously, leading to interference [9].

Similar to the outdoor applications, the usage of mmWave sensors for indoor/in-car monitoring has gained recently a lot of attention. Few major applications are People counting, occupancy detection, driver vital signs monitoring, flash and run-through body scanners, robot positioning, industrial machine lock/cut-off etc.[14]. In this sense, it is known that multiple connected/collaborated sensors enhance the target detection and parameter estimation performance. However, multi-sensor setup leads to mutual interference from neighboring radars operating simultaneously in each others FoV [12], [15]. Analyses and test results involving multiple radar sensors indicate that mutual interference can be substantial unless suitable mitigation techniques are employed. For example, two 77GHz long range radars with 18dB antenna gains and 10dBm transmit powers, facing each other, would cause -45dBm interference to each other [16], [17]. Interference becomes inevitable from other sensors when the application insists to have best pos-

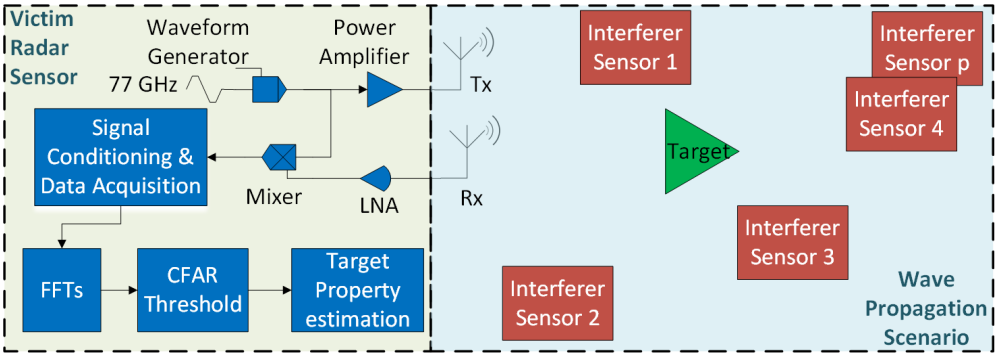

Figure 2.1: System Model description

sible resolution for better classification of targets which leads to utilizing full bandwidth available in an operating band which is the case in many indoor and outdoor sensing scenarios. For a given system, its interference quantification (maximum possible rise in Signal-to-Interference Ratio (SIR)) and robustness is required to understand the target detection and classification capability of a sensor in worst scenarios. In this chapter, an effort has been made to explore the interference occurring from "close proximity" and direct Line of Sight (LoS) sensors which are arranged in a multi-sensor arrangement for indoor sensing application. The investigation has been conducted using mm-Wave FMCW radar sensor measurement set-up supported by an elaborate simulation. Further, the backscatter and interference characteristics similarity between indoor sensing and outdoor sensing has also been discussed.

The outline of this chapter is as follows: Section II presents the system model detailing the interference set-up and sets up the signal model incorporating the interference phenomenon. Section III analyses the impact of interference in Indoor scenarios using an elaborate simulation setup. This section highlights the perturbations in the Range-Doppler domain due to interference and its impact on target detection. Section IV presents an Indoor Interference measurement setup for corroborating the findings of section III using commercial-off-the-shelf (COTS) mmWave radar modules. The results from this measurement are analysed and section V presents the conclusions drawn.

2.2 System Model

In a generic FMCW radar Figure 2.1, the frequency sweep, i.e., a chirp, is generated by a waveform generator and this chirp is utilized in two different signal paths: one is directed to the Transmitter (Tx) antenna, while the other is directed towards the mixer correlator. Before the chirp is transmitted from the Tx antenna, it passes through a power amplifier to boost the transmitted energy.

2.2.1 Received signal model

The FMCW waveform with *L* consecutive linear FM chirps (or sweeps) can be expressed as

$$s(t) = \sum_{l=0}^{L-1} x(t - lT_c), \tag{2.1}$$

where the individual chirps are given by

$$x(t) = e^{j\phi(t)} rect_{T_v}(t), \quad \phi(t) = 2\pi(f_c t + 0.5\alpha t^2). \tag{2.2}$$

Here, $\alpha = BW_v/T_v$ is the chirp slope, BW_v denotes the sweep bandwidth, T_v represents the chirp duration, f_c is the carrier frequency, $rect_{T_v}(t)$ is rectangular pulse of duration T_v of the victim radar and T_c is the pulse repetition time (PRT). The reflected signal from target is very weak due to two-way free-space propagation path loss and the absorption loss at the target. This requires the receive signal to be amplified with a low-noise amplifier (LNA) to maintain an acceptable signal level. The amplified signal from the target reflection is mixed with the Tx signal at the mixer, this is called *dechirping*. The round-trip delay and doppler shift caused by the relative velocity of the target, shift the frequency of the received signal compared to that of the transmitted signal. As a result, the mixer creates a beat signal that will pass through a low-pass filter and be digitized, yielding delay and Doppler estimates after transforming into frequency domain. In modern automotive radars, it is also possible to estimate azimuth and elevation of targets using multiple antennas by acquiring the signal in spatial domain and further transforming them into frequency domain as an additional signal dimension (Range-fast chirp and Doppler-slow chirp as the first two dimensions).

Assuming there exists a single target (point scatterer), whose impact on the received signal is characterized by a complex amplitude γ (incorporating the effects of path loss, antenna gain and radar cross section (RCS)) with an overall round-trip propagation delay $\tau = 2R/c$ and a doppler shift of $\nu_{T_c} = 2v_t/\lambda$, where R and v_t denotes, respectively, the distance and relative radial velocity between the radar and the target; c is the speed of the EM wave propagation in air. In a general case for a single target scenario, the received signal contaminated with clutter, noise and the interference from multiple sensors can be written as,

$$r(t) = \gamma s(t - \tau) e^{j2\pi\nu_T} + c(t) + y(t) + w(t), \tag{2.3}$$

where $x_l(t)$ is the l-th transmitted signal (chirp) which is attenuated by γ and delayed by τ, $y(t)$ is the interference (to be discussed below) and $w(t)$ is the receiver noise considered as a zero-mean white Gaussian process. In the above equation, $c(t)$ and γ is the clutter and attenuation of

the transmitted signal respectively which can be expressed as

$$c(t) = \sum_{k=0}^{K-1} \alpha_k s(t - \tau_k).e^{j2\pi\nu_{T_c}} \tag{2.4}$$

and $\gamma = \frac{P_v G_v^2 \lambda^2 \sigma_{tgt}}{(4\pi)^3 R_{tgt} L}$ where α_k is the backscatter power received from the k^{th} scatterer in clutter with τ_k delay and ν_{T_c} doppler shift due to the motion of victim sensor.
We assume P interferers in the FoV of the victim sensor, located at R_p relative distance with unique chirp time T_I, chirp repetition time T_p and bandwidth BW_p which leads to non-identical chirp slopes β_p (where $\beta_p = \frac{\text{BW}_p}{T_p}$). Further, the p^{th} interferer is assumed to have M chirps, all of which are attenuated by ζ_p due to the propagation loss in the medium between the interferers and the victim (P_I, G_I, G_v, L are the Tx power, Tx gain, Receiver (Rx) gain at victim and other losses respectively). The cumulative signal received from all the interferers can then be given by

$$y(t) = \sum_{p=0}^{P-1} \sum_{m=0}^{M-1} \zeta_p y_p(t - mT_p), \tag{2.5}$$

where individual interferers are

$$y_p(t) = e^{j\psi(t)} rect_{T_p}(t), \psi(t) = 2\pi(f_c t + 0.5\beta_p t^2), \tag{2.6}$$

$M = LT_c/T_p$ and $\zeta_p = \frac{P_I G_I G_v \lambda^2}{(4\pi)^2 R_p^2 L}$.

Let τ_{max} denote the round-trip delay corresponding to a maximum target range of interest (i.e. $\tau_{max} \geq \tau$); this is related to the radar bandwidth of interest B_s as $\tau_{max} = B_s/\alpha$. The analog-to-digital converter (ADC) bandwidth $B_{adc} \leq B_s$ imposes a limit on B_s and thus the maximum detectable range r_{max}. After low pass filtering, the beat signal with bandwidth B_s, sampling with a period of T_s, it is rearranged into a slow time - fast time data matrix, where l^{th} row contains the samples of the l^{th} chirp (slow time), while the n^{th} column contains the n^{th} sample of each chirp (fast time). The number of receive channels present in the receiver array be Q. Thus, let this discretized sampled data be denoted as $\mathbf{Y}_F \in \mathbb{C}^{N \times L \times Q}$ in the frame F. This data array is further analysed to understand the impact of interference on the target detection using the measurement setup for indoor scenarios defined in the next section.

2.2.2 Types of Interference

In [18], two types of interference are described: Parallel and Sweeping. After understanding the nature of interference possible in the practical scenarios, in order to form a holistic categorization of interference its extension to the following categories is warranted.

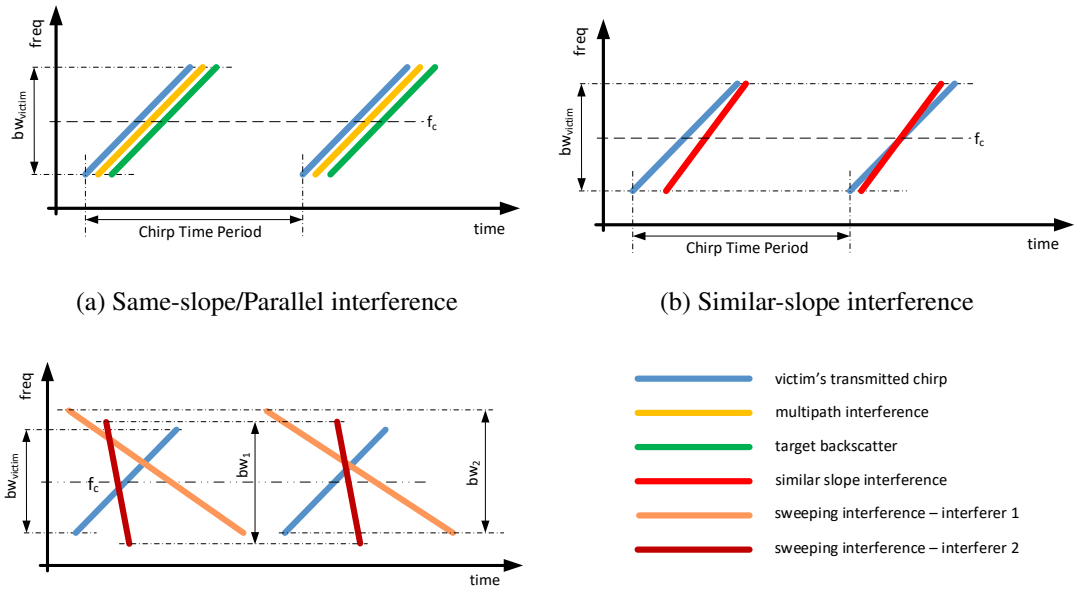

(a) Same-slope/Parallel interference

(b) Similar-slope interference

(c) Sweeping interference

Figure 2.2: Three types of Interference

1. *Same Slope Interference*: This typically arises through the multipath reflections that have a strong return (i.e. do not suffer from severe path and backscatter losses), and can be called clutter. These types of interference are generally observed in both outdoor and indoor scenarios. In outdoor scenarios it is observed in tunnels and highways with high guard rails on the road borders in rainy conditions. In indoor scenarios, it is generally observed in underground parking and rooms with highly reflecting walls and floor.

2. *Similar Slope Interference*: This type of interference occurs when the interfering sensor is operating with similar bandwidth and chirp time. The redefinition was required because practically the probability of another sensor to operate with exactly same slope chirp is very low because the Crystal Oscillators (XO) operating on every hardware have their own linearity properties which will never yield absolutely parallel slope chirp. Here, it is worth a mention that the criteria for defining the similar slope should be w.r.t. the Victim sensor's slope. Therefore, if the interferer slope varies within 10% of the victim slope, then it could be categorized in it.

3. *Sweeping Interference*: When the interfering sensor does not lie in the similar slope interference category, it may be operating at a significantly different slope (i.e. very high or low bandwidth, chirp time and up/down chirp in comparison to the victim sensor) Figure2.2.

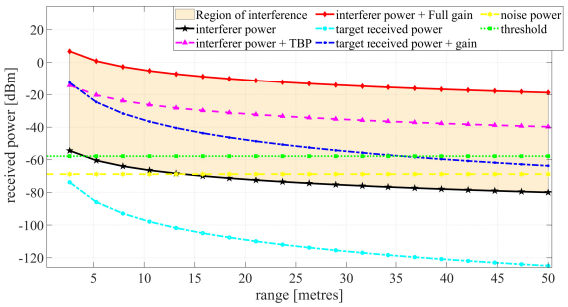

Parameter	Value
Target RCS	0 dBsm
Victim / Interferer Power	12dBm
Time-Bandwidth Product	40.1773dB
Processing Gain	21.0721dB
Noise Power	-68.83dB
Noise Power + CFAR	-57.83dB

Figure 2.3: Received power variation with range at different processing stages of the system

The new characterization with regards to [18] involves addition of a new category of interference i.e. *same slope interference* and redefinition of *parallel slope* as *similar slope interference*.

2.3 Interference Analysis

Prior to the measurement campaign, a flexible software simulator for the considered scenarios is set-up. This would enable better identification of measurement set-ups, benchmarking results from measurements and validating the models used. Using the developed software, the link budget analysis was performed and the results are reported in Figure 2.3.

Simulations were performed on MATLAB with the parameters which are indicated in the table next to the figure, keeping in view the indoor sensing capability of the sensor. Considering the operation of victim sensor at room temperature (300K), the average noise power P_n is -68.83dB and the constant false alarm rate (CFAR) threshold typically should be 12dB above the noise floor for a false alarm probability of $6.428 \times 1e-4$. With the TBP gain of 40dB and coherent processing gain of 24dB, the receive power from the target and the interferer is shown in the Figure2.3. The interferer power received at the victim will vary within the region of interference depending upon the amount of pulse compression between the victim and the interferer chirp. This plot provides an explanation to the results shown in Figure2.4, where the receive power of the interferer is always dominating the range-doppler spectrum in similar-slope interference. As evident from the Figure2.3, if the interferer is present in the neighborhood of the target and undergoes a similar-slope interference, target's receive power will only dominate if the target range is less than 5 meters (approx). This shows that the likelihood of the weak targets getting masked by the strong targets is very high.

In Figure2.4, the deterioration of the range-doppler spectrum caused due to similar-slope and sweeping slope interference can be observed when compared with the No interference case. With the help of mitigation techniques such as chirp randomization (start phase change for every chirp, binary phase encoding across transmitted chirps, jittering the chirp repetition time)

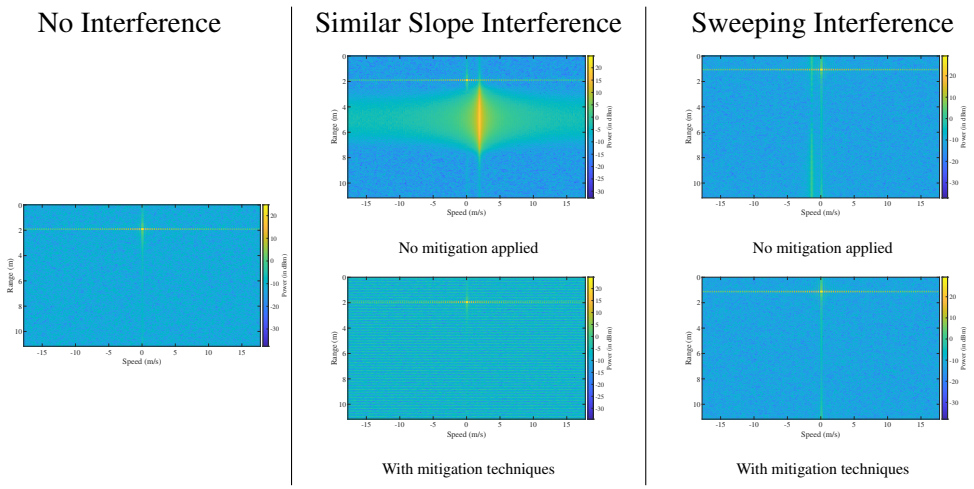

Figure 2.4: Simulation results: Range-Doppler Spectrum in similar-slope and sweeping interference

and inherent non-synchronous nature of the XO, the peak derived from the known interferer is spread across the spectrum [19]. These techniques may save the peak derived from the target from getting masked by the strong interferer peak but it ends up raising the noise-floor. Increment in the noise floor may not be a problem for 1 or 2 interferers in the FoV of the victim sensor as is commonly the case in indoor sensing. In case, the application requires more number of sensors to operate with the same sensor parameters (such as carrier frequency, bandwidth, chirp time etc.), similar slope interference is a bigger problem as compared to the sweeping interference case.

For completely non-deterministic scenarios interference detection can be performed using various approaches such as complex baseband oversampled receiver architecture [16], energy detector and matched filter approaches [20]. For deterministic scenarios, conventional techniques such as time division multiplexing (TDM), frequency division multiplexing (FDM), adaptive beam nulling and time domain localization and sample nulling can be used. In case of TDM, frame based synchronization with global positioning system (GPS) should be performed before chirping happens in any sensor and later the chirping duration of other sensors can be carefully brought into the silent time of the victim sensor. Assuming minor non-linearities in the XO behavior, this technique should be helpful. But, this technique also has an upper bound for the number of sensors that can be accommodated in it as the duty cycle (chirping time / frame time) varies according to the application requirement [21].

As evident from the sensor parameters, the maximum range sensing capability of the sensor is far greater than the required range for indoor application. Further, in these scenarios if multiple sensors have to be employed, the average probability of similar slope interference is low [18].

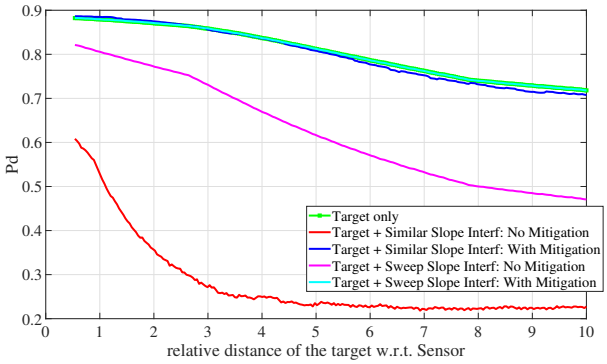

Parameter	Value
Target RCS	0 dBsm
Target range variation	0 to 10m
Target speed	0 m/s
Interferer distance	3.48 m
Interferer Speed	0 m/s
Victim/Interferer Tx Power	12dBm

Figure 2.5: Detection probability vs Range for No Interference, Similar-slope and Sweeping slope interference

Using Monte-Carlo simulations, the worst case similar-slope and sweeping slope interference for Single Input Single Output (SISO) system have been shown in Figure2.5. As evident from the plot, without any mitigation technique applied, the detection probability for similar-slope interference starts rising once the target range is less than 5 metres and is maximum at 0.5m to a value of 0.6. Whereas, with the same receiver properties, the sweeping slope interference starts increasing from 0.45 at range of 10m and increases till 0.84 at 0.5m. With mitigation techniques applied, in the presence of both the types of interference, the detection probability is close to the non-interfered case. Note that these results are indication of a single target - single interferer scenario which is the first case study in Indoor environment. Further, as the number of interferer increases, the mitigation techniques may not perform well and the detection probability is bound to deteriorate significantly. The simplified version of the actual implementation can be found in the Algorithm 1. Details such as object oriented programming (OOP) based implementations and normalization of data at various stages have been omitted to maintain ease of reading.

2.4 Measurement Setup

In this section, we evaluate the effect of interference for indoor scene using *Texas Instrument (TI)* COTS mmWave evaluation modules.

Two types of experimental setups are deployed.

- Indoor sensing: inside a room/ hall or enclosed space with multiple radars operating in each others FoV.

- In-cabin sensing: inside a cabin of a passenger car.

Algorithm 1 derive detection probability and SNR with decreasing range of single target

```
Configure Chirp characteristics of Victim Sensor & Interferer Sensors
Configure Target initial state, dynamics & Reflection property
while target distance ≥ 1 meter do
    for L Chirps do
        Rx Signal ⟵ Tx Signal manipulation: Tx gain, channel gain, Rx gain
        RxSignal ⟵ superimpose the Interferer signal & Rx signal
        RxSignal ⟵ Add thermal noise
        De-chirp Rx Signal with Tx Signal
        RxSignal_composite ⟵ Accumulate current chirp data
    Windowing
    Perform 2D FFT
    Perform OS-CFAR
    Thresholding
    SNR evaluation at known target location
    Update Target location
Evaluate the P_D from the SNR characteristics with range
return P_D = (P_FA)^(1/(1+SNR))
```

In both the cases, the conditions in the FoV were static and no mechanical disturbances were involved.

2.4.1 Indoor Sensing

To this end, we first validate the measurement set-up by using TI web-based graphical user interface (GUI) and *mmWave Studio* as described in following section. Then, we perform a measurement in a controlled environment and validate the result we obtained by simulation.

Test Validation

In order to validate the interference measurement set-up, a test case based on Figure2.6 was created. Here, the victim and interferer sensor hardware was flashed with two different set of sensor parameters which will be further mentioned as configurations (or Config - A and B). TI provides a easy to use web-based GUI and analog-to-digital converter (ADC) data recording software *mmWave Studio - version:02.01.01.00* coupled with *DCA1000 + AWR1642BOOST* evaluation module (mentioned as mmWave GUI and mmStudio respectively in Figure 2.6). Mutual interference of Similar slope type and sweeping type was created using different combinations of configs and the data recorded on mmWave Studio was matched with the mmWave GUI results. Post-processing steps were performed on MATLAB and the analysis results are shown in Figure2.7.

In Figure2.7, the signal level increment in the time domain is the initial confirmation of the

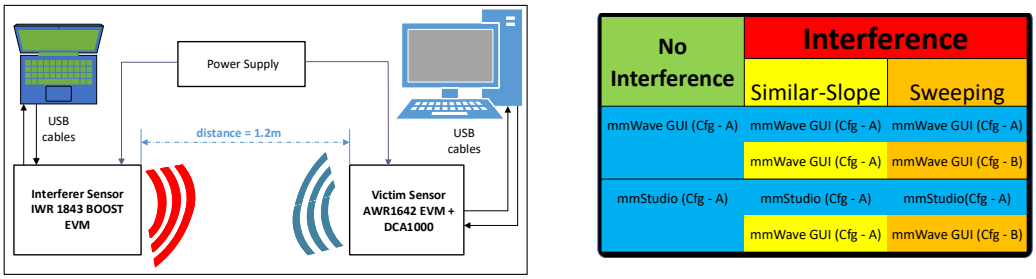

Figure 2.6: Interference validation Setup (left) and different combinations for measurement validation setup (right).

interference occurrence. With minute observation at this level, the peak-to-peak variation in the *similar-slope interference* is higher than the *no interference* case. Further, the glitch is observed in the *sweeping interference* which happens because the interferer chirp is present in the ADC bandwidth of victim for a short duration. The impact of sweeping interference is also evident in the range-doppler spectrum where an overall increment occurs in the noise floor. Average noise floor comparison shows that there is negligible increment between similar slope and no interference case whereas there is a $\sim$ 30dB increment in the case of sweeping interference. This proves the decrements in Signal to Noise Ratio (SNR) which may lead to loss of weak targets.

Indoor Measurement

The tests and measurements were performed in a controlled environment with less clutter from other stray objects as shown in the Figure2.8. The hardware used for Victim radar sensor was: $AWR\ 1642 - BOOST + DCA\ 1000$ and Interferering sensor hardwares were $AWR\ 1443$, $IWR\ 1843 - BOOST$ from TI. As the placement of interferers is almost in the LoS relative to the victim, therefore, mutual interference has been maximized (mutual interference degradation due to azimuthal and elevational variations can be overlooked). The target detection was not impacted despite 3 interferers in the FoV. However, one important assumption in this whole experiment is that the target of interest is expected to have non-zero dopplers and the environment around including the interferers is ought to be static. It results in easy removal of clutter and interfering signal which improves the detection. Finally, this lead us to the conclusion that with carefully designed sensor parameters and mitigation techniques, reliable indoor sensing in the presence of interference can be accomplished using mmWave radar sensors. The table 2.1[1] mentions the chirp parameters of the sensors used for the experiment.

[1] "x" denotes that the parameters are unknown as their tuning was not possible due to limited options in the HW setup of TI-1843

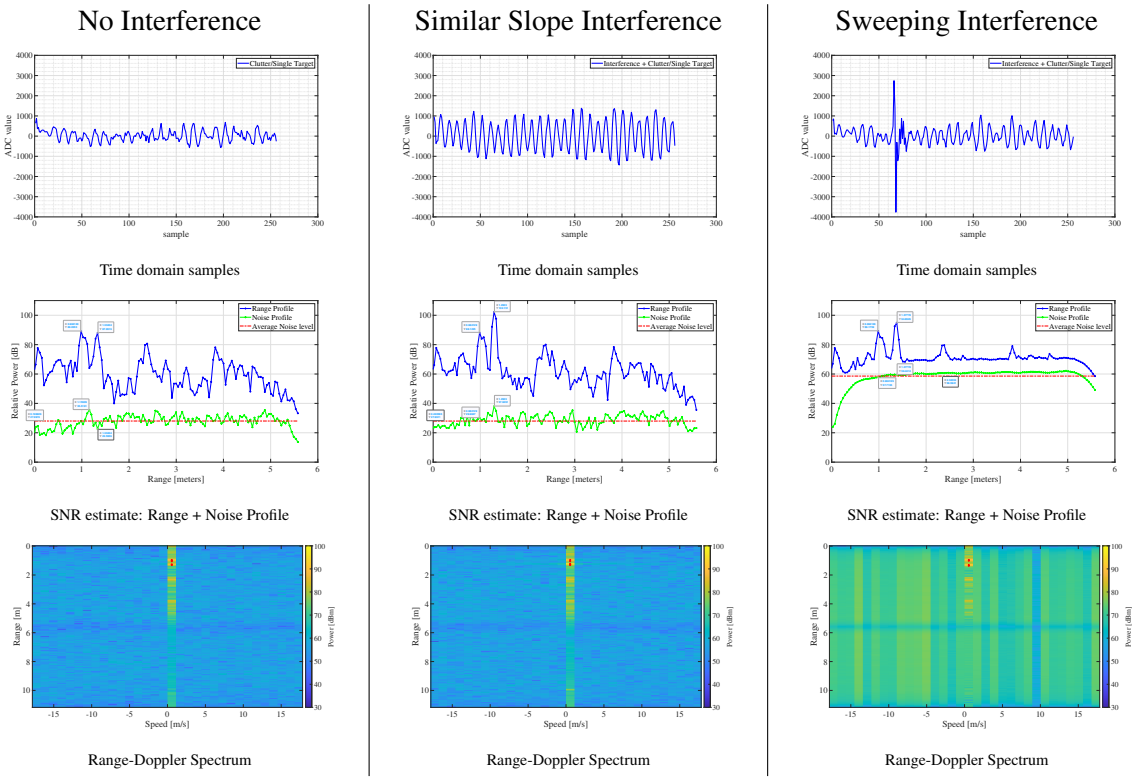

Figure 2.7: Results of mutual interference at hardware level

Table 2.1: Chirp parameters of the sensors used for the experiment in controlled conditions inside a measurement room

	Freq (GHz)	Slope (MHz/us)	Chirp Time (us)	BW (GHz)	Gain (dB)	Sampling Freq (MHz)	Frame Time (ms)
Victim	77.00	29.982	60	1.7982	30	10	40
Interferer 1, 2 and 3	77.00	30	59	1.7845	x	12.49	100

Figure 2.8: Details of the arrangement of the victim and interferer sensors along with the picture of actual measurement setup.

2.4.2 In-cabin sensing in automotive vehicle

Sensor mounting Setup and specifications

In this experimental setup, two radar sensors are mounted inside a car cabin for the purpose of occupancy detection. This type of mounting setup addresses the applications of unattented babies inside a car, vital signs of the car occupants and intruder detection. The mounting setup of the radars is depicted in Figure. The sensor specifications for both the sensors were identical

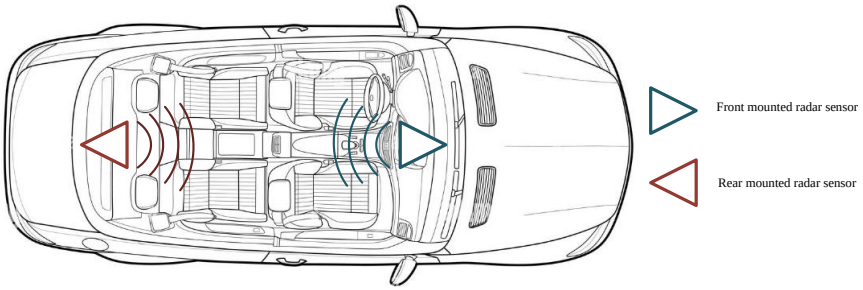

Figure 2.9: In-cabin sensing

and un-synchronized in time. The parameters settings used in this experiment are as described in the Table 2.2.

Table 2.2: Radar sensor specifications and hardware settings

Parameter	Value
ADC Start Time	3.6μs
Burst Period	500μs
Frame Period	50ms
High Pass Filter	350kHz
Idle Period	8μs
MIMO Mode	TDM-MIMO
Number of bursts per frame	32
Number of chirps accumulated per Tx	8
Number of chirps per Burst	2
Number of Rx Antennas	3
Number of samples per chirp	128
Number of Tx Antennas	2
Ramp end time	18μs
Ramp Slope	330 MHz/μs
Sampling rate decimator	10
Start frequency	57GHz
Tx start time	1μs

Received signal processing model

Considering the signal model derived in section 2.2.1, we further derive the energy of the received signal in every frame. The steps to evaluate the signal energy is described in the algorithm 2[2].

Algorithm 2 Received signal energy estimation

Require: $\mathbf{Y}_F, \mathbf{Y}_{F+1}$

while $F \leq$ total recorded frames **do**
  for $l \leftarrow 1$ *to* L **do**
    for $q \leftarrow 1$ *to* Q **do**
      $\mathbf{Z}_{:,L-1,q} = \text{fft}(\mathbf{Y}_F(:, L-1, q))$
      $\mathbf{Z}_{:,L,q} = \text{fft}(\mathbf{Y}_F(:, L, q))$
      $\mathbf{Z}^{MTI}_{:,L,q} = \mathbf{Z}_{:,L,q} - \mathbf{Z}_{:,L-1,q}$
    $\mathbf{rd} = \text{fft}(\mathbf{Z}^{MTI}_{N,:,q}, \text{Doppler})$
  $\mathbf{rda} = \text{fft}(\mathbf{rd}_{N,L,:}, \text{Channel})$
  $\mathbf{E}_F = |\mathbf{rda}|^2_F$

Results

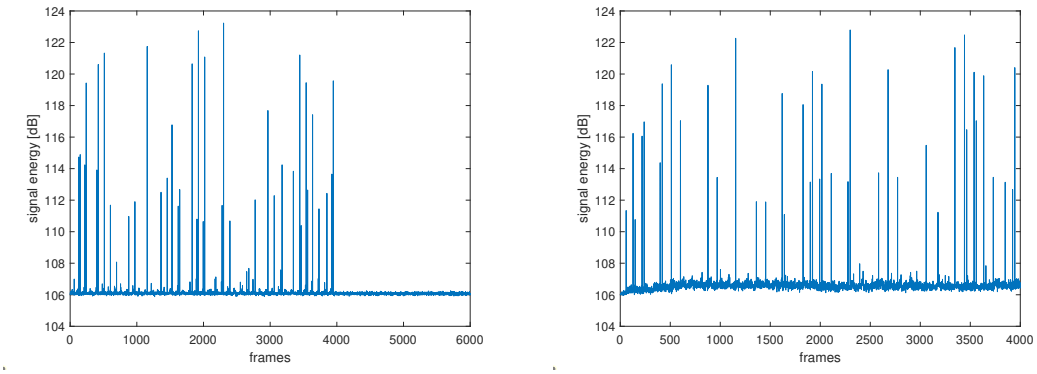

(a) Front Radar (b) Rear Radar

Figure 2.10: Signal energy over multiple frames when both the sensors are operating simultaneously.

The signal energy $\mathbf{E}_F$ in frame F is calculated for the entire recording (consisting of multiple frames) acquired in the experimental setup. In Figure 2.10, the average signal energy is shown for multiple frames when both the sensors are operating simultaneously. We observe multiple spikes (sharp rise and decay in the signal energy) in various frames. As the sensing environment is static, therefore these spikes are a result of strong interference from the other

[2] $|\cdot|_F$ represents the Frobenius norm of the multi-dimensional array

sensor in the experimental setup. The spikes have a peak-to-average energy difference (PAED) of around 16dB. While analyzing multiple recordings that were affected with interference, no periodicity or patterns were observed in the spikes. This indicates that the interference phenomenon is stochastic in nature.

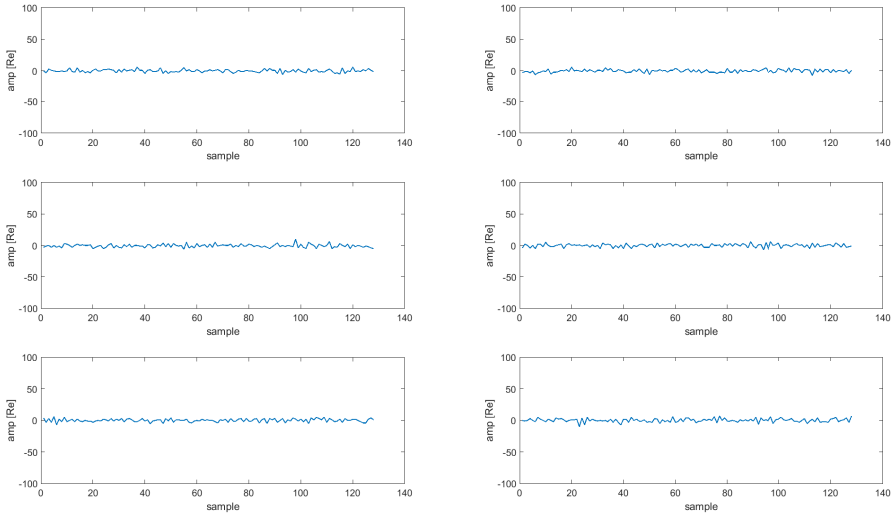

(a) ADC data in normal conditions

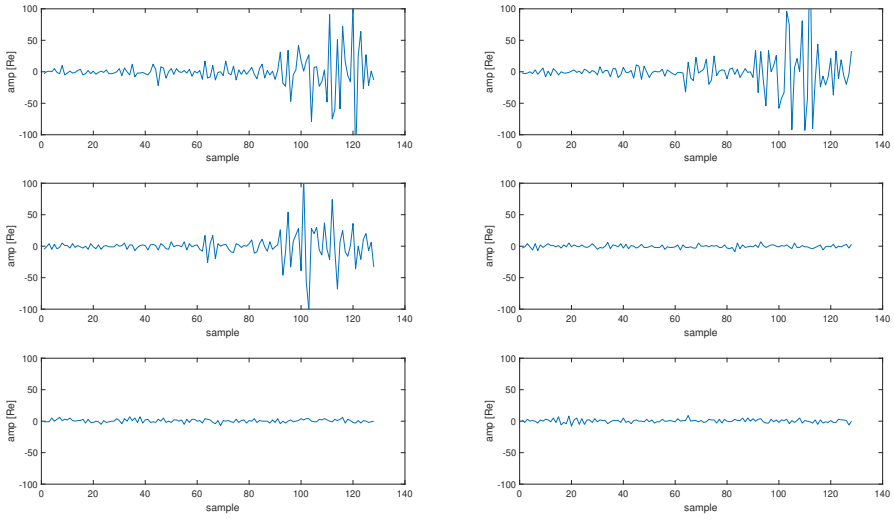

(b) ADC data while interfered

Figure 2.11: Virtual ADC channels for a frame where interference is observed.

In addition, the ADC data for all the virtual channels was analyzed and the results are seen in Figure 2.11. Under normal circumstances, the ADC signal in every channel has a maximum peak-to-peak variation of 20 units as observed in Figure 2.11a. However, when the interference

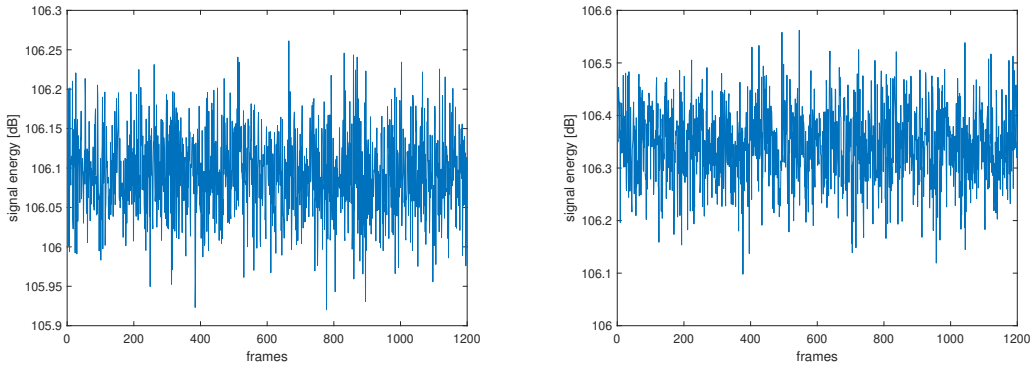

(a) Front Radar (b) Rear Radar

Figure 2.12: Signal energy over multiple frames when one of the sensor is switched off.

occurs, the ADC data for few channels show an unusually high rise in the peak-to-peak variation of around 200 units as observed in the Figure 2.11b. Thus, we were able to precisely identify the frame and pulse in which similar-slope interference was observed. In other, instances, when the sweeping slope interference is observed the ADC channels do not exhibit significant peak-to-peak variation instead it exhibits small impulsive changes in the ADC data.

On the other hand, when either of the sensor is switched off and the other sensor is operating, we do not observe power spikes in any frame as seen in Figure 2.12. This is a strong evidence that interference exists in multi-sensor simultaneous operation only. In addition, it also rules out any other environmental interference or signal artifact that may have been misidentified as MI in the previous case.

2.5 Conclusion

The present work highlights different types of interference possible in the real scenarios in indoor sensing and its impact on the received signal to noise level of the target. It indicates the seriousness of the issue and insists on the need of robust interference mitigation techniques on top of the cognitive handshake mechanisms which must be applied at victim and interferer sensors' end in FMCW radars. In case of PMCW radars, waveform design techniques can be employed to mitigate interference as would be discussed in the upcoming chapters.

Chapter 3

Background and Methodology

3.1 Background and Related Works

3.1.1 SISO Waveform Design Efforts in Dynamic Scenarios

Currently, high-resolution FMCW radar sensors operating at 60GHz, 79GHz, and 140GHz with sometimes finer than 10cm range resolution are becoming integral in a variety of applications ranging from automotive safety and autonomous driving [22, 23], indoor positioning [14, 24] to infant and elderly health monitoring [25]. As the penetration of these low-cost high-performance sensors grows, the likelihood of radar signal interference and the associated ghost target problems also grows [18, 26].

The transmit waveform that is commonly used in a large number of modern millimeter wave (mmWave) radar sensors is based on Linear Frequency Modulation (LFM). LFM is well-known in radar literature due to its distinctive properties of large time-bandwidth product (high pulse compression ratio) and high Doppler-tolerance [27, 28]. In automotive FMCW radars, LFM is typically used as the waveform modulation scheme, since it can be compressed with a very low-cost and efficient technique known-as *de-chirping* operation[1] [29]. The primary benefit of de-chirping is that the received signal can be sampled at much lower rates in comparison to its bandwidth [30–32]. Not surprisingly, this advantage has been motivating many automotive manufactures to build their radar system based on FMCW technology.

Alternatively, polyphase sequences [33, 34] have been proposed as a way to mitigate interference for different applications [34–36]. Using polyphase sequences or PMCW technology, Doppler-tolerant property can be obtained by utilizing a class of codes characterized by a systematic generation formula [35], called chirplike sequences [6], such as Frank [37], P1, P2, P3, and P4 [38], Golomb [39], Chu [40], PAT [41], etc. These codes typically exhibit small

[1] Also referred to as *stretch processing*.

PSL and ISL values in their aperiodic autocorrelation function; however, they are unfortunately sometimes constrained to the specific lengths [6]. Also, due to a lack of uniqueness in these codes, they are equally vulnerable to MI similar to LFM.

In emerging automotive radar application, the radar sensors use FMCW as the standard sensing waveform. Vast deployment of FMCW radars in multiple passenger and commercial vehicles has led to a significant vehicle-to-vehicle radar interference. The interference in all these cases is largely due to simultaneous use of shared spectrum when operating in the detection range of the other sensor and the inherent lack of coordination between radars resulting from the lack of a centralized control and resource allocation mechanism [12, 42, 43].

Further, in this context, FMCW radars experience similar-slope and sweeping slope interference [18], [26] from other sensors operating in the FoV. Even though sweeping interference can be avoided or repaired (using original signal reconstruction), similar-slope interference is hard to manage [26]. In [44], the interference mitigation problems in similar radar systems are addressed with two slow-time coding schemes to modulate the pulses within a coherent processing interval (CPI). Another approach in [45] suggests a waveform design algorithm that seeks to minimize a collective cross-ambiguity function. Overall, the mitigation techniques are able to address both the interference[2] but enhances the average noise resulting in the decrement of SNR [15]. As all the available degrees of freedom (time, operating frequency, bandwidth) to design the FMCW radars has already been exploited, PMCW based sensors are being looked upon as a promising solution to match the sensing performance of FMCW waveform and alleviate the problem of interference.

PMCW radars employ phase codes in their transmitter which are constant modulus and can drive the transmit amplifier at maximum efficiency. These waveforms are highly immune to interference as every radar may employ its own unique phase code with small auto- and cross-correlation sidelobes [34, 48]. On the flip side, it suffers from Doppler intolerance which makes it hard to employ in high-speed applications.

3.1.2 MIMO Waveform Design for Doppler tolerant waveforms

FMCW and PMCW radars are both types of Continuous Wave (CW) radar systems, and they share some similarities. Nevertheless, distinctions arise in their modulation methodologies, with each radar type possessing its unique set of pros and cons. FMCW radar typically requires simpler signal processing compared to PMCW radar. The LFM used in FMCW radar simplifies the processing of the received signals using “de-chirp” [29, 49]. This technique allows sampling the received signal at lower rates than its bandwidth, motivating automotive manufacturers to

[2] Although a comprehensive solution to mutual interference still remains an open issue, there has been some prior work in the design of mitigation techniques to diminish the problem of interference [9, 46, 47].

adopt FMCW-based radar systems for cost-effective radar sensors.

The state-of-the-art mmWave FMCW radar sensors often use Multiple Input Multiple Output (MIMO) technique to create large virtual antennas without increasing the amount of Tx-Rx physical elements [50, 51]. Recently, Radar-on-Chip (RoC) which utilize 24 Tx, 24 Rx antennas (576 virtual channels) [52], and 48 Tx, 48 Rx (2304 virtual channels) [53], have been commercialized [54]. In the context of a MIMO FMCW radar system with a large number of Tx-Rx channels, various multiplexing schemes can be employed to achieve distinct orthogonal waveforms for different channels. Some commonly used multiplexing schemes in the context of MIMO FMCW radar are TDM, Binary Phase Modulation (BPM), Doppler Division Multiplexing (DDM)[55, 56], slow-time Code Division Multiplexing (CDM) [57], and FDM [58]. TDM stands out among them for its prevalence in conventional mmWave MIMO radars due to its hardware simplicity. In TDM-MIMO radars, each transmitter gets a different time slot, ensuring orthogonality in the time domain. However, this multiplexing scheme increases the required time for the transmission and decreases the Doppler resolution. FDM allocates distinct frequency bands to each transmitter, but with an increasing number of antennas, the available frequency spectrum might become limited. DDM and slow-time CDM involve encoding information digitally for transmission, but as the number of antennas increases, the complexity of encoding, decoding, and maintaining orthogonality among the signals becomes more challenging [57].

Yet, as the number of transmit antennas increases, limitations become apparent in these multiplexing approaches for FMCW MIMO radars. In addition, vehicle-to-vehicle radar interference is another uprising issue in this case. The interference in these instances primarily arises from the concurrent use of shared spectrum within the detection range of other sensors, compounded by the absence of centralized control and resource allocation mechanisms, which leads to uncoordinated radar operations. PMCW MIMO radars, despite higher implementation costs, offer potential advantages [23]. They provide intra-pulse CDM, potentially enhancing performance and offering increased degrees of freedom [59]. Additionally, PMCW radars permit waveform optimization, improving their overall efficiency and effectiveness [60].

In this paper, we enhance the scope of designing radar waveforms for FMCW and PMCW MIMO radars by imposing additional polynomial phase constraint to the design problem. This constraint enhances adaptability by allowing for the adjustment of the polynomial degree, serving as a tuning parameter facilitating transitions between PMCW and FMCW radar technologies. Particularly, when the constraint's polynomial degree is set to 2, the resulting quadratic phase polynomials represent chirps characterized by specific slopes, as detailed in [61].

The background to the polynomial phase constraint is grounded in [62], where the first computational approach aimed at designing these sequences was introduced. However, the design

codes in this paper were limited to being piecewise linear. Building upon this, in [49], we utilized the Majorization-Minimization (MM) technique to derive optimal sequences possessing a property of degree Q polynomial in unwrapped phase within their sub-sequences, but only for SISO radar systems. This work achieved optimal solutions for ISL and PSL with guaranteed convergence. In addition to this, in [63], we proposed a subpulse processing-based receiver tailored for radars employing sequences exhibiting polynomial phase behavior within their sub-sequences.

3.1.3 Related Works

Recent research has strengthened the capacity of radar manufacturers to enhance sensor resolution, explore additional degrees of freedom, and introduce novel operational modes through exploiting waveform diversity [64], as evidenced by the number of publications in this domain [65]. In state-of-the-art automotive FMCW MIMO radar, each antenna transmits LFM in a certain manner that guarantees waveform orthogonality [66]. A comprehensive comparison of all the standard techniques can be found in [57]. In addition, other variations of the standard approaches such as fast time - code division multiple access (FT-CDMA) and slow time - code division multiple access (ST-CDMA) are widely used and described in [67–72].

On the other hand, PMCW (spread spectrum, pseudo-noise (PN), and polyphase modulated CW) radars transmit a wide-band code sequence modulated on the carrier frequency. Various optimization approaches have been proposed to achieve orthogonality in code sequences in PMCW MIMO radars using CDM scheme [73–78]. The prevailing approaches in waveform design predominantly prioritize the optimization of constant modulus phase waveforms, primarily relying on the correlation (auto/cross) characteristics of individual signals. Nonetheless, these approaches do not account for the influence of phase shifts induced by dynamic radar platforms in automotive scenarios featuring dynamic targets and stationary detections. In such scenarios, static detections, often disregarded as clutter in conventional sensing applications, assume critical importance. Consequently, the consideration of Doppler tolerance becomes paramount in the formulation of sequence set design challenges.

To this end, several neural network based approaches have also been proposed in this regard [79, 80]. However, while these approaches may demonstrate efficacy in certain predictable scenarios, their reliability is contingent upon the extent of supervised or unsupervised training employed to train the deep Residual Network (RN) and Recurrent Neural Network (RNN). For instance, in environments such as highways, bridges, tunnels and underground parking facilities, where dynamic targets and road blockages due to constructions can alter the detection profile beyond the confines of the known static environment [81, 82], the network models may lack awareness of such variations.

In [36, 67, 83, 84], the authors have presented sequence design methods in the presence of non-negligible Doppler shifts. The limitation here lies in the fact that these approaches cater only to binary/quaternary sequence designs, thereby having limited degrees of freedom in terms of phase allocation. Finally, other approaches for joint MIMO transmit and receive filter design have also been proposed [85–89]. Typically, these approaches deal with maximization of the worst-case SINR over the unknown Doppler and angle of the target of interest. In the case of automotive scenarios, the dilemma is that the target and clutter are not deterministic in nature due to the randomness in the vehicle dynamics (and eventually the radar sensor), necessitating a different problem-solving approach.

3.2 Scenarios of Interest and Assumptions

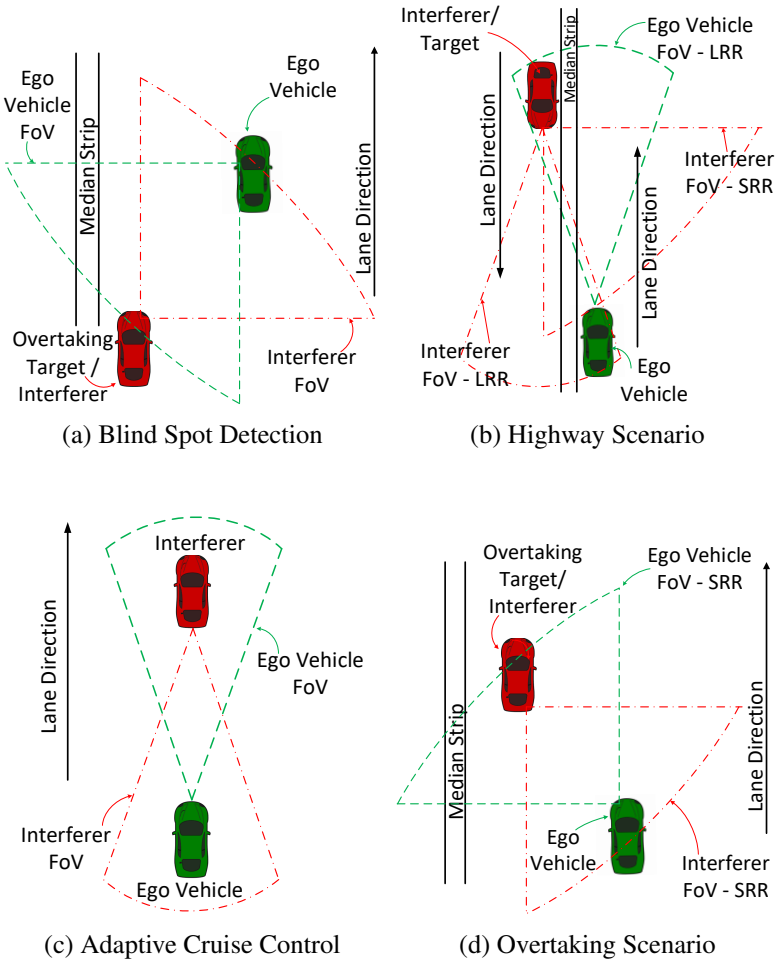

(a) Blind Spot Detection

(b) Highway Scenario

(c) Adaptive Cruise Control

(d) Overtaking Scenario

Figure 3.1: Automotive scenarios with mutual interference.

The scenarios addressed in our research focuses on automotive applications where the sen-

sors and the targets are dynamic in nature.

3.2.1 Every detection is important

Typically, the unwanted detections in other applications, static targets for airborne measurements or dynamic targets for remote sensing applications, standard clutter suppression techniques are used. For example, Moving Target Indicator (MTI) filters for Ground Clutter mitigation in defense applications [90], identification and removal of sea clutter in maritime applications [91, 92], discrimination and characterization of geologic surfaces [93] in remote sensing applications. However, in automotive applications every detection is important to construct a freespace map to maneuver the vehicle through the structured/unstructured environments.

3.2.2 Interference in Automotive Scenarios

In addition to the challenge of radar sensing with dynamic platforms and targets, the challenge of mutual interference from other radar sensors in automotive applications exists. In this context, different scenarios of interest for our research are shown in Figure 3.1. In these highway/ city scenarios the interferer signals appear at random range and Doppler at different instances rendering the radar frame of interest useless for processing. Further, as the market penetration increases for the radar sensors, this issue will become more pronounced due to increase in the probability of interference.

3.2.3 4D Imaging Radars

Synthetic-Aperture Radar (SAR), commonly referred to as imaging radars, uses the motion of the radar antenna over a target region to provide finer spatial resolution than conventional stationary beam-scanning radars. Transmission and reception correspond to separate tiny positions since they happen at different times. The virtual aperture created by the coherent synthesis of the incoming signals is far larger than the antenna's actual width. The phrase "synthetic aperture" refers to this idea, which makes imaging possible with radar systems.

A similar phenomenon known as "virtual aperture" is produced in colocated Multiple Input Multiple Output (MIMO) radars via waveform diversity and sparse antenna placement. This MIMO capacity has significantly aided in the development of automobile radar sensors, which strive to create affordable sensors with excellent resolution and accuracy. It reduces the physical component count of radar sensors while enabling excellent angular resolution. With a broad virtual array in both azimuth and elevation, the recently developed 4D-imaging MIMO radars provide significant benefits over traditional automobile radars, especially when it comes to precisely estimating an object's height.

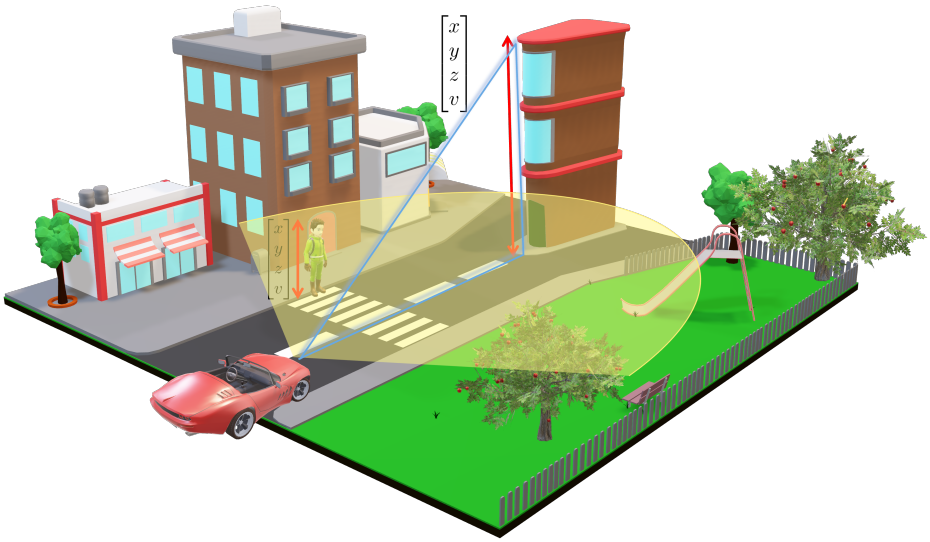

Figure 3.2: 4D Radar Sensing in state-of-the-art technology

Considering the rapidly improving state-of-the-art 4D (three dimensional space + Doppler) mmWave MIMO radar sensors, we considered extending the scope of our research to incorporate the waveform design solutions to the problem of dynamic target sensing under the influence of interference. Typically, the four dimensions are depicted in Figure 3.2. In state-of-the-art chipsets, manufacturers like Arbe create large virtual aperture by employing 48 Tx, 48 Rx (2304 virtual channels) [53] (refer Figure 3.3).

3.2.4 Unrestricted Spatial dimension

In remote sensing, maritime sensing, and communication, the direction of arrival of interfering signals is closely monitored. Upon detection, the receiver processing modifies the spatial domain to create spatial nulls in the direction of the interference. Signals arriving from other directions are prioritized over the interferer's direction, which enhances interference mitigation.

In automotive radar sensing, however, this approach is not feasible, as all directions within the field of view (FoV) are essential for detecting both static and dynamic targets to safely nav-

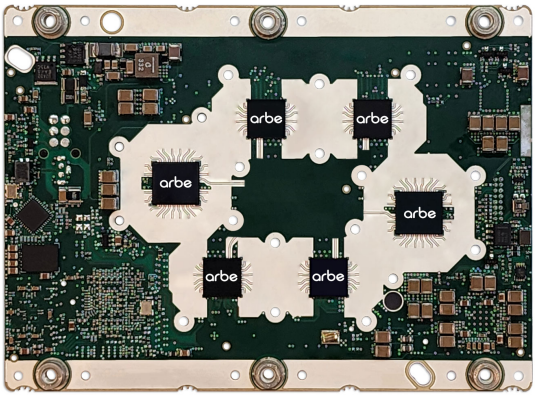

Figure 3.3: Arbe Chipset

igate the vehicle. Implementing spatial nulls would obscure radar coverage in those directions, potentially compromising the sensing and tracking accuracy required by the onboard Electronic Control Units (ECUs) or Sensor Fusion Unit.

In specific scenarios, it may be necessary to limit the wide field of view (FoV) and utilize a narrower FoV. For instance, when a vehicle enters a tunnel where multipath interference could produce excessive targets for the sensor, a narrower FoV can be advantageous. This adjustment enables critical functions, such as Emergency Braking Assistance (EBA) and Adaptive Cruise Control (ACC), to remain effective despite the challenging conditions. This example can be illustrated in Figure 3.4. The beampattern of a MIMO radar sensor with a broad FoV, shown in Figure 6.9a, generates substantial clutter from the tunnel surface and other objects. In contrast, as seen in Figure 6.9b, a narrower beampattern effectively reduces this clutter, allowing essential functions to remain operational.

3.3 Design Methodology

3.3.1 Statistical Analysis

In this study, various statistical analyses were performed to assess interference levels generated by other radar sensors in both SISO and MIMO radar waveforms. The goal was to determine worst-case interference scenarios where the victim and interfering sensors operate simultaneously with complete overlap in each transmission pulse.

The interference analysis in both simulations and hardware primarily focused on a single victim and single interferer sensor arrangement. In some cases, multiple interferers were also examined. However, statistical analysis to establish reliable operational limits for scenarios with

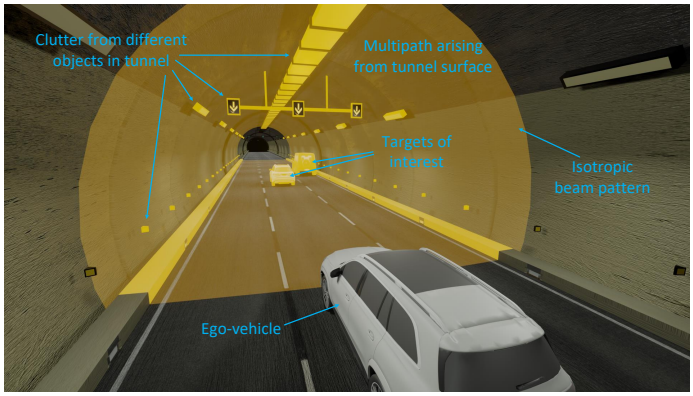

(a) Beampattern of the state-of-the-art MIMO radar for outdoor sensing

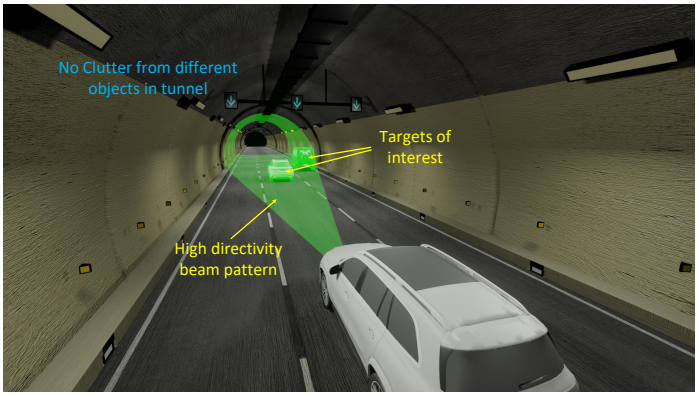

(b) Beampattern adaptation for a cognitive MIMO radar inside a tunnel using algorithm-10

Figure 3.4: Case Study: Beampattern adaptation to avoid ghost object formation inside a tunnel

N sensors, where $N \geq 100$, is beyond the scope of this study.

3.3.2 Experimental Work and Limitations

There were different experimental analysis performed in this study. In order to emulate the outdoor sensing, a Universal Software Radio Peripheral (USRP) based experimental setup was used. The parameters:

- Operating frequency
- Bandwidth
- Pulse repetition frequency
- Static Targets
- Static Victim Sensor

- Static Interferer Sensor

had to be adjusted according to the available hardware - USRP X310 in the laboratory.

On the other hand, in the actual analysis for an automotive car in-cabin sensing, two COTS sensors from TI were used. As this experiment was focused to identify interference in static conditions of in-cabin monitoring, no dynamic targets/interferers were involved.

3.3.3 Waveform Design

MIMO radar waveform design problems have been studied in [94, 95] and the references there in. In this study, we have focused our work on transmit waveform design for colocated MIMO radars. We seek to establish a framework for designing waveforms with polynomial phase characteristics within every sub-sequence for improving the sensing performance of dynamic targets. The sole thread in this study has been introducing quadratic phase behavior in every transmitted pulse. By introducing the quadratic phase behavior in the waveform and maximizing the time-bandwidth product (optimizing the ISL/PSL), the Doppler tolerance of every pulse can be is improved.

LFM waveforms used in FMCW radars are Doppler tolerant, and under identical operational specifications (such as bandwidth, pulse width and operating frequency) cause MI with other radars due to high correlation. Therefore, to cater to this issue, a single pulse has been broken down into multiple sub-pulses. Further, every sub-pulse characteristic has been evaluated in the proposed framework to generate MIMO radar waveforms which are immune to interference. In this context, the receiver design problem is focused on Subpulse processing [96] to achieve high TBP for the joint transmit - receive MIMO waveform design for radars.

Part II

SISO Radar Waveform Design and Implementation

Chapter 4

Designing Interference-Immune Doppler-Tolerant Waveforms for Radar Systems

Preamble

This chapter is the first part of our SISO sequence design problem. In this manuscript, we present a waveform design framework known as PECS, which designs a sequence with optimal aperiodic auto-correlation sidelobes. As discussed in the section: 1.5 and marked as $J2$, this chapter introduces a novel constraint of polynomial phase behavior in every subsequence/sequence in the ISL/PSL minimization problem using ℓ_p norm minimization of the autocorrelation sidelobes.

By using the proposed algorithm and varying the input parameters, we analyzed different properties of a sequence such as ambiguity function, Doppler tolerance and interference immunity. We showcased that the proposed method offers superior performance and is a reliable solution for the rising issue of interference in automotive radars by statistically analyzing the cross-correlations of multiple sequences over multiple trials.

4.1 Manuscript: Designing Interference-Immune Doppler-Tolerant Waveforms for Radar Systems

Robin Amar[1], Mohammad Alaee-Kerahroodi[1], Prabhu Babu,[2], Bhavani Shankar M.R.[1]

[1] SnT - Interdisciplinary Centre for Security, Reliability and Trust, University of Luxembourg

[2] Centre for Applied Research in Electronics (CARE), IIT Delhi

Published in: *IEEE Transactions on Aerospace and Electronic Systems,* vol. 59, no. 3, pp. 2402-2421, June 2023,
DOI: 10.1109/TAES.2022.3215116

The following sections are a copy of the paper referenced above.

Abstract

Dynamic target detection using LFM waveform is challenging in the presence of interference for different radar applications. Degradation in SNR is irreparable and interference is difficult to mitigate in time and frequency domain. In this paper, a waveform design problem is addressed using the Majorization-Minimization (MM) framework by considering PSL/ISL cost functions, resulting in a code sequence with Doppler-tolerance characteristics of an LFM waveform and interference immune characteristics of a tailored polyphase sequence (unique phase code + minimal ISL/PSL). The optimal design sequences possess polynomial phase behavior of degree Q amongst its sub-sequences and obtain optimal ISL and PSL solutions with guaranteed convergence. By tuning the optimization parameters such as degree Q of the polynomial phase behavior, sub-sequence length M and the total number of sub-sequences L, the optimized sequences can be as Doppler tolerant as LFM waveform in one end, and they can possess small cross-correlation values similar to random-phase sequences in polyphase sequence on the other end. The numerical results indicate that the proposed method is capable to computationally design chirplike sequences which prior to this work, were obtained by mimicking phase variations of LFM waveform. An application of the proposed method for the automotive scenario is also illustrated in the numerical results.

4.2 Introduction

RADAR has traditionally been associated with military and law enforcement applications due to its development, but it is now a common solution for civil situations. Currently, high-resolution FMCW radar sensors operating at 60GHz, 79GHz, and 140GHz with sometimes finer than 10cm range resolution are becoming integral in a variety of applications ranging from automotive safety and autonomous driving [22, 23], indoor positioning [14, 24] to infant and elderly health monitoring [25]. As the penetration of these low-cost high-performance sensors grows, the

likelihood of radar signal interference and the associated ghost target problems also grows [18, 26].

The transmit waveform that is commonly used in a large number of modern millimeter wave (mmWave) radar sensors is based on LFM. LFM is well-known in radar literature due to its distinctive properties of large time-bandwidth product (high pulse compression ratio) and high Doppler-tolerance [27, 28]. In automotive FMCW radars, LFM is typically used as the waveform modulation scheme, since it can be compressed with a very low-cost and efficient technique known-as *de-chirping* operation[1] [29]. The primary benefit of de-chirping is that the received signal can be sampled at much lower rates in comparison to its bandwidth [30–32]. Not surprisingly, this advantage has been motivating many automotive manufactures to build their radar system based on FMCW technology. Alternatively, polyphase sequences [33, 34] have been proposed as a way to mitigate interference for different applications [34–36]. Using polyphase sequences or PMCW technology, Doppler-tolerant property can be obtained by utilizing a class of codes characterized by a systematic generation formula [35], called chirplike sequences [6], such as Frank [37], P1, P2, P3, and P4 [38], Golomb [39], Chu [40], PAT [41], etc

These codes typically exhibit small PSL and ISL values in their aperiodic autocorrelation function; however, they are unfortunately sometimes constrained to the specific lengths [6]. Also, due to a lack of uniqueness in these codes, they are equally vulnerable to MI similar to LFM. We aim to overcome this limitation in this paper by proposing a framework for designing constant modulus polyphase Doppler-tolerant sequences that are also immune to interference for variety of radar applications.

4.2.1 Doppler-Tolerant Waveforms

When a target is stationary, i.e., the Doppler distortions of the returned radar signals can be neglected, then correlation or matched-filter processing is relatively straight-forward [97]. In those applications where high resolution requirements and high target speeds combine, the distortions in the waveform lead to severe degradations, and a knowledge of the Doppler shift of the target should be available, or a bank of mismatched filter needs to be considered in the receive side to compensate loss in SNR [98]. However, using so-called Doppler-invariant waveforms in the transmit side is a simpler alternative approach to dealing with high Doppler shifts. In this case, even in the presence of an arbitrarily large Doppler shift, the received signal remains matched to the filter, but a range-Doppler coupling may occur as an unintended consequence [97].

It is known that FMCW technology utilizes LFM waveform and has the Doppler-tolerant property by its nature. Thus, a possible solution to build PMCW with Doppler-tolerant proper-

[1] Also referred to as *stretch processing*.

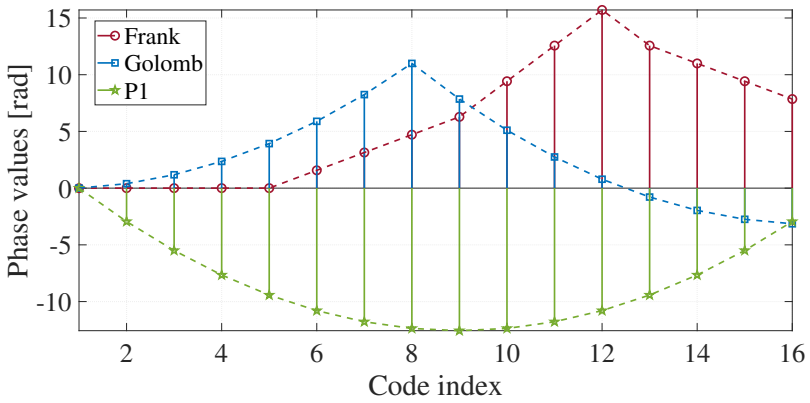

Figure 4.1: The unwrapped phase values of three polyphase codes of length $N = 16$: Frank, Golomb, and P1.

ties is to mimic the behaviour of FMCW waveforms by using the phase history of a pulse with linearly varying frequency, which leads to chirplike polyphase sequences [6]. Indeed, because frequency is the derivative of phase, in order to have linear frequency properties like FMCW, the phase variation of PMCW sequences should be quadratic throughout the length of the sequence, as shown in Figure 4.1 for Frank, Golomb, and P1 sequences of length $N = 16$. Interestingly, chirplike polyphase sequences are known to typically have good autocorrelation properties with respect to random-phase sequences in terms of PSL and/or ISL values[2], the metrics which are strictly connected to the sharpness of the code autocorrelation function [59, 98–105].

Recently, several studies have considered the design of polyphase sequences with good Doppler tolerance properties [106–113]. In [106] Linear-FM Synthesized (LFM-Syn) waveform has been proposed to achieve low range sidelobes and high Doppler tolerance in the synthesized waveform. The study combines the random noise waveform and the conventional LFM waveform. In [110] a Coordinate Descent (CD)-based approach is proposed for designing waveform with high Doppler tolerance properties. In both [106] and [110], a template-matching objective function is established and optimized to obtain waveforms with low range sidelobes and high Doppler tolerance properties. Unlike the template matching approaches, in [62] a computational approach is proposed for designing polyphase sequences with *piecewise linear phase properties*. Despite the fact designing Frank-like sequences was considered in this paper, the overall quadratic phase trend of this sequence was not taken into account during the proposed optimization framework. As a result, the optimization method mentioned in it does not result in Doppler-tolerant waveforms. Different from designing waveform with Doppler tolerance properties, several studies like [77, 114–116] have considered the problem of shaping AF by

[2]PSL shows the maximum autocorrelation sidelobe of a transmit waveform. If this value is not small, then either a false detection or a miss detection may happen. Similar properties hold for ISL of transmitting waveforms where the energy of autocorrelation sidelobes should be small to mitigate the deleterious effects of distributed targets.

minimizing sidelobes on range-Doppler plane around the origin to improve the detection performance. However, the optimized waveform by these studies is not resilient to Doppler shifts.

In Table 4.1, we mention relevant approaches in the literature to the problem considered in this paper. Primarily, we categorize them into three broad parts: Ambiguity function shaping, ISL/PSL minimization and ℓ_p norm minimization. Unlike the aforementioned references, the

Approach	Paper
Ambiguity function shaping	[108–110, 114, 117]
ISL/PSL minimization	[62, 73, 83, 101]
ℓ_p **norm**	[100, 102, 118]
Others	[45, 119–124]

Table 4.1: Different approaches available in literature

problem addressed in this paper provides a generic framework which has the characteristics of constant modulus, polynomial phase behavior and ISL/PSL minimization using ℓ_p norm.

4.2.2 Interference in FMCW Radars

Interference is a well-known and unavoidable problem in many fields. In emerging automotive radar application, the radar sensors use FMCW as the standard sensing waveform. Vast deployment of FMCW radars in multiple passenger and commercial vehicles has led to a significant vehicle-to-vehicle radar interference. The interference in all these cases is largely due to simultaneous use of shared spectrum when operating in the detection range of the other sensor and the inherent lack of coordination between radars resulting from the lack of a centralized control and resource allocation mechanism [12, 42, 43].

Further, in this context, FMCW radars experience similar-slope and sweeping slope interference [18], [26] from other sensors operating in the FoV. Even though sweeping interference can be avoided or repaired (using original signal reconstruction), similar-slope interference is hard to manage [26]. In [44], the interference mitigation problems in similar radar systems are addressed with two slow-time coding schemes to modulate the pulses within a coherent processing interval (CPI). Another approach in [45] suggests a waveform design algorithm that seeks to minimize a collective cross-ambiguity function. Overall, the mitigation techniques are able to address both the interference[3] but enhances the average noise resulting in the decrement of SNR [15]. As all the available degrees of freedom (time, operating frequency, bandwidth) to design the FMCW radars has already been exploited, PMCW based sensors are being looked upon as a promising solution to match the sensing performance of FMCW waveform and alleviate the problem of interference.

[3] Although a comprehensive solution to mutual interference still remains an open issue, there has been some prior work in the design of mitigation techniques to diminish the problem of interference [9, 46, 47].

PMCW radars employ phase codes in their transmitter which are constant modulus and can drive the transmit amplifier at maximum efficiency. These waveforms are highly immune to interference as every radar may employ its own unique phase code with small auto- and cross-correlation sidelobes [34, 48]. On the flip side, it suffers from Doppler intolerance which makes it hard to employ in high-speed applications. This is overcome by the proposed framework in this paper which includes the Doppler tolerance property as an additional advantage. The technique suggested in this study refers to a class of constant-modulus sequences whose phase belongs to the range $[0, 2\pi]$ and whose sub-sequences are more constrained to exhibit polynomial phase behavior. This restriction is included primarily to offer a new degree of freedom, which principally offers the potential of constructing a unimodular waveform with Doppler-tolerant features, which was not previously addressed in the literature. Following Golomb, Frank, etc., this research can be seen as the first study to build chirplike sequences computationally. It should be noted that chirplike sequences had previously been created by simulating the phase behavior of the LFM, but in this study they are created computationally.

4.2.3 Contribution

The idea of this framework is to design polyphase sequences that have good Doppler-tolerance properties and sharp autocorrelation functions. Unlike FMCW, potentially distinct PMCW sequences meeting these requirements exist. This richness in selection of PMCW sequences allows for better interference management than FMCW. In this context, we propose a methodology for generating such a rich set of sequences which can be integrated into existing optimization-based waveform design tools (like Cyclic Algorithm New (CAN) [99], monotonic minimizer for integrated sidelobe level (MISL) [118], Monotonic Minimizer for the ℓ_p-norm of autocorrelation sidelobes (MM-PSL) [100], etc.) to provide the designed waveforms with Doppler tolerance properties.

The main contributions of this work can be summarized as follows:

- *Optimization framework*: The problem formulation leads to an objective function which considers the design of phase sequences with polynomial behavior while simultaneously considering other important properties like ISL and PSL. Although ISL and PSL minimization has been considered earlier, but all these properties are not addressed simultaneously in literature.

- *Doppler tolerance*: The optimization problem can handle phase sequences with a degree Q polynomial behavior while building on the literature of ℓ_p norm minimization for generic objective subsuming ISL and PSL. Using MM based approach, we design sequences with superior properties as compared to the conventional sequences mentioned

in literature. Doppler tolerance property arises in a sequence when its phase changes in a quadratic manner (i.e. $Q = 2$). As this is being handled directly in the objective function, the resultant sequence is bound to have better performance for moving targets.

- *Flexibility of design - divide and conquer interference*: This approach offers the flexibility of having multiple sub-sequences, designed in parallel while optimizing the ISL and PSL of the entire sequence. Since each sub-sequence has unique polynomial phase coefficients of degree Q, length, and code, the entire sequence can avoid interference. This provides an additional degree of freedom for waveform design by partitioning the entire sequence into multiple sub-sequences of varying lengths which enables us to tune the optimization variable and generate diverse waveforms whose AF is varying from *Thumbtack type* on one extreme to *Doppler-Tolerant* type on the other end. The proposed formulation provides the possibility of designing sequences of any length N with piecewise polynomial phase behavior amongst its L sub-sequences each of length M_l where $N = M_1 + M_2 + \cdots + M_L$ if the sub-sequences have different lengths. This approach can be considered for the scenarios in which sequence lengths other than perfect square (unlike Frank) are required.

- *Application in automotive scenarios*: A simulation environment is created which generates various automotive scenarios where interference is possible. Using the proposed optimization framework, different sequences have been generated and utilized to interfere with each other. The results of the simulation indicate high interference immunity in sensing. This alleviates the necessity for the requirement of additional sensing and communication protocol for safe operation in dense automotive scenarios where MI is possible amongst multiple cars equipped with radar sensors.

Finally, by using the proposed method, one can construct many new such polyphase sequences which were not known and/or could not be constructed by the previous formulations in the literature. Thus, the proposed approach is capable of generating unique sequences which in turn would lead to decrement in the interference amongst multiple sensors operating in the nearby region.

4.2.4 Organization and Notations

Notation: Boldface upper case letters denote matrices, bold-face lower case letters denote column vectors, and italics denote scalars. $\mathbb{Z}$, $\mathbb{R}$ and $\mathbb{C}$ denote the integer, real and complex field, respectively. $\Re(\cdot)$ and $\Im(\cdot)$ denote the real and imaginary part respectively. $\arg(\cdot)$ denotes the phase of a complex number. The superscripts $(\cdot)^T$, $(\cdot)^*$, $(\cdot)^H$ and $(\cdot)^\dagger$ denote transpose, complex conjugate, conjugate transpose, and pseudo-inverse respectively. $X_{i,j}$ denotes the $(i,j)^{th}$

element of a matrix and x_i denotes the i^{th} element of vector $\mathbf{x}$. $\mathrm{Diag}(\boldsymbol{X})$ is a column vector consisting of all the diagonal elements of $\boldsymbol{X}$. $\mathrm{Diag}(\mathbf{x})$ is a diagonal matrix formed with $\mathbf{x}$ as its principal diagonal. $\mathrm{vec}(\boldsymbol{X})$ is a column vector consisting of all the columns of $\boldsymbol{X}$ stacked.

4.3 Problem Formulation

Let $\{x_n\}_{n=1}^{N}$ be the transmitted complex unit-modulus radar code sequence of length N. The aperiodic autocorrelation of the transmitting waveform at lag k (e.g. matched filter output at the PMCW radar receiver) is defined as

$$r_k = \sum_{n=1}^{N-k} x_n x_{n+k}^* = r_{-k}^*, \quad k = 0, \ldots, N-1. \tag{4.1}$$

The ISL and PSL can be mathematically defined by

$$\mathrm{ISL} = \sum_{k=1}^{N-1} |r_k|^2, \tag{4.2}$$

$$\mathrm{PSL} = \max_{k=1,2,\ldots,N-1} |r_k|. \tag{4.3}$$

It is clear that the ISL metric is the squared ℓ_2-norm of the autocorrelation sidelobes. Further, the ℓ_∞-norm of autocorrelation sidelobes of a sequence is the PSL metric. These can, in fact, be generalized by considering the ℓ_p norm, $p \geq 2$ which offers additional flexibility in design while subsuming ISL and PSL. In general ℓ_p-norm metric of the autocorrelation sidelobes is defined as

$$\left(\sum_{k=1}^{N-1} |r_k|^p \right)^{1/p}, \quad 2 \leq p < \infty. \tag{4.4}$$

Sequences are designed to minimize the various ℓ_p norm metric in literature [100, 102, 118, 125, 126]. It is known that in general longer the code, better are the ISL/PSL [100], but the system suffers from high design complexity. One possible solution for reducing complexity is to design long sequences with multiple segments, which is considered in this paper. Let the sequence $\{x_n\}_{n=1}^{N}$ be partitioned into L sub-sequences each having length of M_l, where $l = 1, 2, \ldots, L$ such that every sub-sequence of it, say

$$\widetilde{\mathbf{x}}_l = [x_{\{1,l\}}, \cdots, x_{\{m,l\}}, \cdots, x_{\{M_l,l\}}]^T \in \mathbb{C}^{M_l}, \tag{4.5}$$

has a polynomial phase, which can be expressed as

$$\arg(x_{\{m,l\}}) = \sum_{q=0}^{Q} a_{\{q,l\}} m^q, \tag{4.6}$$

where $m = 1, 2, \ldots, M_l$ and $a_{\{q,l\}}$ is the Q^{th} degree polynomial coefficient for the phase of the l-th sub-sequence with $q \in \{0, 1, 2, \ldots, Q\}$. It can be observed that the length of each sub-sequence can be arbitrarily chosen. The problem of interest is to design the code vector $\{x_n\}_{n=1}^{N}$ with a generic polynomial phase of a degree Q in its sub sequences while having impulse-like autocorrelation function. Therefore, by considering $\sum_{k=1}^{N-1} |r_k|^p$ as the objective function, the optimization problem can be compactly written as

$$\mathcal{P}_1 \begin{cases} \underset{a_{\{q,l\}}}{\text{minimize}} & \displaystyle\sum_{k=1}^{N-1} |r_k|^p \\ \text{subject to} & \arg(x_{\{m,l\}}) = \displaystyle\sum_{q=0}^{Q} a_{\{q,l\}} m^q, \\ & |x_{\{m,l\}}| = 1, \end{cases} \tag{4.7}$$

where $m = 1, \ldots, M_l$, and $l = 1, \ldots, L$.

Figure 4.2 depicts the workflow of the proposed method, called PECS, in which the code sequence $\{x_n\}_{n=1}^{N}$ is divided into different segments, which are designed to have a polynomial phase behavior during its code entries. In $\mathcal{P}_1$, the polynomial phase constraint is introduced with the intention of designing waveforms with arbitrary polyphase constraints in their sub-sequences. By setting $Q = 2$, the constraint forces the optimization problem to produce chirp-like sequences, which have the Doppler-tolerant properties. Indeed, LFM signal is recognized as a waveform that maintains a constant compression factor in the matched filter output of the received signal, even when there is a Doppler shift in the received signal [6, 27]. Due to this property, LFM is known as a Doppler tolerant waveform [127], ch. 7, pg. 264-265. In this context, our goal is to offer a framework for the analytical design of polyphase sequences that replicate the behavior of the LFM waveform.

In the following section, we propose an efficient algorithm to design a set of sub-sequences with polynomial phase relationship of degree Q amongst its sub-sequences based on MM framework.

The MM (majorization-minimization) - is an approach to solve optimization problems that are difficult to solve directly. The principle behind the MM method is to transform a difficult problem into a series of simple problems. Suppose, we want to minimize $f(\mathbf{x})$ over $\boldsymbol{\chi} \subseteq \mathbb{C}$. Instead of minimizing the cost function $f(\mathbf{x})$ directly, the MM approach optimizes the

sequence of approximate objective functions that majorize $f(\mathbf{x})$. More specifically, starting from a feasible point $\mathbf{x}^{(0)}$, the algorithm produces a sequence $\mathbf{x}^{(i)}$ according to the following update rule

$$\mathbf{x}^{(i+1)} \in \underset{\mathbf{x}\in\boldsymbol{\chi}}{\arg\min}\, u(\mathbf{x}, \mathbf{x}^{(i)}), \tag{4.8}$$

where $\mathbf{x}^{(i)}$ is the point generated by the algorithm at iteration i, and $u(\mathbf{x}, \mathbf{x}^{(i)})$ is the majorization function of $f(\mathbf{x})$ at $\mathbf{x}^{(i)}$. Formally, the function $u(\mathbf{x}, \mathbf{x}^{(i)})$ is said to majorize the function $f(\mathbf{x})$ at the point $\mathbf{x}^{(i)}$ if [128],

$$\begin{aligned} u(\mathbf{x}, \mathbf{x}^{(i)}) \geq & f(\mathbf{x}), \forall \mathbf{x} \in \boldsymbol{\chi}, \\ u(\mathbf{x}^{(i)}, \mathbf{x}^{(i)}) = & f(\mathbf{x}^{(i)}), \\ \nabla u(\mathbf{x}^{(i)}, \mathbf{x}^{(i)}) = & \nabla f(\mathbf{x}^{(i)}). \end{aligned} \tag{4.9}$$

In other words, function $u(\mathbf{x}, \mathbf{x}^{(i)})$ is an upper bound of $f(\mathbf{x})$ over $\boldsymbol{\chi}$ and coincides with $f(\mathbf{x})$ at $\mathbf{x}^{(i)}$. To summarize, in order to minimize $f(\mathbf{x})$ over $\boldsymbol{\chi} \subseteq \mathbb{C}^n$, the main steps of the majorization-minimization scheme are:

1. Find a feasible point $\mathbf{x}^{(0)}$ and set $i = 0$.
2. Construct a function $u(\mathbf{x}, \mathbf{x}^{(i)})$ that majorizes $f(\mathbf{x})$ at $\mathbf{x}^{(i)}$ and is easier to optimize.
3. Let $\mathbf{x}^{(i+1)} \in \underset{\mathbf{x}\in\boldsymbol{\chi}}{\arg\min}\, u(\mathbf{x}, \mathbf{x}^{(i)})$.
4. If some convergence criterion is met, exit; otherwise, set $i = i + 1$ and go to step (2).

It is easy to show that with this scheme, the objective value is monotonically decreasing at every iteration, i.e.,

$$f(\mathbf{x}^{(i+1)}) \leq u(\mathbf{x}^{(i+1)}, \mathbf{x}^{(i)}) \leq u(\mathbf{x}^{(i)}, \mathbf{x}^{(i)}) = f(\mathbf{x}^{(i)}). \tag{4.10}$$

The first inequality and the third equality follow from the properties of the majorization function, namely (4.9) and the second inequality follows from (4.8). The monotonicity makes MM algorithms very stable in practice. For more details on MM framework, refer [125, 129, 130] and references therein.

4.4 Proposed Method

The optimization problem mentioned in (4.7) is hard to solve since each r_k is quadratically related to $\{x_n\}_{n=1}^N$ and each $\{x_n\}_{n=1}^N$ is non-linearly related to $a_{\{q,l\}}$. Moreover, the ℓ_p norm of autocorrelation sidelobes becomes difficult to solve using classical optimization approach. As a result MM is considered and after several majorization steps (refer Appendix-xx), simplifies to

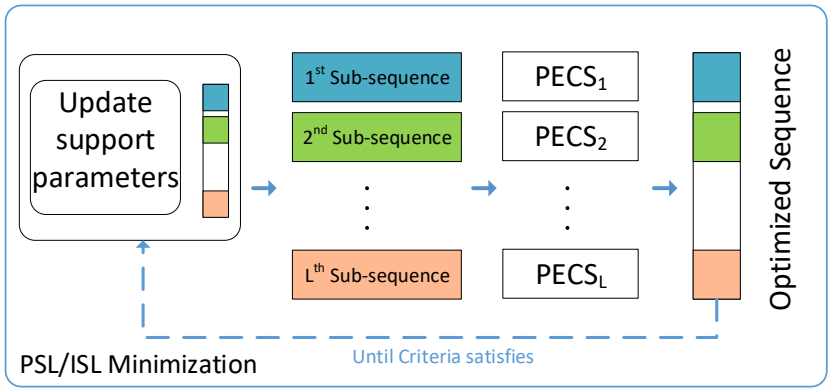

Figure 4.2: Workflow of PECS for PSL/ISL Minimization.

the following optimization problem

$$\mathcal{P}_2 \begin{cases} \underset{a_{\{q,l\}}}{\text{minimize}} & ||\mathbf{x}-\mathbf{y}||_2 \\ \text{subject to} & \arg(x_{\{m,l\}}) = \sum_{q=0}^{Q} a_{\{q,l\}} m^q, \\ & |x_{\{m,l\}}| = 1, \end{cases} \tag{4.11}$$

where

$$\mathbf{y} = (\lambda_{\max}(\boldsymbol{L})N + \lambda_u)\,\mathbf{x}^{(i)} - \widetilde{\boldsymbol{R}}\mathbf{x}^{(i)} \in \mathbb{C}^N,$$

with $\lambda_{\max}, \boldsymbol{L}, \lambda_u$ and $\widetilde{\boldsymbol{R}}$ defined in Appendix xx. Note that in [100] the polynomial phase constraint was not considered. Since the objective in (4.11) is separable in the sequence variables, the minimization problem can now be split into L sub-problems (each of which can be solved in parallel). Let us define, $\boldsymbol{\rho} = |\mathbf{y}|$, and $\boldsymbol{\psi} = \arg(\mathbf{y})$, where ρ_n and ψ_n, $n = 1, 2, \ldots, N$, are the magnitude and phase of every entry of $\mathbf{y}$, respectively. Also, for ease of notation let us assume that the polynomial phase coefficients and sub-sequence length of the l-th sub-sequence, say $a_{\{q,l\}}$ and M_l are indicated as $\widetilde{a}_q$ and $\widetilde{M}$ respectively. Thus, dropping the subscript-l, each of the sub-problem can be further defined as

$$\mathcal{P}_3 \begin{cases} \underset{\widetilde{a}_q}{\text{minimize}} & \sum_{m=1}^{\widetilde{M}} \left| e^{j(\sum_{q=0}^{Q} \widetilde{a}_q m^q)} - \rho_m e^{j\psi_m} \right|^2, \end{cases} \tag{4.12}$$

where we have considered the unimodular and polynomial phase constraints of Problem $\mathcal{P}_2$ directly in the definition of the code entries in Problem $\mathcal{P}_3$. Further, the above problem can be

simplified as

$$\left\{ \underset{\widetilde{a}_q}{\text{minimize}} \quad -\left[\sum_{m=1}^{\widetilde{M}} \rho_m \cos\left(\sum_{q=0}^{Q} \widetilde{a}_q m^q - \psi_m \right) \right]. \right. \tag{4.13}$$

The ideal step would be to minimize the majorized function in (4.13) for $\widetilde{a}_q$ given the previous value of $\widetilde{a}_q^{(i)}$, the objective function can be upper-bounded (at a given $\widetilde{a}_q^{(i)}$). However, since the optimization variables are in the argument of the cosine function in the objective of 4.13, the solution to this problem is not straight-forward. Hence, we resort to a second MM step. Towards this, let us define[4]

$$\theta_m = \sum_{q=0}^{Q} \widetilde{a}_q m^q - \psi_m, \tag{4.14}$$

a majorizer ($g(\theta_m, \theta_m^{(i)})$) of the function $f(\theta_m) = -\rho_m \cos(\theta_m)$ can be obtained by

$$\begin{aligned} g(\theta_m,\theta_m^{(i)}) = -\rho_m \cos(\theta_m^{(i)}) + (\theta_m - \theta_m^{(i)})\rho_m \sin(\theta_m^{(i)}) + \\ \frac{1}{2}(\theta_m - \theta_m^{(i)})^2 \rho_m \cos(\theta_m^{(i)}) \geq -\rho_m cos(\theta_m), \end{aligned} \tag{4.15}$$

where θ_m is the variable and $\theta_m^{(i)}$ is the phase value of the last iteration. This follows from exploiting the fact that if a function is continuously differentiable with a Lipschitz continuous gradient, then second order Taylor expansion can be used as a majorizer [125]. Using the aforementioned majorizer function, at i-th iteration of MM algorithm, the optimization problem

$$\mathcal{P}_4 \left\{ \begin{array}{ll} \underset{\widetilde{a}_q}{\text{minimize}} & \sum_{m=1}^{\widetilde{M}} \Bigg[-\rho_m \cos(\theta_m^{(i)}) + \\ & \left(\theta_m - \theta_m^{(i)}\right) \rho_m \sin(\theta_m^{(i)}) \\ & + \frac{1}{2}\left(\theta_m - \theta_m^{(i)}\right)^2 \rho_m \cos(\theta_m^{(i)}) \Bigg] \end{array} \right. \tag{4.16}$$

The objective function in (4.16) can be rewritten into perfect square form and the constant terms independent to the optimization variable $\widetilde{a}_q$ can be ignored. Thus, a surrogate optimization problem deduced from (4.16) is given below

$$\mathcal{P}_5 \left\{ \underset{\widetilde{a}_q}{\text{minimize}} \quad \sum_{m=1}^{\widetilde{M}} \left[\rho_m \cos(\theta_m^{(i)}) \left(\sum_{q=0}^{Q} \widetilde{a}_q m^q \right) - \widetilde{b}_m \right]^2 \right. \tag{4.17}$$

where $\widetilde{b}_m = \rho_m \cos(\theta_m^{(i)}) \left(\psi_m + \theta_m^{(i)}\right) - \rho_m \sin(\theta_m^{(i)})$.

[4] θ_m depends on the optimization variables $\widetilde{a}_q$.

Table 4.2: Supporting parameters for Algorithm 3 [5].

S.No	Parameter	Relation
1	$\boldsymbol{F}$	$2N \times 2N$ FFT Matrix with $F_{m,n} = e^{-j\frac{2mn\pi}{2N}}$
2	f	$\boldsymbol{F}[\mathbf{x}^{(i)T}, \mathbf{0}_{1\times N}]$
3	$\mathbf{r}$	$\frac{1}{2N}\boldsymbol{F}^H\lvert\mathbf{f}\rvert^2$
4	t	$\lvert\lvert\mathbf{r}_{2:N}\rvert\rvert_p$
5	a_k	$\frac{1+(p-1)\left(\frac{\lvert r_{k+1}\rvert}{t}\right)^p - p\left(\frac{\lvert r_{k+1}\rvert}{t}\right)^{p-1}}{(t-\lvert r_{k+1}\rvert)^2}$
6	$\hat{w}_k$	$\frac{p}{2t^2}\left(\frac{\lvert r_{k+1}\rvert}{t}\right)^{p-2}, k = 1, \ldots, N-1$
7	$\tilde{\mathbf{c}}$	$\mathbf{r} \circ [\hat{w}_1, \ldots, \hat{w}_{N-1}, 0, \hat{w}_{N-1}, \ldots, \hat{w}_1]^T$
8	$\widetilde{\boldsymbol{\mu}}$	$\boldsymbol{F}\tilde{\mathbf{c}}$
9	λ_L	$\max_k\{\tilde{\alpha}_k(N-k) \lvert k = 1, \ldots, N\}$
10	λ_u	$\frac{1}{2}(\max_{(1\le\tilde{i}\le N)}\tilde{\mu}_{2\tilde{i}} + \max_{(1\le\tilde{i}\le N)}\tilde{\mu}_{2\tilde{i}-1})$

Algorithm 3 PECS

Require: Seed sequence $\mathbf{x}^{(0)}$, N, $\widetilde{M}$, L and p
Ensure: $\mathbf{x}$

Set $i = 0$, initialize $\mathbf{x}^{(0)}$.
while stopping criterion is not met **do**
  Calculate $\boldsymbol{F}, \widetilde{\boldsymbol{\mu}}, \mathbf{f}, \lambda_L, \lambda_u$ from Table 4.2
  $\mathbf{y} = \mathbf{x}^{(i)} - \frac{\boldsymbol{F}_{:,1:N}(\widetilde{\boldsymbol{\mu}}\circ\mathbf{f})}{2N(\lambda_L N+\lambda_u)}$
  $\boldsymbol{\psi} = \arg(\boldsymbol{y}) \mid \boldsymbol{\psi} = [\widetilde{\boldsymbol{\psi}}_1^T, \cdots, \widetilde{\boldsymbol{\psi}}_L^T]^T \in \mathbb{R}^N$
  $\boldsymbol{\rho} = \lvert\mathbf{y}\rvert \mid \boldsymbol{\rho} = [\widetilde{\boldsymbol{\rho}}_1^T, \cdots, \widetilde{\boldsymbol{\rho}}_L^T]^T \in \mathbb{R}^N$
  for $l \leftarrow 1$ *to* L **do**
    $\widetilde{\boldsymbol{\psi}}_l = [\psi_1, \cdots, \psi_{\widetilde{M}}]^T \in \mathbb{R}^{\widetilde{M}}$
    $\widetilde{\boldsymbol{\rho}}_l = [\rho_1, \cdots, \rho_{\widetilde{M}}]^T \in \mathbb{R}^{\widetilde{M}}$
    $\theta_m^{(i)} = \sum_{q=0}^{Q}\widetilde{a}_q m^q - \psi_m,\ m = 1, \ldots, \widetilde{M}$
    $\widetilde{b}_m = \rho_m\cos\theta_m^{(i)}\left(\psi_m + \theta_m^{(i)}\right) - \rho_m\sin\theta_m^{(i)}$
    $\boldsymbol{\eta} = [1, 2, 3, \cdots, \widetilde{M}]^T \in \mathbb{Z}_+^{\widetilde{M}}$
    $\boldsymbol{\gamma} = \rho_m\cos(\theta_m^{(i)}) \odot [1, \cdots, 1]^T \in \mathbb{R}^{\widetilde{M}}$,
    $\widetilde{\boldsymbol{A}} = \mathrm{Diag}\,(\boldsymbol{\gamma})[\boldsymbol{\eta}^0, \boldsymbol{\eta}^1, \cdots, \boldsymbol{\eta}^Q] \in \mathbb{R}^{\widetilde{M}\times Q+1}$,
    $\mathbf{z} = [\widetilde{a}_0, \widetilde{a}_1, \cdots, \widetilde{a}_Q]^T \in \mathbb{R}^{Q+1}$
    $\widetilde{\mathbf{b}} = [\widetilde{b}_1, \widetilde{b}_2, \cdots, \widetilde{b}_{\widetilde{M}}]^T \in \mathbb{R}^{\widetilde{M}}$
    $\mathbf{z}^\star = \widetilde{\boldsymbol{A}}^{(\dagger)}\widetilde{\mathbf{b}}$
    $\widetilde{\mathbf{x}}_l = e^{(j(\widetilde{\boldsymbol{A}}\mathbf{z}^\star))}$
  $\mathbf{x}^{(i+1)} = [\widetilde{\mathbf{x}}_1^T, \widetilde{\mathbf{x}}_2^T, \cdots, \widetilde{\mathbf{x}}_L^T]^T \in \mathbb{C}^N$
  $i \leftarrow i + 1$
return $\mathbf{x}^{(i+1)}$

Now, considering a generic sub-sequence index l we define

$$\boldsymbol{\eta} = [1, 2, 3, \cdots, \widetilde{M}]^T \in \mathbb{Z}_+^{\widetilde{M}},$$

$\boldsymbol{\eta}^q$ implying each element of $\boldsymbol{\eta}$ is raised to the power of q, $q = 0, 1, \ldots, Q$. Further,

$$\begin{aligned}
\boldsymbol{\gamma} &= \rho_m \cos(\theta_m^{(i)}) \odot [1, \cdots, 1]^T \in \mathbb{R}^{\widetilde{M}}, \\
\widetilde{\boldsymbol{A}} &= \mathrm{Diag}\,(\boldsymbol{\gamma})[\boldsymbol{\eta}^0, \boldsymbol{\eta}^1, \cdots, \boldsymbol{\eta}^Q] \in \mathbb{R}^{\widetilde{M} \times Q+1}, \\
\mathbf{z} &= [\widetilde{a}_0, \widetilde{a}_1, \cdots, \widetilde{a}_Q]^T \in \mathbb{R}^{Q+1}, \\
\widetilde{\mathbf{b}} &= [\widetilde{b}_1, \widetilde{b}_2, \cdots, \widetilde{b}_{\widetilde{M}}]^T \in \mathbb{R}^{\widetilde{M}},
\end{aligned} \tag{4.18}$$

the optimization problem in (4.17) can be rewritten as

$$\Big\{ \underset{\mathbf{z}}{\text{minimize}} \quad ||\widetilde{\boldsymbol{A}}\mathbf{z} - \widetilde{\mathbf{b}}||_2^2, \tag{4.19}$$

which is the standard Least Squares (LS) problem. As a result, the optimal $\mathbf{z}^\star = \widetilde{\boldsymbol{A}}^{(\dagger)}\widetilde{\mathbf{b}} = [\widetilde{a}_0^\star, \widetilde{a}_1^\star, \cdots, \widetilde{a}_Q^\star]^T$ would be calculated[5] and the optimal sequence will be synthesized.

Using the aforementioned setup for a generic sub-sequence index l, we calculate all the $\widetilde{\mathbf{x}}_l$s pertaining to different sub-sequences and derive $\{x_n\}_{n=1}^N$ by concatenating all the $\widetilde{\mathbf{x}}_l$s. The algorithm successively improves the objective and an optimal value of $\mathbf{x}$ is achieved. Details of the implementation for the proposed method in the form of pseudo code are summarized in Algorithm 3 and would be referred further as PECS.

Remark 1. *Convergence of the proposed method*
It is easy to show that with the proposed scheme, the objective value is monotonically decreasing at every iteration. Let us assume that $\mathbf{x}^{(i)}$ is the point generated by the algorithm at iteration i, and $u(\mathbf{x}, \mathbf{x}^{(i)})$ is the majorization function of $f(\mathbf{x})$ at $\mathbf{x}^{(i)}$. Then,

$$f(\mathbf{x}^{(i+1)}) \leq u(\mathbf{x}^{(i+1)}, \mathbf{x}^{(i)}) \leq u(\mathbf{x}^{(i)}, \mathbf{x}^{(i)}) = f(\mathbf{x}^{(i)}). \tag{4.20}$$

The first inequality and the third equality follow from the fact that for every feasible $\mathbf{x}$

$$u(\mathbf{x}, \mathbf{x}^{(i)}) \geq f(\mathbf{x}), \tag{4.21}$$

and the second inequality is clear since,

$$u(\mathbf{x}^{(i)}, \mathbf{x}^{(i)}) = f(\mathbf{x}^{(i)}). \tag{4.22}$$

This monotonic decrement in the objective function makes the proposed method very stable in practice. Given the convergence property of MM detailed in section 4.3, the monotonic decrement of the objective function can be guaranteed.

[5]We can use "lsqr" in *Sparse Matrices Toolbox* of MATLAB 2021a to solve (4.19).

Remark 2. *Computational complexity*
Assuming L sub-sequences are processed in parallel, the computational complexity of Algorithm - 1 can be derived by dividing the complete set of operations into two major steps.

- *computational cost of deriving the supporting parameters: $\mathbf{f}$, $\mathbf{r}$, t, $\mathbf{a}$ and $\hat{\mathbf{w}}$ mentioned in Table I. Here, the order of computational complexity is $\boldsymbol{O}(2N)$ real additions/subtractions, $\boldsymbol{O}(Np)$ real multiplications, $\boldsymbol{O}(N)$ real divisions and $\boldsymbol{O}(N\log_2 N)$ for Fast Fourier Transform (FFT).*

- *computational load for the least squares operation in every iteration of the algorithm. We assume $M_1 = M_2 = \cdots = M_l = M$ for simplicity, therefore, the complexity of least squares operation: $\boldsymbol{O}(M^2Q)$ + $\boldsymbol{O}(Q^2M)$ + $\boldsymbol{O}(QM)$ real matrix multiplications and $\boldsymbol{O}(Q^3)$ real matrix inversion [131] [132]. It should be noted that there may be some other approaches that are less computationally expensive than matrix inversion, which is used here.*

Therefore, the overall computational complexity is $\boldsymbol{O}(M^2Q)$ (provided $M > Q$ which is true in general).

In case the L sub-sequences are processed sequentially, the complexity increases by an amount proportional to the number of sub-sequences required in a given sequence. As this is defined in the algorithm by the variable L, therefore the overall complexity in the sequential processing is $\boldsymbol{O}(M^2LQ)$.

Extension of other methods to PECS

In the previous section, by applying a constraint of Q-th degree polynomial phase variation on the sub-sequences, we have addressed the problem of minimizing the autocorrelation sidelobes to obtain optimal ISL/PSL of the complete sequence using ℓ_p norm minimization with the method MM-PSL.

In this section, we extend other methods, such as MISL [118] and CAN [99], to enable us to design sequences with polynomial phase constraints.

Extension of MISL

In [118], the ISL metric minimization is addressed with a different approach. As discussed previously in (4.2), it is just the squared ℓ_2-norm of the autocorrelation sidelobes. Therefore, the ISL minimization problem under piece-wise polynomial phase constraint of degree Q can

be written as follows

$$\mathcal{M}_1 \begin{cases} \underset{a_{\{q,l\}}}{\text{minimize}} & \sum_{k=1}^{N-1} |r_k|^2 \\ \text{subject to} & \arg(x_{\{m,l\}}) = \sum_{q=0}^{Q} a_{\{q,l\}} m^q, \\ & |x_{\{m,l\}}| = 1, \;\; m = 1, \ldots, M, \\ & \qquad\qquad l = 1, \ldots, L. \end{cases} \tag{4.23}$$

where $a_{\{q,l\}}$ indicate the coefficients of l-th segment of the optimized sequence whose phase varies in accordance to the degree of the polynomial Q. It has been shown in [99] that the ISL metric of the aperiodic autocorrelations can be equivalently expressed in the frequency domain as

$$\text{ISL} = \frac{1}{4N} \sum_{g=1}^{2N} \left[\left| \sum_{n=1}^{N} x_n e^{-j\omega_g (n-1)} \right|^2 - N \right]^2 \tag{4.24}$$

where $\omega_g = \frac{2\pi}{2N}(g-1)$, $g = 1, ..., 2N$. Let us define $\mathbf{x} = [x_1, x_2, \ldots, x_N]^T$, $\mathbf{b}_g = [1, e^{j\omega_g}, ..., e^{j\omega_g (N-1)}]^T$, where $g = 1, \ldots, 2N$.
Therefore, writing (4.24) in a compact form

$$\text{ISL} = \sum_{g=1}^{2N} \left(\mathbf{b}_g^H \mathbf{x}\mathbf{x}^H \mathbf{b}_g \right)^2 \tag{4.25}$$

The ISL in (4.25) is quartic with respect to $\mathbf{x}$ and its minimization is still difficult. The MM based algorithm (MISL) developed in [118] computes a minimizer of (4.25). So given any sequence $\mathbf{x}$, the surrogate minimization problem in MISL algorithm is given by

$$\mathcal{M}_2 \begin{cases} \underset{a_{\{q,l\}}}{\text{minimize}} & \Re(\mathbf{x}^H (\grave{\boldsymbol{A}} - 2N^2 \mathbf{x}^{(i)} (\mathbf{x}^{(i)^H})) \mathbf{x}^{(i)}) \\ \text{subject to} & \arg(x_{\{m,l\}}) = \sum_{q=0}^{Q} a_{\{q,l\}} m^q \\ & |x_{\{m,l\}}| = 1. \end{cases} \tag{4.26}$$

where $\boldsymbol{A} = [b_1, \ldots, b_{2N}]$, $\mathbf{f}^{(i)} = |\boldsymbol{A}^H \mathbf{x}^{(i)}|^2$, $f_{max}^{(i)} = \max_f \{ f_g^{(i)} : g = 1, \ldots, 2N \}$, $\grave{\boldsymbol{A}} =$

$\mathbf{A}(\mathrm{Diag}(\mathbf{f}^{(i)}) - f_{\max}^{(i)}\mathbf{I})\mathbf{A}^H$. The problem in (4.26) can be rewritten as

$$\begin{cases} \underset{a_{\{q,l\}}}{\text{minimize}} & \|\mathbf{x}-\mathbf{y}\|_2 \\ \text{subject to} & \arg(x_{\{m,l\}}) = \sum_{q=0}^{Q} a_{\{q,l\}} m^q \\ & |x_{\{m,l\}}| = 1. \end{cases} \tag{4.27}$$

where $\mathbf{y} = -\mathbf{A}(\mathrm{Diag}(\mathbf{f}^{(i)}) - f_{\max}^{(i)}\mathbf{I})\mathbf{A}^H\mathbf{x}^{(i)}$. Once the optimization problem in (4.27) is achieved, i.e $\mathcal{M}_3$, it is exactly equal to the problem in (4.11), i.e. $\mathcal{P}_2$ and hence its solution can be pursued further. The details of the implementation can be found in Algorithm 4 and 5.

Algorithm 4 PECS subroutine

procedure PECS($\mathbf{y}^{(i)}, L, \widetilde{M}, a_{q,l}^{(i)}$)
  $\boldsymbol{\psi} = \arg(\boldsymbol{y}) \mid \boldsymbol{\psi} = [\widetilde{\boldsymbol{\psi}}_1^T, \cdots, \widetilde{\boldsymbol{\psi}}_L^T]^T \in \mathbb{R}^N$
  $\boldsymbol{\rho} = |\mathbf{y}| \mid \boldsymbol{\rho} = [\widetilde{\boldsymbol{\rho}}_1^T, \cdots, \widetilde{\boldsymbol{\rho}}_L^T]^T \in \mathbb{R}^N$
  for $l \leftarrow 1$ *to* L **do**
    $\widetilde{\boldsymbol{\psi}}_l = [\psi_1, \cdots, \psi_{\widetilde{M}}]^T \in \mathbb{R}^{\widetilde{M}}$
    $\widetilde{\boldsymbol{\rho}}_l = [\rho_1, \cdots, \rho_{\widetilde{M}}]^T \in \mathbb{R}^{\widetilde{M}}$
    $\theta_m^{(i)} = \sum_{q=0}^{Q} \widetilde{a}_q m^q - \psi_m,\ m = 1, \ldots, \widetilde{M}$
    $\widetilde{b}_m = \rho_m \cos\theta_m^{(i)} \left(\psi_m + \theta_m^{(i)}\right) - \rho_m \sin\theta_m^{(i)}$
    $\boldsymbol{\eta} = [1, 2, 3, \cdots, \widetilde{M}]^T \in \mathbb{Z}_+^{\widetilde{M}}$
    $\boldsymbol{\gamma} = \rho_m \cos(\theta_m^{(i)}) \odot [1, \cdots, 1]^T \in \mathbb{R}^{\widetilde{M}}$,
    $\widetilde{\boldsymbol{A}} = \mathrm{Diag}\,(\boldsymbol{\gamma})[\boldsymbol{\eta}^0, \boldsymbol{\eta}^1, \cdots, \boldsymbol{\eta}^Q] \in \mathbb{R}^{\widetilde{M}\times Q+1}$,
    $\mathbf{z} = [\widetilde{a}_0, \widetilde{a}_1, \cdots, \widetilde{a}_Q]^T \in \mathbb{R}^{Q+1}$
    $\widetilde{\mathbf{b}} = [\widetilde{b}_1, \widetilde{b}_2, \cdots, \widetilde{b}_{\widetilde{M}}]^T \in \mathbb{R}^{\widetilde{M}}$
    $\mathbf{z}^\star = \widetilde{\boldsymbol{A}}^{(\dagger)}\widetilde{\mathbf{b}}$
    $\widetilde{\mathbf{x}}_l = e^{(j(\widetilde{\boldsymbol{A}}\mathbf{z}^\star))}$
  $\mathbf{x}^{(i+1)} = [\widetilde{\mathbf{x}}_1^T, \widetilde{\mathbf{x}}_2^T, \cdots, \widetilde{\mathbf{x}}_L^T]^T \in \mathbb{C}^N$
return $\mathbf{x}^{(i+1)}$

Extension of CAN

In addition to the above mentioned procedure using MISL, the optimization problem in (4.23) can also be addressed using CAN method [99]. As opposed to the approach pursued in [118] of directly minimizing a quartic function, in [99] the solution of the objective function in (4.23) is

Algorithm 5 Optimal sequence with minimum ISL and polynomial phase parameters $a_{\{q,l\}}$ using MISL

Require: N, L and $\widetilde{M}$
Ensure: $\mathbf{x}^{(i)}$
1: Set $i = 0$, initialize $\mathbf{x}^{(0)}$
2: **while** Stopping criterion is not met **do**
3: $\quad \mathbf{f} = \left|\mathbf{A}^H \mathbf{x}^{(i)}\right|^2$
4: $\quad f_{\max} = \max(\mathbf{f})$
5: $\quad \mathbf{y}^{(i)} = -\mathbf{A}\left(\mathrm{Diag}(\mathbf{f}) - f_{\max}\mathbf{I} - N^2\mathbf{I}\right)\mathbf{A}^H\mathbf{x}^{(i)}$
6: $\quad \mathbf{x}^{(i+1)} = \mathrm{PECS}(\mathbf{y}^{(i)}, L, \widetilde{M}, \widetilde{a}_q^{(i)})$
7: **return** $\mathbf{x}^{(i+1)}$

assumed to be "almost equivalent" to minimizing a quadratic function [121]

$$\underset{\{x_n\}_{n=1}^N;\{\psi_g\}_{g=1}^{2N}}{\text{minimize}} \sum_{g=1}^{2N} \left| \sum_{n=1}^{N} x_n e^{-j\omega_g n} - \sqrt{N} e^{j\psi_g} \right|^2 . \tag{4.28}$$

It can be written in a more compact form (to within a multiplicative constant)

$$||\boldsymbol{A}^H \bar{\mathbf{x}} - \mathbf{v}||^2 \tag{4.29}$$

where $\mathbf{a}_g^H = [e^{-j\omega_g}, \cdots, e^{-j2N\omega_g}]$ and $\boldsymbol{A}^H$ is the following unitary $2N \times 2N$ Discrete Fourier Transform (DFT) matrix

$$\boldsymbol{A}^H = \frac{1}{\sqrt{2N}} \begin{bmatrix} \mathbf{a}_1^H \\ \vdots \\ \mathbf{a}_{2N}^H, \end{bmatrix} \tag{4.30}$$

$\bar{\mathbf{x}}$ is the sequence $\{x_n\}_{n=1}^N$ padded with N zeros, i.e. $\bar{\mathbf{x}} = [x_1, \cdots, x_N, 0, \cdots, 0]_{2N\times 1}^T$ and $\mathbf{v} = \frac{1}{\sqrt{2}}[e^{j\psi_1}, \cdots, e^{j\psi_{2N}}]^T$. For given $\{x_n\}$, CAN minimizes (4.29) by alternating the optimization between $\bar{\mathbf{x}}$ and $\mathbf{v}$. Let $\bar{\mathbf{x}}^{(i)} = [x_1^{(i)}, \cdots, x_N^{(i)}, 0, \cdots, 0]_{2N\times 1}^T$, and let D_i represent the value of $||\boldsymbol{A}^H\bar{\mathbf{x}}^{(i)} - \mathbf{v}^{(i)}||$ at iteration i. Then we have $D_{i-1} \geq D_i$. Further in the i^{th} iteration, the objective can be minimized using the technique proposed for solving (4.11) by assuming

$$\begin{aligned} &\mathbf{x} = \bar{\mathbf{x}}^{(i)}, \\ &\mathbf{y} = e^{j\arg(\mathbf{d})}, \;\; \mathbf{d} = \boldsymbol{A}\mathbf{v}^{(i)} \end{aligned} \tag{4.31}$$

in the objective function of (4.11). The details of the implementation can be found in Algorithm 6.

Algorithm 6 Optimal sequence with minimum ISL and polynomial phase parameters $a_{\{q,l\}}$ using CAN

Require: N, L and $\widetilde{M}$
Ensure: $\mathbf{x}^{(i)}$
1: Set $i = 0$, initialize $\mathbf{x}^{(0)}$.
2: **while** Stopping criterion is not met **do**
3: $\quad \mathbf{f} = \mathbf{A}^H \bar{\mathbf{x}}^{(i)}$
4: $\quad v_g = e^{j(\arg(f_g))},\ g = 1, \ldots, 2N$
5: $\quad \mathbf{d} = \mathbf{A}\mathbf{v}^{(i)}$
6: $\quad y_n^{(i+1)} = e^{j(\arg(d_n))},\ n = 1, \ldots, N$
7: $\quad \mathbf{x}^{(i+1)} = \text{PECS}(\mathbf{y}^{(i)}, L, \widetilde{M}, \widetilde{a}_q^{(i)})$
8: **return** $\mathbf{x}^{(i+1)}$

4.5 Performance Analysis

In this section, we assess the performance of the proposed PECS algorithm[6] and compare it with prior work in the literature. We then emphasize its potential to design sequences for various automotive radar applications while considering the effects of Doppler and interference.

4.5.1 ℓ_p norm Minimization

At first, we evaluate the performance of the proposed Algorithm-3 in terms of ℓ_p norm minimization by several examples. For the initialization, we chose a random seed sequence and $Q = 2$.

Figure 4.3 shows the convergence behaviour of the proposed algorithm when the simulation is mandatorily run for 10^6 iterations. We chose different values of p (i.e. 2, 5, 10, 100 and $1e3$) as an input parameter of the Algorithm-3, these allow to trade-off between good PSL and ISL. For this figure, we keep the values of sequence length, sub-sequence length and polynomial degree fixed, by setting $N = 300$, $M = 5$, and $Q = 2$. Nevertheless, we observed similar behaviour in the convergence for the different values of N, M, and Q.

As evident from the Figure 4.3, the objective function is reduced rapidly for $p = 2$ and this rate reduces with the objective saturating after 10^5 iterations. Whereas, by increasing the value of p to $5, 10$ and 100, we achieve similar convergence rate as observed earlier. Uniquely, while computing the ℓ_{1000} norm[7], the objective converges slowly and continues to decrease until 10^6 iterations.

Further, while analysing the autocorrelation sidelobes in Figure 4.3 for the same set of input

[6]Source code is available at "https://github.com/robin-amar/ResearchPapers/blob/eb83e644c164ac998bac7820268ee5929563583e/PECS.m"

[7]Computationally, we cannot use $p = \infty$, but by setting p to a tractable value, e.g., $p \geq 10$, we find that the peak sidelobe is effectively minimized.

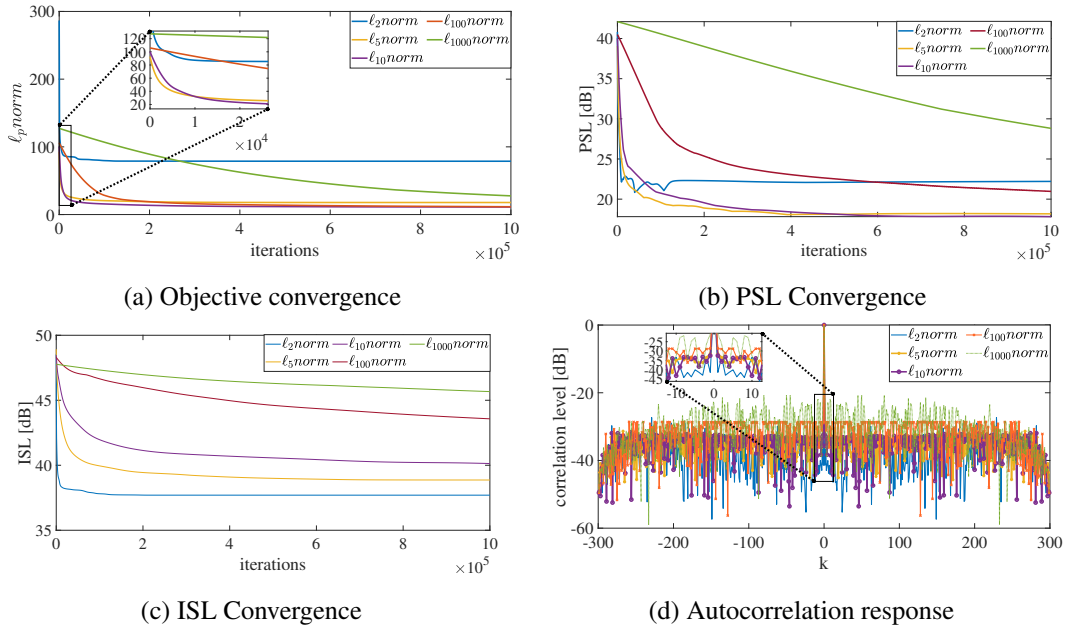

(a) Objective convergence

(b) PSL Convergence

(c) ISL Convergence

(d) Autocorrelation response

Figure 4.3: ℓ_p norm convergence, PSL convergence and Autocorrelation comparison with varying p in ℓ_p norm for a sequence with input parameters $N = 300, M = 5, Q = 2$ and iterations $= 10^6$.

parameters of p, N, M and maximum number of iterations, we numerically observe that the lowest PSL values[8] are observed for ℓ_{10} norm and other PSL values are higher for $p \neq 10$.

Since PSL is the not the objective of the minimization, its monotonic convergence is not guaranteed and the same is evident from Figure 4.3b, for lower values of p. It should be noted that for these values of p the objective function converges quickly in Figure 4.3a. On the other hand, for large p, the PSL values tend to decerease monotonically, albeit at a much lower rate (Figure 4.3b). Infact, the objective also decreases at a much lower rate. These observations imply a stable, but slow convergence of PSL for larger values of p. Similarly, ISL convergence is preserved for all values of p in the ℓ_p norm, though the minimum ISL values achievable decrease as p increases (Figure 4.3c).

In Figure 4.4, we assess the relationship of Polynomial phase of degree Q as a tuning parameter with PSL and ISL. The parameter Q, can be considered as another degree of freedom available for the design problem. Other input parameters are kept fixed (i.e. $N = 300$ and $M = 5$) and same seed sequence is fed to the algorithm. As the value of Q is increased, we observe a decrement in the optimal PSL and ISL values generated from PECS for different norms (i.e. $p = 2, 5, 10, 100$ and 10^3). Therefore, the choice of the input parameters would vary depending upon the application.

[8] $\text{PSL}_{dB} \triangleq 10\log_{10}(\text{PSL})$, $\text{ISL}_{dB} \triangleq 10\log_{10}(\text{ISL})$.

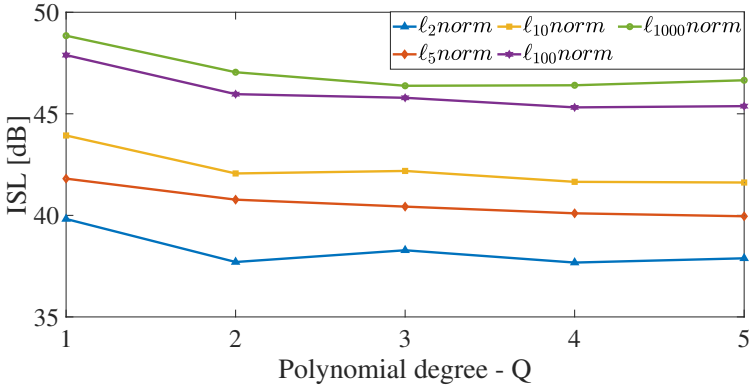

(a) ISL vs Q

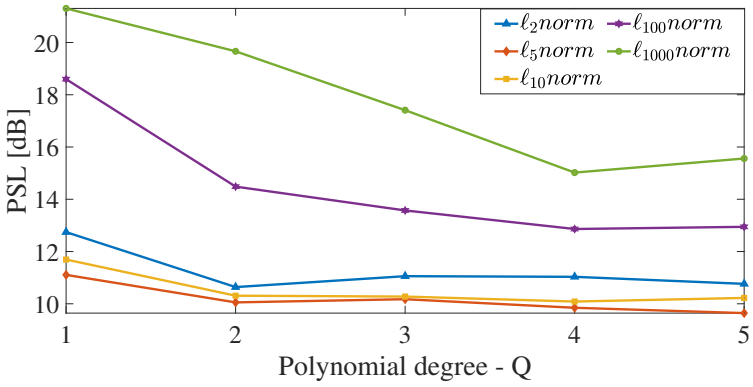

(b) PSL vs Q

Figure 4.4: ISL and PSL variation with increasing Q.

4.5.2 Shaping the Ambiguity Function

In Table (4.3), we show the capability and effectiveness of the PECS algorithm to shape the AF by changing the input parameters. For the plots shown here, the input parameters are $N = 300$, varying sub-sequence lengths of $M = 5, 50, 150$ and 300, $Q = 2$ and p limited to $2, 10$ and 100. In the unwrapped phase plots of the sequences, the quadratic nature of the sub-sequence is retained for all values of M and p. As evident, the AF achieves the thumbtack type shape for $M = 5$ keeping quadratic behaviour in its phase and as the value of M increases, it starts evolving into a ridge-type shape. For $M = N = 300$ (i.e. only one sub-sequence, $L = 1$), it achieves a perfect ridge-shaped AF. Further, the sharpness of the ridge-shape is observed as the value of p increases (i.e. $p = 10, 100$).

4.5.3 Doppler Tolerance Evaluation

In Figure 4.5, we compare the Doppler tolerance characteristics of sequences: Frank, Golomb, Random and PECS with length $N = 100$. In the automotive case study considered in this paper, the maximum expected Doppler frequency for a radar operating at 79GHz from the targets cruising at the highest absolute relative velocity of 400kmph is roughly 58KHz. By considering range resolution of 1m (or equivalently 150MHz bandwidth), this Doppler frequency is less than 1% of the transmit signal bandwidth. Therefore for a single chirp time period the normalized Doppler frequency range of interest shown in the figure is limited to 0.01Hz. In PECS algorithm, the input parameters are: polynomial degree, $Q = 2$ and the sub-sequence length, M varies with a relation: $\{5 \leq M \leq 100\}$ and the variations in the peak amplitude of the autocorrelation as a function of normalized Doppler are shown in Figure 4.5a. As is evident from the plot, the peak of the matched filter decays for all the sequences as the Doppler shift increases due to target motion. But, a sharp decay of the peak value is observed in the case of Random sequence as compared to a Golomb sequence where the decay is rather linear in manner. In relation to these when the sequence is generated using PECS, and $M = N = 100$, its response is better than Frank sequence and similar to Golomb sequence. Further, as we decrease M, we observe that the Doppler shift impacts the peak and the response starts resembling the Random sequence for $M = 5$. Similar conclusions can be drawn from the Figure 4.5c where Integrated Sidelobe Level Ratio (ISLR) values of various sequences are observed. Further, the correlation level, Peak Sidelobe Level Ratio (PSLR) and the ISLR variation with normalized Doppler is shown in

Table 4.3: Unwrapped phase and Ambiguity Function comparison for $N = 300$, $Q = 2$, $M \in [5, 50, 150, 300]$ and $p \in [2, 10, 100]$ in ℓ_p norm.

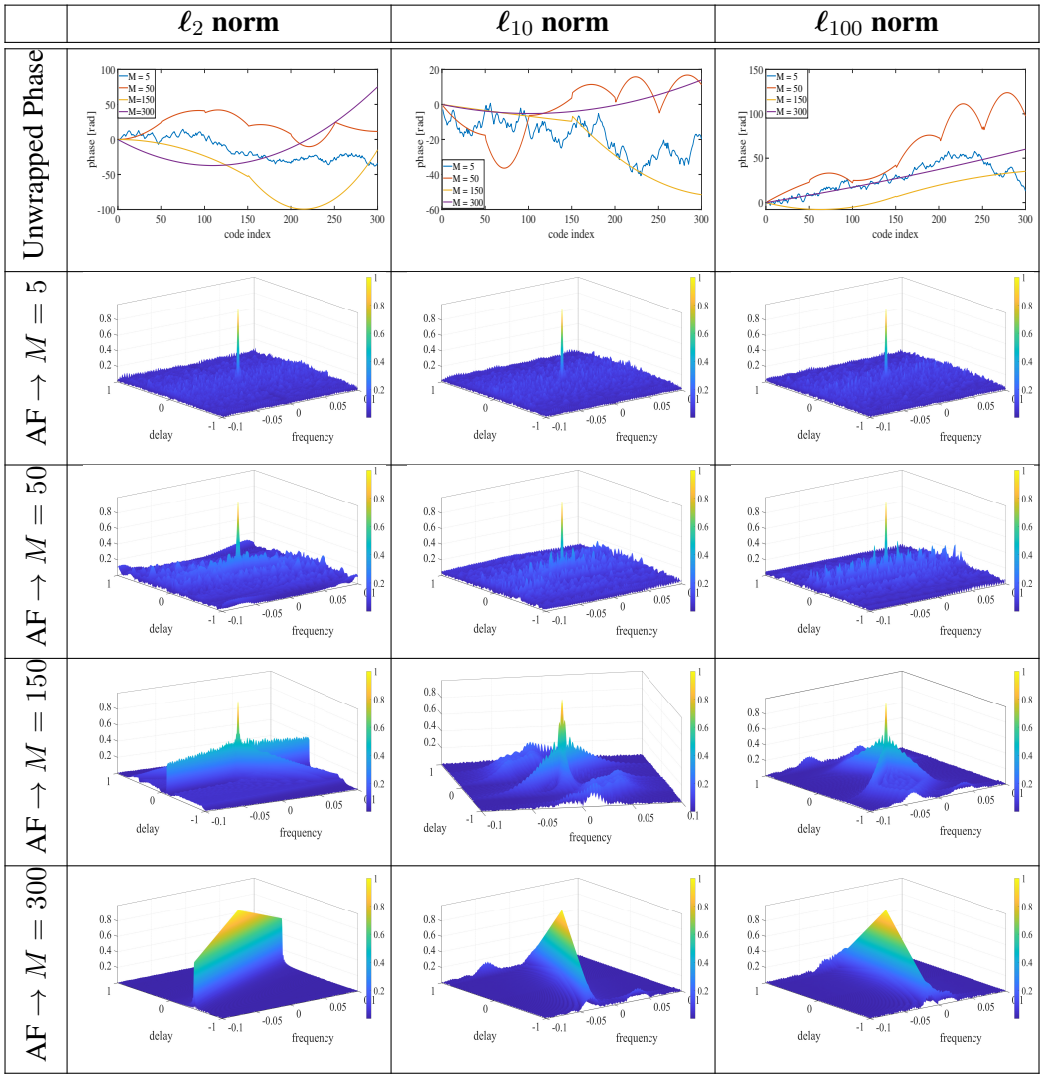

Figure 4.5b and Figure 4.5c respectively.

$$\begin{aligned} \text{correlation level} &\triangleq \Big|\frac{r_k}{r_0}\Big|, \\ \text{PSLR}_{dB} &\triangleq 20\log_{10}\frac{\text{PSL}}{\max\{|r_k|\}_{k=0}^{k=N-1}}, \\ \text{ISLR}_{dB} &\triangleq 20\log_{10}\frac{\text{ISL}}{\max\{|r_k|\}_{k=0}^{k=N-1}} \end{aligned} \tag{4.32}$$

On the other hand, as the number of sub-sequences increase in the PECS sequences (e.g "PECS M25" and "PECS M5") the PSL begins to rise and eventually lowers the PSLR. This may impact the detection probability of the target.

4.5.4 Comparison with the Counterparts

We found [110] from the Ambiguity function shaping category and [62] from the ISL/PSL minimization category more closed to our work. Detailed comparison between [62, 110] and our work is indicated in Table 4.4.

Table 4.4: Comparison of different waveform design approaches with desired characteristics.

Constraint → Algorithm ↓	**Constant Modulus**	**Linear phase**	**Polynomial Phase**
[110]	✓	×	×
[62]	✓	✓	×
PECS	✓	✓	✓

Performance

In [62], an approach was presented for designing polyphase sequences with piecewise linearity and impulse like autocorrelation properties (further referred as "LinearPhaseMethod"). In order to compare the performance of the LinearPhaseMethod with the proposed PECS, we use both the algorithms to design a piecewise linear polyphase sequence of length $N = 128$ with sub-sequence length 8 and thereby the total number of sub-sequences are 16. Normalized autocorrelation of the optimized sequences from both the approaches is shown in Figure 4.6a and it shows lower PSL values of the autocorrelation for PECS as compared to LinearPhaseMethod. Unwrapped phase of the optimized sequences are shown in Figure 4.6b[9]. Linear Phase Method

[9] the phase unwrapping operation can be expressed mathematically as

$$\mathbf{x}_U = \mathcal{F}[\mathbf{x}_W] = \arg(\mathbf{x}_W) + 2k\pi$$

where $\mathcal{F}$ is the phase unwrapping operation, k is an integer, $\mathbf{x}_W$ and $\mathbf{x}_U$ are the wrapped and unwrapped phase sequence, respectively

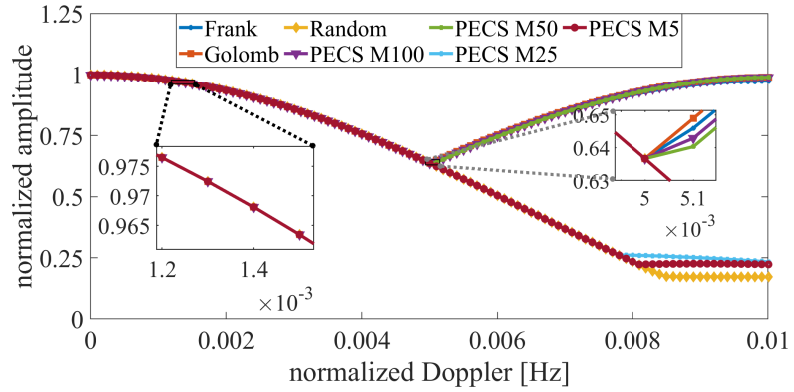

(a) Autocorrelation response comparison with Doppler shift

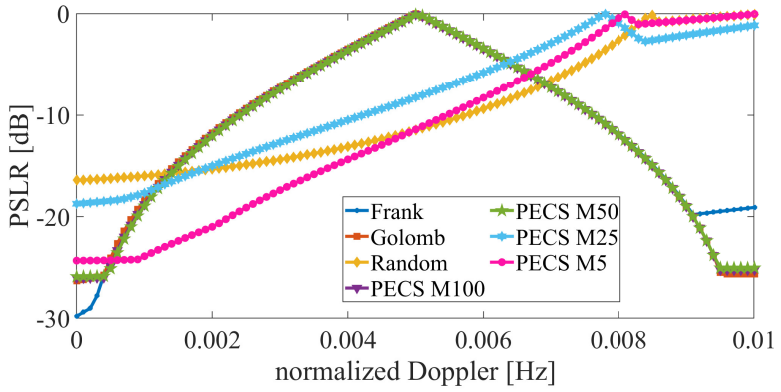

(b) PSLR

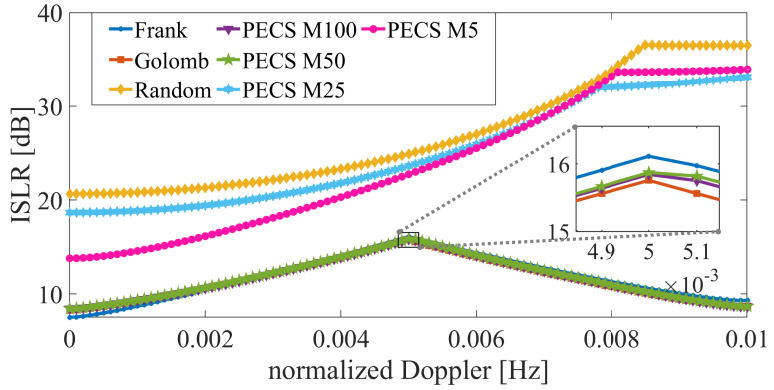

(c) ISLR

Figure 4.5: Comparison of various sequences for evaluating the Doppler tolerance.

generates an optimal sequence whose ISL and PSL values are 36.47dB and 12.18dB respectively whereas PECS results in an optimal sequence whose ISL and PSL values are 32.87dB and 9.09dB. Therefore, better results are obtained using PECS approach.

In [110], an approach to shape the AF of a given sequence w.r.t. a desired sequence was proposed (later referred as "AF shape method"). In Figure 4.7, we consider an example where the two approaches (i.e. AF shape method and PECS) strive to achieve the desired AF of a Golomb sequence of length $N = 64$. In the PECS method, the sub-sequence length is equal to the sequence length, i.e. $M = N$ and $Q = 2$. The performance of the two approaches would be assessed by comparing the autocorrelation responses, ambiguity function and ISL/PSL values of the optimal sequences. Both the algorithms are fed with the same seed sequence and the convergence criterion is kept the same for better comparison. As evident from the Figure 4.7, the autocorrelation function of the optimal sequence derived from PECS shows improvement as compared to the optimal sequence of benchmark approach. The initial ISL of the seed sequence was 49.30dB and the desired Golomb sequence was 22.050dB. After the optimization was performed, the optimal ISL using AF shaping approach was 22.345dB and using PECS was 22.002dB. In addition, the ridge shape of the AF generated using both the approaches is equally matched to the desired AF of Golomb sequence. Noteworthy point over here is that the monotonic convergence of ISL is absent in the AF shape method as it optimizes a different objective function rather than ISL using the CD approach whereas in the PECS method, monotonic convergence is achieved.

As a result, PECS has the capability of achieving better ISL values than the Golomb sequence as it aims to minimize the objective in (4.7) and its proof can be seen from the optimal ISL value quoted above (i.e. 0.048dB improvement w.r.t. ISL of Golomb sequence).

Run-time

To calculate run-time of the algorithm we used a PC with the following specifications: 2.6GHz $\mathrm{i}9-11950$H CPU and 32GB RAM. No acceleration schemes (i.e. Parallel Computing Toolbox in MATLAB) are used to generate the results and are evaluated from purely sequential processing.

For a sequence length of $N = 300$, computational time was derived by varying two input parameters: sub-sequence length $M = 5, 50, 150$ & 300 and $Q = 2, 3, 4, 5$ & 6. The results mentioned in Table 4.5 indicate that the computation time increases in proportion to the increasing values of Q keeping M fixed. On the other hand, computation time decreases as we keep Q fixed and increase M.

The computational complexity of both approaches (LinearPhaseMethod [62] and AFShapeMethod [110]) is compared with PECS using the runtime observed on the hardware mentioned earlier

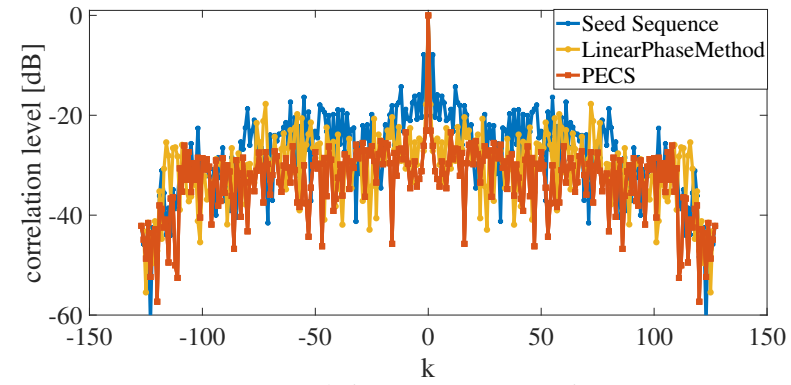

(a) Autocorrelation response comparison

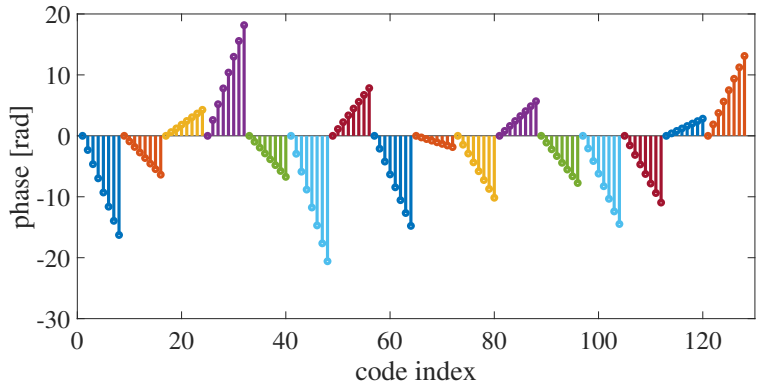

(b) Unwrapped phase: Linear Phase Method

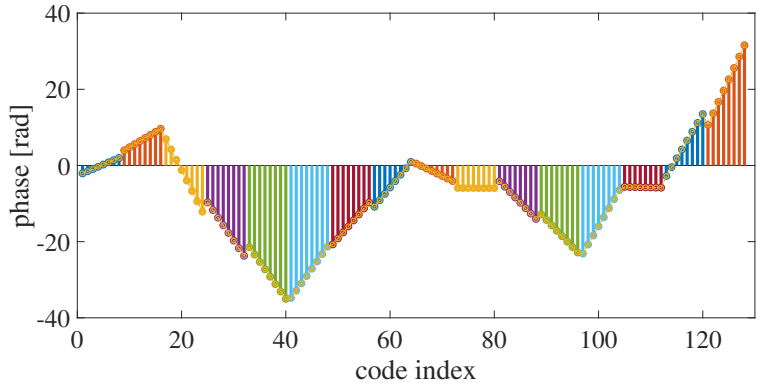

(c) Unwrapped phase: PECS Method

Figure 4.6: Comparison of Linear Phase Method and PECS to design linear polyphase sequence with good autocorrelation properties.

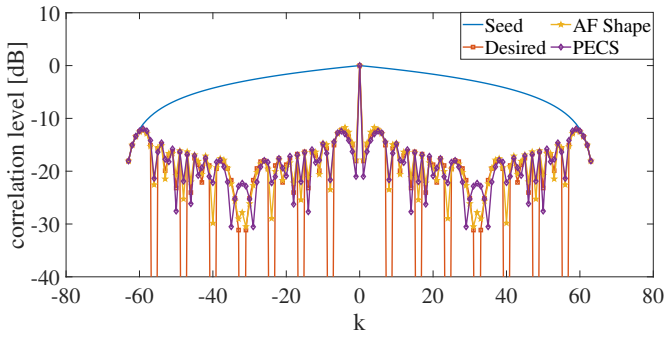

(a) Autocorrelation response comparison

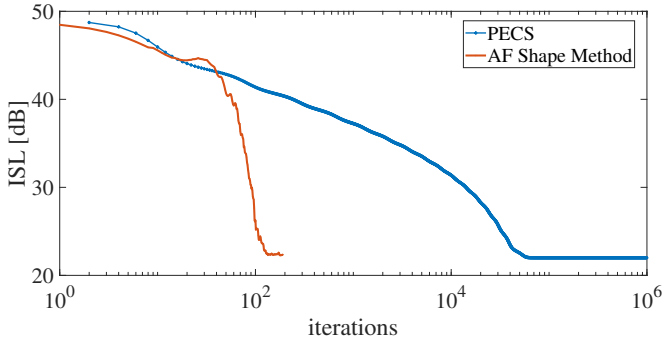

(b) ISL Convergence: PECS Method

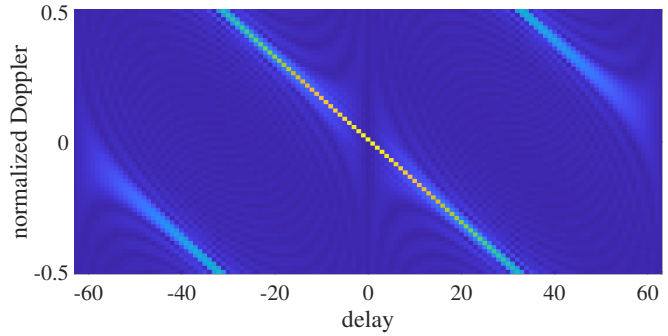

(c) AF Shape method

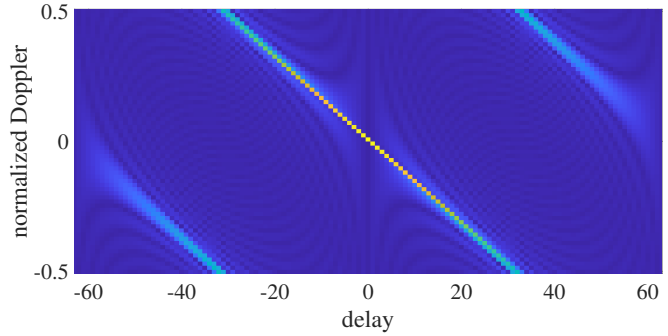

(d) AF using PECS

Figure 4.7: Performance comparison of AF Shape method and PECS algorithms.

Table 4.5: PECS runtime - sequence length $N = 300$.

	M$= 5$	**M**$= 50$	**M**$= 150$	**M**$= 300$
Q$= 2$	429.25s	84.26s	52.53s	45.15s
Q$= 3$	521.41s	88.32s	55.03s	47.42s
Q$= 4$	562.04s	97.20s	64.55s	56.54s
Q$= 5$	573.72s	108.37s	73.47s	65.47s
Q$= 6$	620.90s	118.82s	83.39s	74.06s

for obtaining sequences with identical properties. To begin, Table 4.6 compares the runtime of LinearPhaseMethod and PECS with varying sub-sequence lengths (i.e.$M \in 5, 50, 150$) for a sequence length of $N = 150$, with each sub-sequence exhibiting linear phase behavior.

Table 4.6: Computation time comparison - Linear Phase Method and PECS.

Method	$M = 16$	$M = 8$	$M = 1$
LinearPhaseMethod	972.59 s	547.01 s	169.77 s
PECS	120.80 s	67.13 s	18.46 s

Second, the runtimes of AF Shape Method and PECS were compared for a sequence of length $N = M = 100$ and $Q = 2$ (i.e. quadratic phase behavior). It is observed that as the length of the sequence increases, so does the computation time.

Table 4.7: Computation time comparison - AF Shape Method and PECS.

Method	$N = 64$	$N = 128$	$N = 256$
AF Shape Method	1.02 s	6.64 s	44.90 s
PECS	155.55 s	204.22 s	277.29 s

4.5.5 Automotive Scenario

The idea is to generate a code sequence using PECS algorithm towards designing a transmission scheme for PMCW and evaluate its performance by comparing it with the FMCW waveform transmission when interference is introduced in the FoV of the victim sensor. Figure 4.8 shows the phase-time plot comparison of both the waveforms. In this plot, the pulse length, T_p (i.e. chirp time period - FMCW and sequence period - PMCW) and pulse repetition frequency (PRF), f_p of both the type of waveforms is matched for simplicity of the concept which results in equal Doppler response of the target. PECS code sequence has input parameters: quadratic phase $Q = 2$, code length $N = \frac{T_p}{\tau_{chip}}$ and varying sub-sequence length M. Thus, the MI occurs within a single pulse time period T_p amongst FMCW waveforms but it is less likely going to occur in

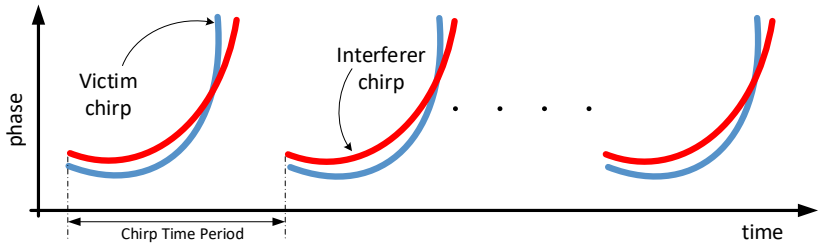

(a) Quadratic phase FMCW waveform

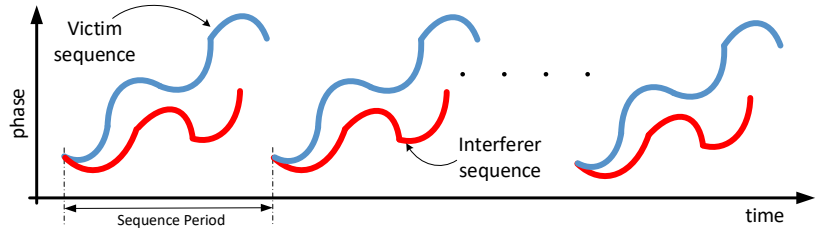

(b) PECS based PMCW waveform

Figure 4.8: Phase variation comparison of FMCW and PMCW waveform.

PECS waveforms. Even though the initial phase in FMCW waveform from two different sensors would start from any random initialization, they tend to interfere as they exhibit similar quadratic phase behavior for the whole chirp time. This phenomenon is not seen in PECS waveforms since every sensor can randomly choose different sub-sequence lengths, while maintaining the quadratic phase behavior in each sub-sequence. This would result in generation of different phase coefficients which yield unique sequences. Uniqueness of every sequence and its phase behavior results in minimal cross-correlation with other transmitting sequences in its FoV.

In Figure 4.9 few automotive scenarios are described where MI may occur. As mentioned in the introduction, two types of interference are witnessed using FMCW i.e. Similar-slope and sweeping slope interference. The similar-slope interference occurs when the sensors operate with same specifications in order to sense the environment for the following applications:

- whenever a sensor is mounted for Blind Spot Detection (BSD) application in ego-vehicle Figure 4.9a and another vehicle with Short Range Radar (SRR) mounted on front side enters the FoV.
- when the ego vehicle is equipped with Adaptive Cruise Control (ACC) function, it follows the trajectory of a car driving ahead. The target vehicle may be equipped with a rear mounted radar and would lie in the FoV of the front mounted radar on the ego vehicle Figure 4.9c.
- Front side mounted radar from the Ego-Vehicle may get interfered by another overtaking vehicle equipped with a rear side mounted radar Figure 4.9d.

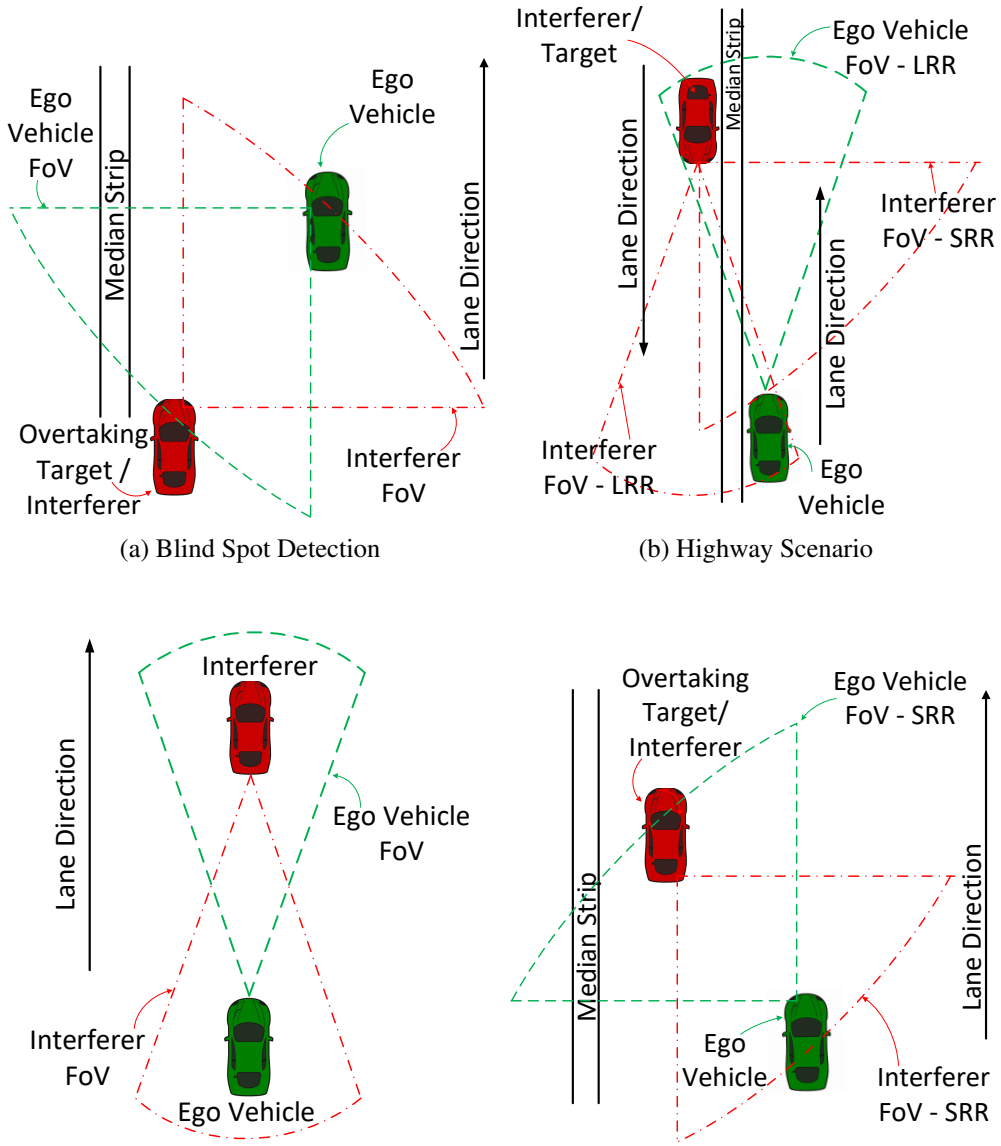

(a) Blind Spot Detection

(b) Highway Scenario

(c) Adaptive Cruise Control

(d) Overtaking Scenario

Figure 4.9: Automotive scenarios with mutual interference.

In Figure 4.9b, Sweeping slope interference may occur when a side looking radar of the oncoming target vehicle is in the FoV of the ego vehicle's front looking radar, provided both are operating in the same band (i.e. $77-81$GHz). In general, any two sensors with same operational transmission band and tuned for different range resolution requirements due to differing sensing functionality on the vehicle would cause sweeping slope interference.

Simulation results

To demonstrate the efficacy of the proposed algorithm, we simulated an automotive driving scenario for the cases described in Figure 4.9. Here, radar sensing performance was evaluated independently in two different cases:

- when the ego-vehicle is operating with FMCW waveform and MI (i.e. similar-slope and sweeping slope) is observed from the target.
- the ego-vehicle is operating with PMCW waveform using PECS algorithm based code sequence and encounters MI from another target in its FoV with the same scheme.

Table 4.8: Radar sensor parameters and Motion information for ego-vehicle and interfering vehicle.

	parameter	**value**
FMCW & PMCW params	Operating Frequency	79GHz
	Antenna Gain	10dB
	Range Resolution	1m
	Transmit Power (Victim / Interferer)	12dBm
	Bandwidth (Victim)	150 MHz
	Bandwidth (Sweeping-slope Interferer)	75 MHz
	Bandwidth (Similar-slope Interferer)	148.5 MHz
	Pulse length (T_p)	60 us
	PRF (f_p)	16.66 kHz
	Number of Pulses	256
	Chip Time	6.66 ns
	Code Length	4500
Motion Info	Target Range	30m
	Target Speed	20kmph
	Target RCS	10dBsm
	Interferer Range	50m
	Interferer Speed	40kmph

The radar sensing parameters for both the FMCW and PMCW waveforms are described in the Table 4.8. In order to have a fair comparison, we have matched the TBP and Doppler

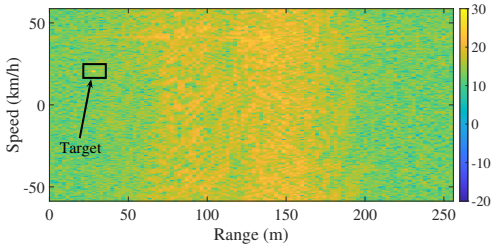

(a) Similar slope interference in FMCW waveform

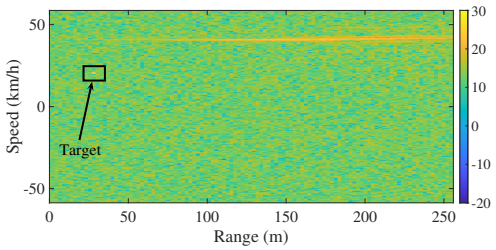

(b) Sweeping slope interference in FMCW waveform

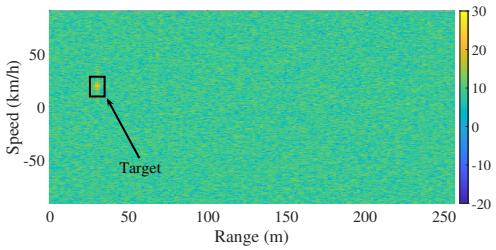

(c) PMCW-PECS waveform based Interference

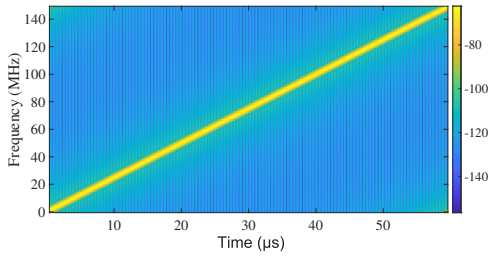

(d) FMCW waveform spectrogram

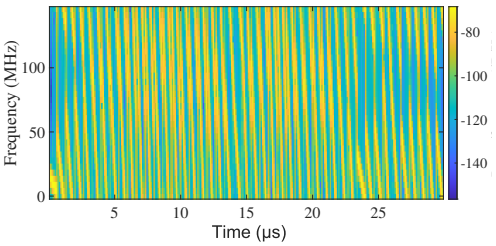

(e) PMCW-PECS waveform spectrogram

Figure 4.10: scenario with FMCW and PMCW type waveforms being used by the Ego-Vehicle and target respectively (Power values on *colorscale* are in dBm).

characteristics (pulse length, PRF) of both the waveforms. Figure 4.10 shows the comparison of the range-Doppler map for similar-slope and sweeping slope interference in FMCW and PMCW waveforms. In FMCW waveforms, the SINR of the victim sensor in an interference free scenario is 13.06dB. When a single interferer is introduced, the similar-slope interference observed by the victim-sensor (driving scenarios mentioned previously in Figure 4.9a, 4.9c & 4.9d) witnessed a SINR of 10.8dB (refer Figure 4.10a). Similarly with single interferer, in the case of sweeping slope interference Figure 4.10b the SINR was 12.9dB. Although, these results have been derived after applying mitigation technique (i.e. varying PRF at the victim sensor), the impact of interference on the detection capability of the victim sensor is evident and weak targets may not be detected in such a scenario. In the current case, the target, interferer position and Doppler have been deliberately kept different for purposes of plotting but if both have similar values, the detectability of target becomes even more arduous in the case of similar-slope interference.

On the other hand for PMCW waveform derived from PECS, both the victim and the interferer sensor transmit an optimized PECS code sequence which is Doppler tolerant and unique. Noteworthy fact here is that both the victim and interferer are operating at the same bandwidth (i.e. same range resolution), center frequency and transmit power without causing MI which proves the robustness of algorithm. As is evident from Figure 4.10c, there is no interference peak present in the range-Doppler spectrum and the SINR in the case of single interferer is 20.7dB better than FMCW in interference free scenario. Further to this result, the reduction in the SINR due to increase in the number of interferers was analyzed. The results from the simulation show that as the number of interferers increase from one to five, the SINR decreases to 16.8dB. As the presence of more than 10 interferers in a certain driving scenario is very unlikely, therefore the interference results were limited to 10 interferers and SINR in this case was 14.65dB.

The spectrum occupancy of FMCW and PECS based PMCW waveform is mentioned in Figure 4.10d and Figure 4.10e. We observed that in the duration of single chirp (where chirp time period = sequence period), the frequency variation of FMCW waveform is linearly increasing upto 150MHz whereas in PECS waveform multiple ramps of linearly increasing frequency can be seen in the time period. This again ascertains the fact that the frequency variation is linear (hence the quadratic phase variation). Randomness in the ramp slopes within a chirp duration and start phase is the reason for the uniqueness of each waveform and can be considered as an additional degree of freedom in the system design which leads to interference immune waveform. Thus, PECS can be considered a new approach in this domain.

Statistical Analysis

Furthermore, in order to comprehend the interference immunity of various waveforms, this concept was statistically validated and compared for five categories:

1. Random sequences
2. PECS based sequences with fixed sub-sequence length
3. PECS based sequences with varying sub-sequence length
4. LFM waveform with almost same slope (i.e. similar-slope interference)
5. LFM waveform with different slope (i.e. sweeping-slope interference)

The procedure of this statistical experiment is as follows:

1. Consider two sequences from a selected category of signals (say $\mathbf{x} = [x_1, \cdots, x_N]^T$ and $\mathbf{y} = [y_1, \cdots, y_N]^T \in \mathbb{C}^N$, $N > 0$).
2. Compute the linear cross-correlation of these signals, and find

$$\bar{c}_k = \sum_{n=1}^{N} x_n y_{n+k}^*, \quad k = -(N-1), \ldots, 0, \ldots, N-1. \tag{4.33}$$

   Here, we use the convention that $x_n = 0$ and $y_n = 0$ when $n \notin \{1, \cdots, N\}$.
3. Calculate $\bar{c}_{max} = \max(|c_k|)$.
4. Let $\xi = 20 \log_{10}(\frac{\bar{c}_{max}}{N})$.
5. Record the value (i.e. ξ) for the current trial and repeat the experiment until the desired number of trials are complete.

Note that ξ which is a stochastic value will be calculated for different categories of waveforms that are mentioned above. In case the sequences $\mathbf{x}$ and $\mathbf{y}$ are similar, ξ is approximately zero, since both the sequences are fully correlated. In the case of partially correlated waveforms, ξ is less than zero, and as the correlation between the waveforms decreases, ξ decreases further.

Now let us statistically analyze the behaviour of ξ for different categories of transmit waveforms. In the first category, we calculate ξ of two complex unimodular random phase sequences. Because the cross-correlation of two randomly generated sequences has the least cross-correlation, this category of sequences has been used as a comparison benchmark. Here, the entries of the random sequence $\mathbf{x} = [x_1, x_2, \ldots, x_N]^T$ is defined as

$$x_n = e^{j\phi_n}, \quad \phi_n = 2\pi z, \;\; n \in 1, \cdots, N, \tag{4.34}$$

where z is drawn from a Gaussian distribution with zero mean and unit variance.

Secondly, the PECS algorithm is used to generate two independent sequences with the same characteristics ($N = 100$, $M = 10$, $Q = 3$, and $p = 10$).

Thirdly, we generate sequences using PECS algorithm with $N = 100$, $Q = 3$, $p = 10$, and $M \in [M_{min}, M_{max}]$ where $M_{min} = 5$ and $M_{max} = 20$. As PECS framework provides an additional degree of freedom in selecting the sub-sequence length at random, the analysis using this category was required.

In the fourth and fifth categories, two independent LFM sequences were designed with time-bandwidth product equal to 100 such that they cause similar-slope and sweeping slope FMCW mutual interference, respectively[10].

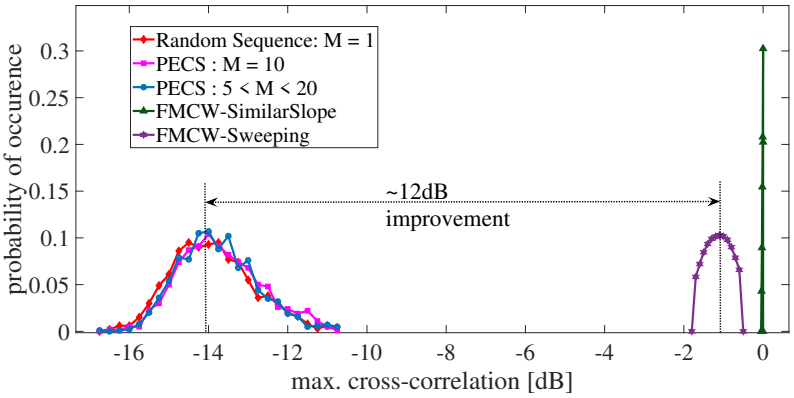

Figure 4.11: Statistical Interference Analysis - Probabilistic comparison of code sequences of length $N = 100$ generated using five categories: completely random sequence, PECS with fixed length sub-sequences $M = 10$, PECS with random length sub-sequences $M_{min} = 5$ and $M_{max} = 20$, LFM waveforms with sweeping interference LFM waveforms with similar-slope interference

The normalized histogram of the statistical analysis of ξ for 10^3 trials is displayed in Figure 4.11 for each waveform category. The x-axis shows the normalized cross-correlation of two signals, while the y-axis shows the histogram level, called *probability of occurrence* in 10^3 trials.

The figure illustrates that the distribution of ξ for similar-slope and sweeping slope are centered at -1.5dB and -0.2dB, respectively. In the case of PECS-based sequences, distribution of ξ is centered at -14.1dB for fixed and variable sub-sequence length.

Interestingly, this category has a major overlap with the distribution of complex unimodular random phase sequences. It is observed that by using the PMCW waveform with PECS-based code sequences for radar sensing results in an overall improvement of 12dB as compared to the

[10]Interested reader may refer to [26] for more details on similar-slope and sweeping-slope interference for FMCW waveforms

categories where FMCW waveforms are used. This demonstrates the credibility of the concept.

4.6 Conclusion

A stable design procedure has been proposed for obtaining polyphase sequences synthesized with a constraint of polynomial phase behavior optimized for minimal PSL/ISL for any sequence length. Results shown in the text indicate the robustness of the method for various scenarios which are prone to interference and offers user additional degrees of freedom to adapt the input parameters in order to design unique waveforms. Its application to automotive scenarios with dense interference prove the feasibility of its use in practical radar systems and provides one of the solution to the current interference issues in multi-sensor applications. The algorithm performance was tested in comparison to the other techniques present in the literature and convincing results were observed. In addition the technique can be used to improve the performance of the state-of-the-art algorithms be extending them with inclusion of PECS which offers additional design parameters for waveform design. The algorithm is implemented by means of FFT and least squares operations and therefore it is computationally efficient. In future, we would like to extend this problem for MIMO radar systems. This work can also be extended by considering the spectrum shaping constraint in the objective which can be further used for 4D imaging cognitive radar applications.

4.7 Appendix

4.7.1 Chirplike phase codes

A summary of chirplike phase codes is reported in Table 4.9. Note that Frank code is derived from the phase history of a linearly frequency stepped pulse. The main drawback of the Frank code is that it only applies for codes of perfect square length ($M = L^2$) [6]. P1, P2, and Px codes are all modified versions of the Frank code, with the DC frequency term in the middle of the pulse instead of at the beginning. Unlike Frank, P1, P2 and Px codes which are only applicable for perfect square lengths ($M = L^2$), the Zadoff code is applicable for any length.

Chu codes are important variant of the Zadoff code, and Golomb, P3, and P4 codes are specific cyclically shifted and decimated versions of the Zadoff-Chu code. Indeed, as P1 and P2/Px codes were linked to the original Frank code, similarly, P3, P4 and Golomb polyphase codes are linked to the Zadoff-Chu code, and are given for any length.

Table 4.9: Expressions of each code and their AF [6]

Type of Code	Phase Expression	AF
Frank Sequence	$\phi_{n,k} = 2\pi\frac{(n-1).(k-1)}{L}$ for $1 \le n \le L,\ 1 \le k \le L,$	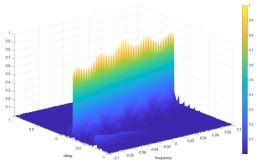
P_x **Sequence**	$\phi_{n,k} = \begin{cases} \frac{2\pi}{L}\left[\left(\frac{(L+1)}{2}-k\right)\left(\frac{(L+1)}{2}-n\right)\right], & \text{L even} \\ \frac{2\pi}{L}\left[\left(\frac{L}{2}-k\right)\left(\frac{(L+1)}{2}-n\right)\right], & \text{L odd} \end{cases}$ for $1 \le n \le L,\ 1 \le k \le L,$	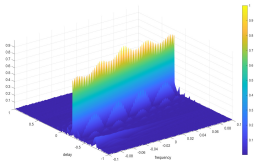
P_1 **Code**	$\phi_{n,k} = \frac{2\pi}{L}\left[\left(\frac{(L+1)}{2}-n\right)((n-1)L+(k-1))\right]$ for $1 \le n \le L,\ 1 \le k \le L,$	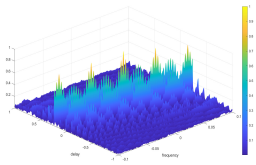
P_2 **Code**	$\phi_m = \frac{2\pi}{M}\left[\frac{(m-1)^2}{2}\right]$ for $1 \le m \le M,$	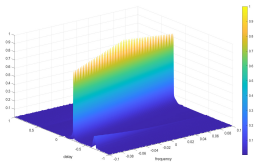
P_4 **Code**	$\phi_m = \frac{2\pi}{M}(m-1)\left[\frac{m-1-M}{2}\right]$ for $1 \le m \le M,$	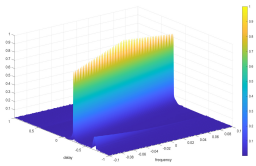
Zadoff Code	$\phi_m = \frac{2\pi}{M}(m-1)\left[r.\left(\frac{M-1-m}{2}\right)-q\right]$ for $1 \le m \le M,\ 0 \le q \le M$ where M is any integer and r is any integer relatively prime to $M,$	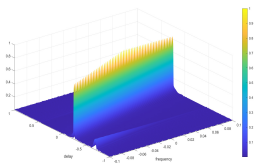
Golomb Sequence	$\phi_m = \frac{2\pi}{M}r''\left[\frac{(m-1)(m)}{2}\right]$ for $1 \le m \le M,$ where M is any integer and r'' is any integer relatively prime to $M.$	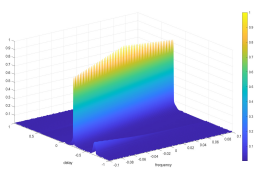

Chapter 5

USRP Implementation of PECS

Preamble

This chapter forms the second part of our SISO sequence design problem. In this manuscript, we present the hardware implementation of the PECS algorithm, which was employed to design PMCW waveforms suitable for low-cost hardware implementation. The polynomial phase constraint was limited to a quadratic phase, resulting in waveforms with LFM characteristics.

Two $X310$ USRPs were used to emulate both the victim and interferer radars. We demonstrated that stretch processing can be effectively applied at the victim receiver to reliably detect the target, even in the presence of significant interference. Despite the interferer being within the FoV and heavily affecting the receive channel, the backscattered signal was successfully recovered after the dechirp process.

This study concludes that the growing issue of radar interference can be effectively mitigated using the proposed method.

5.1 Manuscript: Designing Interference-Immune Doppler-Tolerant Waveforms for Radar Systems

Robin Amar[1], Moein Ahmadi,[1], Mohammad Alaee-Kerahroodi[1], Bhavani Shankar M.R.[1], Björn Ottersten [1]

[1] SnT - Interdisciplinary Centre for Security, Reliability and Trust, University of Luxembourg

Published in: *IEEE Transactions on Aerospace and Electronic Systems,* vol. 59, no. 3, pp. 2402-2421, June 2023,
DOI: 10.1109/TAES.2022.3215116

The following sections are a copy of the paper referenced above.

Abstract

This paper addresses the issue of mutual interference (MI) in automotive radar systems. It explores a sub-pulse based design approach for phase modulated continuous wave (PMCW) radars using USRPs (Universal Software Radio Peripheral). Each sub-pulse exhibits a unique quadratic phase variation, ensuring optimal sidelobe levels for the entire pulse. These sub-pulses are integrated into a single transmit pulse. The receiver operates with stretch processing, and the received signal is observed at various stages of range processing. Evaluating MI between radar sensors with identical specifications, the study utilizes the signal to interference plus noise ratio (SINR) metric. A versatile solution for PMCW radars applicable to both indoor and outdoor sensing environments is proposed. It demonstrates reduced MI and improved radar detection performance with low sampling rate ADCs.

5.2 Introduction

MI amongst FMCW radars presents a significant challenge in ADAS used in contemporary vehicles [9]. This issue arises because radar sensors installed in each vehicle function within a common frequency band without coordination, leading to unregulated transmissions [12]. MI in FMCW radars often appears as bursts in the time domain [18], potentially causing reduced sensitivity [133].

Alternatively, MI can be managed better in PMCW radar systems where Merit Factor (MF) is a commonly employed component for pulse compression. It offers exceptional dynamic range, particularly when the code sequences are carefully crafted. Nonetheless, a significant limitation is the vulnerability to Doppler shifts, resulting in a discrepancy between the received code sequence and the reference signal [6], [83]. This mismatch leads to heightened sidelobe levels and a reduction in signal-to-noise ratio (SNR).

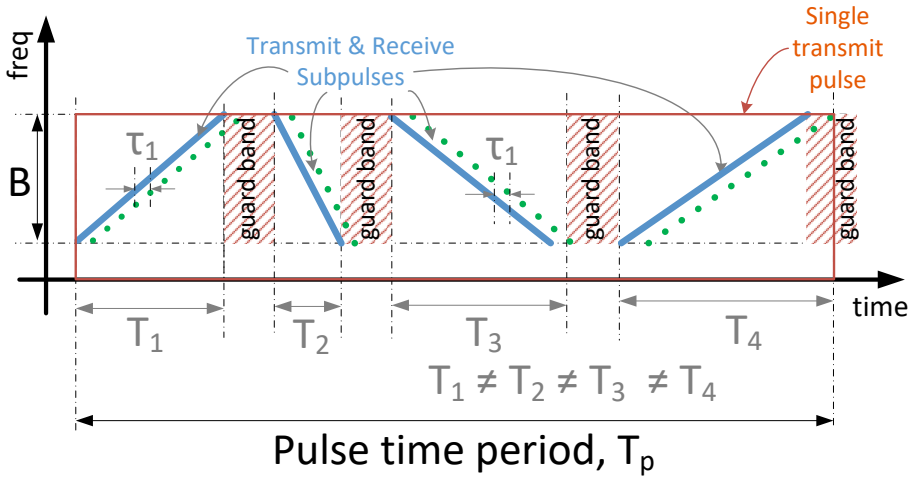

Figure 5.1: Single Transmit Pulse with varying sub-pulses of different slopes

Certain methods for mitigating the Doppler shifts include sub-pulse processing [96], fast Time Doppler Compensation (FTDC) [134], code sequence diversity [135], Doppler matched filter banks, and mismatched filters [89, 136]. Another direct approach is to use the polyphase codes which are inherently robust to Doppler shifts [49, 63] by incorporating linear or quadratic phase variation in subsequent elements within a sub-sequence or sequence.

While some of these techniques are supplementary and can be integrated, it is often beneficial to choose one that offers direct hardware compatibility and lower sampling requirements. To this end, the purpose of this paper is to showcase the hardware implementation of an existing technique which encompasses the polynomial phase behavior in sequence design problem [49]. In the current context, we design the sub-sequences with quadratic phase behavior by evaluating phase coefficients for each sub-sequence which results in optimal sidelobe levels of the MF for the entire sequence. The quadratic phase variation implies LFM, which makes it possible to transmit every sub-sequence using stretch processing technique that requires a low sampling rate ADC for transmitting PMCW waveforms. Finally, we prove the interference immunity of the proposed waveforms in terms of SINR improvement as compared to the state-of-the-art FMCW waveform.

5.3 Problem Statement

Let the transmit signal be $\widetilde{s}(t)$ and is represented as:

$$\begin{aligned} \widetilde{s}(t) &= e^{j\widetilde{\theta}(t)}\text{rect}\left[\frac{t-T_p/2}{T_p}\right], \\ \widetilde{\theta}(t) &= 2\pi(f_c t + \frac{1}{2}\zeta\alpha t^2), \end{aligned} \tag{5.1}$$

where, $\widetilde{\theta}(t)$ denotes the time-varying phase of the signal $\widetilde{s}(t)$, f_c represents the carrier frequency, t is the continuous time variable, ζ takes values of either $+1$ for up-chirp or -1 for down-chirp, and $\alpha = \frac{B}{T_p}$ represents the slope of the LFM, with B, bandwidth and T_p, pulse duration.

The entire pulse can be divided into L sub-pulses (refer Figure5.1, where $L = 4$). A given sub-pulse l, spans a part of the entire bandwidth B, and has a sub-pulse duration of T_l. Two subsequent sub-pulses are separated by a guard band of width $T_{gb} \geq 2R_{max}/c$, where R_{max} is the maximum range of the radar sensor and c is the speed of light.

The phase variation of $\widetilde{\theta}_l(t)$ for the l-th sub-pulse in discrete time, represented for $t = T_s n$, where T_s stands for the sampling time, and $n = (l-1)M_l + m \in [1, \ldots, N]$, $m = 1, \ldots, M_l$, and $l = 1, \ldots, L$ with entire sequence length $N = \widetilde{T}_p \times B$, where $\widetilde{T}_p = T_1 + \ldots T_L$, and $N = M_1 + \ldots, M_l$ can be expressed as:

$$\widetilde{\theta}_l = \widetilde{a}_{0,l} + \widetilde{a}_{1,l} n + \widetilde{a}_{2,l} n^2, \tag{5.2}$$

where $\widetilde{a}_{0,l} = \theta_{init}$, $\widetilde{a}_{1,l} = 2\pi f_c T_s$, and $\widetilde{a}_{2,l} = \pi \alpha T_s^2$ are the quadratic phase coefficients of $\widetilde{\theta}_l$ for the l-th pulse. It is important to note that θ_{init} represents an arbitrary initial phase value of the chirp sequence and $\widetilde{a}_{1,l}$ is constant for a certain f_c and T_s. The discrete-time signal generated using the phase code sequence $\widetilde{\theta}_n$ can be expressed as:

$$\widetilde{s}_n = e^{j\widetilde{\theta}_n}, \;\; |\widetilde{s}_n| = 1. \tag{5.3}$$

and $\mathbf{x} = [\widetilde{s}_1, \widetilde{s}_2, \ldots, \widetilde{s}_N]^T \in \mathbb{C}^N$ represents the transmit complex unit-modulus radar code sequence.

The aperiodic autocorrelation of the transmitting waveform at lag k (e.g. matched filter output at the receiver) is defined as

$$r_k = \sum_{n=1}^{N-k} x_n x_{n+k}^* = r_{-k}^*, \quad k = 0, \ldots, N-1. \tag{5.4}$$

The problem of interest is to design the code vector $\mathbf{x}$ with a polynomial phase of a degree 2 in its sub sequences while having impulse-like autocorrelation function by minimizing the ISL. Therefore, ISL $= \sum_{k=1}^{N-1} |r_k|^2$ as the objective function, the optimization problem can be

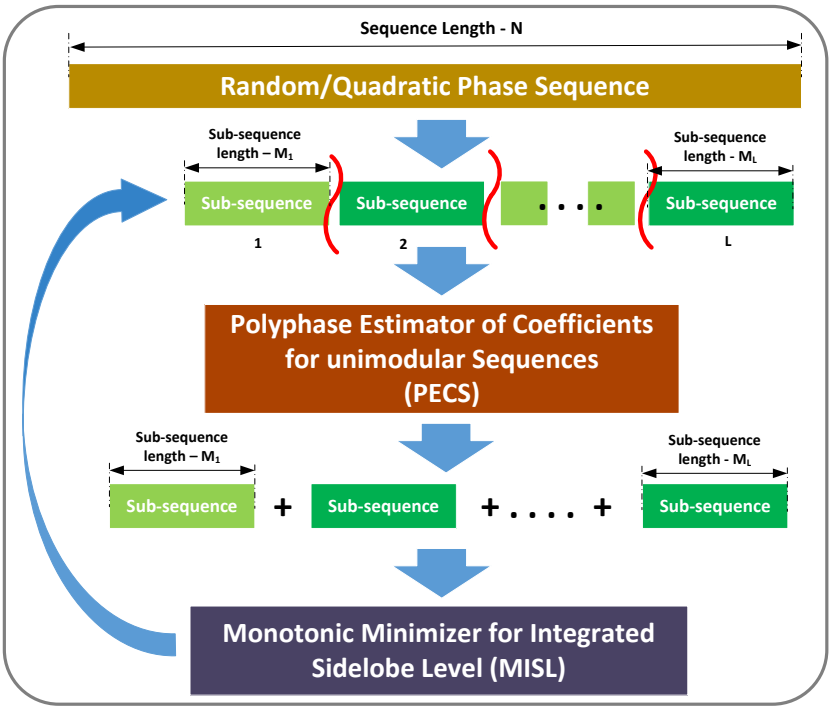

Figure 5.2: Sequence design flow

compactly written as

$$\mathcal{P}_1 \begin{cases} \underset{\widetilde{a}_{\{0,l\}},\widetilde{a}_{\{1,l\}},\widetilde{a}_{\{2,l\}}}{\text{minimize}} & \sum_{k=1}^{N-1} |r_k|^2 \\ \text{subject to} & \arg(x_n) = \widetilde{a}_{\{0,l\}} + \widetilde{a}_{\{1,l\}} n + \widetilde{a}_{\{2,l\}} n^2, \\ & |x_n| = 1, \end{cases} \tag{5.5}$$

where $n = (l-1)M_l + m$, $m = 1, \ldots, M_l$, and $l = 1, \ldots, L$. The details of the solution for (5.5), Doppler tolerance characteristic due to quadratic phase behavior and the algorithm - PECS can be found in [49]. In the next sections, we analyze the interference immunity of the synthesized waveforms using the Algorithm 2 and 3 in [49]. A simplified flowchart of the implementation is shown in Figure5.2.

5.4 USRP based implementation

The experimental setup consists of a victim radar, an interferer radar (both are implemented using two USRP $X310$ with dedicated antenna setup), spectrum analyzer ($SA44B$), RF cables and splitters/combiners as shown in Figure5.3a. The experiment was conducted in a controlled environment in an anechoic chamber. The receive signal from the target and the interferer was

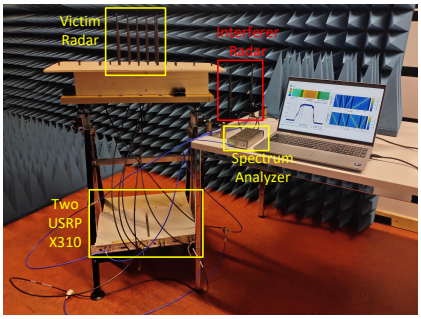

(a) In-lab USRP hardware setup

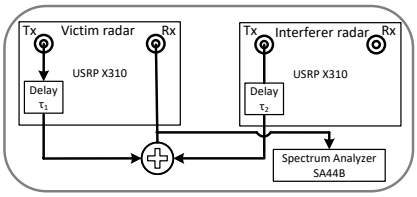

(b) Block Diagram

Figure 5.3: Hardware setup for emulation of Victim and Interferer radars in the presence of target

Table 5.1: Radar sensor parameters for victim and interferer

Parameter	**Value**
Operating Frequency (Victim / Interferer)	3.45GHz
Transmit Power (Victim / Interferer)	12dBm
Bandwidth (Victim / Interferer)	100 MHz
Chirp length (T_p) (Victim / Interferer)	120 μs
PRF (f_p) (Victim / Interferer)	16.66 kHz
Maximum Range	300m
Number of Pulses (Victim / Interferer)	128
Target Range	30m
Target / Interferer Speed	0kmph
Target RCS	10dBsm
Interferer Range	100m

independently digitally delayed in software to simulate the time of flight for each of the signal, refer Figure5.3b. Other radar parameters are provided in Table5.1.

5.5 Results

To measure the performance of the proposed waveform design technique, we calculate the SINR of the known target while the victim radar is operating with an interferer in its FoV. The pro-

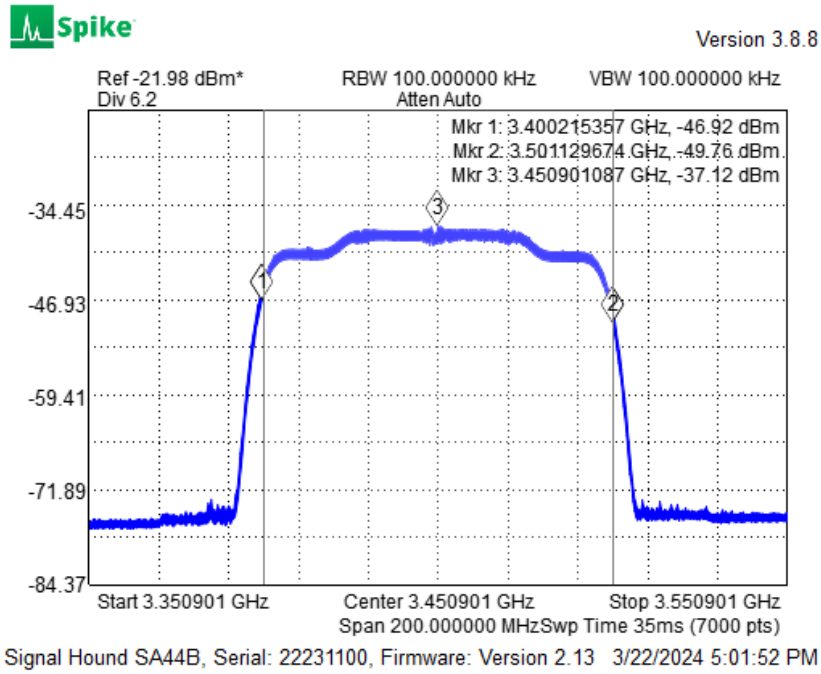

Figure 5.4: Bandlimited Spectral Occupancy

posed waveform was compared with the state-of-the-art FMCW radars where LFM is employed in every transmit pulse. The entire experiment was divided into three categories represented along each column in the Table5.3. The spectrogram output is shown for the transmit signal for victim and interferer in the first two rows. Further, the spectrogram output of the received signal and the dechirp signal at the victim sensor is shown in the third and fourth row, respectively where the interferer signal is dominant due to the one way path loss as compared to the two way path loss from the target returns. Finally, the range profile is obtained using stretch processing (dechirp followed by FFT processing). The chirp slope for the LFM in the entire pulse is $+0.833$MHz/μs in Category 1 and 2. In category 2 and 3, the details of the slopes for each of the 10 sub-pulses constituents of the entire waveform using PECS are given in the Table5.2. A fixed guard band interval of 22μs is used between each sub-pulse in the PECS transmit waveform.

The strong presence of interferer peak in the first category with SINR of $+22.6$dB was observed. In the second category, the SINR of -10.7dB is observed and the interferer is absent in the range profile. Finally, the third category demonstrates the SINR of -10.45dB, with no discernible interference peak when employing the proposed waveform. While, the sub-pulses are subjected to different slopes, the transmitted signals are always limited to a bandwidth 30MHz as observed in the spectrum analyzer, Figure5.4. Hence, the interference immunity of the PECS waveforms is apparent as compared to the LFM waveform when the start and stop time of all the transmit pulses in a given CPI are matched while the radar sensors are operating

with identical operating specifications.

5.6 Conclusion

A USRP based PMCW radar implementation using low sampling rate ADCs was discussed in this paper. The feasibility of this transmission scheme using stretch processing was evaluated. The key advantage of this transmission scheme is that it provides optimal sidelobe level suppression, good Doppler tolerance and interference immunity. We conclude that PECS based transmit waveforms are capable of solving the rising issue of interference.

Table 5.2: Sub-pulse (sp) slope details for PECS waveform in MHz/μs

	sp1	**sp2**	**sp3**	**sp4**	**sp5**	**sp6**	**sp7**	**sp8**	**sp9**	**sp10**
Victim	2.527	−1.264	8.145	5.522	5.164	10.858	−12.236	13.184	18.151	8.551
Interferer	5.732	−7.685	−6.461	1.282	−16.712	2.409	17.699	27.631	−6.951	−3.058

Table 5.3: Spectrogram and range profile for different waveforms of victim and interferer

	Category - 1, **LFM (Victim) - LFM (Interferer)**	**Category -** 2, **PECS (Victim) - LFM (Interferer)**	**Category -** 3, **PECS (Victim) - PECS (Interferer)**
Victim	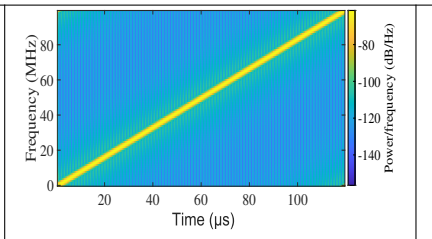	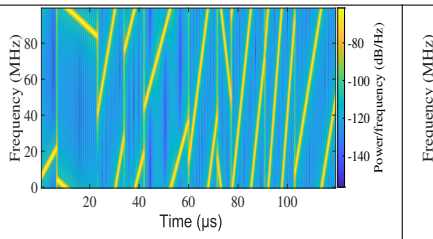	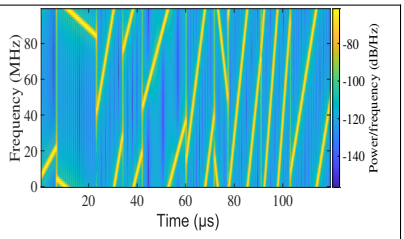
Interferer	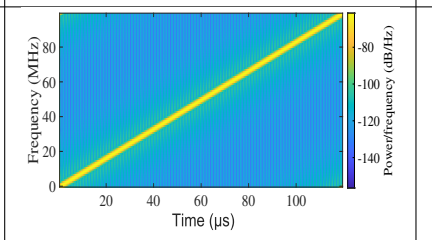	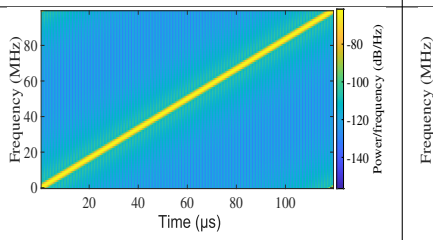	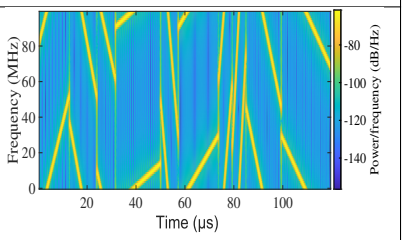
received signal	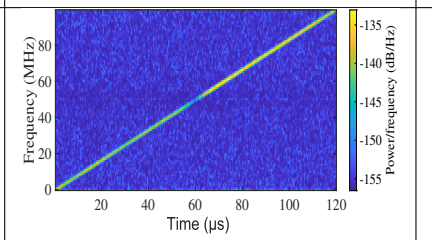	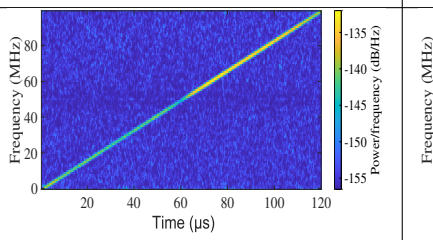	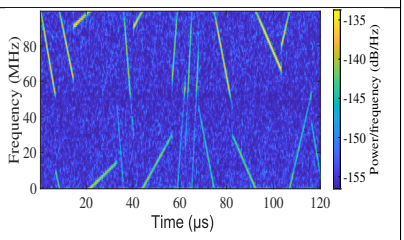
dechirp signal	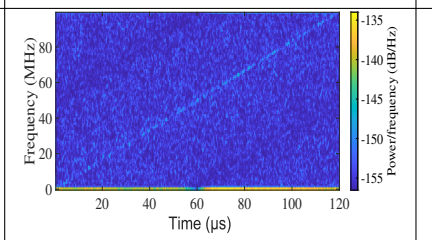	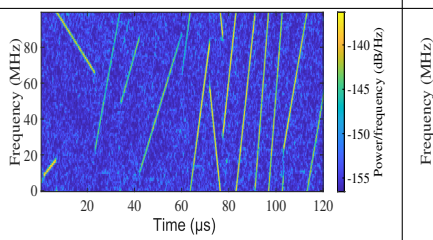	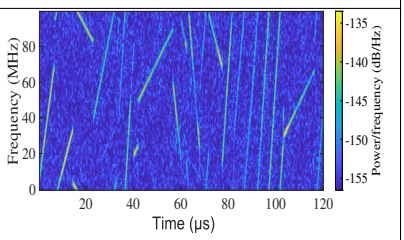
range profile	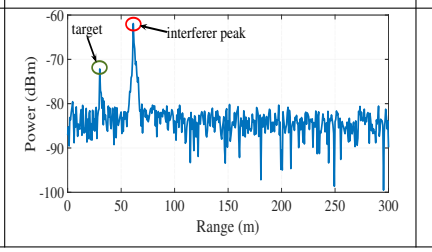	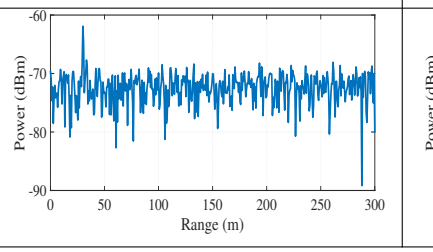	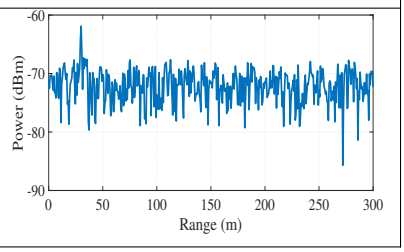

Part III

MIMO Radar Waveform Design

Chapter 6

Polynomial Phase Constrained Waveforms for mmWave MIMO Radars

Preamble

This chapter, presents our efforts to generalize the problem for MIMO radar waveform design using polynomial phase behavior, mentioned as manuscript $J2$ in section 1.5.

We propose a comprehensive framework for designing interference-resistant waveforms and sequence sets for Frequency Modulated Continuous Wave (FMCW) and Phase Modulated Continuous Wave (PMCW) multiple-input multiple-output (MIMO) radar systems. The framework integrates advanced optimization techniques, including Majorization-Minimization (MM) and Block Coordinate Descent (BCD), to enhance system performance. By incorporating cost functions to optimize complementary/ integrated sidelobe level and spatial beam shaping, the proposed algorithms generate sequences both within and across pulses to achieve radar system optimization. Each sequence exhibits a degree Q polynomial in unwrapped phase within its sub-sequences, ensuring optimal performance with monotonic convergence.

The effectiveness of the framework is demonstrated through two case studies: (1) intra-pulse modulation with beampattern adaptation for tunnel-based scenarios in FMCW radars, and (2) Doppler-tolerant sequence set design for dynamic target detection and interference mitigation in MIMO PMCW radars. These case studies illustrate the framework's ability to significantly improve radar performance, especially in challenging environments and in the presence of mutual interference.

6.1 Manuscript: Polynomial Phase Constrained Waveforms for mmWave MIMO Radars

Robin Amar[1], Mohammad Alaee-Kerahroodi[1], Bhavani Shankar M.R.[1]

[1] SnT - Interdisciplinary Centre for Security, Reliability and Trust, University of Luxembourg

Submitted to: *IEEE Transactions on Aerospace and Electronic Systems,* 6 June 2024,

The following sections are a copy of the paper referenced above.

Abstract

In this paper, we propose a generic framework to design interference immune waveforms for Frequency Modulated Continuous Wave (FMCW) / Phase Modulated Continuous Wave (PMCW) multiple-input multiple output (MIMO) radar systems. This framework is composed of diverse set of algorithms that improves the overall system performance. The waveform design approach uses the majorization-minimization (MM) and Block Coordinate Descent (BCD) optimization frameworks by considering complementary, integrated sidelobe level and spatial beam shaping cost functions. The proposed algorithms generate waveform sequence sets in every pulse and across multiple pulses where a sequence in each pulse possesses a property of degree Q polynomial in unwrapped phase within its sub-sequences. The algorithm culminates by obtaining an optimal solution with monotonic convergence. In addition, the discussion is complemented by two case studies. Firstly, intra-pulse modulation in FMCW radars with beampattern design adaptation for tunnel-based scenarios. Secondly, Doppler-tolerant sequence set design in MIMO PMCW radars for efficient detection of dynamic targets and mitigation of mutual interference amongst concurrent radar systems.

6.2 Introduction

FMCW and PMCW radars are both types of CW radar systems, and they share some similarities. Nevertheless, distinctions arise in their modulation methodologies, with each radar type possessing its unique set of pros and cons. FMCW radar typically requires simpler signal processing compared to PMCW radar. The LFM used in FMCW radar simplifies the processing of the received signals using "de-chirp" [29, 49]. This technique allows sampling the received signal at lower rates than its bandwidth, motivating automotive manufacturers to adopt FMCW-based radar systems for cost-effective radar sensors.

The state-of-the-art mmWave FMCW radar sensors often use MIMO technique to create large virtual antennas without increasing the amount of Tx-Rx physical elements [50, 51]. Recently, RoC which utilize 24 Tx, 24 Rx antennas (576 virtual channels) [52], and 48 Tx, 48 Rx

(2304 virtual channels) [53], have been commercialized [54]. In the context of a MIMO FMCW radar system with a large number of Tx-Rx channels, various multiplexing schemes can be employed to achieve distinct orthogonal waveforms for different channels. Some commonly used multiplexing schemes in the context of MIMO FMCW radar are TDM, BPM, DDM[55, 56], slow-time CDM [57], and FDM [58]. TDM stands out among them for its prevalence in conventional mmWave MIMO radars due to its hardware simplicity. In TDM-MIMO radars, each transmitter gets a different time slot, ensuring orthogonality in the time domain. However, this multiplexing scheme increases the required time for the transmission and decreases the Doppler resolution. FDM allocates distinct frequency bands to each transmitter, but with an increasing number of antennas, the available frequency spectrum might become limited. DDM and slow-time CDM involve encoding information digitally for transmission, but as the number of antennas increases, the complexity of encoding, decoding, and maintaining orthogonality among the signals becomes more challenging [57].

Yet, as the number of transmit antennas increases, limitations become apparent in these multiplexing approaches for FMCW MIMO radars. In addition, vehicle-to-vehicle radar interference is another uprising issue in this case. The interference in these instances primarily arises from the concurrent use of shared spectrum within the detection range of other sensors, compounded by the absence of centralized control and resource allocation mechanisms, which leads to uncoordinated radar operations. PMCW MIMO radars, despite higher implementation costs, offer potential advantages [23]. They provide intra-pulse CDM, potentially enhancing performance and offering increased degrees of freedom [59]. Additionally, PMCW radars permit waveform optimization, improving their overall efficiency and effectiveness [60].

In this paper, we enhance the scope of designing radar waveforms for FMCW and PMCW MIMO radars by imposing additional polynomial phase constraint to the design problem. This constraint enhances adaptability by allowing for the adjustment of the polynomial degree, serving as a tuning parameter facilitating transitions between PMCW and FMCW radar technologies. Particularly, when the constraint's polynomial degree is set to 2, the resulting quadratic phase polynomials represent chirps characterized by specific slopes, as detailed in [61].

The background to the polynomial phase constraint is grounded in [62], where the first computational approach aimed at designing these sequences was introduced. However, the design codes in this paper were limited to being piecewise linear. Building upon this, in [49], we utilized the MM technique to derive optimal sequences possessing a property of degree Q polynomial in unwrapped phase within their sub-sequences, but only for SISO radar systems. This work achieved optimal solutions for ISL and PSL with guaranteed convergence. In addition to this, in [63], we proposed a subpulse processing-based receiver tailored for radars employing sequences exhibiting polynomial phase behavior within their sub-sequences.

Unlike the previous studies, in the current paper, we explore applying the polynomial phase constraint to three interconnected yet unaddressed problems. The first problem focuses on designing codes with complementary behavior while adhering to the polynomial phase constraint. In the subsequent two problems, we delve into sequence design aspects specific to MIMO radar systems. One problem tackles transmit beampattern shaping for waveforms with impulse like auto-correlation function, while the other revolves around the requirement for a set of orthogonal sequences.

6.2.1 Background and Related Works

Recent research has strengthened the capacity of radar manufacturers to enhance sensor resolution, explore additional degrees of freedom, and introduce novel operational modes through exploiting waveform diversity [64], as evidenced by the number of publications in this domain [65]. In state-of-the-art automotive FMCW MIMO radar, each antenna transmits LFM in a certain manner that guarantees waveform orthogonality [66]. A comprehensive comparison of all the standard techniques can be found in [57]. In addition, other variations of the standard approaches such as FT-CDMA and ST-CDMA are widely used and described in [67–72].

On the other hand, PMCW (spread spectrum, PN, and polyphase modulated CW) radars transmit a wide-band code sequence modulated on the carrier frequency. Various optimization approaches have been proposed to achieve orthogonality in code sequences in PMCW MIMO radars using CDM scheme [73–78]. The prevailing approaches in waveform design predominantly prioritize the optimization of constant modulus phase waveforms, primarily relying on the correlation (auto/cross) characteristics of individual signals. Nonetheless, these approaches do not account for the influence of phase shifts induced by dynamic radar platforms in automotive scenarios featuring dynamic targets and stationary detections. In such scenarios, static detections, often disregarded as clutter in conventional sensing applications, assume critical importance. Consequently, the consideration of Doppler tolerance becomes paramount in the formulation of sequence set design challenges.

To this end, several neural network based approaches have also been proposed in this regard [79, 80]. However, while these approaches may demonstrate efficacy in certain predictable scenarios, their reliability is contingent upon the extent of supervised or unsupervised training employed to train the deep RN and RNN. For instance, in environments such as highways, bridges, tunnels and underground parking facilities, where dynamic targets and road blockages due to constructions can alter the detection profile beyond the confines of the known static environment [81, 82], the network models may lack awareness of such variations.

In [36, 67, 83, 84], the authors have presented sequence design methods in the presence of non-negligible Doppler shifts. The limitation here lies in the fact that these approaches cater

only to binary/quaternary sequence designs, thereby having limited degrees of freedom in terms of phase allocation. Finally, other approaches for joint MIMO transmit and receive filter design have also been proposed [85–89]. Typically, these approaches deal with maximization of the worst-case SINR over the unknown Doppler and angle of the target of interest. In the case of automotive scenarios, the dilemma is that the target and clutter are not deterministic in nature due to the randomness in the vehicle dynamics (and eventually the radar sensor), necessitating a different problem-solving approach.

6.2.2 Contributions

In this paper, we present a sequence design problem in the time, spatial and pulse domains and optimize the ISL for auto/cross-correlation, and complementary behavior of the sequence sets while keeping Doppler tolerance, and interference immunity as the essential design constructs. The main contributions of this paper are summarized as below:

- Designing Complementary Codes: We focus on crafting complementary waveforms that adhere to a polynomial phase constraint for both PMCW and FMCW radars. These codes are designed to ensure not only lower range sidelobes but also specific phase behaviors within their sub-sequences.

- Beampattern Shaping: Utilizing the polynomial phase constraint within the fast-time domain, we shape the beampattern of MIMO waveforms. This involves controlling the directionality and strength of the radar beam, allowing for targeted and precise radar signal transmission and reception.

- Establishing Orthogonal Waveform Sets: We create a set of optimized ISL MIMO waveforms integrated with a polynomial phase constraint. These waveforms maintain orthogonality by performing intra-pulse modulation, while also ensuring that they remain distinct and non-interfering during simultaneous transmission. In addition, spectral shaping criterion provides coexistence capability with communications signals and deterministic spectrum of other radar sensors.

- Doppler Tolerance Enhancement: By introducing the polynomial phase constraint, the designed waveforms exhibit enhanced Doppler tolerance. This property enables the radar sensor to effectively handle Doppler shifts caused by the motion of objects, ensuring accurate detection and tracking of moving targets without compromising waveform integrity.

- Designing Very Long Sequence Sets: Sequence lengths are not restricted to perfect square lengths, instead they can assume arbitrary lengths - useful for PMCW radar sequence de-

sign. As the fundamental components of sequence sets are represented not by individual elements, but rather by the phase coefficients corresponding to each sub-sequence, it becomes feasible to generate extensive sequence sets possessing optimal auto/cross-correlation characteristics without the need to directly compute sequences of considerable length.

- Radar-to-Radar Interference Mitigation: Interference immunity amongst sequence sets from different radar sensors can be enhanced if the uniqueness of each sequence is inherent by design. Therefore, we introduced a construction of sub-sequence based design method to achieve uniqueness. Every sub-sequence has a quadratic phase behavior which ensures Doppler tolerance and at the same time its distinct phase coefficients ensure uniqueness. This effectively mitigates MI issues that may arise among concurrent radar systems.

This paper employs MM and Block Coordinate Descent (BCD) optimization techniques to effectively address the outlined optimization problems. The details of these optimization frameworks and their convergence behaviors are discussed in details in [60].

6.2.3 Notations

Matrices are represented by bold uppercase letters, column vectors by bold lowercase letters, and scalars by italics. The sets $\mathbb{Z}$, $\mathbb{R}$, and $\mathbb{C}$ signify the integer, real, and complex fields, respectively. The functions $\Re(\cdot)$ and $\Im(\cdot)$ extract the real and imaginary parts, respectively, and $\arg(\cdot)$ gives the phase of a complex number. The notations $(\cdot)^T$, $(\cdot)^*$, $(\cdot)^H$, and $(\cdot)^\dagger$ stand for transpose, complex conjugate, conjugate transpose, and pseudo-inverse, respectively. $\odot$ stands for hadamard product and optimal value of an optimization variable is represented as $(\cdot)^\star$. The element in the i^{th} row and j^{th} column of a matrix is denoted by $x_{i,j}$, while x_i represents the i^{th} element of the vector $\mathbf{x}$. $\mathrm{Diag}(\boldsymbol{X})$ creates a column vector containing all diagonal elements of $\boldsymbol{X}$, and $\mathrm{Diag}(\mathbf{x})$ forms a diagonal matrix, where $\mathbf{x}$ forms the principal diagonal elements of the matrix. Lastly, $\mathrm{vec}(\boldsymbol{X})$ stacks all the columns of $\boldsymbol{X}$ into a single column vector.

6.3 Waveform Optimization

This section explores three optimization problems, all of which are linked by the incorporation of the polynomial phase property that serves as a core principle throughout this paper in designing waveforms for both PMCW and FMCW radars. Through these problems, we showcase the versatility and adaptability enabled by this common constraint across multiple radar applications in different settings.

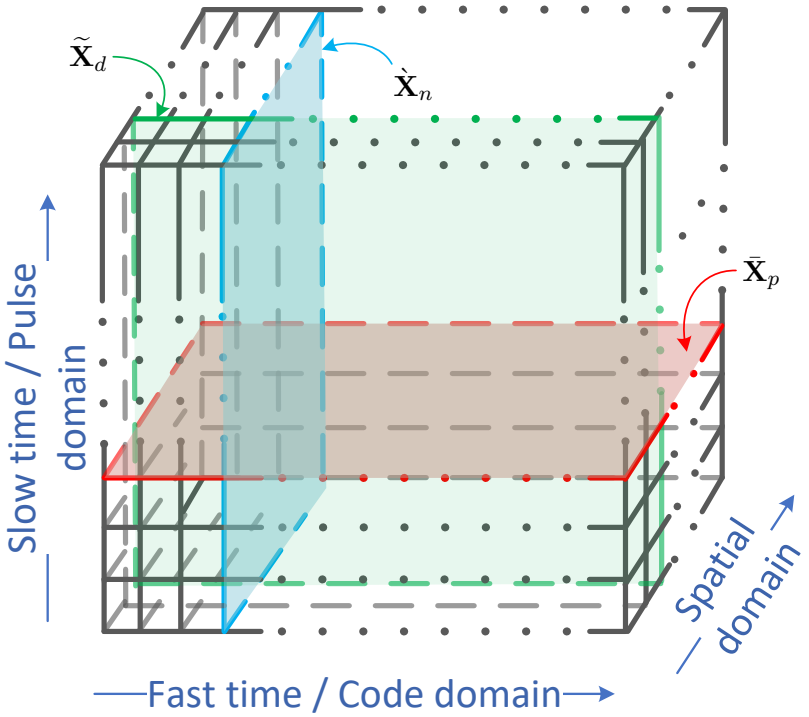

Figure 6.1: Third-order transmit waveform tensor

We consider a MIMO radar system to design unimodular sequence sets with good complementary behavior in slow time, auto/cross-correlation properties and polynomial phase characteristics in fast time. In a single transmit pulse, each antenna transmits a sequence $\mathbf{x}_d$ of length N, where $n = 1, \ldots, N$, and $d = 1, \cdots, \mathcal{M}_t$, with $\mathcal{M}_t$ transmit sequences for all antennas. The sequences are stacked to form the matrix $\bar{\mathbf{X}}_p = [\bar{\mathbf{x}}_1, \cdots, \bar{\mathbf{x}}_d, \cdots, \bar{\mathbf{x}}_{\mathcal{M}_t}] \in \mathbb{C}^{N \times \mathcal{M}_t}$ for the p-th transmit pulse. Further, $\mathcal{M}_p$ such pulses compose a single CPI and in order to comprehend the entire data, it is denoted as a third-order tensor $\boldsymbol{\mathcal{X}} \in \mathbb{C}^{N \times \mathcal{M}_t \times \mathcal{M}_p}$ shown in Figure 6.1. It consists of the raw data acquired in the code domain (fast-time) with N elements, spatial domain with $\mathcal{M}_t$ elements, and the pulse domain (slow-time) with $\mathcal{M}_p$ elements, respectively. Throughout the paper, this tensor is often reorganized into matrices for waveform design and calculation, which is known as matricizing or unfolding. The matricizing operation on $\boldsymbol{\mathcal{X}}$ along the first dimension at the n-th code element is represented as $[\boldsymbol{\mathcal{X}}]_1^n = \grave{\mathbf{X}}_n \in \mathbb{C}^{\mathcal{M}_t \times \mathcal{M}_p}$, where elements of $\grave{\mathbf{X}}_n$ are represented as $x_{d,p}^n$. With reference to the Figure 6.1, similar operations along the second and third dimension at the n-th and p-th element is $[\boldsymbol{\mathcal{X}}]_2^d = \widetilde{\mathbf{X}}_d \in \mathbb{C}^{N \times \mathcal{M}_p}$ and $[\boldsymbol{\mathcal{X}}]_3^p = \bar{\mathbf{X}}_p \in \mathbb{C}^{N \times \mathcal{M}_t}$, respectively. The elements of $\widetilde{\mathbf{X}}_d$ and $\bar{\mathbf{X}}_p$ are represented as $x_{n,p}^d$ and $x_{n,d}^p$, respectively. The elements of $\boldsymbol{\mathcal{X}}$ are denoted as $x_{\{n,d,p\}}|_{n=1}^{N}|_{d=1}^{\mathcal{M}_t}|_{p=1}^{\mathcal{M}_p}$.

Let us define $\check{\mathbf{x}}_{l,d}$ as the l-th sub-sequence of the d-th transmit sequence $\bar{\mathbf{x}}_d$ as $\check{\mathbf{x}}_{l,d} = [\bar{x}_{\{1+(l-1)M,d\}}, \ldots, \bar{x}_{\{m+(l-1)M,d\}}, \ldots, \bar{x}_{\{M+(l-1)M,d\}}]^T$, where $m \in [1, \ldots, M]$ and $l \in [1, \ldots, L]$.

Note that the n-th element in $\bar{\mathbf{x}}_d = [\bar{x}_{1,d}, \ldots, \bar{x}_{n,d}, \ldots, \bar{x}_{N,d}]$ is identified as $\bar{x}_{n,d}$ where $n = m+(l-1)M$ such that $n \in [1, \ldots, N]$. Similarly, $\check{\mathbf{x}}_{l,p}$ is the l-th sub-sequence of $\tilde{\mathbf{x}}_p$ for the d-th transmit sequence of the p-th pulse as $\tilde{\mathbf{x}}_{l,p} = [\tilde{x}_{\{1+(l-1)M,p\}}, \ldots, \tilde{x}_{\{m+(l-1)M,p\}}, \ldots, \tilde{x}_{\{M+(l-1)M,p\}}]^T$ where $p = 1, \cdots, \mathcal{M}_p$.

The polynomial phase variation in each of the sub-sequence of a particular sequence is governed by the coefficients which can be compactly represented in a matrix $\mathbf{A}$ whose $(q,l)-th$ element $a_{q,l}$ represents the coefficient for the l-th sub-sequence, $l = 1, \ldots, L$, with q-th degree polynomial. Note that we consider Q as the maximum degree of the polynomial, where $q = 0, 1, \ldots, Q$. Thus, the phase variation for the all the $\mathcal{M}_t$ transmit sequences in the p-th pulse can be represented by a third order tensor $\boldsymbol{\mathcal{A}}_p$ where each of its element is $a_{\{q,l,d\}}$. Similarly, the phase variation for the all the $\mathcal{M}_p$ pulses for the d-th transmit sequence can be represented as $\boldsymbol{\mathcal{A}}_d$ where each of its element is $a_{\{q,l,p\}}$. Further, by integrating the phase information for all the $\mathcal{M}_p$ pulses and all the $\mathcal{M}_t$ transmit sequences, the coefficients are organized into another fourth order tensor, denoted as $\boldsymbol{\mathcal{A}} = a_{\{q,l,d,p\}}|_{q=0}^{Q}|_{l=1}^{L}|_{d=1}^{\mathcal{M}_t}|_{p=1}^{\mathcal{M}_p} \in \mathbb{R}^{Q\times L\times \mathcal{M}_t\times \mathcal{M}_p}$.

6.3.1 Complementary Sequences for PMCW and FMCW radars across pulse domain

We consider designing almost complementary sequence sets by incorporating a phase constraint of degree Q, such that it imbibes a specific phase characteristic in the l-th sub-sequence within the d-th transmit sequence across $\mathcal{M}_p$ pulses in a CPI[1].

Let us consider a sequence set $\widetilde{\mathbf{X}}_d = [\tilde{\mathbf{x}}_1^T, \ldots, \tilde{\mathbf{x}}_p^T, \ldots, \tilde{\mathbf{x}}_{\mathcal{M}_p}^T] \in \mathbb{C}^{N\times \mathcal{M}_p}$ with $\mathcal{M}_p$ sequences and each sequence of length N where $\tilde{\mathbf{x}}_p = [\tilde{x}_{1,p}, \ldots, \tilde{x}_{N,p}]^T \in \mathbb{C}^N$. The Complementary Integrated Sidelobe Level (CISL) metric is defined as [7]

$$\text{CISL} = \sum_{k=1}^{N-1} \left| \sum_{p=1}^{\mathcal{M}_p} \tilde{r}_{p,p}(k) \right|^2, \tag{6.1}$$

where $\tilde{r}_{p,p}(k) = \sum_{n=1}^{N-k} \tilde{x}_{n+k,p}\tilde{x}_{n,p}^* = \tilde{r}_{p,p}^*(-k), p = 1, \ldots, \mathcal{M}_p$, $k = 1-N, \ldots, N-1$ and $n = 1, \ldots, N$.

A distinctive phase behavior is introduced in a sub-sequence within a set of sequences by imposing a polynomial phase constraint expressed as $\arg(\tilde{\mathbf{x}}_{l,p}) = \sum_{q=0}^{Q} a_{\{q,l,p\}} m^q$, where $\arg(\tilde{\mathbf{x}}_{l,p}) = [\arg(\tilde{x}_{1+(l-1)M,p}), \ldots, \arg(\tilde{x}_{lM,p})]$, $a_{\{q,l,p\}}$ denotes the coefficients of the polynomial of degree q for the l-th sub-sequence in the p-th pulse. Hence, the objective is to address

[1] In general the number of pulses for the complementary code design $\widetilde{\mathcal{M}}_p$ is a subset of $\mathcal{M}_p$, but for the notational simplicity we assume that $\widetilde{\mathcal{M}}_p = \mathcal{M}_p$.

the following optimization problem,

$$\mathcal{P}_{\{\tilde{\mathbf{x}}_d\}}\begin{cases} \underset{\boldsymbol{\mathcal{A}}_d\in\mathbb{R}^{Q\times L\times \mathcal{M}_p}}{\text{minimize}} & \displaystyle\sum_{k=1}^{N-1}\left|\sum_{p=1}^{\mathcal{M}_p}\tilde{r}_{p,p}(k)\right|^2 \\ \text{subject to} & \arg(\tilde{\mathbf{x}}_{l,p}) = \displaystyle\sum_{q=0}^{Q} a_{\{q,l,p\}}m^q, \\ & |x_{n,p}^d| = 1, \forall \begin{cases} n = m+(l-1)M, \\ l = 1,\ldots,L, \\ m = 1,\ldots,M, \\ p = 1,\ldots,\mathcal{M}_p. \end{cases} \end{cases} \tag{6.2}$$

After several majorization steps, the objective in (6.2) along with the constraint $(|x_{n,p}^d| = 1)$[2] simplifies to an iterative optimization problem (for details refer [7]) where the i-th step involves

$$\begin{aligned} &\underset{\boldsymbol{\mathcal{A}}_d}{\text{minimize}} \quad \| \mathbf{z}-\mathbf{y} \|_2^2, \\ &\text{subject to} \quad \arg(\tilde{\mathbf{x}}_{l,p}) = \sum_{q=0}^{Q} a_{\{q,l,p\}}m^q, \\ &\qquad |\tilde{x}_{n,p}| = 1, \forall \begin{cases} n = m+(l-1)M, \\ l = 1,\ldots,L, \\ m = 1,\ldots,M, \\ p = 1,\ldots,\mathcal{M}_p, \end{cases} \end{aligned} \tag{6.3}$$

where $\mathbf{z} = [\tilde{\mathbf{x}}_1^T, \mathbf{0}_{N-1}^T, \ldots \tilde{\mathbf{x}}_{\mathcal{M}_p}^T, \mathbf{0}_{N-1}^T]^T \in \mathbb{C}^{\mathcal{M}_p(2N-1)}$, $\mathbf{y} = ((\tilde{K}-1)\mathcal{M}_pN+\lambda_u)\mathbf{z}^{(i)} - \mathbf{R}\mathbf{z}^{(i)}$. Let $\mathbf{z}$ has a length of $\tilde{K} = \mathcal{M}_p(2N-1)$, $\mathbf{U}_k$, $k = 1-\tilde{K},\ldots,\tilde{K}-1$ be $\tilde{K}\times\tilde{K}$ Toeplitz matrix, and $\mathbf{R}$ is a Hermitian Toeplitz matrix. Other additional parameters are defined in Table 6.1. Parameters $\mathbf{f}$ and $\mathbf{r}$ can be evaluated using standard FFT/IFFT operation.

As (6.3) is separable in the variables composing the sequence, the objective $\mathcal{O} = \| \mathbf{z}-\mathbf{y} \|_2^2$

[2]Hereafter, $x_{n,p}^d$ is represented as $\tilde{x}_{n,p}$ for ease of notation.

Table 6.1: Additional parameters for equation (6.3) [7].

S.No	Parameter	Expression
1	$\mathbf{F}$	$F_{n,k} = e^{-j\frac{2nk\pi}{2\tilde{K}}}, 0 \leq n,k \leq 2\tilde{K}$
2	$\mathbf{f}$	$\mathbf{F}[\mathbf{z}^{(i)^T}, \mathbf{0}_{1\times L}]^T$
3	$\mathbf{r}$	$\frac{1}{2L}\mathbf{F}^H\lvert\mathbf{f}\rvert^2$
4	$\mathbf{c}$	$\mathbf{r}\odot[0, \mathbf{1}_{N-1}^T, \mathbf{0}_{2(\mathcal{M}_p(2N-1)-N)+1}^T, \mathbf{1}_{N-1}^T]^T$
5	$\boldsymbol{\mu}$	$\mathbf{Fc}$,
6	λ_u	$\frac{1}{2}\left(\max\limits_{1\leq k\leq\tilde{K}} \mu_{2i} + \max\limits_{1\leq k\leq\tilde{K}} \mu_{2i-1}\right)$
7	$\mathbf{U}_k$	$\begin{cases}1 \text{ if } j-i=k \\ 0 \text{ if } j-i\neq k,\end{cases} i,j = 1,\ldots,\tilde{K}$
8	$r_z(k)$	$\mathbf{z}^H\mathbf{U}_k\mathbf{z}, k = 1-\tilde{K},\ldots,\tilde{K}-1$
9	w_k	$\begin{cases}1,\ 1\leq k\leq N-1 \\ 0,\ N\leq k\leq\tilde{K},\end{cases} i,j = 1,\ldots,\tilde{K}$
10	$\mathbf{R}$	$\sum_{\substack{k=1-\tilde{K}\\k\neq 0}}^{\tilde{K}-1} w_k r_z(-k)\mathbf{U}_k$

can now be split into $\mathcal{M}_p$ subproblems and represented as

$$\begin{aligned}\mathcal{O} &= \sum_{n'=1}^{\mathcal{M}_p(2N-1)} |z_{n'} - y_{n'}|_2^2, \\ &= \sum_{n'=1}^{N} |z_{n'} - y_{n'}|_2^2 + \sum_{n'=2N}^{3N} |z_{n'} - y_{n'}|_2^2 \\ &\quad + \ldots + \sum_{n'=1+(\mathcal{M}_p-1)(2N-1)}^{N+(\mathcal{M}_p-1)(2N-1)} |z_{n'} - y_{n'}|_2^2 + \text{ cnst.}\end{aligned} \tag{6.4}$$

Let $\mathbf{y} = \text{vec}(\mathbf{Y})$ where

$$\begin{aligned}\mathbf{Y} &= [\quad \mathbf{y}_1 \ , \ \ldots \ , \ \mathbf{y}_p \ , \ \ldots \ , \ \mathbf{y}_{\mathcal{M}_p} \quad] \\ &= [\overbrace{[\widetilde{\mathbf{y}}_1^T, \bar{\bar{\mathbf{y}}}_1^T]^T}, \ldots, \overbrace{[\widetilde{\mathbf{y}}_p^T, \bar{\bar{\mathbf{y}}}_p^T]^T}, \ldots, \overbrace{[\widetilde{\mathbf{y}}_{\mathcal{M}_p}^T, \bar{\bar{\mathbf{y}}}_{\mathcal{M}_p}^T]^T}]\end{aligned} \tag{6.5}$$

where $\widetilde{\mathbf{y}}_p = [\rho_{\{1,p\}}e^{j\psi_{\{1,p\}}}, \ldots, \rho_{\{N,p\}}e^{j\psi_{\{N,p\}}}]^T \in \mathbb{C}^N$ and $\bar{\bar{\mathbf{y}}}_p^T \in \mathbb{C}^{N-1}$. The constant part in (6.4) is obtained from the norm of the elements of $\mathbf{z}$ which corresponds to $\mathbf{0}_{N-1}$ and $\bar{\bar{\mathbf{y}}}_p$ where $p = 1,\ldots,\mathcal{M}_p$. As the constant part is independent of the variable, hence it can be omitted

from the objective. The remaining part of the objective is

$$\begin{aligned}\widetilde{\mathcal{O}} &= \sum_{n'=1}^{N} |z_{n'} - \rho_{n',p} e^{j\psi_{n',p}}|_2^2 + \dots \\ &+ \sum_{n'=2N}^{3N} |z_{n'} - \rho_{n',p} e^{j\psi_{n',p}}|_2^2 + \dots \\ &+ \sum_{n'=1+(\mathcal{M}_p-1)(2N-1)}^{N+(\mathcal{M}_p-1)(2N-1)} |z_{n'} - \rho_{n',p} e^{j\psi_{n',p}}|_2^2 \\ &= \mathcal{O}_1 + \ldots + \mathcal{O}_p + \ldots + \mathcal{O}_{\mathcal{M}_p} = \sum_{p=1}^{\mathcal{M}_p} \mathcal{O}_p\end{aligned} \tag{6.6}$$

Each of the M_p objectives are independent and can be solved in parallel. In (6.6) for brevity of expression, we consider the minimization of the p-th objective $\mathcal{O}_p$ as

$$\underset{a_{\{q,l,p\}}}{\text{minimize}} \sum_{n=1}^{N} |z_n - \rho_{n,p} e^{j\psi_{n,p}}|_2^2. \tag{6.7}$$

The objective $\mathcal{O}_p$ for the p-th pulse is further separable in the sequence variables, therefore it is split into L parallel sub-problems as:

$$\mathcal{O}_p = \mathcal{O}_{p,1} + \ldots + \mathcal{O}_{p,l} + \ldots + \mathcal{O}_{p,L}. \tag{6.8}$$

Now, we introduce the constraints of Problem $\mathcal{P}_{\{\widetilde{\mathbf{x}}_d\}}$ in $\mathcal{O}_{p,l}$ directly in the entries of the sub-sequence. Hence,

$$\mathcal{O}_{p,l} = \sum_{m=1}^{M} |e^{j(\sum_{q=0}^{Q} a_{\{q,l,p\}} m^q)} - \rho_{n,p} e^{j\psi_{n,p}}|_2^2. \tag{6.9}$$

In furtherance of this, let us define

$$\begin{aligned}\theta_{n,p} &= \sum_{q=0}^{Q} a_{\{q,l,p\}} m^q - \psi_{n,p}, \text{and} \\ f_m(\theta_{n,p}, \psi_{n,p}) &= |e^{j(\sum_{q=0}^{Q} a_{\{q,l,p\}} m^q)} - \rho_{n,p} e^{j\psi_{n,p}}|_2^2\end{aligned} \tag{6.10}$$

therefore,

$$\mathcal{O}_{p,l} = \sum_{m=1}^{M} f_m(\theta_{n,p}, \psi_{n,p}), \tag{6.11}$$

where $f_m(\theta_{n,p}, \psi_{n,p})$ can be simplified as

$$\begin{aligned} f_m(\theta_{n,p}, \psi_{n,p}) &= |(\cos(\theta_{n,p}) + j\sin(\theta_{n,p})) \\ &\quad - \rho_{n,p}(\cos(\psi_{n,p}) + j\sin(\psi_{n,p}))|_2^2 \\ &= (\cos(\theta_{n,p}) - \rho_{n,p}\cos(\psi_{n,p}))^2 \\ &\quad + (\sin(\theta_{n,p} - \rho_{n,p}\sin(\psi_{n,p})))^2 \\ &= \Big[\cos^2(\theta_{n,p}) + \rho^2\cos^2(\psi_{n,p}) \\ &- 2\rho_{n,p}\cos(\theta_{n,p})\cos(\psi_{n,p})\Big] \\ &\quad + \Big[\sin^2(\theta_{n,p}) + \rho^2\sin^2(\psi_{n,p}) \\ &- 2\rho_{n,p}\sin(\theta_{n,p})\sin(\psi_{n,p})\Big] \\ &= 1 + \rho_{n,p}^2 \\ &- 2\rho_{n,p}\Big(\cos(\theta_{n,p})\cos(\psi_{n,p}) + \sin(\theta_{n,p}\sin(\psi_{n,p}))\Big) \end{aligned} \tag{6.12}$$

As the first two terms (i.e. 1 and $\rho_{n,p}^2$) are constant for the current iteration, therefore, the sub-problem after ignoring the constant terms corresponding to $\mathcal{O}_{p,l}$ can be represented as

$$\mathcal{P}_{\{\mathcal{O}_{p,l}\}}\left\{\underset{a_{\{q,l,p\}}}{\text{minimize}} \quad -\Big[\sum_{m=1}^{M}\rho_{n,p}\cos\left(\sum_{q=0}^{Q}a_{\{q,l,p\}}m^q - \psi_{n,p}\right)\Big]. \right. \tag{6.13}$$

A majorizer $g(\theta_{n,p}, \theta_{n,p}^{(i)})$ of the function $f(\theta_{n,p}) = -\rho_{n,p}\cos(\theta_{n,p})$ at the i-th iteration of majorization can be obtained as

$$\begin{aligned} g(\theta_{n,p}, \theta_{n,p}^{(i)}) &= -\rho_{n,p}\cos(\theta_{n,p}^{(i)}) \\ &\quad + \left(\theta_{n,p} - \theta_{n,p}^{(i)}\right)\rho_{n,p}\sin(\theta_{n,p}^{(i)}) \\ &\quad + \frac{1}{2}\left(\theta_{n,p} - \theta_{n,p}^{(i)}\right)^2\rho_{n,p}\cos(\theta_{n,p}^{(i)}) \end{aligned} \tag{6.14}$$

where the variable is $\theta_{n,p}$ and it has a phase value in the last iteration which is denoted as $\theta_{n,p}^{(i)}$. This result stems from the principle that a function which is continuously differentiable and has a Lipschitz continuous gradient allows for the use of a second-order Taylor expansion as a majorizer[125]. Employing this majorizer function, at the i-th iteration of the MM algorithm,

the optimization problem can be expressed as

$$\begin{cases} \underset{a_{\{q,l,p\}}}{\text{minimize}} & \sum_{m=1}^{M} \Bigg[-\rho_{n,p}\cos(\theta_{n,p}^{(i)}) + \\ & \left(\theta_{n,p} - \theta_{n,p}^{(i)}\right)\rho_{n,p}\sin(\theta_{n,p}^{(i)}) \\ & +\frac{1}{2}\left(\theta_{n,p} - \theta_{n,p}^{(i)}\right)^2 \rho_{n,p}\cos(\theta_{n,p}^{(i)}) \Bigg] \end{cases} \tag{6.15}$$

An equivalent perfect square form can be written for the objective function in (6.15), where the constant terms independent of the variable $a_{\{q,l,p\}}$ are omitted. With this assumption, the surrogate problem from (6.15) is

$$\left\{ \underset{a_{\{q,l,p\}}}{\text{minimize}} \quad \sum_{m=1}^{M} \left[\rho_{n,p}\cos(\theta_{n,p}^{(i)}) \left(\sum_{q=0}^{Q} a_{\{q,l,p\}} m^q \right) - b_{n,p} \right]^2 \right. \tag{6.16}$$

where

$$b_{n,p} = \rho_{n,p}\cos(\theta_{n,p}^{(i)}) \left(\psi_{n,p} + \theta_{n,p}^{(i)}\right) - \rho_{n,p}\sin(\theta_{n,p}^{(i)}).$$

Now, considering a generic pulse index p and l-th sub-sequence, let

$$\begin{aligned} \widetilde{\boldsymbol{\eta}} &= [1, 2, 3, \cdots, M]^T \in \mathbb{Z}_+^M, \\ \widetilde{\boldsymbol{\gamma}}_p &= \rho_{n,p}\cos(\theta_{n,p}^{(i)}) \odot [1, \cdots, 1]^T \in \mathbb{R}^M, \\ \widetilde{\mathfrak{A}} &= \text{Diag}\,(\widetilde{\boldsymbol{\gamma}_p})[\widetilde{\boldsymbol{\eta}}^0, \cdots, \widetilde{\boldsymbol{\eta}}^Q] \in \mathbb{R}^{M\times(Q+1)}, \\ \widetilde{\mathbf{s}} &= [a_{0,p}, \cdots, a_{Q,p}]^T \in \mathbb{R}^{Q+1}, \\ \widetilde{\mathbf{b}} &= [b_{1,p}, \cdots, b_{M,p}]^T \in \mathbb{R}^M. \end{aligned} \tag{6.17}$$

In this context, $\widetilde{\boldsymbol{\eta}}^q$ signifies that all elements of $\widetilde{\boldsymbol{\eta}}$ are elevated to the power q individually, with q spanning from 0 to Q. By using the variables defined in (6.17), the optimization problem in (6.16) is

$$\left\{ \underset{\widetilde{\mathbf{s}}}{\text{minimize}} \parallel \widetilde{\mathfrak{A}}\widetilde{\mathbf{s}} - \widetilde{\mathbf{b}} \parallel_2^2 \right. \tag{6.18}$$

which represents a standard least squares problem. Consequently, the optimal $\widetilde{\mathbf{s}}^\star = \widetilde{\mathfrak{A}}^\dagger\widetilde{\mathbf{b}}$ would be calculated[3]. By applying this method for all the L sub-sequences, the entire sequence $\tilde{\mathbf{x}}_p$ for the p-th pulse is calculated.

Further, using sequence index p, we calculate all $\tilde{\mathbf{x}}_p$s pertaining to the complementary sequence set $\widetilde{\mathbf{X}}_d$. The objective is montonically optimized by the algorithm, and an optimal sequence set $\widetilde{\mathbf{X}}_d^{(i+1)}$ is obtained. The iterations are terminated with the following criterion:

[3]We can use "lsqr" in *Sparse Matrices Toolbox* of MATLAB 2022a to solve (6.18).

$\left(\frac{1}{\sqrt{NM_p}} \parallel \widetilde{\mathbf{X}}_d^{(i+1)} - \widetilde{\mathbf{X}}_d^{(i)} \parallel < \epsilon\right)$ where $\epsilon \approx 10^{-6}$. The implementation details of the proposed method are summarized in algorithm 7 and 8.

Algorithm 7 Algorithm for complimentary sequence set design with polynomial phase characteristic in every sequence

Require: $\mathcal{M}_p, N, Q, \boldsymbol{\mathcal{A}}_d^{(i)}$
$\tilde{K} = \mathcal{M}_p(2N-1)$
Set $i = 0$, initialize $\widetilde{\mathbf{X}}_d^{(0)}$
while stopping criterion is true **do**
  $\mathbf{z}^{(i)} = [\tilde{\mathbf{x}}_1^{(i)^T}, \mathbf{0}^T, \ldots, \tilde{\mathbf{x}}_{\mathcal{M}_p}^{(i)^T}, \mathbf{0}^T]^T \in \mathbb{C}^{\mathcal{M}_p(2N-1)}$
  Calculate $\mathbf{F}, \mathbf{c}, \boldsymbol{\mu}, \lambda_u$ from Table 6.1
  $\mathbf{y}^{(i)} = ((\tilde{K}-1)\mathcal{M}_p N + \lambda_u)\mathbf{z}^{(i)} - \mathbf{R}\mathbf{z}^{(i)}$
  for $p \leftarrow 1$ *to* $\mathcal{M}_p$ **do**
    derive $\widetilde{\mathbf{y}}_p$ from (6.5)
    $\widetilde{\mathbf{y}}_p^{(i)} = [\tilde{\mathbf{y}}_{1,p}^{T^{(i)}}, \ldots, \tilde{\mathbf{y}}_{l,p}^{T^{(i)}}, \ldots, \tilde{\mathbf{y}}_{L,p}^{T^{(i)}}] \in \mathbb{C}^N$
    for $l \leftarrow 1$ *to* L **do**
      $\tilde{\mathbf{y}}_{l,p}^{(i+1)} = \text{PECS Gen}(\tilde{\mathbf{y}}_{l,p}^{(i)}, N, \boldsymbol{\mathcal{A}}_{\{:,l,p\}}^{(i)})$
    $\widetilde{\mathbf{y}}_p^{(i+1)} = [\tilde{\mathbf{y}}_{1,p}^{T^{(i+1)}}, \ldots, \tilde{\mathbf{y}}_{l,p}^{T^{(i+1)}}, \ldots, \tilde{\mathbf{y}}_{L,p}^{T^{(i+1)}}]$
  $\mathbf{y}^{(i+1)} = [\widetilde{\mathbf{y}}_1^{T^{(i+1)}}, \bar{\widetilde{\mathbf{y}}}_1^{T^{(i+1)}}, \ldots, \widetilde{\mathbf{y}}_{\mathcal{M}_p}^{T^{(i+1)}}, \bar{\widetilde{\mathbf{y}}}_{\mathcal{M}_p}^{T^{(i+1)}}]^T$
  $x_{n,p}^{(i+1)} = e^{j \arg(y_{n,p}^{(i)})} \; \forall \begin{cases} n=1,\ldots,N, \\ p=1,\ldots,\mathcal{M}_p \end{cases}$
$i \leftarrow i+1$
return $\tilde{\mathbf{X}}_d^{(i+1)}$

Algorithm 8 PECS Gen

procedure PECS GEN($\mathbf{z}, M, \mathbf{s}$)
  $\boldsymbol{\rho} = |\mathbf{s}|$
  $\boldsymbol{\psi} = \arg(\mathbf{s})$
  $\theta_m = \sum_{q=0}^{Q} a_q m^q - \psi_m, \; m = 1, \ldots, M$
  $b_m = \rho_m \cos(\theta_m)\,(\psi_m + \theta_m) - \rho_m \sin(\theta_m)$
  $\boldsymbol{\eta} = [1, 2, 3, \cdots, M]^T \in \mathbb{Z}_+^M$
  $\boldsymbol{\gamma} = \rho_m \cos(\theta_m) \odot [1, \cdots, 1]^T \in \mathbb{R}^M$,
  $\widetilde{\boldsymbol{A}} = \text{Diag}\,(\boldsymbol{\gamma})[\boldsymbol{\eta}^0, \boldsymbol{\eta}^1, \cdots, \boldsymbol{\eta}^Q] \in \mathbb{R}^{M \times Q+1}$,
  $\mathbf{z} = [a_0, a_1, \cdots, a_Q]^T \in \mathbb{R}^{Q+1}$
  $\widetilde{\mathbf{b}} = [b_1, b_2, \cdots, b_M]^T \in \mathbb{R}^M$
  $\mathbf{z}^\star = \widetilde{\boldsymbol{A}}^{(\dagger)}\widetilde{\mathbf{b}}$ (Least Squares Operation)
  $\tilde{\mathbf{s}} = \widetilde{\boldsymbol{A}}\mathbf{z}^\star \in \mathbb{C}^M$
  return $\tilde{\mathbf{s}}$

6.3.2 Waveform design in PMCW/FMCW MIMO radars with polynomial phase constraint for ISL minimization within a single pulse

We consider the design of sequence sets $\bar{\mathbf{X}}_p$ for the p-th pulse. Each antenna transmits a sequence $\bar{\mathbf{x}}_d$ of length N, where $d = 1, \cdots, \mathcal{M}_t$. The sequences are stacked to form the matrix $\bar{\mathbf{X}}_p = [\bar{\mathbf{x}}_1, \cdots, \bar{\mathbf{x}}_d, \cdots, \bar{\mathbf{x}}_{\mathcal{M}_t}] \in \mathbb{C}^{N \times \mathcal{M}_t}$, where $x^p_{n,d}$ represents the element in the n-th row and d-th column for the p-th pulse.

A key aspect of creating orthogonality for MIMO radar signal involves assessing the aperiodic auto/cross-correlation between different transmit waveforms $\bar{\mathbf{x}}_d$ and $\bar{\mathbf{x}}_{d'}$ ($d \neq d'$ and $d, d' \in [1, \cdots, \mathcal{M}_t]$). This correlation is calculated directly from the transmit sequences as,

$$\bar{r}_{d,d'}(k) = \sum_{n=k+1}^{N} \bar{x}_{n,d} \bar{x}^*_{n-k,d'} = \bar{r}_{d',d}(-k),\ k = 0, \cdots, N-1. \tag{6.19}$$

We formulate the following optimization problem to achieve the design of unimodular sequence sets exhibiting desirable correlation characteristics and polynomial phase behavior as:

$$\mathcal{P}_{\{\bar{\mathbf{X}}_p\}} \begin{cases} \underset{\boldsymbol{\mathcal{A}}_p \in \mathbb{R}^{Q \times L \times \mathcal{M}_t}}{\text{minimize}} & \displaystyle\sum_{d=1}^{\mathcal{M}_t} \sum_{d'=1}^{\mathcal{M}_t} \sum_{\substack{k=1-N \\ k \neq 0, d=d'}}^{N-1} |\bar{r}_{d,d'}(k)|^2 \\ \text{subject to} & \arg(x^p_{n,d}) = \displaystyle\sum_{q=0}^{Q} a_{\{q,l,d\}} m^q, \\ & |x^p_{n,d}| = 1, \forall \begin{cases} n = m + (l-1)M, \\ l = 1, \ldots, L, \\ m = 1, \ldots, M, \\ d, d' = 1, \ldots, \mathcal{M}_t. \end{cases} \end{cases} \tag{6.20}$$

where the polynomial phase constraint is expressed as $\arg(\bar{x}_{n,d}) = \sum_{q=0}^{Q} a_{\{q,l,d\}} m^q$[4].

After reformulating the objective using MM framework [7], above problem can be written

[4]Hereafter, $x^p_{n,d}$ is represented as $\bar{x}_{n,d}$ for ease of notation.

Table 6.2: Supporting parameters for (6.22) and algorithm 9 [7].

S.No	Parameter	Relation
1	$\mathbf{h}_p$	$[1, e^{j\omega_p}, \ldots, e^{j\omega_p(N-1)}]^T, p = 1, \ldots, 2N,$
2	$\mathbf{H}$	$[\mathbf{h}_1, \ldots, \mathbf{h}_{2N}] \in \mathbb{C}^{N\times 2N}$
3	ω_p	$\frac{2\pi}{2N}(p-1)$
4	t	$\left(\sum_{p=1}^{2N} \parallel \bar{\mathbf{X}}_p^{(i)^H}\mathbf{h}_p\|_2^4\right)^{\frac{1}{4}}$
5	a_p	$t^2 + 2t \parallel \bar{\mathbf{X}}_p^{(i)^H}\mathbf{h}_p \parallel_2 + 3 \parallel \bar{\mathbf{X}}_p^{(i)^H}\mathbf{h}_p \parallel_2^2$
6	λ_a	$N\left(\max_{(1\le i\le N)} a_{2i} + \max_{(1\le i\le N)} a_{2i-1}\right)$
7	$\mathbf{q}$	$\left\lvert\mathbf{H}\bar{\mathbf{X}}_p^{(i)}\right\rvert^2 \mathbf{1}_{M\times 1}$

as

$$\begin{cases} \underset{\boldsymbol{\mathcal{A}}_p}{\text{minimize}} & \displaystyle\sum_{n=1}^{N}\sum_{d=1}^{\mathcal{M}_t} \Re(\bar{x}_{n,d}^*\, \bar{y}_{n,d}) \\ \text{subject to} & \arg(\bar{x}_{n,d}) = \displaystyle\sum_{q=0}^{Q} a_{\{q,l,d\}} m^q, \\ & |\bar{x}_{n,d}| = 1, \forall \begin{cases} n = m + (l-1)M, \\ l = 1, \ldots, L, \\ m = 1, \ldots, M, \\ d, d' = 1, \ldots, \mathcal{M}_t. \end{cases} \end{cases} \tag{6.21}$$

where $\bar{y}_{n,d}$ is an element of $\bar{\mathbf{Y}}_p$ and

$$\begin{aligned} \bar{\mathbf{Y}}_p &= 4\left(\sum_{p=1}^{2N} ||\bar{\mathbf{X}}_p^{(i)^H}\mathbf{h}_p||_2^2 \mathbf{h}_p\mathbf{h}_p^H\right)\bar{\mathbf{X}}_p^{(i)} - 2\lambda_a\bar{\mathbf{X}}_p^{(i)}, \\ &= 4\mathbf{H}^H \,\mathrm{Diag}\,(\mathbf{q})\mathbf{H}\bar{\mathbf{X}}_p^{(i)} - 2\lambda_a\bar{\mathbf{X}}_p^{(i)} \end{aligned} \tag{6.22}$$

The computation of $\mathbf{q}$ can be performed via standard FFT/IFFT operation. Other parameters are defined in Table 6.2. Let $\bar{\mathbf{X}}_p^{(i)}$ represent the value of $\bar{\mathbf{X}}_p$ in the i^{th} iteration of majorization, and the elements of $\bar{\mathbf{X}}_p$ which constitute the objective can be separated. Hence, the objective in (6.21) can be written in terms of each sub-sequence of the dth transmit sequence as

$$\begin{aligned} \bar{\mathcal{O}} = \sum_{d=1}^{\mathcal{M}_t}\Bigg[&\sum_{n=1}^{M} \Re(\bar{x}_{n,d}^*\, \bar{y}_{n,d}) + \sum_{n=M+1}^{2M} \Re(\bar{x}_{n,d}^*\, \bar{y}_{n,d}) + \cdots \\ &+ \sum_{n=M(L-1)+1}^{N} \Re(\bar{x}_{n,d}^*\, \bar{y}_{n,d})\Bigg]. \end{aligned} \tag{6.23}$$

Now, rewriting the above equation using sub-sequence based notation as

$$\begin{aligned}\bar{\mathcal{O}} &= \Bigg[\sum_{d=1}^{\mathcal{M}_t}||\check{\mathbf{x}}_{1,d}-\check{\mathbf{y}}_{1,d}||_2^2+\cdots+\sum_{d=1}^{\mathcal{M}_t}||\check{\mathbf{x}}_{l,d}-\check{\mathbf{y}}_{l,d}||_2^2+\cdots \\ &\quad+\sum_{d=1}^{\mathcal{M}_t}||\check{\mathbf{x}}_{L,d}-\check{\mathbf{y}}_{L,d}||_2^2\Bigg], \\ &= \Big[\bar{\mathcal{O}}_1+\cdots+\bar{\mathcal{O}}_l+\cdots+\bar{\mathcal{O}}_L\Big]\end{aligned} \tag{6.24}$$

where $\check{\mathbf{x}}_{l,d},\in\mathbb{C}^N$ such that $N=M\times L$. Now, each term in the objective function $\bar{\mathcal{O}}$ (i.e. $\bar{\mathcal{O}}_1,\ldots,\bar{\mathcal{O}}_L$) above can be solved in parallel as it is independent of the other terms. We consider a sub-problem as $\bar{\mathcal{O}}_l$

$$\begin{aligned}\bar{\mathcal{O}}_l &= \sum_{d=1}^{\mathcal{M}_t}||\check{\mathbf{x}}_{l,d}-\check{\mathbf{y}}_{l,d}||_2^2, \\ &= \sum_{d=1}^{\mathcal{M}_t}\sum_{n=(l-1)M}^{lM}|\bar{x}_{n,d}-\bar{y}_{n,d}|_2^2, \\ &= \sum_{n=(l-1)M}^{lM}|\bar{x}_{n,1}-\bar{y}_{n,1}|_2^2+\cdots \\ &\qquad+\sum_{n=(l-1)M}^{lM}|\bar{x}_{n,\mathcal{M}_t}-\bar{y}_{n,\mathcal{M}_t}|_2^2, \\ &= \bar{\mathcal{O}}_l^1+\cdots+\bar{\mathcal{O}}_l^d+\cdots+\bar{\mathcal{O}}_l^{\mathcal{M}_t}.\end{aligned} \tag{6.25}$$

Thus, the solution to each term can be pursued as described in Appendix-6.6.1 similar to the approach mentioned in section -6.3.1 [49]. Now, the optimization problem $\mathcal{P}_{\{\bar{\mathcal{O}}_l^d\}}$ corresponding to $\bar{\mathcal{O}}_l^d$ is defined as

$$\mathcal{P}_{\{\bar{\mathcal{O}}_l^d\}}\Big\{\underset{\bar{\mathbf{s}}}{\text{minimize}}\quad ||\bar{\mathfrak{A}}\bar{\mathbf{s}}-\bar{\mathbf{b}}||_2^2, \tag{6.26}$$

where

$$\begin{aligned}\bar{\mathfrak{A}} &= \text{Diag}\,(\boldsymbol{\gamma})[\boldsymbol{\eta}^0,\boldsymbol{\eta}^1,\cdots,\boldsymbol{\eta}^Q]\in\mathbb{R}^{M\times(Q+1)}, \\ \bar{\mathbf{s}} &= [\bar{a}_{\{0,l,d\}},\bar{a}_{\{1,l,d\}},\cdots,\bar{a}_{\{Q,l,d\}}]^T\in\mathbb{R}^{(Q+1)}, \\ \bar{\mathbf{b}} &= [\bar{b}_{1,d},\cdots,\bar{b}_{n+M,d}]^T\in\mathbb{R}^M, \\ \boldsymbol{\gamma} &= \bar{\rho}_{n,d}\cos(\bar{\theta}_{n,d}^{(i)})\odot[1,\cdots,1]^T\in\mathbb{R}^M, \\ \boldsymbol{\eta} &= [1,2,3,\cdots,M]^T\in\mathbb{Z}_+^M, \\ \bar{b}_{n,d} &= \bar{\rho}_{n,d}\cos(\bar{\theta}_{n,d}^{(i)})\left(\bar{\psi}_{n,d}+\bar{\theta}_{n,d}^{(i)}\right)-\bar{\rho}_{n,d}\sin(\bar{\theta}_{n,d}^{(i)}).\end{aligned} \tag{6.27}$$

Thus, (6.26) represents a standard least squares problem. Consequently, the optimal $\bar{\mathbf{s}}^\star=\bar{\mathfrak{A}}^\dagger\bar{\mathbf{b}}$ would be calculated, and the optimal sub-sequence will be synthesized. Utilizing the described

approach for a generic sub-sequence index l, we calculate all $\check{\mathbf{x}}_{l,d}$s pertaining to the sequence $\bar{\mathbf{x}}_d$ and eventually the sequence set $\bar{\mathbf{X}}_p$. The algorithm optimizes the objective, resulting in an optimal sequence set $\bar{\mathbf{X}}_p^{(i+1)}$. The overall method is described in algorithm 9.

Algorithm 9 MIMO sequence set ISL minimization with polynomial phase characteristic in every sub-sequence

Require: $\bar{\mathbf{X}}_p^{(0)}, \mathcal{M}_t, L, M, N, \boldsymbol{\mathcal{A}}_p^{(i)}$

while stopping criterion is true **do**
  Calculate $\mathbf{h}_p, t, a_p, \lambda_a$from Table 6.2
  $\bar{\mathbf{Y}}_p = 4\mathbf{H}^H \operatorname{Diag}(\mathbf{q})\mathbf{H}\bar{\mathbf{X}}_p^{(i)} - 2\lambda_a \mathbf{X}^{(i)}$
  for $l \leftarrow 1$ *to* L **do**
    for $d \leftarrow 1$ *to* $\mathcal{M}_t$ **do**
      $\check{\mathbf{y}}_{l,d} = [\bar{y}_{1,d}, \ldots, \bar{y}_{M,d}] \in \mathbb{C}^M$
      $\check{\mathbf{y}}_{l,d}^{(i+1)} = \text{PECS Gen}(\check{\mathbf{y}}_{l,d}^{(i)}, M, \boldsymbol{\mathcal{A}}_{\{:,l,d\}}^{(i)})$
    $\tilde{\mathbf{Y}}_l = [\check{\mathbf{y}}_{l,1}, \ldots, \check{\mathbf{y}}_{l,d}, \ldots, \check{\mathbf{y}}_{l,\mathcal{M}_t}] \in \mathbb{C}^{M \times \mathcal{M}_t}$
  $\mathbf{Y}^{(i)} = [\tilde{\mathbf{Y}}_1^T, \cdots, \tilde{\mathbf{Y}}_l^T, \cdots, \tilde{\mathbf{Y}}_L^T]^T \in \mathbb{C}^{N \times \mathcal{M}_t}$
  $\bar{x}_{n,d}^{(i+1)} = e^{j(\arg(\bar{y}_{n,d}^{(i)}))}, \begin{cases} d=1,\ldots,\mathcal{M}_t \\ n=1,\ldots,N \end{cases}$
  $i \leftarrow i+1$

6.3.3 Transmit beampattern design with polynomial phase constraint for PM-CW/FMCW MIMO radars

Previously, the objective in $\mathcal{P}_{\{\bar{\mathbf{X}}_p\}}$ constituted of both auto and cross-correlation. Cross-correlation minimization leads to orthogonality of the sequences in a set which is used for creating intra-pulse coding as described in the previous section for MIMO radar systems. In the current context, the sequences need to be correlated in a manner where the differential phase shift in every sequence leads to the beam pattern shaping.

In furtherance to this, we assume that the transmit antennas are configured in an arbitrary two-dimensional (2-D) arrangement. Consider the position vector of the d^{th} antenna, denoted as $\mathbf{p}_d = [p_{x_d}, p_{y_d}, p_{z_d}]^T$, within a Cartesian coordinate system where the origin is located at the center of the transmit antenna array. The antenna beampattern is characterized through $\Theta = (\theta, \phi)$ where θ and ϕ denote, repectively, the elevation and azimuth angles with respect to the origin of the array. The steering vector for the d^{th} element is $\mathbf{u}(\theta, \phi) = [u_1(\theta, \phi), \ldots, u_{\mathcal{M}_t}(\theta, \phi)]$ where $u_d(\theta, \phi) = \exp j\frac{2\pi}{\lambda} c_0 \tau_d,\ d = 1, \ldots, \mathcal{M}_t$. Here, $c_0 = 3 \times 10^8$ m/s and λ denote the speed of light and signal wavelength, respectively. τ_d represents the incremental time delay from the target to the d^{th} antenna element with respect to the origin. In this case, the transmit antenna

beampattern is given as

$$g(\grave{\mathbf{x}}_p, \theta, \phi) = |\mathbf{u}^H(\theta, \phi)\grave{\mathbf{x}}_p|^2 = \grave{\mathbf{x}}_p^H \mathbf{U}(\theta, \phi)\grave{\mathbf{x}}_p \tag{6.28}$$

where $\mathbf{U}(\theta, \phi) \triangleq \mathbf{u}(\theta, \phi)\mathbf{u}^H(\theta, \phi)$ and $\grave{\mathbf{x}}_p = [x_{1,p}^n, \cdots, x_{d,p}^n, \cdots, x_{\mathcal{M}_t,p}^n]^T \in \mathbb{C}^{\mathcal{M}_t}$. We denote Ψ_d as the collection of desired angles, represented by pairs (θ_i, ϕ_i), where i ranges from 1 to I_D, and Ψ_u as the collection of undesired angles, represented by pairs (θ_j, ϕ_j), where j ranges from 1 to J_U, in the spatial domain.

We consider

$$g_1(\widetilde{\mathbf{X}}_d) = \sum_{k=1}^{N-1} \left| \sum_{p=1}^{\mathcal{M}_p} \tilde{r}_{p,p}(k) \right|^2 \; \forall \; \begin{cases} q = 1, \ldots, Q, \\ l = 1, \ldots, L, \\ p = 1, \ldots, \mathcal{M}_p, \end{cases} \tag{6.29}$$

as the first objective function.

As a next step, we use the n-th element in the code domain of $\widetilde{\mathbf{X}}_d^\star$ for $d = 1$, we intend to obtain the transmit sequence in the spatial domain. To steer the transmit beampattern to a desired direction, we consider the following objective function,

$$g_2(\grave{\mathbf{X}}_n) = \frac{\grave{\mathbf{x}}_p^H \mathbf{U}_u \grave{\mathbf{x}}_p}{\grave{\mathbf{x}}_p^H \mathbf{U}_d \grave{\mathbf{x}}_p} \quad \forall \quad \begin{cases} n \in [1, \ldots, N] \\ d \in [1, \ldots, \mathcal{M}_t], \end{cases} \tag{6.30}$$

where $\grave{\mathbf{X}}_n = [\grave{\mathbf{x}}_1, \ldots, \grave{\mathbf{x}}_p, \ldots, \grave{\mathbf{x}}_{\mathcal{M}_p}] \in \mathbb{C}^{\mathcal{M}_t \times \mathcal{M}_p}$ and its elements are represented as $x_{d,p}^n$ with $n \in [1, \ldots, N]$, $p = 1, \ldots, \mathcal{M}_p$, $d = 1, \ldots, \mathcal{M}_t$, $\mathbf{U}_d \triangleq \sum_{i=1}^{I_D} \mathbf{U}(\theta_i, \phi_i)$, and $\mathbf{U}_u \triangleq \sum_{j=1}^{J_U} \mathbf{U}(\theta_j, \phi_j)$. Our focus is on minimizing $g_1(\widetilde{\mathbf{X}}_d)$ and $g_2(\grave{\mathbf{X}}_n)$ under polynomial and continuous phase constraints, formulated as

$$\begin{cases} \underset{\boldsymbol{\mathcal{A}} \in \mathbb{R}^{Q \times L \times \mathcal{M}_t \times \mathcal{M}_p}}{\text{minimize}} & g_1(\widetilde{\mathbf{X}}_d), g_2(\grave{\mathbf{X}}_n) \\ \text{subject to} & \arg(x_{\{n,d,p\}}) = \sum_{q=0}^{Q} a_{\{q,l,d,p\}} m^q, \\ & |x_{\{n,d,p\}}| = 1, \forall \begin{cases} n = m + (l-1)M, \\ l = 1, \ldots, L, \\ m = 1, \ldots, M, \\ d = 1, \ldots, \mathcal{M}_t, \\ p = 1, \ldots, \mathcal{M}_p. \end{cases} \end{cases} \tag{6.31}$$

Considering the non-convex nature of the objective function and the non-affine, non-convex

nature of the constraints, the overall optimization problem is non-convex, involving multiple variables, and deemed NP-hard. To address this problem, we approach the solution using methods based on MM and BCD.

In particular, we consider the design of $\widetilde{\mathbf{X}}_d$ for $d = 1$ using the algorithm -7. By applying the constraints related to the fast time and pulse domain, the optimization problem is

$$\mathcal{P}_1 \begin{cases} \underset{\widetilde{\mathbf{X}}_d \in \mathbb{C}^{N \times \mathcal{M}_p}}{\text{minimize}} & g_1(\widetilde{\mathbf{X}}_d) \\ \text{subject to} & \arg(\mathbf{x}_{n,p}^d) = \sum_{q=0}^{Q} a_{\{q,l,p\}} m^q, \\ & |x_{n,p}^d| = 1, \forall \begin{cases} n = m + (l-1)M, \\ l = 1, \ldots, L, \\ m = 1, \ldots, M, \\ p = 1, \ldots, \mathcal{M}_p. \end{cases} \end{cases} \tag{6.32}$$

Considering the first row of $\widetilde{\mathbf{X}}_d^\star$ as the seed for the first pulse, the first entries of $\grave{\mathbf{X}}_n$ along the pulse dimension (i.e. $d = 1$, and $n = 1, \ldots, N$) are available. The element $\tilde{x}_{n,d+1}$[5] in the position $n, d+1$ of $\grave{\mathbf{X}}_n$, where n ranges from 1 to N, is the sole variable adjusted while holding all other variables constant. We then optimize the objective function with respect to this specific variable. Hence, the optimization problem to be dealt in the next step is

$$\mathcal{P}_2 \begin{cases} \underset{\grave{\mathbf{X}}_n \in \mathbb{C}^{\mathcal{M}_t \times \mathcal{M}_p}}{\text{minimize}} & g_2(\grave{\mathbf{X}}_n) \\ \text{subject to} & \arg(x_{d,p}^n) = \sum_{q=0}^{Q} a_{\{q,l,d,p\}} m^q, \\ & |x_{d,p}^n| = 1, \forall \begin{cases} n = m + (l-1)M, \\ l = 1, \ldots, L, \\ m = 1, \ldots, M, \\ p = 1, \ldots, \mathcal{M}_p, \\ d, d' = 1, \ldots, \mathcal{M}_t. \end{cases} \end{cases} \tag{6.33}$$

Finally, solving these two problems (i.e. $\mathcal{P}_1$ and $\mathcal{P}_2$) sequentially, the equivalent overall problem in (6.31) is solved. This approach proves efficient when the objective function can be expressed in a simplified manner concerning the designated variable. In this regard, let us assume that $x_{d',p}$ where $d' = d + 1$ is the only variable at the i-th iteration of the optimization procedure. The

[5]For notational simplicity, we represent $x_{n,p}^d$ as $\tilde{x}_{n,p}$ and $x_{d,p}^n$ as $\grave{x}_{d,p}$.

resulting single-variable objective function at i-th iteration can be written as (refer Appendix-6.6.2)

$$g_2(\grave{x}_{d',p}, \grave{\mathbf{x}}^{(i)}_{-(p)}) = \frac{\bar{a}_0\grave{x}_{d',p} + \bar{a}_1 + \bar{a}_2\grave{x}^*_{d',p}}{\bar{b}_0\grave{x}_{d',p} + \bar{b}_1 + \bar{b}_2\grave{x}^*_{d',p}}. \tag{6.34}$$

Here, $\grave{\mathbf{x}}^{(i)}_{-(p)} = \grave{\mathbf{x}}^{(i)}_p|_{\grave{x}_{d',p}=0}$ refers to the fixed entries (i.e. all entries in $\grave{\mathbf{x}}_p$ except $\grave{x}_{d',p}$). By substituting $\grave{x}_{d',p} = e^{j\Theta_{d',p}}$, the variable in the objective in (6.30) depends only on the parameter Θ[6] and can be recast as

$$(\bar{\mathcal{P}})^{(i)} \begin{cases} \underset{\Theta}{\text{minimize}}\, g_2^{(i)}(\Theta) & = \dfrac{\bar{a}_0 e^{j\Theta} + \bar{a}_1 + \bar{a}_2 e^{-j\Theta}}{\bar{b}_0 e^{j\Theta} + \bar{b}_1 + \bar{b}_2 e^{-j\Theta}} \\ \text{subject to} & \Theta \in \Omega_\infty \end{cases} \tag{6.35}$$

As a result, the optimal phase of the code entry $x_{d',p}$ can be determined by solving

$$\Theta^{\star(i)} = \arg\min_{\Theta}\{g_2^{(i)}(\Theta) | \Theta \in \Omega_\infty\}. \tag{6.36}$$

Subsequently, the variable $x_{d',p}$ will be updated by $x^{(i)\star}_{d',p} = e^{j\Theta^{\star(i)}}$. This process is iterated to obtain consecutive optimal phase entries until all entries in $\grave{\mathbf{X}}_n$ are updated, resulting in a stationary point. The outlined approach is presented in Algorithm 10.

To this end, we obtain the optimal solution by examining the derivative of $g_2(\Theta)$ while adhering to a continuous phase constraint. As $g_2^{(i)}(\Theta)$ is a real, differentiable and periodic function, it has at least two extrema. Therefore, its derivative has at least two real roots. By standard mathematical manipulations, the derivative of $g_2^{(i)}(\Theta)$ can be obtained as

$$g_2^{\prime(i)}(\Theta) = \frac{c_0 e^{j\Theta} + c_1 + c_2 e^{-j\Theta}}{(\bar{b}_0 e^{j\Theta} + \bar{b}_1 + \bar{b}_2 e^{-j\Theta})^2}, \tag{6.37}$$

where $c_0 = j(\bar{a}_0\bar{b}_1 - \bar{a}_1\bar{b}_0)$, $c_1 = j2(\bar{a}_0\bar{b}_2 - \bar{a}_2\bar{b}_0)$ and $c_2 = c_0^*$. By introducing the auxiliary variable $z \triangleq e^{-j\Theta}$, the critical points are derived from the roots of a second-degree polynomial, specifically $g_2^{\prime(i)}(\Theta) \triangleq c_2 z^2 + c_1 z + c_0 = 0$. These roots are given by $z^{(i)}_{1,2} = \frac{-c_1 \pm \sqrt{c_1^2 - 4c_2c_0}}{2c_2}$. Therefore, the extremum point of $g_2^{(i)}(\Theta)$ is $\Theta^{(i)}_{\{1,2\}} \triangleq j\ln(z^{(i)}_{1,2})$ and subsequently the optimized phase is

$$\Theta^{\star(i)} = \arg\min_{\Theta} \left\{ g_2^{(i)}(\Theta) \,|\, \Theta \in \Theta^{(i)}_{\{1,2\}} \right\}. \tag{6.38}$$

Remark 3. *Computational complexity - The computational complexity for algorithm 7 and 9 can be divided into two major steps:*

- *Computational cost of deriving supporting parameters mentioned in Table6.1 and Ta-*

[6]For brevity, we will use Θ instead of $\Theta_{d',p}$ in the following text.

Algorithm 10 MIMO Beampattern shaping using Polynomial phase characteristic in temporal domain

Require: $\boldsymbol{\mathcal{X}}^{(0)}, \mathcal{M}_t, N, \mathcal{M}_p, \Psi_d, \Psi_u$

Evaluate $\widetilde{\mathbf{X}}^{\star}_{d|d=1}$ using algorithm-7
while stopping criterion is true **do**
  for $p \leftarrow 1\ to\ \mathcal{M}_p$ **do**
    for $n \leftarrow 1\ to\ N$ **do**
      for $d' \leftarrow 2\ to\ \mathcal{M}_t$ **do**
        Optimize $\grave{x}^{(i)}_{d',p}$ and obtain $\grave{x}^{\star}_{d',p}$
        Update $\grave{x}^{(i+1)}_{d',p} = \grave{x}^{\star}_{d',p}$
        $\grave{\mathbf{X}}^{(i+1)}_{n} = \grave{\mathbf{X}}^{(i+1)}_{n}|_{\grave{x}_{d',p}=\grave{x}^{(i+1)}_{d',p}}$
return $\boldsymbol{\mathcal{X}}^{(i+1)}$

ble6.2 as $\mathbf{O}(\mathcal{M}_t N log N)$ *and* $\mathbf{O}(\mathcal{M}_p N log N)$ *respectively.*

- *Computational load for algorithm 8 in sequential mode is* $\mathbf{O}(LM^2 logQ)$ *and parallel mode is* $\mathbf{O}(M^2 logQ)$*[49].*

Algorithm 10 is composed of an additional step which has a computational complexity of $\mathbf{O}(\mathcal{M}_t \mathcal{M}_p)$.

As the second stage of both the algorithms is computationally less intensive, resulting in the total complexity of algorithm - 7 and 10 being limited to $\mathbf{O}(\mathcal{M}_p N log N)$*, while the complexity of algorithm 9 is limited to* $\mathbf{O}(\mathcal{M}_t N log N)$.

Remark 4. *Computation Time -*
In Table 6.4, we present the performance of different algorithms in terms of computation time for designing $\boldsymbol{\mathcal{X}}$ *(and its constituent cuts i.e.* $\bar{\mathbf{X}}_p$*,* $\tilde{\mathbf{X}}_d$ *and* $\grave{\mathbf{X}}_n$*). In the table, the parameters* N*,* M*,* $\mathcal{M}_t$*, and* Q *are adjusted across different rows, while some conditions are kept constant to observe the corresponding changes in computation performance. The table entries represent the performance metric measured in seconds, with the value of* $\mathcal{M}_p$ *indicating the role of pulse domain in the computations. In all the above simulations, we set the stopping criterion as* $|\mathbf{X}^{(i+1)} - \mathbf{X}^{(i)}| \leq \epsilon$*, where* $\epsilon = 10^{-6}$.

To calculate the runtime of the algorithm, we used a PC with the following specifications: 2.6 *GHz* $i9-11950H$ *CPU and* 32*-GB RAM. No acceleration schemes (i.e., Parallel Computing Toolbox in MATLAB) are used to generate the results and are evaluated from purely sequential processing.*

Table 6.3: Computation time for different algorithms

Algorithm → **Input Parameters ↓**	**Algorithm** 1 [sec] ($\mathcal{M}_p = 5$)	**Algorithm** 3 [sec] ($\mathcal{M}_p = 1$)	**Algorithm** 4 [sec] ($\mathcal{M}_p = 3$)
$N = 128, M = 16, L = 8, \mathcal{M}_t = 3, Q = 2$	0.13	102.44	3.118
$N = 128, M = 16, L = 8, \mathcal{M}_t = 3, Q = 3$	0.12	123.23	3.425
$N = 512, M = 32, L = 16, \mathcal{M}_t = 8, Q = 2$	1.08	1019.91	13.27
$N = 512, M = 64, L = 8, \mathcal{M}_t = 8, Q = 4$	0.83	4732.07	13.25
$N = 1024, M = 128, L = 8, \mathcal{M}_t = 16, Q = 1$	2.51	5642.51	25.25
$N = 1024, M = 256, L = 4, \mathcal{M}_t = 16, Q = 3$	3.45	6124.32	31.41

6.4 Performance Analysis

In this section, we provide experimental findings demonstrating the performance of the suggested methods in obtaining elements of $\boldsymbol{\mathcal{X}}$ across various dimensions and parameters with varying constraints.

6.4.1 Convergence Analysis

The methods in the preceding sections are based on the general MM and BCD optimization frameworks. In these approaches [60] (chapter 5), we know that the objective values generated by the algorithm at every iteration are decreasing until saturation is achieved. Since the objective values in (6.20), (6.29) and (6.31) are bounded below by 0, the objectives are guaranteed to converge to finite values.

Firstly, we evaluate the performance of the proposed algorithm 9 for various values of Q (i.e. $1, 2, 3$ and 4) as an input parameter and other parameters as follows: $N = 128$, $M = 8$, $\mathcal{M}_t = 3$. Figure 6.2 demonstrates the convergence of the proposed method when the simulation is run for 5000 iterations and saturation is achieved.

Secondly, the convergence of objectives $g_1(\widetilde{\mathbf{X}}_d)$ in (6.29) and $g_2(\grave{\mathbf{X}}_n)$ in (6.30) is shown in Figure 6.3 for the algorithm- 7 and 10. In case of algorithm-7, the input parameters are: $Q = 2$, $\mathcal{M}_t = 12$, $N = 128$. In order to validate the convergence of the proposed method, we consider different sub-sequence lengths, where $M = 8, 16$, and 32 with fixed sequence length of $N = 128$ (refer Figure6.3a). For algorithm - 10, we consider a Uniform Rectangular Array (URA)

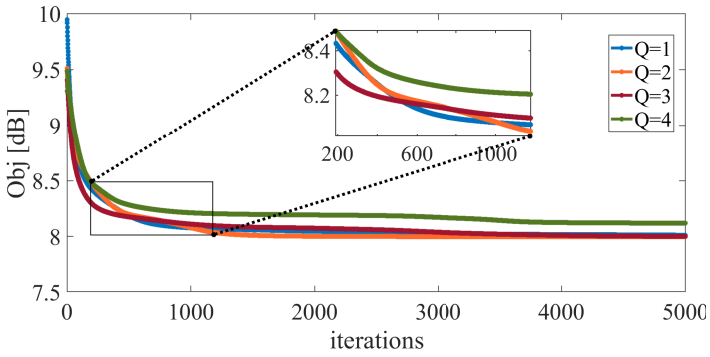

Figure 6.2: Objective convergence; Algorithm-9

configuration for transmitters where $\mathcal{M}_t = 16, 64$ and 256 with M_x and M_y as the number of transmitters along X and Y axis in URA layout where $\{M_x, M_y\} \in \{\{4,4\},\{8,8\},\{16,16\}\}$, respectively in Figure6.3b. The desired and undesired angles are $\Psi_d = \{\Theta_{i_1}\}$ where $\Theta_{i_1} = \{-40, \ldots, -30\}$ and $\Psi_u = \{\Theta_{i_2}\}$ where $\Theta_{i_2} = \{-50, \ldots, -40\}$.

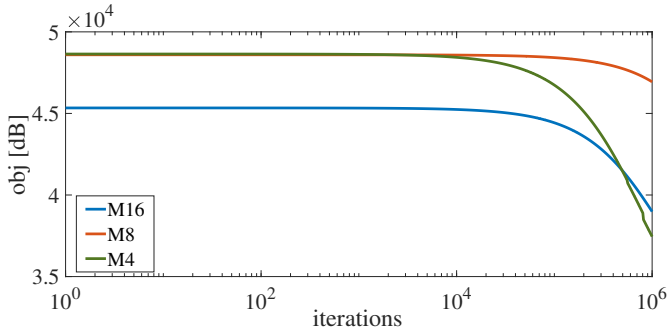

(a) $g_1(\widetilde{\mathbf{X}}_d)$ convergence with varying sub-sequence lengths

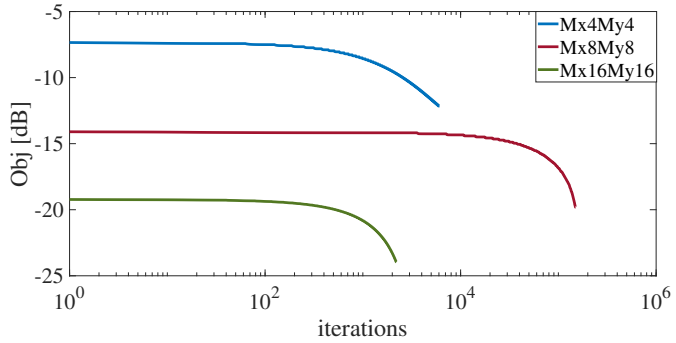

(b) $g_2(\grave{\mathbf{X}}_n)$ convergence for different number of transmitters along X/Y axis

Figure 6.3: Convergence of both the objectives in algorithm-10

6.4.2 MIMO Sequence Set Design

In MIMO sequence design, the fundamental aspect of design is the interaction of every sequence with respect to the entire sequence set. On one end, the waveform diversity enables higher sensitivity and better parameter identifiability whereas on the other hand, the coherence amongst different sequences can lead to better beam focusing capabilities which can avoid unnecessary interference in the system.

Orthogonality

In terms of orthogonality, the degree of non-coherence can be measured using the auto/cross-correlation within a sequence set. We aim to assess the effectiveness of Algorithm 9. For this evaluation, we assume a sequence length of $N = 128$, $L = 16$, $Q = 2$, and $\mathcal{M}_t = 3$. As shown in the Figure 6.4, the sidelobes are effectively reduced to 20dB in the auto/cross-correlation level in Figure6.4a, Figure6.4b, while inducing the polynomial phase constraint where $Q = 2$ amongst all the sub-sequences. The unwrapped quadratic phase behavior ($Q = 2$) is observed for every sub-sequence of length $M = 8$ in Figure 6.4c.

The performance of the proposed algorithm is compared with other algorithms in the literature such as CAN-MIMO [4], MM-Corr[7], pMM [75]. A normalized metric ISLR which is defined as

$$\text{ISLR (dB)} = 10\log_{10}\frac{\text{ISL}}{N^2}, \tag{6.39}$$

is used. In Figure 6.5, we consider varying sequence length, $N = [8, 16, 32, 64, 128, 256]$, $\mathcal{M}_t = 2$ for the algorithms CAN-MIMO [4], MM-Corr[7], pMM [75]. In addition to the earlier settings, we configured $Q = 2$ and $L = 2$ for the proposed algorithm. In all the above simulations, we set the stopping criterion as $|\mathbf{X}^{(i+1)} - \mathbf{X}^{(i)}| \leq \epsilon$, where $\epsilon = 10^{-6}$. As shown in Figure 6.5, the ISLR for the proposed Algorithm 3 (labeled "PECS var M") is the highest compared to other algorithms for $L = 2$. This is due to the restriction in the degrees of freedom for sequence elements caused by the quadratic phase constraint applied in the algorithm. However, by configuring $M = 2$ and varying L (labeled "PECS M2"), the ISLR achieved by the proposed algorithm is equivalent to MM-Corr. Later, in 6.4.4, we show the performance of the algorithm 3 by introducing a metric to evaluate the Doppler tolerance of a MIMO sequence set.

Further, in Table 6.4, we provide the computational complexity and time of various algorithms along with the proposed algorithm 3. Here, we observe that although the actual computation time of algorithm 3 is 730.01 sec but the phase coefficients derived in category 1, can be reused to derive the sequence set for category 2 without losing the auto/cross-correlation properties.

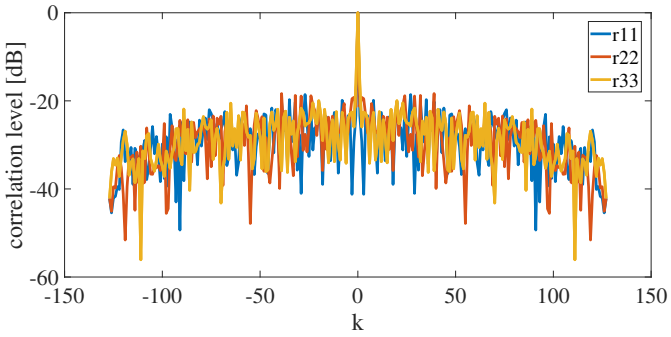

(a) Auto-correlation level

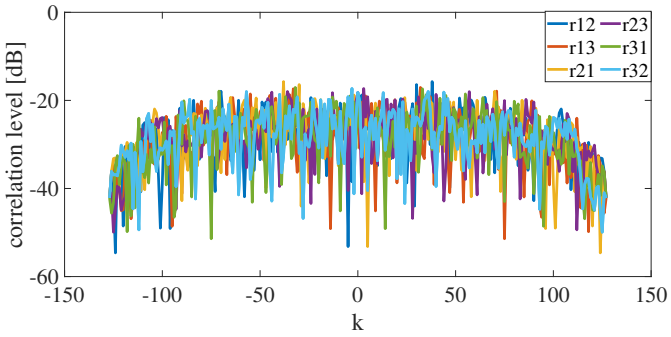

(b) Cross-correlation level

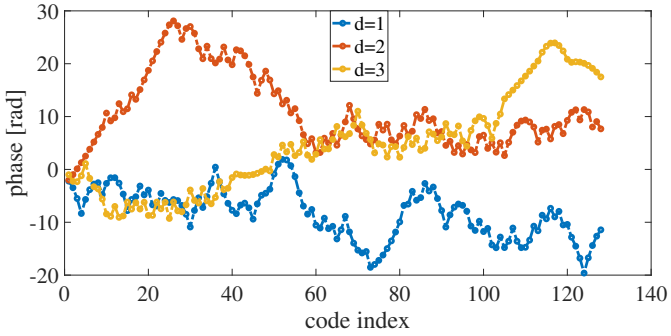

(c) Unwrapped Phase

Figure 6.4: MIMO sequence set design with quadratic phase behavior ($Q = 2$) in every sub-sequence using algorithm-9

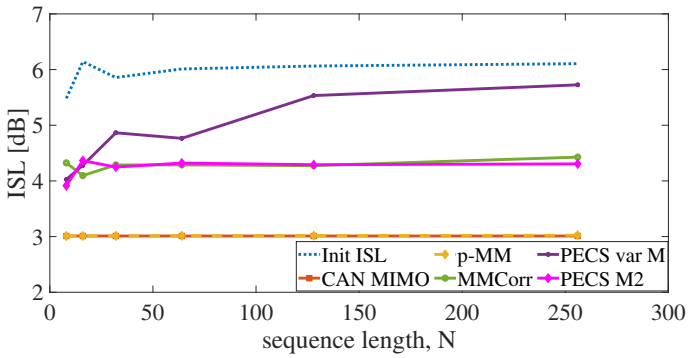

Figure 6.5: Comparison between aperiodic ISLR values when starting from same initial sequence set for different MIMO ISL minimization algorithms

Table 6.4: Comparison of computation complexity and time for different algorithms in the literature

Categories → Algorithm ↓	**Computational Complexity**	**Computation Time [sec] (Input param category 1)**	**Computation Time [sec] (Input param category 2)**
BIST[73]	$\mathcal{O}(N^3\mathcal{M}_t)$	9.34	130.62
Multi-CAN [74]	$\mathcal{O}(\mathcal{M}_t^2 N \log N)$	0.1	1.256
MM-Corr [7]	$\mathcal{O}(\mathcal{M}_t N \log N)$	132.33	634.99
p-MM [75]	$\mathcal{O}(\mathcal{M}_t^2 N \log N)$	4.64	300.54
Proposed Method: Algorithm 3	$\mathcal{O}(\mathcal{M}_t N \log N)$	191.77	730.01

Beampattern Design

To this intent, we strive to achieve phase coherence across sequences within a defined set while upholding the quadratic phase constraint within the code domain. For simplicity, we consider a URA configuration for transmitters where $\mathcal{M}_t = 16 \times 12$ with $M_x = 16$ and $M_y = 12$, respectively. Other input parameters are: $Q = 2$, $N = 128$, $M = 8$, $\Psi_d = \{\theta_{i_1}, \phi_{j_1}\}$, $\Psi_u = \{\theta_{i_2}, \phi_{j_2}\}$, where $\theta_{i_1} = \{-40^\circ, \ldots, -30^\circ\}$, $\phi_{j_1} = \{30^\circ, \ldots, 40^\circ\}$, $\theta_{i_2} = \{\{-90^\circ, \ldots, -45^\circ\} \cup \{-25^\circ, \ldots, 90^\circ\}\}$, and $\phi_{j_2} = \{\{-90^\circ, \ldots, 25^\circ\} \cup \{45^\circ, \ldots, 90^\circ\}\}$. The overall complementary sidelobes reduction of 8.51dB is observed for $\mathcal{M}_p = 3$ in Figure6.6a for algorithm - 7 with the optimized sequences (represented as $r - css$), for one of the transmit sequence $\tilde{\mathbf{X}}_{d|d=1}$, while the beam pattern is shaped with its maxima observed at $(\theta_{i^*}, \phi_{j^*}) = (-35^\circ, 35^\circ)$ in Figure 6.6b using algorithm-10.

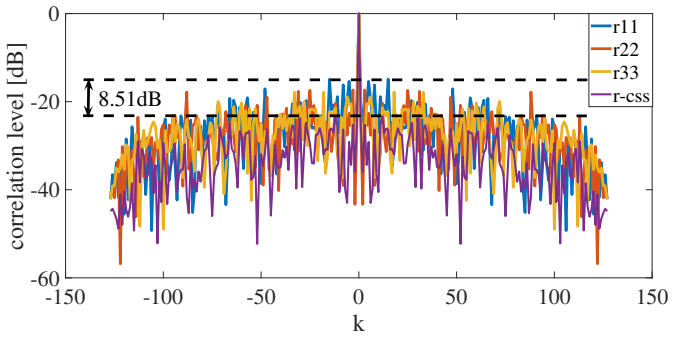

(a) CISL obtained using $g_1(\widetilde{\mathbf{X}}_d)$

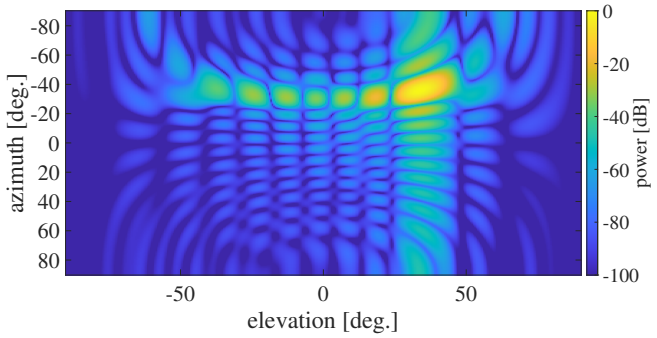

(b) Azimuth and elevation beampattern obtained using $g_2(\grave{\mathbf{X}}_n)$

Figure 6.6: Complementary sidelobe behavior and beam pattern for the synthesized sequences using algorithm-10

6.4.3 Comparison with state-of-the-art techniques

In the state-of-the-art automotive FMCW MIMO radars, techniques such as TDM, BPM, DDM are used to generate orthogonality amongst transmit signals in different channels over the entire CPI, alternatively called inter-pulse code modulation. TBP across all the waveforms are equalized such that different waveforms can be compared. We compare the results with different techniques under two categories, FMCW and PMCW waveforms as shown in Table 6.5.

In algorithm - 9, the intra-pulse code modulation for obtaining optimal ISL is achieved for a sequence set $\bar{\mathbf{X}}_p$ with the following parameters: $N = 128$, $L = 16$, $M = 8$, and $\mathcal{M}_t = 12$. In order to obtain a LFM equivalent behavior typical to FMCW waveforms, the quadratic phase variation is obtained by tuning $Q = 2$ in each sub-pulse. On the other hand, for obtaining higher order polynomial phase behaviors, the parameter is tuned to $Q = 5$ which can be easily accommodated on PMCW waveforms.

Firstly, while considering the FMCW category for 12 transmitters, the ISL and PSL for TDM, BPM and DDM based approaches is always greater than the the proposed method. For BPM MIMO setup, we use Hadamard sequences. A matrix $\mathbf{H} \in \mathbb{R}^{N \times N}$ with each entry being either $+1$ and -1, is considered a Hadamard matrix if it satisfies $\mathbf{H}\mathbf{H}' = n\mathbf{I}$ [137]. It is well

established that n must be $1, 2$ or a multiple of 4 for such a matrix to exist. However, it is not confirmed whether Hadamard matrices exist for every n that is a multiple of 4 which imposes a restriction on the choice of the number of pulses within a CPI. Similar to the previous case, in DDM, the code division multiplexing is coupled in both spatial and pulse domain which results in quasi-orthogonality in spatial domain and aliasing in the Doppler dimension over an entire CPI. In addition, the design poses a limitation on the upper limit of PRF . In TDM, the best orthogonality is achieved as expected but at the cost of decreased PRF in a given CPI. Noteworthy in the proposed method, the orthogonality of sequence sets with quadratic phase behavior (intra-pulse modulation) is achieved without compromising the PRF or introducing aliasing in the Doppler dimension.

Secondly, in PMCW category, the proposed method has ISL/PSL of 21.2dB/-12.38dB for $Q = 5$. The Linear Phase Method [62] was adapted to MIMO using BPM technique and achieved an ISL/PSL of 41.65dB/0dB. Further, Gold codes [138] result in the highest ISL/PSL values. Finally, the values obtained from p-MM method [75] were provided for reference (without polynomial phase constraint).

Table 6.5: ISL and PSL comparison with the existing techniques for intra-pulse modulation

	FMCW				**PMCW**			
	Proposed Method $Q = 2$	**TDM**[66]	**BPM**[1][58]	**DDM**[55]	**Linear Phase Method**[1][62]	**Gold**[1][138]	**p-MM**[2][75]	**Proposed Method** $Q \geq 3$
ISL	21.20dB	-2.68dB	23.21dB	23.24dB	22.91dB	29.92dB	21.21dB	21.20dB
PSL	-13.09dB	-6.02dB	0dB	0dB	0dB	0dB	-14.06 dB	-12.38dB

[1] Grating lobes emerge due to the application of Hadamard sequences and give rise to high PSL.
[2] Without polynomial phase constraint

6.4.4 Doppler tolerance evaluation

Doppler tolerance of the synthesized transmit sequence set is analyzed for various input specifications and evaluated using the method described in [139]. For a given waveform $x(t)$, the discretized narrowband ambiguity function S as a function of relative lag τ and Doppler shift f_D is

$$S(\tau, f_D) = \left| \int_{-\infty}^{\infty} e^{j2\pi f_D t} x(t) x^*(t+\tau) dt \right|^2 \tag{6.40}$$

Firstly, we select a reference point on the ambiguity function S that is common to any constant amplitude waveform. We obtain a slice along the Doppler axis of the AF in (6.40) at the zero-delay cut. For this cut, the first Doppler null is chosen as a reference point which occurs at

$f_D = \pm 1/T$, where T is the pulse width. Further, the maximum value of (6.40) across delay axis in then determined for this particular Doppler $f_D = \pm 1/T$ which ensures that the characteristic ridge is intercepted (if it exists) and the peak of the AF is never encountered.

A metric ψ is used to measure the Doppler tolerance of a particular waveform as $\psi = 10\log_{10}(\eta(f_D = 1/T))$dB where

$$\eta(f_D) = \max_{\tau} \frac{S(\tau, f_D)}{S(0,0)}, \tag{6.41}$$

Table 6.6: Doppler tolerance variation with different number of sub-sequences for a sequence set with parameters: $N = 128$, $Q = 2$, and $\mathcal{M}_t = 4$

$\boldsymbol{\psi}$	$\mathbf{L = 8}$	$\mathbf{L = 4}$	$\mathbf{L = 2}$	$\mathbf{L = 1}$
$\mathbf{x}_1$	-13.24dB	-12.55dB	-9.27dB	-2.66dB
$\mathbf{x}_2$	-14.51dB	-10.98dB	-7.63dB	-1.53dB
$\mathbf{x}_3$	-14.44dB	-12.00dB	-12.20dB	-3.67dB
$\mathbf{x}_4$	-16.47dB	-13.19dB	-7.54dB	-1.94dB
$\boldsymbol{\psi}_{mean}$	$\mathbf{-14.65}$dB	$\mathbf{-12.18}$dB	$\mathbf{-9.16}$dB	$\mathbf{-2.45}$dB

As evident from Table 6.6, ψ gradually decreases for each transmit sequence as the number of sub-sequences, L increases (each of the sub-sequence possesses a unique quadratic phase variation, $Q = 2$ amongst its elements). The gradual decrement in ψ is highlighted by $\psi_{mean} = \frac{(\sum_{i=1}^{\mathcal{M}_t} \psi_i)}{\mathcal{M}_t}$.

We provide the Doppler tolerance of other standard waveforms for comparison in Table 6.7, where higher values of ψ corresponds to better Doppler tolerance and vice-versa.. As expected, LFM waveforms have the best Doppler tolerance ($\psi = -0.069$ dB). Golomb sequences, being the discretized equivalent of LFM, exhibit the same ψ value. Additionally, ψ decreases for Frank and P2 sequences. Finally, the complex random sequence, with a thumbtack ambiguity function (AF) response, has the lowest ψ value of -13.91 dB and exhibits high Doppler sensitivity.

Table 6.7: Doppler tolerance of standard sequences/waveforms with sequence length, $N = 128$ (in case of **LFM**, TBP $= 128$)

	LFM	**Golomb**	**Frank Sequence**	**P2 sequence**	**Complex Random Sequence**
$\boldsymbol{\psi}$	-0.069dB	-0.069dB	-0.187dB	-1.761dB	-13.91dB

Further, the variation in Doppler tolerance, ψ with $Q \in [1, \ldots, 4]$ in Table 6.8 is presented. The input parameters for the sequence set generation are $N = 128$, $L = 1$, and $\mathcal{M}_t = 4$. Uniquely for $Q = 2$, the mean value of ψ has the highest value. Other values of Q (i.e. $Q = 1, 3,$

and 4), gives rise to low values of ψ_{mean} and show high Doppler sensitivity of the sequence set. Further, in Figure 6.7, we compare the performance the proposed method (labeled "PECS")

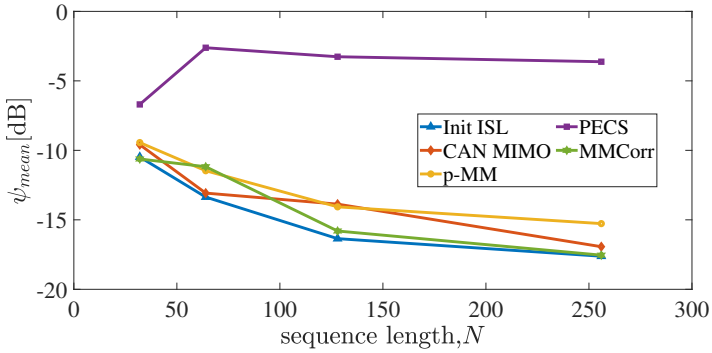

Figure 6.7: Comparison of Doppler tolerance using ψ_{mean} for various algorithms

with other algorithms available in the literature by evaluating ψ_{mean} for each using the following input configuration, $N = [32, 64, 128, 256]$, and $\mathcal{M}_t = 2$. Here, it is apparent that the Doppler tolerance for the proposed algorithm (with $N = M$, $L = 1$ and $Q = 2$) is the highest and outperforms the counterparts. This exhibits the significance of quadratic phase behavior in deriving Doppler tolerance characteristic. Thus, while comparing the results obtained in Figure 6.5 and Figure 6.7, we showcase that the proposed approach offers a flexible framework to balance between low ISLR and Doppler tolerance.

To understand the AF response, we generate a sequence set with following input parameters $N = 128$, $Q = 2$, and $\mathcal{M}_t = 3$ with varying number of sub-sequences, $L = [1, 2, 4]$. As a special case, when $L = 1$, then $M = 128$ making the sub-sequence length equal to the sequence length. In Table 6.9, the rows correspond to increasing number of sub-sequences L amongst a sequence, while the columns represent different channels. The ridge shape arises in the AF due to the quadratic phase behavior along the elements of the sequence/sub-sequence by tuning $Q = 2$. This is most apparent in the AF for $L = 1$. However, as L increases (i.e. for $L = 2$ and $L = 4$), the ridge deteriorates and an elliptical main lobe becomes prominent.

Table 6.8: Doppler tolerance variation with different values of Q for a sequence set with parameters: $N = 128$, $L = 1$, and $\mathcal{M}_t = 4$

$\boldsymbol{\psi}$	$\mathbf{Q = 1}$	$\mathbf{Q = 2}$	$\mathbf{Q = 3}$	$\mathbf{Q = 4}$
$\mathbf{x}_1$	-9.855dB	-1.238dB	-17.049dB	-13.754dB
$\mathbf{x}_2$	-9.855dB	-3.154dB	-16.388dB	-14.490dB
$\mathbf{x}_3$	-9.855dB	-1.088dB	-15.720dB	-15.983dB
$\mathbf{x}_4$	-9.855dB	-3.356dB	-15.820dB	-15.038dB
$\boldsymbol{\psi}_{mean}$	$\mathbf{-9.85}$dB	$\mathbf{-2.209}$dB	$\mathbf{-16.244}$dB	$\mathbf{-14.813}$dB

Table 6.9: Ambiguity functions for input parameters, $N = 128$, $Q = 2$, $\mathcal{M}_t = 3$ and different number of sub-sequences, $L \in [1, 2, 4]$.

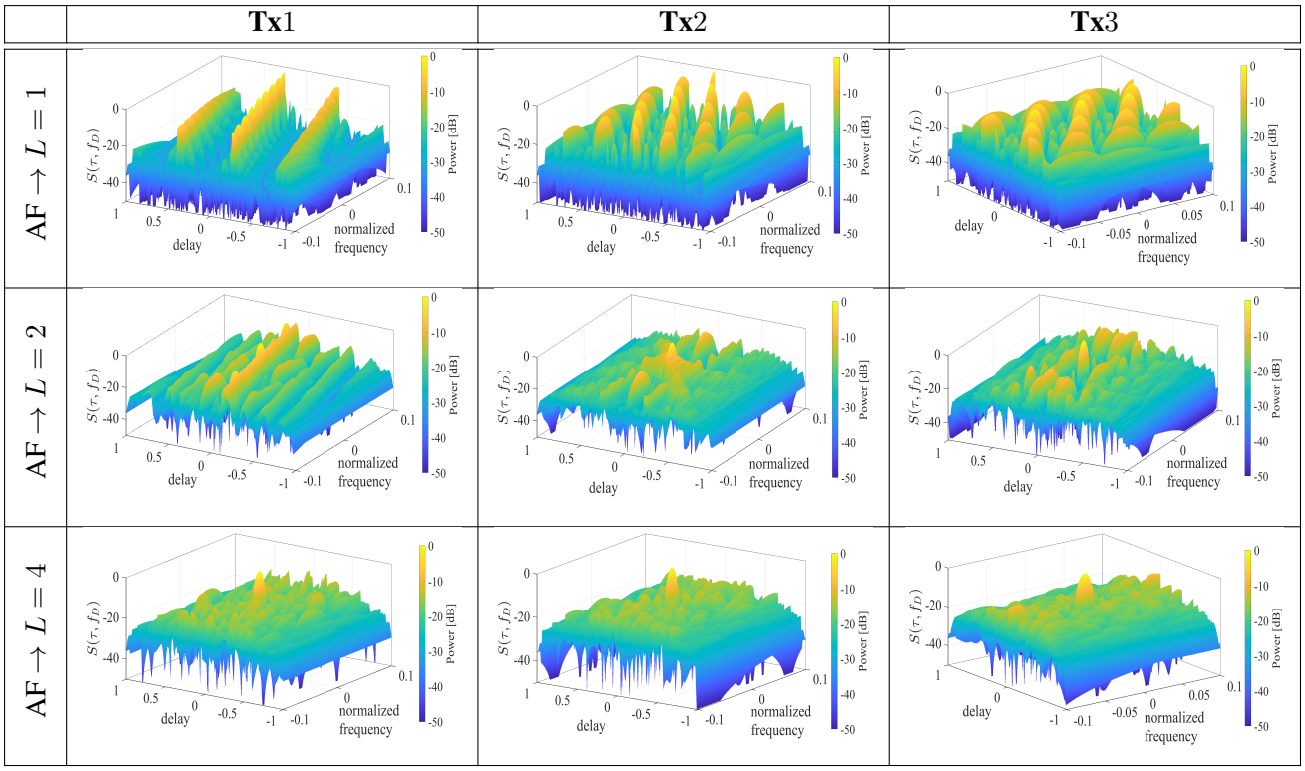

6.4.5 Case Study: Beampattern design with Linear Frequency modulation type signals

LFM waveforms are utilized for each transmission channel within every pulse in the modern automotive MIMO radar systems. Orthogonality among transmit channels is achieved using TDM, FDM, and DDM. However, as traffic scenarios grow more intricate with a greater number of vehicles equipped with radar sensors, interference between these sensors becomes inevitable. Complex environments such as tunnels and concrete/metallic bridges exacerbate the issue by generating ghost targets from their structures, overwhelming radar sensors. This can lead to incorrect interpretations of the surroundings or necessitate sensor deactivation to prevent saturation with targets.

In such scenarios, instead of the isotropic beam pattern, a focused beam pattern which is restricted to the area of interest (i.e. the roadway suitable for driving) is better for reliable sensing. Thus, unique waveforms employing dynamic beampattern shaping presents a solution to mitigate interference among sensors. Currently, it is implemented at the hardware level through the introduction of phase shifters. These phase shifters manipulate the phase in the feed lines

for each transmit channel. While effective, this approach increases both the complexity and cost of the hardware.

With this motivation, we discuss further the implementation of algorithm-10 for generating dynamic beampattern shaping for an automotive scenario. Here, the requirements for the FoV are $\Psi_d = \{\theta_{i_1}, \phi_{j_1}\}$ and $\Psi_u = \{\theta_{i_2}, \phi_{j_2}\}$ where $\theta_{i_1} = \{-30°, \ldots, 30°\}$, $\theta_{i_2} = \{-90°, \ldots, -40°\} \cup \{40°, \ldots, 90°\}$, $\phi_{j_1} = \{-5°, \ldots, 20°\}$, and $\phi_{j_2} = \{-90°, \ldots, -10°\} \cup \{30°, \ldots, 90°\}$.

Let the transmit signal for one transmit channel of a MIMO FMCW radar with $\mathcal{M}_t$ transmitters be $\widetilde{s}(t)$ and is represented as:

$$\begin{aligned} \widetilde{s}(t) &= e^{j\widetilde{\theta}(t)} \text{rect}\left[\frac{t - T_c/2}{T_c}\right], \\ \widetilde{\theta}(t) &= 2\pi(f_c t + \frac{1}{2}\zeta\alpha t^2), \end{aligned} \tag{6.42}$$

where, $\widetilde{\theta}(t)$ denotes the time-varying phase of the signal $\widetilde{s}(t)$, f_c represents the carrier frequency, t is the continuous time variable, ζ takes values of either $+1$ for up-chirp or -1 for down-chirp, and $\alpha = \frac{B}{T_c}$ represents the slope of the LFM, with B bandwidth and T_c, pulse duration.

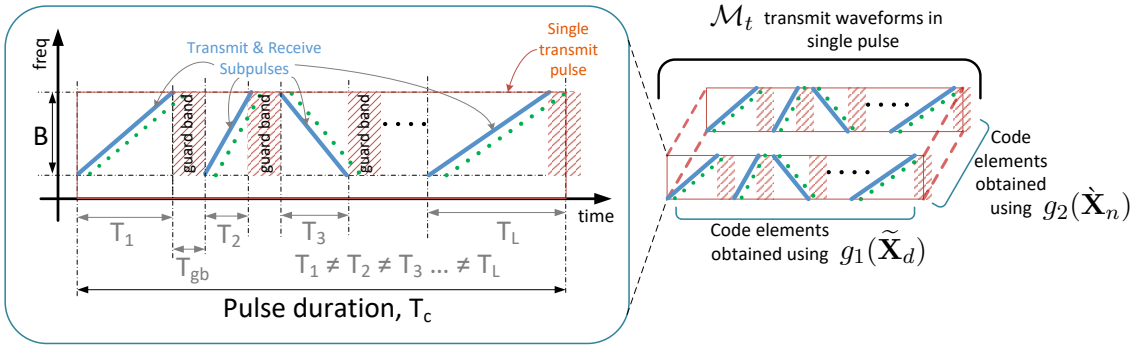

Figure 6.8: Single transmit pulse consisting of multiple transmit waveforms from each channel, each with varying sub-pulses of different slopes obtained according to algorithm - 10.

The entire transmit pulse for a particular transmit channel can be divided into L sub-pulses (refer Figure6.8). A given sub-pulse l, spans a part of the entire bandwidth B, and has a sub-pulse duration of T_l. Two subsequent sub-pulses are separated by a guard band of width $T_{gb} \geq 2R_{max}/c$, where R_{max} is the maximum range of the radar sensor and c is the speed of light.

Due to the linear frequency variation over the entire pulse time inherent in LFM, the phase variation exhibits a quadratic pattern. Similarly, the phase variation of $\widetilde{\theta}_l(t)$ of the l-th sub-pulse can be expressed in discrete time as $\widetilde{\boldsymbol{\theta}}_l = [\widetilde{\theta}_1, \ldots, \widetilde{\theta}_m, \ldots, \widetilde{\theta}_M]^T$, for $t = T_s n$, where T_s stands for the sampling time, and $n = (l-1)M_l + m \in [1, \ldots, N]$, $m = 1, \ldots, M_l$, $l = 1, \ldots, L$ with

$N = T_c \times B = M_1 + \cdots + M_l$. Thus,

$$\widetilde{\theta}_l = \widetilde{a}_{0,l} + \widetilde{a}_{1,l} m + \widetilde{a}_{2,l} m^2, \tag{6.43}$$

where $\widetilde{a}_{0,l} = \theta_{init}$, $\widetilde{a}_{1,l} = 2\pi f_c T_s$, and $\widetilde{a}_{2,l} = \pi \alpha T_s^2$ are the quadratic phase coefficients of the l-th sub-pulse. It is important to note that $\widetilde{a}_0$ represents an arbitrary initial phase value of the chirp sequence. The discrete-time signal generated for the entire pulse using the phase code sequence $\widetilde{\boldsymbol{\theta}} = [\widetilde{\boldsymbol{\theta}}_1^T, \ldots, \widetilde{\boldsymbol{\theta}}_L^T]^T = [\widetilde{\theta}_1, \ldots, \widetilde{\theta}_n, \ldots, \widetilde{\theta}_N]^T$ can be expressed as:

$$\widetilde{s}_n = e^{j\widetilde{\theta}_n}, \;\; |\widetilde{s}_n| = 1. \tag{6.44}$$

and $\bar{\mathbf{x}}_d = [\widetilde{s}_1, \widetilde{s}_2, \ldots, \widetilde{s}_N]$ represents the d-th transmit sequence for the p-th pulse. The sequences are stacked to form the matrix $\bar{\mathbf{X}}_p = [\bar{\mathbf{x}}_1, \cdots, \bar{\mathbf{x}}_d, \cdots, \bar{\mathbf{x}}_{\mathcal{M}_t}] \in \mathbb{C}^{N \times \mathcal{M}_t}$ for the p-th pulse. Further steps can be followed from section -6.3.3 to generate the transmit sequence sets in every pulse and eventually synthesize $\boldsymbol{\mathcal{X}}$ for the whole CPI.

In order to implement the proposed algorithm 10 on the existing FMCW hardware, we propose a sub-pulse based implementation with waveform diagram provided in Figure6.8. A single transmit pulse obtained from $\bar{\mathbf{x}}_d$ of time period T is split into L sub-pulses each of time period $\in \{T_1, \ldots, T_L\}$, respectively. Each of the sub-pulse obeys LFM and spans the whole bandwidth, B. As dechirping operation is mandated at every receiver, thus each of the sub-pulse is separated in time from the next sub-pulse, referred as "guard band". The duration of guard band depends on the maximum range of the sensor and it helps in avoiding the overlap of the dechirp of the ongoing sub-pulse with the received signal from the next sub-pulse.

Further, the radiation pattern of the FMCW MIMO radar which is isotropic in nature is represented in Figure6.9a for a tunnel based scenario. The isotropic beampattern is obtained over the entire CPI by aggregating the beampattern generated by all the $\mathcal{M}_t$ transmit sequences in every pulse. Figure6.9c shows the beampattern for first, second, and third pulse in different color scales. In addition, the isotropic beampattern for the whole CPI is also shown with normalized transmit power along the z-axis.

The tunnel structure is known for generating multiple ghost targets due to the multipath reflections. The overhead signboards, reflectors and temporary road safety barriers for construction work further escalate the problem by increasing the multipath and hence the ambiguity in detecting a target reliably in azimuth and elevation.

On the other hand, the proposed scheme (modified LFM waveform) can be adopted to obtain focused beampattern inside the tunnel, sense the absolutely necessary vehicles and objects on the drivable region of the tunnel Figure6.9b. Its beampattern (refer Figure6.9d), is generated with the beamwidth of 25° each and focused at the $(0^\circ, 0^\circ)$ in azimuth and elevation, respectively

for every pulse in a given CPI. As apparent from Figure6.9b, the focused beampattern avoids unnecessary multipath from the tunnel surface and unwanted detections from the overhead objects. As every transmit sequence is composed of unique sub-pulses, it provides robustness to interference from other sensors mounted on target vehicles (refer 6.4.7 for interference statistical analysis). Once the vehicle crosses the tunnel, the normal isotropic beampattern can be resumed.

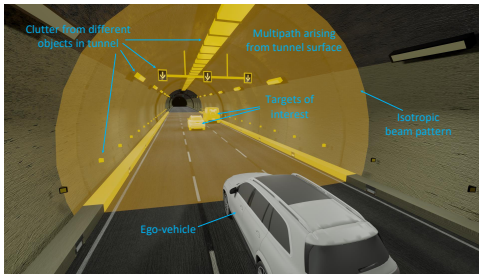

(a) Beampattern of the state-of-the-art MIMO radar for outdoor sensing

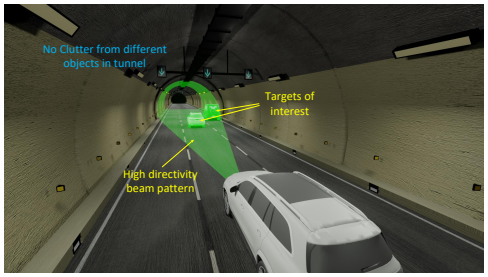

(b) Beampattern adaptation for a cognitive MIMO radar inside a tunnel using algorithm-10

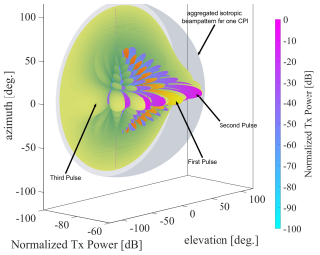

(c) Aggregated beampattern over one CPI

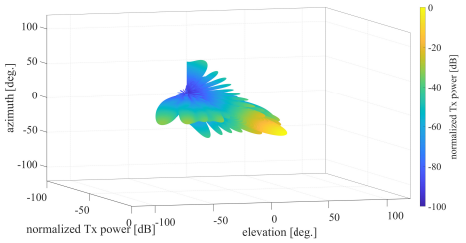

(d) Adapted beampattern using algorithm-10 in a single pulse

Figure 6.9: Case Study: Beampattern adaptation to avoid ghost object formation inside a tunnel

6.4.6 Sequence Set Design: very long sequence length

In furtherance to the previous sections, we now consider the design of orthogonal MIMO sequence sets of very long sequence length with optimal ISL using the phase coefficients obtained from algorithm-9 by employing the Subpulse processing technique [63] discussed in the last section. Let the initial sequence length $N = 128$, $\mathcal{M}_t = 4$, $Q = 3$, and $L = 8$ for the algorithm. After evaluating the optimal phase coefficients $\mathcal{A}_p^*$ for the p-th pulse, we can easily generate sequence sets with varying sequence length using the same optimal phase coefficients $\mathcal{A}_p^*$ evaluated for a given configuration (i.e. $\mathcal{M}_t, Q$ and L). Table 6.10 shows the calculated subpulse slopes corresponding to $\mathcal{A}_p^*$ for a chirp, $T_c = 150\mu$s and bandwidth, $B = 1$GHz, where the sequence length of a single transmit sequence is $N = 150$k equal to the TBP with a relative increment in ISL of 1.9685dB with respect to the optimized sequence set of length $N = 128$.

Therefore, with the proposed method the computational cost is minimal for generating sequence sets with optimal ISL and alleviates the complexity of runtime adaptation of waveforms in cognitive radars.

Table 6.10: Subpulse slopes (in MHz/μs) with bandwidth, $B = 1$GHz and pulse duration, $T_c = 150\mu$s for a set of $\mathcal{M}_t = 4$ sequences with length $N = 150k$.

Subpulse → Sequence ↓	$\mathbf{L=1}$	$\mathbf{L=2}$	$\mathbf{L=3}$	$\mathbf{L=4}$	$\mathbf{L=5}$	$\mathbf{L=6}$	$\mathbf{L=7}$	$\mathbf{L=8}$
$\mathbf{x}_1$	$+18.1396$	-44.6045	-17.7803	-34.5458	$+31.8028$	-20.5545	$+31.6783$	-8.1641
$\mathbf{x}_2$	-28.1692	-38.603	$+29.7083$	$+22.7839$	$+26.4388$	-21.0571	$+12.1767$	-26.3656
$\mathbf{x}_3$	$+27.3986$	-26.2396	$+16.3183$	-13.5169	$+6.5109$	-26.4023	-16.8673	$+6.1534$
$\mathbf{x}_4$	$+20.6964$	-9.3078	$+27.1690$	-14.2144	-50.9811	-19.6269	-40.5442	-25.4232

6.4.7 Case Study: MIMO to MIMO interference

In this section, we analyze the maximum SIR reduction at the MF output for a MIMO radar in operation, using the sequence set synthesis technique mentioned in algorithm 9. We assume that the automotive MIMO radar of interest (victim) is interfered by another MIMO radar sensor (aggressor), also operating with the same transmission scheme as the victim sensor. Additionally, the pulses from aggressor are assumed to entirely overlap in the time domain with those of the victim sensor making this analysis a worst-case scenario of MI (refer types of FMCW radar interference in [26]). It will be statistically analyzed using the following procedure:

1. Consider two sequence sets $\mathfrak{U}$ for victim and $\mathfrak{V}$ for aggressor generated independently using algorithm - 9.
2. Consider d-th sequence, $\mathbf{u}_d^{\mathfrak{U}} = [u_1, \ldots, u_N]^T$ from $\mathfrak{U}$.
3. Evaluate the sum of all the sequences, $\mathbf{v}_d^{\mathfrak{V}} = [v_{1,d}, \ldots, v_{n,d}, \ldots, v_{N,d}]^T$ in $\mathfrak{V}$ (superposition of all the transmit signals from the aggressor in the sensing channel for a given pulse) as $\mathbf{v}_{sum}^{\mathfrak{V}} = \sum_{d=1}^{\mathcal{M}_t} v_{n,d} \; \forall \; n = 1, \ldots, N$ where $v_{n,d}$ is the n-th element of the d-th sequence and $\mathbf{v}_{sum}^{\mathfrak{V}} = [v_1, \ldots, v_N]$.
4. Compute the aperiodic cross-correlation of $\mathbf{v}_{sum}^{\mathfrak{V}}$ with $\mathbf{u}_d^{\mathfrak{U}}$ as $\mathfrak{r}_k = \sum_{n=1}^{N} u_{n,d} v_n \; \forall \; d = 1, \ldots, \mathcal{M}_t$. Note, when $u_{n,d} = 0$ and $v_n = 0$ when $n \neq \{1, \ldots, N\}$.
5. Find $\mathfrak{r}_{max} = \max(|\mathfrak{r}_k|)$.
6. Let $\zeta = 20 \log_{10}(\frac{\mathfrak{r}_{max}}{N})$.
7. Store the value (ζ) for the present iteration for the d-th sequence.
8. Continue the experiment for the desired number of trials.

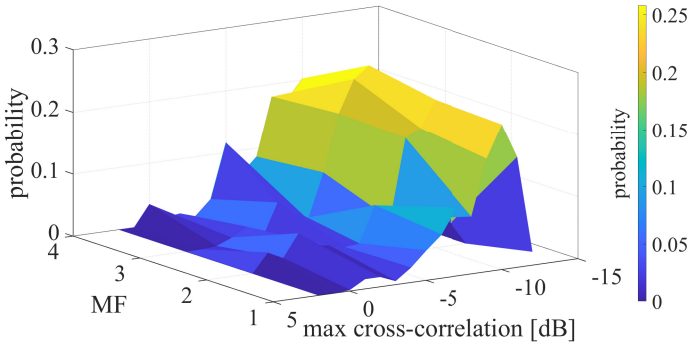

Figure 6.10: Statistical interference analysis of algorithm - 9 for a victim radar sensor

9. Repeat the above steps for all the sequences of the victim radar.

In Figure6.10, the normalized histogram is shown for the statistical analysis of ζ for 10^3 trials. The maximum cross-correlation, ζ between one of the victim sequence and cumulative sum of all the sequences of aggressor is displayed along the x-axis and the d-th MF output is represented along the y-axis where $d \in \{1, \ldots, 4\}$, while the z-axis shows the histogram level, called the probability of occurrence calculated from 10^3 trials. The figure illustrates that the distribution of ζ is centered at -10dB for all the MFs with the initialization details for each sequence as $N = 128$, $L = 16$, $Q = 2$ and $\mathcal{M}_t = 4$. This signifies the interference immunity of the Doppler tolerant waveforms generated using the proposed algorithm.

6.5 Conclusion

Multiple approaches were discussed for generating polynomial phase sequence sets using MM and BCD based frameworks. All the methods described are stable and achieve optimal CISL/ISL values depending on the input parameters. These algorithms are implemented using standard FFT and Least Squares operations as highlighted in the algorithms, ensuring computational efficiency. Keeping Doppler tolerance in perspective, a variant of the polynomial phase function in the form of a quadratic phase variation was explained with the help of a case study. Another case study presented a statistical analysis to prove the interference immunity of the sequence sets derived using the proposed method. The discussion also illustrated intra-pulse MIMO orthogonality for FMCW radars using quadratic phase coefficients for every subpulse as the building blocks for generating very long sequence sets. It makes the proposed algorithms suitable for both PMCW and FMCW radars and compatible with current and future hardware.

6.6 Appendix

6.6.1 PECS Generalization

$$\mathcal{P}_{\{\bar{\mathcal{O}}_l^d\}}\left\{\underset{a_{\{q,l,d\}}}{\text{minimize}}\sum_{m=1}^{M}|e^{j(\sum_{q=0}^{Q}a_{\{q,l,d\}}m^q)}-\bar{\rho}_{n,d}e^{j\bar{\psi}_{n,d}}|_2^2,\right. \tag{6.45}$$

where the magnitude and phase of each entry of $\check{\mathbf{y}}_{l,d}$ is represented as

$$\begin{aligned}\bar{\boldsymbol{\rho}}_{l,d}&=[|y_{\{1+(l-1)M,d\}}|,\ldots,|y_{\{n,d\}}|,\ldots,|y_{\{lM,d\}}|]\\&=[\bar{\rho}_{\{1+(l-1)M,d\}},\ldots,\bar{\rho}_{\{n,d\}},\ldots,\bar{\rho}_{\{lM,d\}}],\ \text{and}\\\bar{\boldsymbol{\psi}}_{l,d}&=[\arg(y_{\{1+(l-1)M,d\}}),\ldots,\arg(y_{\{n,d\}}),\ldots,\arg(y_{\{lM,d\}})]\\&=[\bar{\psi}_{\{1+(l-1)M,d\}},\ldots,\bar{\psi}_{\{n,d\}},\ldots,\bar{\psi}_{\{lM,d\}}],\end{aligned}$$

for $n=m+(l-1)M\ \forall\ m=1,\ldots,M$, and $l=1,\ldots,L$. In addition to it, the unimodular and the polynomial phase constraint is introduced in the objective as defined in (6.21).

Further, let us define

$$\bar{\theta}_{n,d}=\sum_{q=0}^{Q}a_{\{q,l,d\}}m^q-\bar{\psi}_{n,d}. \tag{6.46}$$

A majorizer $g(\bar{\theta}_{n,d},\bar{\theta}_{n,d}^{(i)})$ of the function $f(\bar{\theta}_{n,d})=-\bar{\rho}_{n,d}\cos(\bar{\theta}_{n,d})$ can be obtained by

$$\begin{aligned}g(\bar{\theta}_{n,d},\bar{\theta}_{n,d}^{(i)})=&-\bar{\rho}_{n,d}\cos(\bar{\theta}_{n,d}^{(i)})+\left(\bar{\theta}_{n,d}-\bar{\theta}_{n,d}^{(i)}\right)\bar{\rho}_{n,d}\sin(\bar{\theta}_{n,d}^{(i)})\\&+\frac{1}{2}\left(\bar{\theta}_{n,d}-\bar{\theta}_{n,d}^{(i)}\right)^2\bar{\rho}_{n,d}\cos(\bar{\theta}_{n,d}^{(i)})\end{aligned} \tag{6.47}$$

where the variable is $\bar{\theta}_{n,d}$ and it has a phase value in the last iteration which is denoted as $\bar{\theta}_{n,d}^{(i)}$. The optimization problem using the majorizer function $g(\bar{\theta}_{n,d},\bar{\theta}_{n,d}^{(i)})$ at the i-th iteration is

$$\left\{\begin{aligned}\underset{a_{\{q,l,d\}}}{\text{minimize}}\quad&\sum_{m=1}^{M}\Bigg[-\bar{\rho}_{n,d}\cos(\bar{\theta}_{n,d}^{(i)})+\\&\left(\bar{\theta}_{n,d}-\bar{\theta}_{n,d}^{(i)}\right)\bar{\rho}_{n,d}\sin(\bar{\theta}_{n,d}^{(i)})\\&+\frac{1}{2}\left(\bar{\theta}_{n,d}-\bar{\theta}_{n,d}^{(i)}\right)^2\bar{\rho}_{n,d}\cos(\bar{\theta}_{n,d}^{(i)})\Bigg].\end{aligned}\right. \tag{6.48}$$

The objective function in (6.48) can be rewritten into perfect square form, and the constant terms independent to the optimization variable $a_{\{q,l,d\}}$ are ignored. An equivalent perfect square form can be written for the objective function in (6.48), where the constant terms independent of the

variable $a_{\{q,l,p\}}$ are omitted. With this assumption, the surrogate problem is

$$\left\{ \underset{a_{\{q,l,d\}}}{\text{minimize}} \quad \sum_{m=1}^{M} \left[\bar{\rho}_{n,d} \cos(\bar{\theta}_{n,d}^{(i)}) \left(\sum_{q=0}^{Q} a_{\{q,l,d\}} m^q \right) - \bar{b}_{n,d} \right]^2 \right. \tag{6.49}$$

where $\bar{b}_{n,d} = \bar{\rho}_{n,d} \cos(\bar{\theta}_{n,d}^{(i)}) \left(\bar{\psi}_{n,d} + \bar{\theta}_{n,d}^{(i)} \right) - \bar{\rho}_{n,d} \sin(\bar{\theta}_{n,d}^{(i)})$.

6.6.2 BeamPattern Shaping

The response of the beam pattern to undesired angles can be expressed as

$$\grave{\mathbf{x}}_p^H \mathbf{U}_U \grave{\mathbf{x}}_p = \sum_{d=1}^{\mathcal{M}_t} \sum_{d'=1}^{\mathcal{M}_t} x_{d,p}^* U_U(d,d') x_{d',p}, \tag{6.50}$$

where $U_U(d,d')$ are the elements of matrix $\mathbf{U}_U$. By a few mathematical manipulations it can be shown that, $\grave{\mathbf{x}}_p^H \mathbf{U}_U \grave{\mathbf{x}}_p = \sum_{d=1}^{\mathcal{M}_t} \sum_{d'=1}^{\mathcal{M}_t} \bar{a}_0 \grave{x}_{d,p} + \bar{a}_1 + \bar{a}_2 \grave{x}_{d',p}^*$, where,

$$\begin{aligned} \bar{a}_0 &= \sum_{\substack{d=1 \\ d \neq d'}}^{\mathcal{M}_t} \grave{x}_{d,p}^* U_U(d,d'), \bar{a}_2 = \bar{a}_0^*, \\ \bar{a}_1 &= \sum_{d,d'=1}^{\mathcal{M}_t} \grave{x}_{d,p}^* U_U(d,d') \grave{x}_{d',p} + U_U(d,d). \end{aligned} \tag{6.51}$$

Similarly, $\grave{\mathbf{x}}_p^H \mathbf{U}_D \grave{\mathbf{x}}_p = \bar{b}_0 \grave{x}_{d,p} + \bar{b}_1 + \bar{b}_2 \grave{x}_{d',p}^*$. The coefficients $\bar{b}_i$'s are calculated in an identical manner to $\bar{a}_i$ with $U_D(d,d')$ replaced with $U_U(d,d')$, and $U_D(d,d')$ are the elements of $\mathbf{U}_D$.

Chapter 7

Spectrum shaping for MIMO sequence set design

Preamble

In this chapter, the next step of the research investigated radar waveform optimization for cognitive MIMO radar systems operating alongside communication systems mentioned in section 1.5 as the manuscript $C2$.

We present an optimization-based approach for designing cognitive MIMO radar waveforms that enable a radar system to operate in the presence of communication systems. Our research addresses the challenge of coexistence between radar and communication by formulating a bi-objective optimization problem. This problem seeks to achieve a balance between spectrum compatibility and minimizing sidelobe correlations, both auto- and cross-correlation, to ensure interference-resistant waveforms.

To solve this problem, we employ the Block Successive Upper-bound Minimization (BSUM) framework, an iterative method that guarantees convergence of the objective function. By optimizing the spectral characteristics of the waveforms, our approach enhances the coexistence of cognitive radar and communication systems. Numerical results demonstrate the superiority of the proposed method compared to conventional approaches, showcasing its ability to deliver spectrally efficient and interference-resistant MIMO waveforms.

7.1 Manuscript: Radar Waveform Design for Sensing and Communications Coexistence

Robin Amar[1], Ehsan Raei,[2], Mohammad Alaee-Kerahroodi[1], Bhavani Shankar M.R.[1]

[1] SnT - Interdisciplinary Centre for Security, Reliability and Trust, University of Luxembourg
[2] Amphinicy Technologies, Luxembourg

Published in: *2023 20th European Radar Conference (EuRAD),* Berlin, Germany, 2023, pp. 407-410,
DOI: 10.23919/EuRAD58043.2023.10289167.

The following sections are a copy of the paper referenced above.

Abstract

The paper proposes an optimization-based method to create radar waveforms for cognitive MIMO systems that coexist with communication systems. We develop a bi-objective optimization problem to balance the objectives of achieving spectrum compatibility and minimizing auto- and cross-correlation sidelobes. We solve the problem iteratively using the Block Successive Upper-bound Minimization (BSUM) framework, ensuring objective function convergence. Numerical results demonstrate the superiority of the proposed method over other methods. The approach can enhance the coexistence of cognitive radar and communication systems by designing waveforms with optimized spectral characteristics.

7.2 Introduction

With the growing demand for spectrum usage, radar and communication systems must coexist in the same frequency bands without causing mutual interference. To achieve this, various approaches from a radar perspective have been proposed, with waveform design at the core, allowing for spectrum sharing while maintaining sensing requirements. This is particularly critical for emerging applications, including autonomous vehicles and smart cities, where multiple systems must operate in the same frequency bands. In recent years, several techniques, such as codesign of radar and communications, have been proposed, and researchers are actively exploring new approaches to address this challenge [140–145].

In general, several optimization frameworks including Block Successive Upper-bound Minimization (BSUM), Block Coordinate Gradient Descent (BCGD), Alternating Direction Method of Multipliers (ADMM), MM, and CD have been proposed for radar waveform design [60]. The choice of method depends on the specific problem being solved and the computational

resources available. BSUM is particularly useful when the objective function can be tightly upper-bounded in a coordinate-wise manner, which is the case considered in this paper.

To begin, an overall objective function is created that takes into account both the spectral shaping criteria for unwanted frequencies (stopbands) and the least cross-correlation across transmit sequences in a MIMO radar system. Spectral shaping is required to avoid spectral overlap with communication systems and is performed through minimization of the transmitted power in stopbands. Low cross-correlation amongst the transmit sequences is considered to leverage on the MIMO capability. The contribution of this paper is to provide a computational technique for designing sequences with a phase constraint that includes both a finite alphabet size and a continuous phase when considering the composite objective mentioned above. The ℓ_p norm-based optimization framework offers an unified approach to generate sequences with optimum ISL or PSL and to tune the transmitted power in stopband according to the spectrum requirements.

7.3 Problem Formulation

We consider a MIMO radar system with M transmit antennas[1]. Each antenna transmits a sequence $\mathbf{x}_m$ of length N, given by $\mathbf{x}_m = [x_{m,1}, \cdots, x_{m,N}]^T \in \mathbb{C}^N$, where $m = 1, \cdots, M$. The sequences are stacked to form the matrix $\mathbf{X} = [\mathbf{x}_1^T, \cdots, \mathbf{x}_M^T] \in \mathbb{C}^{N \times M}$. The bandwidth is divided into N equally spaced discrete frequencies and, for spectral transformations, we define $\mathbf{F}$ as the DFT matrix with $\mathbf{F} \triangleq [\mathbf{f}_0, \cdots, \mathbf{f}_{N-1}] \in \mathbb{C}^{N \times N}$, where $\mathbf{f_k} \triangleq [1, e^{-j\frac{2\pi k}{N}}, \cdots, e^{-j\frac{2\pi k(N-1)}{N}}]^T \in \mathbb{C}^N$ and $k = 0, \cdots, N-1$. We also define $\mathcal{U}$ as the union of K_u normalized discrete frequency stop-bands to avoid mutual interference, where $0 \leq u_{k,1} < u_{k,2} \leq 1$ and $\bigcap_{k=1}^{K_u}(u_{k,1}, u_{k,2}) = \emptyset$. Hence, the undesired discrete frequency bands are given by $\mathcal{V} = \bigcup_{k=1}^{K_u}(\lfloor Nu_{k,1} \rceil, \lfloor Nu_{k,2} \rceil)$. The spectral amplitude for undesired frequency bins is represented by $|\mathbf{V}_m \mathbf{x}_m|$, where $\mathbf{V}_m \in \mathbb{C}^{K \times N}$ contains the rows of $\mathbf{F}$ corresponding to the frequencies in $\mathcal{V}$, and undesired frequency bins are K.

We define the objective function $f_1(\mathbf{X})$ as the ℓ_p norm of the difference between the transmitted radar waveforms spectral pattern and the desired spectral pattern, where $\mathbf{z}_m$ represents the desired spectral pattern of the m^{th} transmitter.

$$f_1(\mathbf{X}) = \sum_{m=1}^{M} || \, |\mathbf{V}_m \mathbf{x}_m|^2 - \mathbf{z}_m||_p^p \tag{7.1}$$

[1]*Notation:* Boldface upper case letters denote matrices, bold-face lower case letters denote column vectors, and italics denote scalars. $\mathbb{R}$ and $\mathbb{C}$ denote the real and complex field, respectively. $X_{i,j}$ denotes the $(i,j)^{th}$ element of a matrix and x_i denotes the i^{th} element of vector $\mathbf{x}$. The Frobenius norm, ℓ_p norm, absolute value and round operator are denoted as $||\cdot||_F$, $||\cdot||_p$, $|\cdot|$ and $\lfloor \cdot \rceil$ respectively. The letter (i) is used as steps of a procedure, and $j = \sqrt{-1}$. Finally, $\odot$ denotes the Hadamard product.

Minimizing this objective function allows the radar waveforms to be designed to match the desired spectral pattern and avoid interfering with communication signals transmitted in specific frequency bands.

Further, the cross-correlation of the transmit waveforms $\mathbf{x}_m$ and $\mathbf{x}_{m'}$ is a measure of the interference caused by the MIMO radar waveforms to each other. To avoid this type of interference, we want to design the waveforms such that their cross-correlation with each other is as small as possible. The aperiodic cross-correlation of the transmit waveforms $\mathbf{x}_m$ and $\mathbf{x}_{m'}$ ($m \neq m', m, m' \in [1, \cdots, M]$) is defined as

$$r_{m,m'}(l) = \sum_{l=-N+1}^{N-1} x_{m,n} x^*_{m',n+l},\ n = 1, \cdots, N.$$

Let $\mathbf{r}_{m,m'} = [r_{m,m'}(-N+1), \ldots, r_{m,m'}(N-1)]^T \in \mathbb{C}^{2N-1}$, then, the objective function for cross-correlation matching is

$$f_2(\mathbf{X}) = \sum_{m=1}^{M} \sum_{m'=1}^{M'} || \, |\mathbf{r}_{m,m'}|^2 - \mathbf{u}_{m,m'}||_p^p, \tag{7.2}$$

where $\mathbf{u}_{m,m'} \in \mathbb{C}^{2N-1}$ is the non-negative cross-correlation mask of m^{th} to the m'^{th} transmit sequence and the objective is element-wise absolute squared.

We aim to find a set of sequences, $\mathbf{X}$, that simultaneously satisfy both objective functions $f_1(\mathbf{X})$ and $f_2(\mathbf{X})$. This is a challenging optimization problem because optimizing one objective function may lead to degradation in the other objective function. Therefore, finding a set of sequences that satisfy both objectives requires a careful balance between the two. One approach to dealing with these objective functions is to minimize a weighted sum of the two objectives, which is called Pareto optimization approach. In this approach, we seek to find a set of solutions that are not dominated by any other solution, meaning that there is no other solution that is better than it in both objectives simultaneously. We can write the combined objective function as follows:

$$f(\mathbf{X}) = \epsilon f_1(\mathbf{X}) + (1-\epsilon) f_2(\mathbf{X}), \tag{7.3}$$

where ϵ is non-negative weight that controls the relative importance of the two objectives. In

this case, the optimization problem is,

$$\mathcal{P}^{\dagger}\begin{cases}\underset{\mathbf{X}}{\text{minimize}}\, f(\mathbf{X}) = \epsilon \sum\limits_{m=1}^{M} || \, |\mathbf{V}_m \mathbf{x_m}|^2 - \mathbf{z}_m||_p^p + \\ \qquad\qquad (1-\epsilon) \sum\limits_{m=1}^{M} \sum\limits_{m'=1}^{M'} || \, |\mathbf{r}_{m,m'}|^2 - \mathbf{u}_{m,m'}||_p^p \\ \text{subject to} \quad \arg(x_{m,n}) \in \Omega_S \;\text{ or }\; \Omega_\infty \end{cases} \tag{7.4}$$

where the optimization variable is the transmit waveform matrix $\mathbf{X}$, which is subject to a set of constraints that depend on the specific modulation scheme used. These constraints are represented by the sets Ω_∞ and Ω_S, which are defined as $\Omega_\infty = [0, 2\pi)$, and $\Omega_S = \{0, \frac{2\pi}{S}; \cdots, \frac{2\pi(S-1)}{S}\}$, respectively. Here, $S \geq 2$ and finitely countable integer. In the sequel, we derive a method called Cognitive Spectral shaping for MIMO Radars (CS4MR) to solve the problem $\mathcal{P}^{\dagger}$ using the BSUM method and evaluate its performance.

7.4 BSUM-based Waveform Optimization

The BSUM framework provides a way to connect the BCD and MM optimization methods by iteratively optimizing a sequence of upper bounds of the original objective function in a coordinate-wise manner [60]. This approach is useful for tackling difficult optimization problems by breaking them down into a series of easier subproblems and is considered in the following. To this end, by selecting a block of variables in $\mathbf{X}$, and calling it $\mathbf{x}_t \in \mathbb{C}^N$, we concentrate the objective function in $\mathcal{P}^{\dagger}$ on this selected variable block, while keeping waveforms transmitted from other antennas fixed. In this case, $f(\mathbf{X})$ is decomposed as

$$f(\mathbf{X}) = \epsilon(f_{-t}(\mathbf{X}_{-t}) + f_{ac}(\mathbf{x}_t) + f_{cr}(\mathbf{x}_t, \mathbf{X}_{-t})) + (1-\epsilon)(g(\mathbf{x}_t) + g(\mathbf{X}_{-t})), \tag{7.5}$$

$$\begin{aligned} f_{ac}(\mathbf{x}_t) &= \sum_{l=-N+1}^{N-1} || \, |\mathbf{r}_{t,t}|^2 - \mathbf{u}_{t,t}||_p^p, \\ f_{cr}(\mathbf{x}_t, \mathbf{X}_{-t}) &= 2 \sum_{\substack{m=1 \\ m\neq t}}^{M} \sum_{l=-N+1}^{N-1} || \, |\mathbf{r}_{t,m}|^2 - \mathbf{u}_{t,m}||_p^p, \\ g(\mathbf{x}_t) &= ||\mathbf{V}_t \mathbf{x}_t|^2 - \mathbf{z}_t||_p^p, \\ f_{-t}(\mathbf{X}_{-t}) &= \sum_{\substack{m=1 \\ m'\neq t}}^{M} \sum_{\substack{m=1 \\ m'\neq t}}^{M} || \, |\mathbf{r}_{m,m'}|^2 - \mathbf{u}_{m,m'}||_p^p, \\ g(\mathbf{X}_{-t}) &= \sum_{\substack{m=1 \\ m\neq t}}^{M} || \, |\mathbf{V}_m \mathbf{x}_m|^2 - \mathbf{z}_m||_p^p. \end{aligned} \tag{7.6}$$

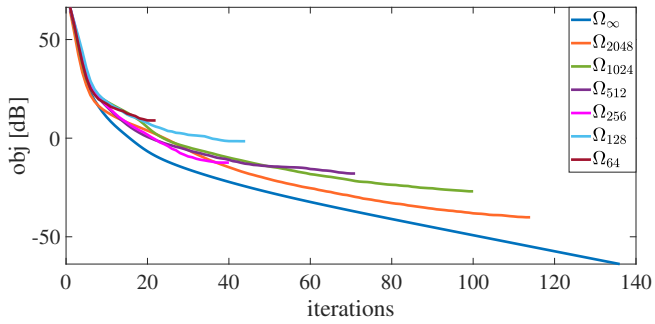

Figure 7.1: Convergence of the objective function with increasing alphabet size

Since the terms $f_{-t}(\mathbf{X}_{-t})$ and $g(\mathbf{X}_{-t})$ do not depend upon $\mathbf{x}_t$, they can be ignored in the objective function. The new objective function is

$$\bar{f}(\mathbf{X}) = \epsilon(f_{ac}(\mathbf{x}_t) + f_{cr}(\mathbf{x}_t, \mathbf{X}_{-t})) + (1-\epsilon)(g(\mathbf{x}_t)). \tag{7.7}$$

Further, by using the Lemma 7.4.1, we find quadratic surrogate functions for $f_{ac}(\mathbf{x}_t)$, $f_{cr}(\mathbf{x}_t, \mathbf{X}_{-t})$, and $g(\mathbf{x}_t)$, which further simplifies the optimization problem based on BSUM framework. Now, calling $x_{t,d}$ as the d-th entry of the variable block $\mathbf{x}_t$, and using Lemma 7.4.1, the following surrogate functions can be obtained,

$$\begin{aligned}
\widetilde{f}_{ttdl}(x_{t,d}) &= \alpha_{ttdl}|f_{ttdl}(x_{t,d})|^2 + \left(\frac{\beta_{ttdl} f_{ttdl}^{(i-1)}(x_{t,d})}{|f_{ttdl}^{(i-1)}(x_{t,d})|}\right) f_{ttdl}(x_{t,d}) + \gamma_{ttdl}, \\
\widetilde{f}_{tmdl}(x_{t,d}) &= \alpha_{tmdl}|f_{tmdl}(x_{t,d})|^2 + \left(\frac{\beta_{tmdl} f_{tmdl}^{(i-1)}(x_{t,d})}{|f_{tmdl}^{(i-1)}(x_{t,d})|}\right) f_{tmdl}(x_{t,d}) + \gamma_{tmdl}, \\
\widetilde{g}_{tdk}(x_{t,d}) &= \alpha_{tdk}|g_{tdk}(x_{t,d})|^2 + \frac{\beta_{tdk} g_{tdk}^{(i-1)}}{|g_{tdk}^{(i-1)}|} g_{tdk}(x_{t,d}) + \gamma_{tdk},
\end{aligned} \tag{7.8}$$

where α_{ttdl}, β_{ttdl}, γ_{ttdl}, α_{tdk}, β_{tdk}, and γ_{tdk} are in Table 7.2.

Lemma 7.4.1. *Let $f(x) = x^p$ with $p \geq 2$ and $x \in [0, t]$. Then for any given $x_0 \in [0, t)$, $f(x)$ is majorized at x_0 over the interval $[0, t]$ by [60]*

$$u(x) = ax^2 + (px_0^{p-1} - 2ax_0)x + ax_0^2 - (p-1)x_0^p \quad \textit{where } a = \frac{t^p - x_0^p - px_0^{p-1}(t-x_0)}{(t-x_0)^2}.$$

with $\frac{t^p - x_0^p - px_0^{p-1}(t-x_0)}{(t-x_0)^2}$.

Thus, a new objective function is obtained which is the summation of $\widetilde{f}_{ttdl}(x_{t,d})$, $\widetilde{f}_{tmdl}(x_{t,d})$, and $\widetilde{g}_{tdk}(x_{t,d})$, that at i^{th} iteration of the optimization procedure, depends only on a single variable $x_{t,d}$. This can be further simplified and written in a polynomial form based on $x_{t,d}$ as

$$\tilde{f}(x_{t,d}, \mathbf{X}_{-(t,d)}) = q_0 x_{t,d}^4 + q_1 x_{t,d}^3 + q_2 x_{t,d}^2 + q_3 x_{t,d} + q_4 + q_5 x_{t,d}^* + q_6 {x_{t,d}^*}^2 + q_7 {x_{t,d}^*}^3 + q_8 {x_{t,d}^*}^4, \tag{7.9}$$

where the coefficients are given in Table 7.1. Here $\mathbf{X}_{-(t,d)} \triangleq \mathbf{X}^{(i)} \mid_{x_{(t,d)=0}}$ refers to a matrix including fixed entries at i^{th} iteration. By substituting $x_{t,d} = e^{j\phi_{t,d}}$, (7.9) depends only on parameter $\phi_{t,d}$[2] and can be represented as

$$\begin{aligned}\tilde{f}(\phi_{t,d}) = q_0 e^{j4\phi_{t,d}} + q_1 e^{j3\phi_{t,d}} + q_2 e^{j2\phi_{t,d}} + q_3 e^{j\phi_{t,d}} + q_4 \\ + q_5 e^{-j\phi_{t,d}} + q_6 e^{-j2\phi_{t,d}} + q_7 e^{-j3\phi_{t,d}} + q_8 e^{-j4\phi_{t,d}}.\end{aligned} \tag{7.10}$$

Thus, at every iteration, the optimization problem is,

Table 7.1: Coefficients of eq: (7.9)

Coeff	**Expression**
q_0	$(1-\epsilon)(\alpha_{tmdl}\bar{\chi}_2^2 e^{+j4\phi} + \alpha_{ttdl}\chi_2^2 e^{+j4\phi})$
q_1	$(1-\epsilon)(2\alpha_{tmdl}\bar{\chi}_2\bar{\chi}_1)$
q_2	$\epsilon(\sum_{k=1}^{K}\alpha_{tdk}a_{tdk}{b_{tdk}^*}^2)+(1-\epsilon)\Big(\big\{\alpha_{tmdl}\big(\bar{\chi}_1^2+2\bar{\eta}\bar{\chi}_2\big)+\widetilde{\beta}_{tmdl}\bar{\chi}_2\big\}$ $+\big\{\alpha_{ttdl}\big(\chi_1^2+2\eta\chi_2\big)+\widetilde{\beta}_{ttdl}\chi_2\big\}\Big)$
q_3	$\epsilon(\sum_{k=1}^{K}a_{tdk}b_{tdk}^*(2\alpha_{tdk}\xi_0+\frac{\beta_{tdk}g_{tdk}^{(i-1)}}{\lvert g_{tdk}^{(i-1)}\rvert}))+(1-\epsilon)(\big\{2\alpha_{tmdl}(\bar{\eta}\bar{\chi}_1+\bar{\chi}_2\bar{\chi}_{-1})+\widetilde{\beta}_{tmdl}\bar{\chi}_1\big\}$ $+\big\{2\alpha_{ttdl}(\eta\chi_1+\chi_2\chi_{-1})+\widetilde{\beta}_{ttdl}\chi_1\big\})$
q_4	$\epsilon(\sum_{k=1}^{K}\alpha_{tdk}\Big(2\lvert\xi_1\rvert^2+\lvert\xi_0\rvert^2+\frac{\beta_{tdk}g_{tdk}^{(i-1)}}{\lvert g_{tdk}^{(i-1)}\rvert}\xi_0+\gamma_{tdk}\Big))$ $+(1-\epsilon)(\alpha_{tmdl}\big\{\bar{\eta}^2+2(\bar{\chi}_{-2}\bar{\chi}_2+\bar{\chi}_{-1}\bar{\chi}_1)\big\}+\widetilde{\beta}_{tmdl}\bar{\eta}+\gamma_{tmdl}$ $+\alpha_{ttdl}\big\{\eta^2+2(\chi_{-2}\chi_2+\chi_{-1}\chi_1)\big\}+\widetilde{\beta}_{ttdl}\eta+\gamma_{ttdl})$

$$\mathcal{P}^{\phi_{t,d}} \begin{cases} \underset{\phi_{t,d}}{\text{minimize}}\ \tilde{f}(\phi_{t,d}) \\ \text{subject to} \quad \phi_{t,d} \in \Omega_S \ \text{ or } \ \Omega_\infty \end{cases} \tag{7.11}$$

The solution to $\mathcal{P}^{\phi_{t,d}}$ is obtained in the sequel depending on the constraint. *Infinite alphabet size,* Ω_∞: In order to find the optimal phase $\hat{\phi}$, $\tilde{f}(\phi)$ in (7.10) is differentiated with respect to ϕ and its critical points contain the solutions to $\tilde{f}'(\phi) = 0$. Using a slack variable $z = e^{j\phi}$, the critical points can be obtained by obtaining the roots of the eight degree polynomial of $\tilde{f}'(z) = 0$. Let us assume that λ_i, $i = \{1, \ldots, 8\}$ are the roots of $\tilde{f}'(z) = 0$. Hence, the critical points for (7.10) can be expressed as, $\phi_i = j\log(\lambda_i)$. Since ϕ is a real variable, we seek only the real extrema points. The critical point corresponding to the minimum value of $\tilde{f}(\phi)$ provides the optimal value of phase, $\hat{\phi}$ for the t^{th} transmitter and d^{th} element. This procedure will continue for other entries until the stationary point is obtained. *Finite alphabet size,* Ω_S: In this case, since $\phi \in \Omega_S$ is chosen from a limited alphabet size of length S, the objective function can be written with

[2]For ease of notation, we will represent $\phi_{t,d}$ as ϕ later in the text.

respect to the indices of Ω_S as

$$f^{(i)}(s) = e^{j\frac{8\pi s}{S}} \sum_{\rho=0}^{8} q_\rho e^{-j\frac{2\pi\rho s}{S}}, \tag{7.12}$$

where $s = 0, \cdots, S-1$. The summation term in the aforementioned equation is exactly the definition of S-point DFT of sequences $[q_0, \cdots, q_8]$. Therefore, we have, $f^{(i)}(s) = \mathbf{h} \odot \mathcal{F}\{q_0, \cdots, q_8\}$, where $\mathbf{h} \triangleq [1, e^{j\frac{8\pi s}{S}}, \cdots, e^{j\frac{8\pi(S-1)}{S}}] \in \mathbb{C}^S$. Therefore, the optimum solution for $f^{(i)}(s)$ is $\hat{s}^{(i)} = \arg \min_{s=1,\cdots,S-1} \{f^{(i)}(s)\}$, then the optimum phase is $\hat{\phi} = 2\pi\hat{s}^{(i)}/S$. The variable $x_{t,d}$ will be updated as $\hat{x}_{t,d}^{(i)} = e^{j\hat{\phi}^{(i)}}$. This procedure continues for other entries until the stationary point is obtained. We consider $\frac{1}{\sqrt{MN}}||\mathbf{X}^{(i)} - \mathbf{X}^{(i-1)}||_F < 10^{-5}$, as stopping criterion for optimization. The proposed method will be referred further in the text as CS4MR.

7.5 Performance Analysis

Now, we evaluate the performance of the proposed method and compare it with the state-of-the-art counterparts.

7.5.1 Convergence

Convergence behavior of the objective function is shown in Figure 7.1 for various alphabet sizes. Here, the undesired normalized frequencies are located at $\mathcal{U} = [0.2, 0.4] \cup [0.6, 0.8]$, $N = 128$, $M = 2$, $p = 2$ and the proposed method is initialized with random phase. The objective function decreases monotonically for all the alphabet sizes. As the alphabet size increases, the performance of the proposed method improves and thus achieves lower objective values. The argument converges to the optimum value for all cases.

7.5.2 Spectral Shaping and Correlation Comparison

In Figure 7.2, we compare the performance of CS4MR with [3] (referred as **rIMSMR**) and **SHAPE** [4]. The authors addressed the spectral shaping and range ISL minimization in MIMO radar system under discrete phase constraint. In SHAPE method, only spectral shaping was addressed. Therefore, we derived two metrics for the quality of spectral shaping achieved by each of these methods, namely the mean μ and standard deviation σ of the spectrum in pass-band and stopband. A single transmit sequence for SHAPE and a MIMO arrangement with two transmit sequences for CS4MR and rIMSMR of length $N = 128$, alphabet size of 2048 and the undesired normalized frequencies $\mathcal{U} = [0.2, 0.4] \cup [0.6, 0.8]$ was used. As apparent from Figure 7.2 and Table 7.3, CS4MR shows the least values for $\mu = -32.58$ and $\sigma = 2.52$ for

stopband. In the context of MIMO, three metrics are defined, i.e. ISL, PSL and Integrated

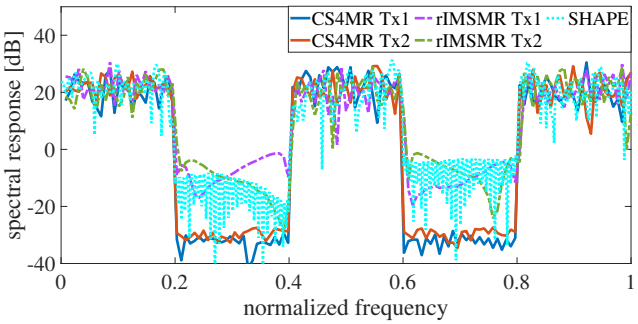

Figure 7.2: Spectral response comparison with methods [3] and [4]

Cross-Correlation Level (ICCL) which can be mathematically defined as ISL $= \sum_{k=1}^{N-1} |r_k|^2$, PSL $= \max_{k=1,2,\ldots,N-1} |r_k|$, and ICCL $= \sum_{m=1}^{M} \sum_{\substack{m'=1 \\ m' \neq m}}^{M} \sum_{l=-N+1}^{N-1} |r_{m,m}(l)|^2$, respectively. Table 7.3 shows the minimum ICCL value for CS4MR while maintaining decent ISL and PSL values as compared to SHAPE and rIMSMR.

7.6 Conclusion

In this paper we addressed the MIMO radar sequence design problem with strict spectral occupancy constraint. In this regard, we converted the combined non-convex NP-hard problem into smaller sub-problems and solved using BSUM technique. The simulation results shows the monotonically decreasing objective function for various alphabet sizes. The performance of CS4MR was evaluated by tuning the weight for spectral shaping on one end to correlation matching on the other end, and it performed better than state-of-the-art approaches.

Table 7.2: Supporting parameters for Table 7.1

Parameter	Expression
α_{tmdl}	$\alpha_{ntmdl}/(\tau_{tmdl} - \lvert r_{t,m}(l)^{(i-1)}\rvert)^2$
β_{tmdl}	$p\lvert r_{t,m}(l)^{(i-1)}\rvert^{p-1} - 2\alpha_{tmdl}\lvert r_{t,m}(l)^{(i-1)}\rvert$
$\widetilde{\beta}_{tmdl}$	$\left(\frac{\beta_{tmdl} f_{tmdl}^{(i-1)}}{f_{tmdl}^{i-1}}\right)$
γ_{tmdl}	$\alpha_{tmdl}\lvert r_{t,m}(l)\rvert^2 - (p-1)\lvert r_{t,m}(l)\rvert^p$
τ_{tmdl}	$\left(\sum_{l=-N+1}^{N-1} \lvert r_{t,m}(l)^{(i-1)}\rvert^p\right)^{1/p}$
α_{ntmdl}	$\tau_{tmdl}^p - \lvert r_{t,m}(l)^{(i-1)}\rvert^p - p\lvert r_{t,m}(l)^{(i-1)}\rvert^{(p-1)}.(\tau_{tmdl} - \lvert r_{t,m}(l)\rvert^p)$
α_{ttdl}	$\alpha_{nttdl}/(\tau_{ttdl} - \lvert r_{t,t}(l)^{(i-1)}\rvert)^2$
β_{ttdl}	$p\lvert r_{t,t}(l)^{(i-1)}\rvert^{p-1} - 2\alpha_{ttdl}\lvert r_{t,t}(l)^{(i-1)}\rvert$
$\widetilde{\beta}_{ttdl}$	$\left(\frac{\beta_{ttdl} f_{ttdl}^{(i-1)}}{f_{ttdl}^{i-1}}\right)$
γ_{ttdl}	$\alpha_{ttdl}\lvert r_{t,t}(l)\rvert^2 - (p-1)\lvert r_{t,t}(l)\rvert^p$
τ_{ttdl}	$\left(\sum_{l=1}^{N-1} \lvert r_{t,t}^{(l)}\rvert^p\right)^{1/p}$
α_{nttdl}	$\tau_{ttdl}^p - \lvert r_{t,t}(l)^{(i-1)}\rvert^p - p\lvert r_{t,t}(l)^{(i-1)}\rvert^{(p-1)}.(\tau_{ttdl} - \lvert r_{t,t}(l)\rvert^p)$
α_{tdk}	$\tau_{td}^p - \lvert g_{tdk}\rvert^p - p\lvert g_{tdk}\rvert^{p-1}(\tau_{td} - \lvert g_{tdk}\rvert)/(\tau_{td} - \lvert g_{tdk}\rvert^2)$
β_{tdk}	$p\lvert g_{tdk}^{p-2} - 2\alpha_{tdk}\rvert$
γ_{tdk}	$\alpha_{tdk}\lvert g_{tdk}\rvert^2 - (p-1)\lvert g_{tdk}\rvert^p$
$\mathbf{g}_{td}$	$\lvert\lvert\mathbf{a}_{td} \odot \mathbf{X}_{t,d} + \mathbf{b}_{td}\rvert\rvert_2 - \mathbf{z}$
τ_{td}	$\sum_{n=1}^{N} \lvert\lvert\mathbf{g}_{tdk}\rvert\rvert_p$
$\mathbf{a}_{td}$	$\mathbf{f}_d$
$\mathbf{b}_{td}$	$\mathbf{V}_m\mathbf{x}_m - \mathbf{a}_{td}\mathbf{X}_{t,d}$
$\bar{\chi}_2$	$a_{tmdl}b_{tmdl}^*$
$\bar{\chi}_1$	$(a_{tmdl}c_{tmdl}^* + b_{tmdl}^* c_{tmdl})$
χ_2	$a_{ttdl}b_{ttdl}^*$
χ_1	$(a_{ttdl}c_{ttdl}^* + b_{ttdl}^* c_{ttdl})$
ξ_1	$a_{tdk}{b_{tdk}}^*$
ξ_0	$\lvert a_{tdk}\rvert^2 + \lvert b_{tdk}\rvert^2 - g_{tk}$

Table 7.3: passband and stopband power level comparison

Parameter	SHAPE	rIMSMR	CS4MR
passband (μ, σ) dB	21.11, 6.03	20.91, 5.44	21.08, 4.83
stopband (μ, σ)dB	-12.86, 8.56	-8.98, 5.28	-32.58, 2.52
auto-correlation (ISL, PSL) dB	3.74, -7.93	1.47, -5.86	0.0464, -5.6711
cross-correlation (ICCL) dB	NA	-0.4411	-1.63

Part IV

Applications in Wireless Sensor Networks

Chapter 8

Dual-Function Waveform Design in Wireless Sensor Networks via SoS Optimization

Preamble

In the final phase, the research expanded to environmental sensing using Wireless Sensor Networks (WSNs), applying waveform optimization techniques for Integrated Sensing and Communication (ISAC) applications referred as manuscript $C4$ in section 1.5. The proposed Doppler-tolerant waveforms embed communication symbols within alternate sub-pulses, while reducing cross-correlation sidelobe levels for the sensing sub-pulse.

We proposed a novel solution for the cross-correlation integrated sidelobe level (CISL) problem using a fusion of multiple optimization techniques: BCD, MM and SoS. This ISAC solution is vital for reliable target detection in dynamic environments where mutual interference (MI) from other sensors is unavoidable, further demonstrating the flexibility and effectiveness of the previously proposed waveform design techniques.

8.1 Manuscript: Dual-Function Waveform Design in Wireless Sensor Networks via SoS Optimization

Robin Amar[1], Linlong Wu[1], Saeid Sedighi,[2], Mohammad Alaee-Kerahroodi[1], Bhavani Shankar M.R.[1]

[1] SnT - Interdisciplinary Centre for Security, Reliability and Trust, University of Luxembourg

[2] Valeo Schalter und Sensoren GmbH

Submitted to: *ICASSP 2025 - IEEE International Conference on Acoustics, Speech and Signal Processing (ICASSP) 2025, Hyderabad, India*

The following sections are a copy of the paper referenced above.

Abstract

Environmental sensing can be achieved using Wireless Sensor Networks (WSNs) with low-complexity sensors. Integrated sensing and communication (ISAC) allows simultaneous sensing and data transmission through optimized waveform, architecture, and protocol design. Given the multiple sensors in WSNs, minimizing interference and ensuring Doppler-tolerant pulses for detecting dynamic targets is crucial. This paper proposes a Doppler-tolerant waveform design that embeds multiple communication symbols within each pulse of a coherent processing interval (CPI). We formulate a Sum-of-Squares (SoS) optimization problem to minimize the cross-correlation integrated sidelobe level (CISL) for a MIMO sensor arrangement, constrained by unwrapped quadratic phase behavior. Simulation results confirm the effectiveness of the proposed approach.

8.2 Introduction

The Internet of Things (IoT) has transformed modern infrastructures by integrating sensing, computation, and communication, paving the way for applications like smart cities and intelligent transportation [146]. Wireless sensor networks (WSNs), the backbone of IoT, facilitate communication and sensing among distributed sensors, coordinating information flow within the network [147]. However, traditional approaches that separate sensing and communication processes can result in reduced real-time performance and inefficient resource use.

To overcome these limitations, the ISAC has emerged as a promising solution, which facilitates simultaneous sensing and communication within the same spectrum by applying dual-function waveforms [148]. Various studies in the literature have examined OFDM-based waveforms for ISAC applications [149–151]. Besides, OFDM waveforms have already been employed in WSN [152–155], with a primary focus on data transmission and estimation.

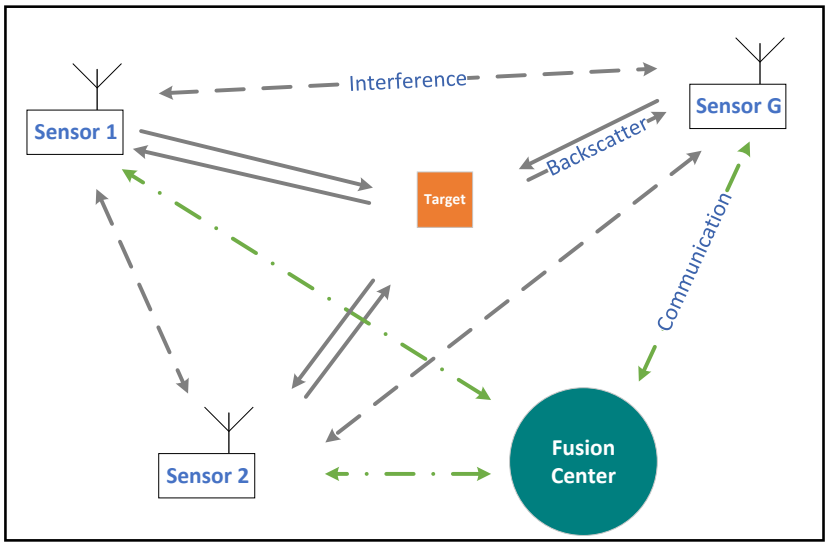

Figure 8.1: ISAC in an IoT Scenario

A recent survey [156] indicates that ISAC is expected to be applied in WSNs as well. The work [157] investigated the design of a combining matrix to further integrate over-the-air computation into ISAC-enabled WSNs, assuming orthogonal waveforms. Considering the nice Doppler-tolerant property of FMCW, several studies have explored using it to enable ISAC in WSNs [158, 159]. The [158] analyzes phase-coded FMCW waveforms and experimentally demonstrates their effectiveness for both sensing and communication. Meanwhile, [159] proposes a symbol embedding scheme for FMCW and designs the combiner at the fusion center, however which has not addressed the issue of mutual interference among sensors.

In this paper, we propose a Doppler-tolerant waveform design that embeds multiple communication symbols within each pulse of a CPI. Unlike existing FMCW waveform approaches, our design achieves higher data rates and lower cross-interference. We formulate a minimization problem for the CISL with an unwrapped quadratic phase constraint, and solve it using multi-layer approach which includes BCD, MM, and Sum-of-Squares (SoS)-based iterative methods that provides a global optimal solution for each subproblem. Simulations confirm the effectiveness of the proposed approach.

8.3 System Model

As shown in Figure8.1, a WSN is considered, where M single-antenna sensors communicate with the Fusion Center (FC) while detect the moving target simultaneously. The target location and velocity are denoted by $l_t = [l_x, l_y, l_z]^T$ and $v_t = [v_x, v_y, v_z]^T$, respectively.

To detect moving targets, LFM waveforms are typically used due to their Doppler tolerance,

stemming from their quadratic phase variation over a pulse. Extending this, a generic waveform model with polynomial phase variation is proposed, with the quadratic phase as a special case. Assuming a single pulse consists of S subpulses, as shown in Figure8.2, the waveform model is described as follows:

$$s_m(t) = \sum_{s=1}^{S} c_g x_g[s] u_g(t - sT_s) e^{j2\pi f_c t} \tag{8.1}$$

where $\mathbf{c}_g$ is the communication symbol for the g-th sensor, u_g is the modulating signal, and f_c is the carrier signal. To achieve ISAC functionality, each pulse is divided into subpulses, with some dedicated to communication and others to sensing. In this paper, an intertwined approach is used: even-indexed subpulses handle communication, while odd-indexed subpulses focus on sensing.

8.3.1 Sensing Scheme

Each pulse of the m-th sensor transmits a sequence $\mathbf{x}_g = [\tilde{\mathbf{x}}_1^T, \ldots, \tilde{\mathbf{x}}_s^T, \ldots, \tilde{\mathbf{x}}_S^T]^T \in \mathbb{C}^{\bar{N}}$, $\bar{N} = N_1 + \ldots + N_s + \ldots, N_S$, which is composed of S subpulses where $\tilde{\mathbf{x}}_s \in \mathbb{C}^{N_s}$, represents the sub-sequence elements for the s-th subpulse. Each subpulse is characterized by its unique phase behavior which is represented as

$$\boldsymbol{\theta}_{s,g} = \arg(\tilde{\mathbf{x}}_s) = \sum_{d=0}^{D} a_{\{d,s,g\}} n^d, \tag{8.2}$$

where $\arg(\tilde{\mathbf{x}}_s) = [\arg(x_{1_s}), \ldots, \arg(x_{N_s})]^T$, $n = 1, \ldots, N_s$, and $g_{\{d,s,g\}}$ denotes the phase coefficients of the polynomial of degree d.

As a special case of $D = 2$, the subpulse phase varies quadratically as

$$\theta_{\{s,g\}} = a_{\{0,s,g\}} + a_{\{1,s,g\}} n + a_{\{2,s,g\}} n^2, \tag{8.3}$$

which resembles the discretized LFM of

$$\theta_{LFM} = \theta_0 + 2\pi f_c n + \pi \beta n^2, \tag{8.4}$$

where $a_{\{0,s,g\}} = \theta_0$ is an arbitrary initial phase, $a_{\{1,s,g\}} = 2\pi f_c$ with f_c being the center frequency, and $a_{\{2,s,g\}} = \pi\beta$ with β being the chirp slope.

8.3.2 Communication Scheme

Denoted by $\mathbf{c}_g = [c_{\{1,g\}}, \ldots, c_{\{D,g\}}]^T \in \mathbb{C}^D$ the communication symbols to be transmitted by the g-th sensor to the FC, where $c_{\{d,g\}}$ is the d-th symbol for a given pulse from the g-th sensor. To embed the communication symbols into the waveform, we map the communication symbols

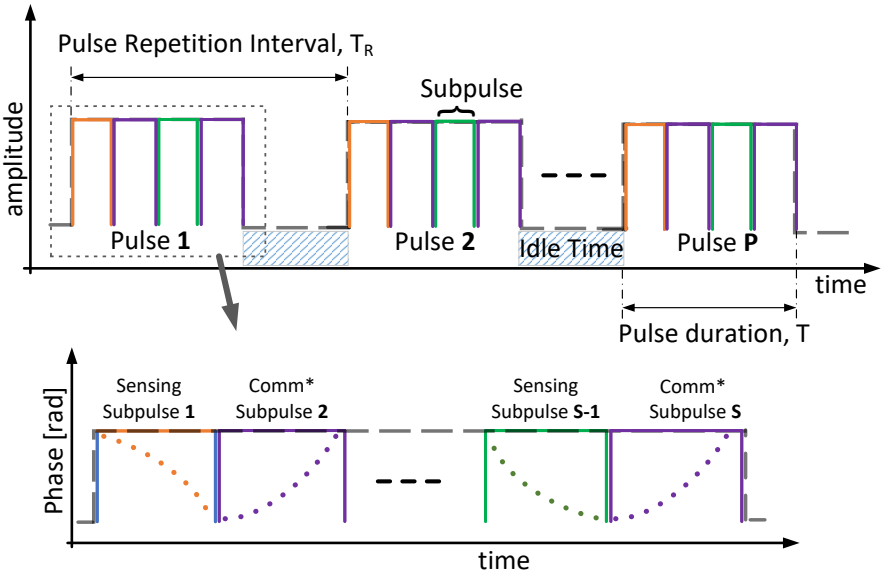

Figure 8.2: Pulse diagram with Sub-pulses

to the phase coefficients as

$$\mathcal{M} : a_{\{d,s,g\}} \rightarrow c_{\{d,g\}}, \; \forall \; d = 1, \ldots, D \tag{8.5}$$

Each subpluse allows the embedding of D communication symbols. Assuming the symbols are from M-PSK constellations, the communication rate for one CPI is

$$r = PSD \log_2 M. \tag{8.6}$$

The received signal at the g-th sensor from the target along with the interfering signals from other sensors is

$$\mathbf{r}_g = \alpha_g \mathbf{x}_g + \sum_{g'=1, g' \neq g}^{G} \beta_{g'} \mathbf{x}_{g'} \tag{8.7}$$

The received signal at the FC which is equipped with W receive elements is

$$\mathbf{y}_{w,c} = \sum_{g=1}^{G} \gamma_{w,g} \mathbf{x}_g + n_c \tag{8.8}$$

where $w = 1, \ldots, W$, $\gamma_{w,g}$ is the complex-valued channel coefficient between g-th sensor and the w-th receive element, and n_c is the noise. The symbol estimation at the FC can refer to the least-square approach of [159] for improved MSE.

8.4 Problem Formulation

The mutual interference among different sensors is caused the non-orthogonal waveforms, which is usually measured by the aperiodic cross-correlation as

$$r_{g,g'}(k) = \sum_{n=k+1}^{\bar{N}} x_{\{\bar{n},g\}} x^*_{\{\bar{n}-k,g'\}} = r_{g',g}(-k), \tag{8.9}$$

where $\bar{n} = 1, \ldots, \bar{N}$, and $g \neq g'$ and $g, g' \in [1, \ldots, G]$),

To suppress the mutual interference, we propose to minimize the cross-correlation levels of these waveform by properly designing these sensing subpulses, and therefore the problem is formulated as[1]

$$\begin{cases} \underset{\mathbf{x}_g, \mathbf{x}_{g'}}{\text{minimize}} & \sum\limits_{\substack{g,g'=1 \\ g \neq g'}}^{M} \sum\limits_{k=1-\bar{N}}^{\bar{N}-1} |r_{g,g'}(k)|^2 - \bar{N}^2 M \\ \text{subject to} & \arg(x_{n,g}) = \sum\limits_{d=0}^{D} a_{\{d,s,g\}} n^d, \\ & |x_{n,g}| = 1, \forall \begin{cases} n = 1, \ldots, N, \\ \bar{n} = n + (s-1)N, \\ g, g' = 1, \ldots, G. \end{cases} \end{cases} \tag{8.10}$$

8.5 A SoS-Based Solution

The cross-correlation between $\mathbf{x}_g$ and $\mathbf{x}_{g'}$ can be rewritten as

$$\sum_k |r_{g,g'}(k)|^2 = \sum_k |\mathbf{x}_g^H \mathbf{U}_k \mathbf{x}_{g'}|^2 \tag{8.11}$$

where $\mathbf{U}_k$ is a Toeplitz matrix with k^{th} diagonal elements being 1 and 0 elsewhere.

$$\begin{aligned} &\sum_k |r_{g,g'}(k)|^2 = \sum_k \left| (\check{\mathbf{x}}_{s,g} + \check{\mathbf{x}}_{-s,g})^H \mathbf{U}_k \mathbf{x}_{g'} \right|^2 \\ =& \sum_k \left| \check{\mathbf{x}}_{s,g}^H \boldsymbol{\alpha}_k + \gamma_k \right|^2 = \sum_k \left| \sum_{n=1}^{N_s} e^{-j\theta_n} \alpha_k(n) + \gamma_k \right|^2 \\ =& \sum_k \left\{ \left[\sum_n \psi_{nk} \Big(\cos(\theta_n - \beta_{nk}) \Big) + \gamma_{kr} \right]^2 \right. \\ &\left. + \left[\sum_n \psi_{nk} \Big(\sin(\theta_n - \beta_{nk}) \Big) + \gamma_{ki} \right]^2 \right\} \end{aligned} \tag{8.12}$$

where $\check{\mathbf{x}}_{s,g} \in \mathbb{C}^M$ is the s^{th} sub-sequence in $\mathbf{x}_g$, $\boldsymbol{\alpha}_k = \mathbf{U}_k \mathbf{x}_{g'}$ and $\gamma_k = \check{\mathbf{x}}_{-s,g}^H \mathbf{U}_k \mathbf{x}_{g'}$, $\cos(\beta_{nk}) = \frac{\alpha_{kr}(n)}{\psi_{nk}}$, $\sin(\beta_{nk}) = \frac{\alpha_{ki}(n)}{\psi_{nk}}$ and $\psi_{nk} = \sqrt{(\alpha_{kr}(n))^2 + (\alpha_{ki}(n))^2}$.

[1] The waveform design is handled in a centralized manner i.e. with a design hub connected to all the sensors.

Further, using MM technique, we apply quadratic majorizers for $\cos(\theta_n - \beta_{nk})$ as

$$\begin{aligned}\cos(\bar{\theta}_{nk}) &\leq \frac{1}{2}(\bar{\theta}_{nk} - \bar{\theta}_{nk}^{(i)})^2 - \sin(\bar{\theta}_{nk}^{(i)})(\bar{\theta}_{nk} - \bar{\theta}_{nk}^{(i)}) + \cos(\bar{\theta}_{nk}^{(i)}) \\ &= \frac{1}{2}\theta_n^2 + \theta_n(-\mathcal{C} - \sin(\bar{\theta}_{nk}^{(i)})) \\ &+ \left(\frac{1}{2}\mathcal{C}^2 + \mathcal{C}\sin(\bar{\theta}_{nk}^{(i)}) + \cos(\bar{\theta}_{nk}^{(i)})\right) \triangleq g_k(\theta_n),\end{aligned} \tag{8.13}$$

where $\bar{\theta}_{nk} = \theta_n - \beta_{nk}, \mathcal{C} = \bar{\theta}_{nk}^{(i)} + \beta_{nk}$.

For $\sin(\bar{\theta}_{nk}) = \cos\left(\frac{\pi}{2} - \bar{\theta}_{nk}\right) = \cos(\phi_{nk})$, we have

$$\begin{aligned}\cos(\phi_{nk}) &\leq \frac{1}{2}\theta_n^2 + \theta_n(-\mathcal{C} + \cos(\bar{\theta}_{nk}^{(i)})) \\ &+ \left(\frac{1}{2}\mathcal{C}^2 - \mathcal{C}\cos(\bar{\theta}_{nk}^{(i)}) + \sin(\bar{\theta}_{nk}^{(i)})\right) \triangleq h_k(\theta_n)\end{aligned} \tag{8.14}$$

By replacing $\cos(\theta_n - \beta_{nk})$ and $\sin(\theta_n - \beta_{nk})$ of (8.12) with the above two majorizers, the majorized subproblem is

$$\begin{cases}\underset{\mathbf{x}_g, \mathbf{x}_{g'}}{\text{minimize}} & \sum_k \left\{ \left[\sum_n \left(\psi_{nk}\, g_k(\theta_n) + \frac{\gamma_{kr}}{N_s} \right) \right]^2 \right. \\ & \left. + \left[\sum_n \left(\psi_{nk}\, h_k(\theta_n) + \frac{\gamma_{ki}}{N_s} \right) \right]^2 \right\} \\ \text{subject to} & \theta_n = \arg(x_{n,g}) = \sum_{d=0}^{D} a_{\{d,s,g\}} n^d.\end{cases} \tag{8.15}$$

By substituting the phase constraint into the objective function, problem (8.15) can be further rewritten as

$$\begin{cases}\underset{\mathbf{x}_g, \mathbf{x}_{g'}}{\text{minimize}} & \mathcal{O} \triangleq \sum_k \left\{ \left[\sum_n \left(\eta_{1nk}\theta_n^2 + \eta_{2nk}\theta_n + \eta_{3nk} \right) \right]^2 \right. \\ & \left. + \left[\sum_n \left(\eta_{4nk}\theta_n^2 + \eta_{5nk}\theta_n + \eta_{6nk} \right) \right]^2 \right\} \\ \text{subject to} & \theta_n = \arg(x_{n,g}) = \sum_{d=0}^{D} a_{\{d,s,g\}} n^d.\end{cases} \tag{8.16}$$

where $\eta_{1nk} = \frac{1}{2}\psi_{nk}$, $\eta_{2nk} = \psi_{nk}\left(-\mathcal{C} - \sin(\bar{\theta}_{nk}^{(i)}) \right)$, $\eta_{3nk} = \psi_{nk}\left(\frac{1}{2}\mathcal{C}^2 + \mathcal{C}\sin(\bar{\theta}_{nk}^{(i)}) + \cos(\bar{\theta}_{nk}^{(i)}) \right) + \frac{\gamma_{kr}}{N_s}$,$\eta_{4nk} = \frac{1}{2}\psi_{nk}$, $\eta_{5nk} = \psi_{nk}\left(-\mathcal{C} + \cos(\bar{\theta}_{nk}^{(i)}) \right)$, and $\eta_{6nk} = \psi_{nk}\left(\frac{1}{2}\mathcal{C}^2 - \right.$

$\mathcal{C}\cos(\bar{\theta}_{nk}^{(i)}) + \sin(\bar{\theta}_{nk}^{(i)})\Big) + \frac{\gamma_{ki}}{N_s}$.

The objective function of problem (8.16) can be rewritten as

$$\mathcal{O} = \sum_k \left\{ \left[\sum_n \left(\boldsymbol{\theta}_n^T \dot{\mathbf{A}}_{nk} \boldsymbol{\theta}_n \right) \right]^2 + \left[\sum_n \left(\boldsymbol{\theta}_n^T \ddot{\mathbf{A}}_{nk} \boldsymbol{\theta}_n \right) \right]^2 \right\}, \tag{8.17}$$

where $\boldsymbol{\theta}_n = [\theta_n \; 1]^T$ and

$$\dot{\mathbf{A}}_{nk} = \begin{bmatrix} \eta_{1nk} & \frac{1}{2}\eta_{2nk} \\ \frac{1}{2}\eta_{2nk} & \eta_{3nk} \end{bmatrix}, \ddot{\mathbf{A}}_{nk} = \begin{bmatrix} \eta_{4nk} & \frac{1}{2}\eta_{5nk} \\ \frac{1}{2}\eta_{5nk} & \eta_{6nk} \end{bmatrix}.$$

Further, we have

$$\sum_n \boldsymbol{\theta}_n^T \dot{\mathbf{A}}_{nk} \boldsymbol{\theta}_n = \tilde{\boldsymbol{\theta}}^T \tilde{\mathbf{D}}^T \dot{\mathbf{A}}_k \tilde{\mathbf{D}} \tilde{\boldsymbol{\theta}}, \tag{8.18}$$

where $\tilde{\boldsymbol{\theta}} = [\theta_1, \ldots, \theta_{N_s}, 1]^T$, $\dot{\mathbf{A}}_k = \mathrm{Diag}(\dot{\mathbf{A}}_{1k}, \ldots, \dot{\mathbf{A}}_{2N_s k})$ and $\tilde{\mathbf{D}} \in \mathbb{R}^{2N_s \times \tilde{N}_s}$ is a constant matrix. Similarly, $\sum_n \left(\boldsymbol{\theta}_n^T \ddot{\mathbf{A}}_{nk} \boldsymbol{\theta}_n \right) = (\tilde{\boldsymbol{\theta}}^T \tilde{\mathbf{D}}^T \ddot{\mathbf{A}}_k \tilde{\mathbf{D}} \tilde{\boldsymbol{\theta}})$.

Using the above reformulation, the problem becomes

$$\begin{cases} \underset{\tilde{\boldsymbol{\theta}}}{\text{minimize}} & \sum_k \left\{ [(\tilde{\boldsymbol{\theta}}^T \dot{\mathbf{B}}_k \tilde{\boldsymbol{\theta}})]^2 + [(\tilde{\boldsymbol{\theta}}^T \ddot{\mathbf{B}}_k \tilde{\boldsymbol{\theta}})]^2 \right\} \\ \text{subject to} & \theta_n = \arg(x_{n,g}) = \sum_{d=0}^{D} a_{\{d,s,g\}} n^d. \end{cases} \tag{8.19}$$

with $\dot{\mathbf{B}}_k = \tilde{\mathbf{D}}^T \dot{\mathbf{A}}_k \tilde{\mathbf{D}} = \left[\begin{array}{c:c} \mathbf{B}_{1k} & \mathbf{b}_{1k} \\ \hdashline \mathbf{b}_{1k}^T & \dot{b}_k \end{array}\right]$, and $\ddot{\mathbf{B}}_k = \tilde{\mathbf{D}}^T \ddot{\mathbf{A}}_k \tilde{\mathbf{D}} = \left[\begin{array}{c:c} \mathbf{B}_{2k} & \mathbf{b}_{2k} \\ \hdashline \mathbf{b}_{2k}^T & \ddot{b}_k \end{array}\right]$.

Now, we substitute the polynomial phase constraint (i.e. $\theta_n = \sum_{d=0}^{D} a_{\{d,s,g\}} n^d$) into problem (8.10) and have

$$\begin{cases} \underset{\mathbf{a}}{\text{minimize}} & \sum_k \Big\{ [\mathbf{a}^T \dot{\mathbf{G}}_k \mathbf{a} + 2\mathbf{a}^T \dot{\mathbf{b}}_k + \dot{b}_k]^2 \\ & \quad + [\mathbf{a}^T \ddot{\mathbf{G}}_k \mathbf{a} + 2\mathbf{a}^T \ddot{\mathbf{b}}_k + \ddot{b}_k]^2 \Big\} \end{cases} \tag{8.20}$$

where $\mathbf{a} = [a_D, a_{D-1}, \ldots, a_0]^T$, $\bar{D} = D + 1$, $\dot{\mathbf{G}}_k = \mathbf{Z}^T \mathbf{B}_{1k} \mathbf{Z} \in \mathbb{R}^{\bar{D} \times \bar{D}}$, $\dot{\mathbf{b}}_k = \mathbf{b}_{1k} \mathbf{Z} \in \mathbb{R}^{\bar{D}}$,

$\ddot{\mathbf{G}}_k = \mathbf{Z}^T\mathbf{B}_{2k}\mathbf{Z}$, $\ddot{\mathbf{b}}_k = \mathbf{b}_{2k}\mathbf{Z} \in \mathbb{R}^{\bar{D}}$ and

$$\mathbf{Z} = \begin{bmatrix} 1^D & 1^{D-1} & \cdots & 1^0 \\ 2^D & 2^{D-1} & \cdots & 2^0 \\ \vdots & & \ddots & \\ N_s^D & N_s^{D-1} & \cdots & N_s^0 \end{bmatrix} \in \mathbb{R}^{N_s \times \bar{D}}.$$

Problem (8.20) is an unconstrained one with a real valued polynomial in $\mathbf{a}$, denoted by $p(a) : \mathbb{R}^{\bar{D}} \to \mathbb{R}$. For example, when $\bar{D} = 3$ for Doppler-tolerant subpulses, the degree 4 polynomial with the monomial basis as

$$1, a_0, a_1, a_2, a_0^2,\ a_0a_1,\ a_0a_2, \ldots,\ a_1^3a_2,\ a_0a_2^3,\ a_1a_2^3.$$

We can express

$$p(a) = \sum_{\alpha} v_\alpha a^\alpha \text{ with } a^\alpha := a_0^{\alpha_0}a_1^{\alpha_1}a_2^{\alpha_2} \text{ and } \sum_i \alpha_i \leq 4. \tag{8.21}$$

Thus, we are now interested in solving

$$\mathbb{P} \mapsto p^* := \underset{a\in\mathbb{R}^{\bar{D}}}{\text{minimize}}\, p(a) \tag{8.22}$$

and evaluating the global minimizer a^* from (8.22). It can be obtained by solving a finite sequence of convex Linear Matrix Inequality (LMI) optimization problem [160]

$$\mathbb{Q} \mapsto \begin{cases} \inf\limits_{y} & \sum\limits_{\alpha} p_\alpha y_\alpha, \\ & M_m(y) \succeq 0 \end{cases} \tag{8.23}$$

where the moment matrix $M_m(y)$ is the block matrix $\{M_{i,j}(y)\}_{0\leq i,j\leq 2m}$ defined as

$$M_{i,j}(y) \begin{bmatrix} y_{i+j,0} & y_{i+j-1,1} & \cdots & y_{i,j} \\ y_{i+j-1,1} & y_{i+j-2,2} & \cdots & y_{i-1,j+1} \\ \cdots & \cdots & \cdots & y_{0,i+j} \\ y_{j,i} & y_{i+j-1,1} & \cdots & y_{0,i+j} \end{bmatrix} \tag{8.24}$$

and $y_{i,j}$ represents the $(i+j)$-order moment $\int a^i y^i \mu(d(a,y))$ for some probability measure μ.

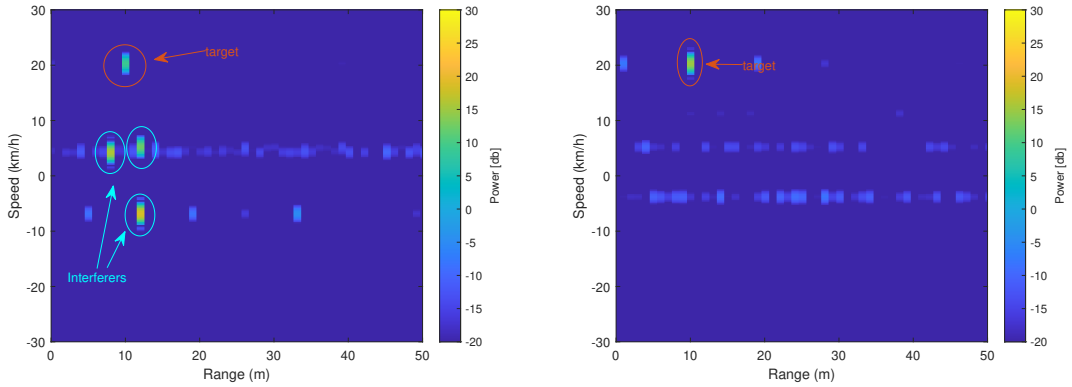

(a) Category 1: Constant phase coefficients for all the sensing subpulses

(b) Category 2: Optimal phase coefficients for every sensing subpulse

Figure 8.3: Range-Doppler map of a reference sensor for two categories

8.6 Results

Now, we evaluate the performance of ISAC scheme with the optimal phase sequences derived from the aforementioned framework. Assume that the entire test scenario spans an area of 50sqm and is equipped with three sensors. The target and the sensor location is randomly generated in this region. Further, the target velocity is 20m/s as a reference. Other parameters such as operating frequency, bandwidth, transmit power, number of pulses, chip time and code length are 60GHz, 150 MHz, 12dBm, 512, 6.66 ns, and 5000 respectively.

In order to understand the advantage of synthesizing the sequences from the proposed framework, we compare sequence sets from two categories. In category 1, the sensing subpulses are repeated for the entire pulse. In category 2, the sensing subpulse coefficients are derived from the proposed method. The range-Doppler maps are generated for a reference sensor (Sensor 1) for a sequence set from each category after processing the received signal in one CPI (Figure 8.3). As evident from the figure, localized strong interference is observed in category 1, whereas in category 2, no interference is observed.

Further, the quadratic phase coefficients of the communication subpulses over an entire CPI are assumed to be Gaussian distributed. As the two sequence sets are composed of subpulses derived from constant/optimally derived deterministic phase coefficients for sensing subpulses and random phase coefficients for communication subpulses, therefore a statistical analysis is mandatory. In Figure 8.4, the CISL distribution for category 1 is centered at -6dB whereas for category 2, the distribution is centered at -28dB. Thus, overall minimization of CISL is evident from this analysis.

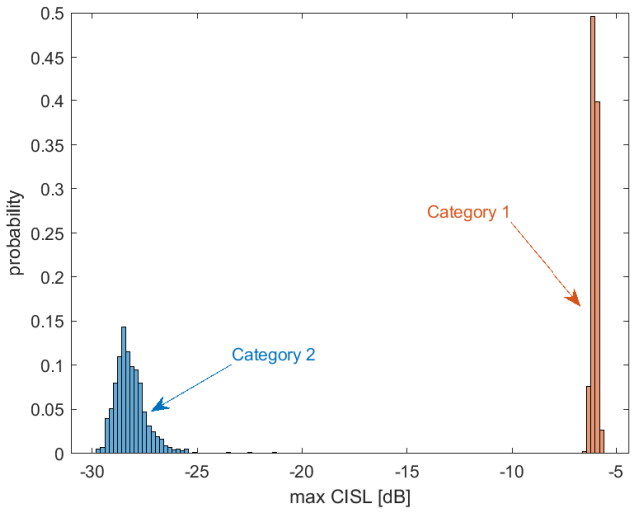

Figure 8.4: Statistical analysis of maximum CISL

8.7 Conclusions

This paper proposed a multi-layer optimization approach. It enables simultaneous sensing and data-transmission, potentially improving real-time computing while handling interference from other sensors effectively. The proposed intra-pulse modulation scheme embeds communication symbols in the communication subpulses. It ensures the Doppler tolerance in every pulse as the sequences possess quadratic phase behavior. Simulation results show the effectiveness of the approach for WSNs.

Part V

Conclusions and Perspectives

Chapter 9

Conclusion

9.1 Summary and conclusions

This research introduces a series of novel approaches for optimizing waveform design and improving radar system performance, with a particular focus on mitigating mutual interference (MI) in radar networks, especially in dense sensor environments.

Key contributions include an in-depth exploration of interference in mmWave radar sensors, highlighting how different interference types degrade SNR in target detection. The findings underscore the critical role of advanced waveform design, interference mitigation techniques and cognitive handshake mechanisms in enabling effective coexistence between victim and interfering sensors.

The proposed PECS framework provides a flexible and computationally efficient approach to minimize peak and integrated sidelobes (PSL and ISL). By introducing quadratic phase behavior in the waveforms and splitting each sequence into multiple sub-sequences, Doppler tolerance and interference immunity can be enhanced. This method proves particularly effective in automotive radar applications, which face significant interference challenges from dense vehicle scenarios.

The development of a PMCW radar system was demonstrated using USRP-hardware considering the low-sampling rate ADC requirements. The use of stretch processing to process sub-pulses within a transmit pulse while keeping the sidelobes low and improving Doppler tolerance, provides more degrees of freedom for the waveform design problem. The successful implementation of PECS algorithm significantly mitigated interference, offering a practical solution for modern radar systems.

Optimization frameworks, such as MM and BCD, enabled the design of Doppler-tolerant sequence sets with polynomial phase characteristics. A systematic approach was provided using these methods which is computationally efficient and offers robust solutions for both PMCW

and FMCW radar systems. The waveforms were optimized in multiple dimensions (i.e. fast-time, slow-time and spatial domain) while retaining the polynomial phase characteristics of the sequence set in the fast-time. Further investigation into MIMO radar sequence design under spectral occupancy constraints resulted in a stable, computationally efficient solution using the BSUM technique. This approach successfully balanced spectrum shaping with correlation matching, outperforming existing methods in scenarios with strict spectral constraints.

Additionally, the multi-layer optimization approach for designing dual function waveforms for WSNs by embedding communication symbols within radar sub-pulses offered simultaneous operation of multiple sensors while communicating reliably with the fusion center. A multi-layered optimization framework was provided by fusing three techniques namely BCD, MM and SoS. The simulation results show better Doppler tolerance for dynamic target detection, and effectively managing interference in WSNs.

This study advances radar waveform optimization, interference mitigation, and system design. The methods introduced in Chapters 4, 6, and 8, which integrate polynomial phase characteristics into MIMO waveform design through robust optimization frameworks, aim to enhance radar system efficiency, performance, and reliability across various sensing applications. These improvements are particularly impactful in dynamic and dense sensor environments with high interference, providing a strong foundation for further developments. This framework supports better coexistence with communication systems and more effective operation in complex scenarios for future applications.

9.2 Future Work

The future work stemming from this research will focus on expanding the theoretical and simulated advancements into practical hardware implementations. Current studies have primarily addressed algorithmic and simulation-based interference mitigation techniques, but a critical next step is to implement these solutions in real-world radar systems and test their effectiveness under practical constraints such as large bandwidths, different operating frequencies and extended targets. Hardware implementations of optimized radar systems will involve using the proposed waveforms into Monolithic microwave integrated circuit (MMIC) to ensure that real-time radar systems can manage interference efficiently without sacrificing performance. Ensuring computational efficiency and energy consumption will also be key considerations for deploying these advanced radar solutions in automotive and industrial settings.

As outlined in chapter 3 3.3.1, the next phase of this research will incorporate statistical modeling of interference in a multi-sensor environment. Given that MI is a stochastic phenomenon, therefore the effect of interference from multiple radar sensors can be probabilisti-

cally modeled. Further, using the probabilistic information from a single pulse, the probability of interference in the subsequent pulses within a CPI can be derived. Integrating this information over the entire CPI provides a useful estimate of the overall deterioration in SINR. Further, this information can be correlated with the results obtained from the hardware experiments to understand the accuracy of each model. Iteratively experimenting with multiple probabilistic models an efficient method to estimate MI for multiple interferers can be developed. Further, using this model and extrapolating the results an estimate of maximum MI for N, where $N \geq 1000$ interferers can be derived.

Additionally, as outlined in Chapter 8, future work will emphasize integrating wireless sensor network (WSN) applications into the proposed waveform design, given the increasing relevance of environmental sensing and Internet of Things (IoT) applications. The next phase of research will incorporate auto-correlation minimization in addition to the cross-correlation minimization problem discussed. This problem can also be handled using the multi-layered optimization framework composed of BCD + MM + SoS techniques. Finally, we estimate the phase coefficients at each receiver end, thereby recovering the communication symbols effectively.

Finally, the integration of AI and machine learning (ML) techniques into radar systems can offer a powerful solution for suppressing interference in diverse sensing environments. Machine learning algorithms can be trained to recognize and adapt to interference patterns in real-time, enabling more intelligent interference mitigation strategies at the receiver end.

Bibliography

[1] World Health Organization, *Global status report on road safety 2018*. Genève, Switzerland: World Health Organization, Jan. 2019.

[2] A. Filippi, F. Laghezza, F. Jansen, J. Overdevest, and D. Terbas, "An introduction to radar-to-radar interference in automotive applications," NXP Semiconductors, Tech. Rep. [Online]. Available: https://www.nxp.com/webapp/Download?colCode=RADARINTERFWP

[3] E. Raei, M. Alaee-Kerahroodi, and B. S. M. R. Rao, "Waveform design for range-isl minimization with spectral compatibility in mimo radars," in *2022 19th European Radar Conference (EuRAD)*, 2022, pp. 101–104.

[4] W. Rowe, P. Stoica, and J. Li, "Spectrally constrained waveform design [sp tips&tricks]," *IEEE Signal Processing Magazine*, vol. 31, no. 3, pp. 157–162, 2014.

[5] S. P. Sankuru, R. Jyothi, P. Babu, and M. Alaee-Kerahroodi, "Designing sequence set with minimal peak side-lobe level for applications in high resolution radar imaging," *IEEE Open Journal of Signal Processing*, vol. 2, pp. 17–32, 2021.

[6] M. E. Levanon Nadav, *Radar Signals*. John Wiley & Sons, Inc., Publication, 2004.

[7] J. Song, P. Babu, and D. P. Palomar, "Sequence set design with good correlation properties via majorization-minimization," *IEEE Transactions on Signal Processing*, vol. 64, no. 11, pp. 2866–2879, 2016.

[8] W. Fleming, "Overview of automotive sensors," *IEEE Sensors Journal*, vol. 1, no. 4, pp. 296–308, 2001.

[9] D. M. Kunert, "Recommendations on sensor design, mounting and operational parameters to minimize radar interference," *MOSARIM*, 2012.

[10] W. Buller, B. Wilson, J. Garbarino, J.and Kelly, N. Subotic, B. Thelen, and B. Belzowski, "Radar congestion study," *(Report No. DOT HS 812 632)*, 2018.

[11] D. Terbas, F. Laghezza, F. Jansen, A. Filippi, and J. Overdevest, "Radar to radar interference in common traffic scenarios," in *2019 16th European Radar Conference (EuRAD)*, 2019, pp. 177–180.

[12] S. Alland, W. Stark, M. Ali, and M. Hegde, "Interference in automotive radar systems: Characteristics, mitigation techniques, and current and future research," *IEEE Signal Processing Magazine*, vol. 36, no. 5, pp. 45–59, 2019.

[13] M. S. Greco, J. Li, T. Long, and A. Zoubir, "Advances in radar systems for modern civilian and commercial applications: Part 1 [from the guest editors]," *IEEE Signal Processing Magazine*, vol. 36, no. 4, pp. 13–15, 2019.

[14] G. Wang, C. Gu, T. Inoue, and C. Li, "A hybrid fmcw-interferometry radar for indoor precise positioning and versatile life activity monitoring," *IEEE Transactions on Microwave Theory and Techniques*, vol. 62, no. 11, pp. 2812–2822, 2014.

[15] C. Aydogdu, M. F. Keskin, G. K. Carvajal, O. Eriksson, H. Hellsten, H. Herbertsson, E. Nilsson, M. Rydstrom, K. Vanas, and H. Wymeersch, "Radar interference mitigation for automated driving: Exploring proactive strategies," *IEEE Signal Processing Magazine*, vol. 37, no. 4, pp. 72–84, 2020.

[16] S. Murali, K. Subburaj, B. Ginsburg, and K. Ramasubramanian, "Interference detection in fmcw radar using a complex baseband oversampled receiver," in *2018 IEEE Radar Conference (RadarConf18)*, 2018, pp. 1567–1572.

[17] S. Trotta, M. Wintermantel, J. Dixon, U. Moeller, R. Jammers, T. Hauck, A. Samulak, B. Dehlink, K. Shun-Meen, H. Li, A. Ghazinour, Y. Yin, S. Pacheco, R. Reuter, S. Majied, D. Moline, T. Aaron, V. P. Trivedi, D. J. Morgan, and J. John, "An rcp packaged transceiver chipset for automotive lrr and srr systems in sige bicmos technology," *IEEE Transactions on Microwave Theory and Techniques*, vol. 60, no. 3, pp. 778–794, 2012.

[18] S. Rao and A. V. Mani, "Interference characterization in fmcw radars," in *2020 IEEE Radar Conference (RadarConf20)*, 2020, pp. 1–6.

[19] "Texas instrument: Interference mitigation for awr/iwr devices, application report, swra662- january2020," https://www.ti.com/lit/an/swra662/swra662.pdf, accessed: 2021-04-15.

[20] C. Fischer, H. L. Blöcher, J. Dickmann, and W. Menzel, "Robust detection and mitigation of mutual interference in automotive radar," in *2015 16th International Radar Symposium (IRS)*, 2015, pp. 143–148.

[21] C. Aydogdu, N. Garcia, L. Hammarstrand, and H. Wymeersch, "Radar communications for combating mutual interference of fmcw radars," in *2019 IEEE Radar Conference (RadarConf)*, 2019, pp. 1–6.

[22] J. Hasch, E. Topak, R. Schnabel, T. Zwick, R. Weigel, and C. Waldschmidt, "Millimeter-wave technology for automotive radar sensors in the 77 ghz frequency band," *IEEE Transactions on Microwave Theory and Techniques*, vol. 60, no. 3, pp. 845–860, 2012.

[23] S. M. Patole, M. Torlak, D. Wang, and M. Ali, "Automotive radars: A review of signal processing techniques," *IEEE Signal Processing Magazine*, vol. 34, no. 2, pp. 22–35, 2017.

[24] S. Chen, C. Luo, B. Deng, Y. Qin, H. Wang, and Z. Zhuang, "Research on characteristics of rough and smooth pedestrian in terahertz band," in *2016 41st International Conference on Infrared, Millimeter, and Terahertz waves (IRMMW-THz)*, 2016, pp. 1–2.

[25] G. Beltrão, M. Alaee-Kerahroodi, U. Schroeder, and M. Bhavani Shankar, "Joint waveform/receiver design for vital-sign detection in signal-dependent interference," in *2020 IEEE Radar Conference (RadarConf20)*, 2020, pp. 1–6.

[26] R. Amar, M. Alaee-Kerahroodi, and M. R. Bhavani Shankar, "Fmcw-fmcw interference analysis in mm-wave radars; an indoor case study and validation by measurements," in *2021 21st International Radar Symposium (IRS)*, 2021, pp. 1–11.

[27] M. A. Richards, J. Scheer, W. A. Holm, and W. L. Melvin, *Principles of modern radar*. Citeseer, 2010.

[28] H. Rohling and M.-M. Meinecke, "Waveform design principles for automotive radar systems," in *2001 CIE International Conference on Radar Proceedings (Cat No.01TH8559)*, 2001, pp. 1–4.

[29] M. Jankiraman, *FMCW Radar Design*. Artech House, 2018.

[30] J. J. de Witt and W. A. Nel, "Range doppler dynamic range considerations for dechirp on receive radar," in *2008 Euro. Radar Conf.*, 2008, pp. 136–139.

[31] Y. Al-Alem, L. Albasha, and H. Mir, "High-resolution on-chip s -band radar system using stretch processing," *IEEE Sensors Journal*, vol. 16, no. 12, pp. 4749–4759, 2016.

[32] Z. Tong, R. Renter, and M. Fujimoto, "Fast chirp FMCW radar in automotive applications," in *IET Intl. Radar Conf.*, 2015, pp. 1–4.

[33] J. J. Benedetto, I. Konstantinidis, and M. Rangaswamy, "Phase-coded waveforms and their design," *IEEE Signal Processing Magazine*, vol. 26, no. 1, pp. 22–31, 2009.

[34] A. Bourdoux, U. Ahmad, D. Guermandi, S. Brebels, A. Dewilde, and W. Van Thillo, "PMCW waveform and MIMO technique for a 79 GHz CMOS automotive radar," in *2016 IEEE Radar Conference (RadarConf)*, 2016, pp. 1–5.

[35] N. Levanon and B. Getz, "Comparison between linear fm and phase-coded cw radars," *IEE Proceedings-Radar, Sonar and Navigation*, vol. 141, no. 4, pp. 230–240, 1994.

[36] J. Overdevest, F. Jansen, F. Uysal, and A. Yarovoy, "Doppler influence on waveform orthogonality in 79 ghz mimo phase-coded automotive radar," *IEEE Transactions on Vehicular Technology*, vol. 69, no. 1, pp. 16–25, 2020.

[37] R. Frank, "Polyphase codes with good nonperiodic correlation properties," *IEEE Transactions on Information Theory*, vol. 9, no. 1, pp. 43–45, 1963.

[38] B. L. Lewis and F. F. Kretschmer, "Linear frequency modulation derived polyphase pulse compression codes," *IEEE Transactions on Aerospace and Electronic Systems*, vol. AES-18, no. 5, pp. 637–641, 1982.

[39] N. Zhang and S. Golomb, "Polyphase sequence with low autocorrelations," *IEEE Transactions on Information Theory*, vol. 39, no. 3, pp. 1085–1089, 1993.

[40] D. Chu, "Polyphase codes with good periodic correlation properties (corresp.)," *IEEE Transactions on Information Theory*, vol. 18, no. 4, pp. 531–532, 1972.

[41] D. Petrolati, P. Angeletti, and G. Toso, "New piecewise linear polyphase sequences based on a spectral domain synthesis," *IEEE Transactions on Information Theory*, vol. 58, no. 7, pp. 4890–4898, 2012.

[42] G. M. Brooker, "Mutual interference of millimeter-wave radar systems," *IEEE Transactions on Electromagnetic Compatibility*, vol. 49, no. 1, pp. 170–181, 2007.

[43] M. Goppelt, H.-L. Blöcher, and W. Menzel, "Analytical investigation of mutual interference between automotive fmcw radar sensors," in *2011 German Microwave Conference*, 2011, pp. 1–4.

[44] B. Tang, W. Huang, and J. Li, "Slow-time coding for mutual interference mitigation," in *2018 IEEE International Conference on Acoustics, Speech and Signal Processing (ICASSP)*, 2018, pp. 6508–6512.

[45] A. Bose, B. Tang, M. Soltanalian, and J. Li, "Mutual interference mitigation for multiple connected automotive radar systems," *IEEE Transactions on Vehicular Technology*, vol. 70, no. 10, pp. 11 062–11 066, 2021.

[46] M. Toth, P. Meissner, A. Melzer, and K. Witrisal, "Performance comparison of mutual automotive radar interference mitigation algorithms," in *2019 IEEE Radar Conference (RadarConf)*, 2019, pp. 1–6.

[47] S. Rao and A. Varghese Mani, "Characterization of some interference mitigation schemes in fmcw radar," in *2021 IEEE Radar Conference (RadarConf21)*, 2021, pp. 1–6.

[48] A. Bourdoux, K. Parashar, and M. Bauduin, "Phenomenology of mutual interference of fmcw and pmcw automotive radars," in *2017 IEEE Radar Conference (RadarConf)*, 2017, pp. 1709–1714.

[49] R. Amar, M. Alaee-Kerahroodi, P. Babu, and B. S. M. R., "Designing interference-immune doppler-tolerant waveforms for radar systems," *IEEE Transactions on Aerospace and Electronic Systems*, vol. 59, no. 3, pp. 2402–2421, 2023.

[50] D. Schwarz, N. Riese, I. Dorsch, and C. Waldschmidt, "System performance of a 79 GHz high-resolution 4D Imaging MIMO radar with 1728 virtual channels," *IEEE Journal of Microwaves*, vol. 2, no. 4, pp. 637–647, 2022.

[51] T. Instruments, "Imaging radar using cascaded mmwave sensor reference design," 2020.

[52] Vayyar, "Vayyar - 60GHz automotive technology," https://vayyar.com/auto/technology/60ghz/, December 2023, accessed: 01.12.2023.

[53] Embedded.com. (2023) Exclusive: Arbe releases 48 RX x 48 TX production radar processor. [Online]. Available: https://www.embedded.com/exclusive-arbe-releases-48-rx-x-48-tx-production-radar-processor/

[54] S. Fortunati, L. Sanguinetti, F. Gini, M. S. Greco, and B. Himed, "Massive MIMO radar for target detection," *IEEE Transactions on Signal Processing*, vol. 68, pp. 859–871, 2020.

[55] F. Xu, S. A. Vorobyov, and F. Yang, "Transmit beamspace ddma based automotive mimo radar," *IEEE Transactions on Vehicular Technology*, vol. 71, no. 2, pp. 1669–1684, 2022.

[56] F. Jansen, "Automotive radar doppler division mimo with velocity ambiguity resolving capabilities," in *2019 16th European Radar Conference (EuRAD)*, 2019, pp. 245–248.

[57] H. Sun, F. Brigui, and M. Lesturgie, "Analysis and comparison of MIMO radar waveforms," in *2014 International Radar Conference*, 2014, pp. 1–6.

[58] N. K. Sichani, M. Ahmadi, E. Raei, M. Alaee-Kerahroodi, B. S. M. R., E. Mehrshahi, and S. A. Ghorashi, "Waveform selection for FMCW and PMCW 4D-Imaging automotive radar sensors," in *2023 IEEE Radar Conference (RadarConf23)*, 2023, pp. 1–6.

[59] E. Raei, M. Alaee-Kerahroodi, and M. B. Shankar, "Spatial- and range- ISLR trade-off in MIMO radar via waveform correlation optimization," *IEEE Transactions on Signal Processing*, vol. 69, pp. 3283–3298, 2021.

[60] M. Alaee-Kerahroodi, P. Babu, M. Soltanalian, and M. B. Shankar, *Signal Design for Modern Radar Systems*. Artech House, 2022.

[61] R. Amar, M. Alaee-Kerahroodi, P. Babu, and B. S. M. R, "Optimized-slope FMCW waveform for automotive radars," in *2022 23rd International Radar Symposium (IRS)*, 2022, pp. 110–115.

[62] M. Soltanalian, P. Stoica, M. M. Naghsh, and A. De Maio, "Design of piecewise linear polyphase sequences with good correlation properties," in *2014 22nd European Signal Processing Conference (EUSIPCO)*, 2014, pp. 1297–1301.

[63] R. Amar, M. Alaee-Kerahroodi, G. Beltrão, and B. S. M. R., "Doppler-tolerant waveform design and signal processing for interference immune radar systems," in *2023 31st European Signal Processing Conference (EUSIPCO)*, 2023, pp. 715–719.

[64] S. D. Blunt and E. L. Mokole, "Overview of radar waveform diversity," *IEEE Aerospace and Electronic Systems Magazine*, vol. 31, no. 11, pp. 2–42, 2016.

[65] Y. Kalkan, "20 years of mimo radar," *IEEE Aerospace and Electronic Systems Magazine*, vol. 39, no. 3, pp. 28–35, 2024.

[66] S. Sun, A. P. Petropulu, and H. V. Poor, "Mimo radar for advanced driver-assistance systems and autonomous driving: Advantages and challenges," *IEEE Signal Processing Magazine*, vol. 37, no. 4, pp. 98–117, 2020.

[67] U. Kumbul, N. Petrov, C. S. Vaucher, and A. Yarovoy, "Phase-coded fmcw for coherent mimo radar," *IEEE Transactions on Microwave Theory and Techniques*, vol. 71, no. 6, pp. 2721–2733, 2023.

[68] X. Hu, Y. Li, M. Lu, Y. Wang, and X. Yang, "A multi-carrier-frequency random-transmission chirp sequence for tdm mimo automotive radar," *IEEE Transactions on Vehicular Technology*, vol. 68, no. 4, pp. 3672–3685, 2019.

[69] J. Bechter, F. Roos, and C. Waldschmidt, "Compensation of motion-induced phase errors in tdm mimo radars," *IEEE Microwave and Wireless Components Letters*, vol. 27, no. 12, pp. 1164–1166, 2017.

[70] C. M. Schmid, R. Feger, C. Pfeffer, and A. Stelzer, "Motion compensation and efficient array design for tdma fmcw mimo radar systems," in *2012 6th European Conference on Antennas and Propagation (EUCAP)*, 2012, pp. 1746–1750.

[71] D. J. Rabideau, "Mimo radar waveforms and cancellation ratio," *IEEE Transactions on Aerospace and Electronic Systems*, vol. 48, no. 2, pp. 1167–1178, 2012.

[72] F. Uysal, "Phase-coded FMCW automotive radar: System design and interference mitigation," *IEEE Transactions on Vehicular Technology*, vol. 69, no. 1, pp. 270–281, 2020.

[73] M. Alaee-Kerahroodi, M. Modarres-Hashemi, and M. M. Naghsh, "Designing sets of binary sequences for MIMO radar systems," *IEEE Transactions on Signal Processing*, vol. 67, no. 13, pp. 3347–3360, July 2019.

[74] H. He, P. Stoica, and J. Li, "Designing unimodular sequence sets with good correlations—including an application to mimo radar," *IEEE Transactions on Signal Processing*, vol. 57, no. 11, pp. 4391–4405, 2009.

[75] T. Liu, J. Sun, G. Wang, X. Du, and W. Hu, "Designing low side-lobe level-phase coded waveforms for mimo radar using p-norm optimization," *IEEE Transactions on Aerospace and Electronic Systems*, vol. 59, no. 4, pp. 3797–3810, 2023.

[76] K. Zhong, J. Hu, Y. Wang, Z. Zhao, X. Yu, G. Cui, B. Liao, and H. Li, "Mimo radar unimodular waveform design with learned complex circle manifold network," *IEEE Transactions on Aerospace and Electronic Systems*, pp. 1–9, 2024.

[77] J. Zhang and N. Xu, "Discrete phase coded sequence set design for waveform-agile radar based on alternating direction method of multipliers," *IEEE Transactions on Aerospace and Electronic Systems*, vol. 56, no. 6, pp. 4238–4252, 2020.

[78] J. Li and P. Stoica, "MIMO radar with colocated antennas," *IEEE Signal Processing Magazine*, vol. 24, no. 5, pp. 106–114, 2007.

[79] Z. Qiu, K. Duan, Y. Wang, Z. Liao, and J. He, "Designing constant modulus approximate binary phase waveforms for multi-target detection in mimo radar using lstm networks," *IEEE Transactions on Geoscience and Remote Sensing*, pp. 1–1, 2024.

[80] J. Hu, Z. Wei, Y. Li, H. Li, and J. Wu, "Designing unimodular waveform(s) for mimo radar by deep learning method," *IEEE Transactions on Aerospace and Electronic Systems*, vol. 57, no. 2, pp. 1184–1196, 2021.

[81] J.-E. Lee, H.-S. Lim, S.-H. Jeong, S.-C. Kim, Y.-S. Choi, and H.-C. Shin, "Enhanced iron-tunnel recognition for automotive radars," in *2015 16th International Radar Symposium (IRS)*, 2015, pp. 149–154.

[82] J. Yoon, S. Lee, S. Lim, and S.-C. Kim, "High-density clutter recognition and suppression for automotive radar systems," *IEEE Access*, vol. 7, pp. 58 368–58 380, 2019.

[83] W. Huang, M. M. Naghsh, R. Lin, and J. Li, "Doppler sensitive discrete-phase sequence set design for mimo radar," *IEEE Transactions on Aerospace and Electronic Systems*, vol. 56, no. 6, pp. 4209–4223, 2020.

[84] F. Wang, X.-G. Xia, C. Pang, X. Cheng, Y. Li, and X. Wang, "Joint design methods of unimodular sequences and receiving filters with good correlation properties and doppler tolerance," *IEEE Transactions on Geoscience and Remote Sensing*, vol. 61, pp. 1–14, 2023.

[85] X. Yu, G. Cui, J. Yang, and L. Kong, "Mimo radar transmit–receive design for moving target detection in signal-dependent clutter," *IEEE Transactions on Vehicular Technology*, vol. 69, no. 1, pp. 522–536, 2020.

[86] X. Yu, K. Alhujaili, G. Cui, and V. Monga, "Mimo radar waveform design in the presence of multiple targets and practical constraints," *IEEE Transactions on Signal Processing*, vol. 68, pp. 1974–1989, 2020.

[87] S. Sun, Y. Hu, K. V. Mishra, and A. P. Petropulu, "Widely separated mimo radar using matrix completion," *IEEE Transactions on Radar Systems*, vol. 2, pp. 180–196, 2024.

[88] C.-Y. Chen and P. P. Vaidyanathan, "Joint mimo radar waveform and receiving filter optimization," in *2009 IEEE International Conference on Acoustics, Speech and Signal Processing*, 2009, pp. 2073–2076.

[89] Y. Chen, R. Lin, Y. Cheng, and J. Li, "Joint design of periodic binary probing sequences and receive filters for pmcw radar," *IEEE Transactions on Signal Processing*, vol. 70, pp. 5996–6010, 2022.

[90] S. Haykin and C. Hawkes, "Adaptive digital filtering for coherent mti radar," *Information Sciences*, vol. 11, no. 4, pp. 335–359, 1976. [Online]. Available: https://www.sciencedirect.com/science/article/pii/0020025576900116

[91] L. Rosenberg, S. Watts, and M. S. Greco, "Modeling the statistics of microwave radar sea clutter," *IEEE Aerospace and Electronic Systems Magazine*, vol. 34, no. 10, pp. 44–75, 2019.

[92] G. Kulemin, 2003.

[93] D. Evans, T. Farr, J. van Zyl, and H. Zebker, "Radar polarimetry: analysis tools and applications," *IEEE Transactions on Geoscience and Remote Sensing*, vol. 26, no. 6, pp. 774–789, 1988.

[94] B. Friedlander, "Waveform design for mimo radars," *IEEE Transactions on Aerospace and Electronic Systems*, vol. 43, no. 3, pp. 1227–1238, 2007.

[95] C.-Y. Chen and P. P. Vaidyanathan, "Mimo radar ambiguity properties and optimization using frequency-hopping waveforms," *IEEE Transactions on Signal Processing*, vol. 56, no. 12, pp. 5926–5936, 2008.

[96] G. Beltrão, L. Pralon, A. Barreto, M. Alaee-Kerahroodi, and M. R. B. Shankar, "Sub-pulse processing for unambiguous doppler estimation in pulse-doppler noise radars," *IEEE Transactions on Aerospace and Electronic Systems*, vol. 57, no. 6, pp. 3813–3826, 2021.

[97] A. Rihaczek, "Doppler-tolerant signal waveforms," *Proceedings of the IEEE*, vol. 54, no. 6, pp. 849–857, 1966.

[98] P. Stoica, J. Li, and M. Xue, "Transmit codes and receive filters for radar," *IEEE Signal Processing Magazine*, vol. 25, no. 6, pp. 94–109, 2008.

[99] P. Stoica, H. He, and J. Li, "New algorithms for designing unimodular sequences with good correlation properties," *IEEE Transactions on Signal Processing*, vol. 57, no. 4, pp. 1415–1425, 2009.

[100] J. Song, P. Babu, and D. P. Palomar, "Sequence design to minimize the weighted integrated and peak sidelobe levels," *IEEE Transactions on Signal Processing*, vol. 64, no. 8, pp. 2051–2064, 2016.

[101] M. Alaee-Kerahroodi, A. Aubry, A. De Maio, M. M. Naghsh, and M. Modarres-Hashemi, "A coordinate-descent framework to design low PSL/ISL sequences," *IEEE Transactions on Signal Processing*, vol. 65, no. 22, pp. 5942–5956, Nov 2017.

[102] J. M. Baden, B. O'Donnell, and L. Schmieder, "Multiobjective sequence design via gradient descent methods," *IEEE Transactions on Aerospace and Electronic Systems*, vol. 54, no. 3, pp. 1237–1252, 2018.

[103] Q. Liu, W. Ren, K. Hou, T. Long, and A. E. Fathy, "Design of polyphase sequences with low integrated sidelobe level for radars with spectral distortion via majorization-minimization framework," *IEEE Transactions on Aerospace and Electronic Systems*, vol. 57, no. 6, pp. 4110–4126, 2021.

[104] S. P. Sankuru, P. Babu, and M. Alaee-Kerahroodi, "UNIPOL: Unimodular sequence design via a separable iterative quartic polynomial optimization for active sensing systems," *Signal Processing*, vol. 190, p. 108348, 2022. [Online]. Available: https://www.sciencedirect.com/science/article/pii/S0165168421003856

[105] R. Jyothi, P. Babu, and M. Alaee-Kerahroodi, "Slope: A monotonic algorithm to design sequences with good autocorrelation properties by minimizing the peak sidelobe level," *Digital Signal Processing*, vol. 116, p. 103142, 2021.

[106] X. Feng, Y. Zhao, Z. Zhou, and Z. Zhao, "Waveform design with low range sidelobe and high doppler tolerance for cognitive radar," *Signal Processing*, vol. 139, pp. 143–155, 2017. [Online]. Available: https://www.sciencedirect.com/science/article/pii/S0165168417301548

[107] W. Wang, "Large time-bandwidth product mimo radar waveform design based on chirp rate diversity," *IEEE Sensors Journal*, vol. 15, no. 2, pp. 1027–1034, 2015.

[108] J. Zhang, C. Shi, X. Qiu, and Y. Wu, "Shaping radar ambiguity function by l -phase unimodular sequence," *IEEE Sensors Journal*, vol. 16, no. 14, pp. 5648–5659, 2016.

[109] O. Aldayel, T. Guo, V. Monga, and M. Rangaswamy, "Adaptive sequential refinement: A tractable approach for ambiguity function shaping in cognitive radar," in *2017 51st Asilomar Conference on Signals, Systems, and Computers*, 2017, pp. 573–577.

[110] M. Alaee-Kerahroodi, S. Sedighi, B. Shankar M.R., and B. Ottersten, "Designing (in)finite-alphabet sequences via shaping the radar ambiguity function," in *ICASSP 2019 - 2019 IEEE International Conference on Acoustics, Speech and Signal Processing (ICASSP)*, 2019, pp. 4295–4299.

[111] Z. Wu, Z. Zhou, C. Wang, Y. Li, and Z. Zhao, "Doppler resilient complementary waveform design for active sensing," *IEEE Sensors Journal*, vol. 20, no. 17, pp. 9963–9976, 2020.

[112] I. A. Arriaga-Trejo, "Design of constant modulus sequences with doppler shift tolerance and good complete second order statistics," in *2020 IEEE International Radar Conference (RADAR)*, 2020, pp. 274–279.

[113] X. Feng, Q. Song, Z. Zhang, and Y. Zhao, "Novel waveform design with low probability of intercept and high doppler tolerance for modern cognitive radar," in *2019 IEEE International Conference on Signal, Information and Data Processing (ICSIDP)*, 2019, pp. 1–6.

[114] A. Aubry, A. De Maio, B. Jiang, and S. Zhang, "Ambiguity function shaping for cognitive radar via complex quartic optimization," *IEEE Transactions on Signal Processing*, vol. 61, no. 22, pp. 5603–5619, 2013.

[115] L. Wu, P. Babu, and D. P. Palomar, "Cognitive radar-based sequence design via sinr maximization," *IEEE Transactions on Signal Processing*, vol. 65, no. 3, pp. 779–793, 2017.

[116] W. Huang and R. Lin, "Efficient design of doppler sensitive long discrete-phase periodic sequence sets for automotive radars," in *2020 IEEE 11th Sensor Array and Multichannel Signal Processing Workshop (SAM)*, 2020, pp. 1–5.

[117] G. Cui, Y. Fu, X. Yu, and J. Li, "Local ambiguity function shaping via unimodular sequence design," *IEEE Signal Processing Letters*, vol. 24, no. 7, pp. 977–981, 2017.

[118] J. Song, P. Babu, and D. P. Palomar, "Optimization methods for designing sequences with low autocorrelation sidelobes," *IEEE Transactions on Signal Processing*, vol. 63, no. 15, pp. 3998–4009, 2015.

[119] K. Alhujaili, X. Yu, G. Cui, and V. Monga, "Spectrally compatible mimo radar beampattern design under constant modulus constraints," *IEEE Transactions on Aerospace and Electronic Systems*, vol. 56, no. 6, pp. 4749–4766, 2020.

[120] A. Y. Gemechu, G. Cui, and X. Yu, "Spectral-compatible transmit beampattern design with minimum peak sidelobe for narrowband mimo radar," *IEEE Transactions on Vehicular Technology*, pp. 1–12, 2022.

[121] R. Lin, M. Soltanalian, B. Tang, and J. Li, "Efficient design of binary sequences with low autocorrelation sidelobes," *IEEE Transactions on Signal Processing*, vol. 67, no. 24, pp. 6397–6410, 2019.

[122] Z. Chen, J. Liang, T. Wang, B. Tang, and H. C. So, "Generalized mbi algorithm for designing sequence set and mismatched filter bank with ambiguity function constraints," *IEEE Transactions on Signal Processing*, vol. 70, pp. 2918–2933, 2022.

[123] B. Tang, J. Tuck, and P. Stoica, "Polyphase waveform design for mimo radar space time adaptive processing," *IEEE Transactions on Signal Processing*, vol. 68, pp. 2143–2154, 2020.

[124] C. A. Mohr, P. M. McCormick, C. A. Topliff, S. D. Blunt, and J. M. Baden, "Gradient-based optimization of pcfm radar waveforms," *IEEE Transactions on Aerospace and Electronic Systems*, vol. 57, no. 2, pp. 935–956, 2021.

[125] Y. Sun, P. Babu, and D. P. Palomar, "Majorization-minimization algorithms in signal processing, communications, and machine learning," *IEEE Transactions on Signal Processing*, vol. 65, no. 3, pp. 794–816, 2017.

[126] E. Raei, M. Alaee-Kerahroodi, P. Babu, and M. R. B. Shankar, "Design of MIMO radar waveforms based on lp-norm criteria," 2021.

[127] A. W. Rihaczek, *Principles of High-Resolution Radar*. Artech House, 1969, ch. 12, Waveforms for Simplified Doppler Processing, pp. 420–422.

[128] A. Arora, C. G. Tsinos, B. S. M. R. Rao, S. Chatzinotas, and B. Ottersten, "Hybrid transceivers design for large-scale antenna arrays using majorization-minimization algorithms," *IEEE Transactions on Signal Processing*, vol. 68, pp. 701–714, 2020.

[129] D. R. Hunter and K. Lange, "A tutorial on mm algorithms," *The American Statistician*, vol. 58, no. 1, pp. 30–37, 2004.

[130] K. Lange, *MM Optimization Algorithms*. Philadelphia, PA, USA: SIAM-Society for Industrial and Applied Mathematics, 2016.

[131] F. L. Gall and F. Urrutia, "Improved rectangular matrix multiplication using powers of the coppersmith-winograd tensor," in *Proceedings of the Twenty-Ninth Annual ACM-SIAM Symposium on Discrete Algorithms*, ser. SODA '18. USA: Society for Industrial and Applied Mathematics, 2018, p. 1029–1046.

[132] G. H. Golub and C. F. Van Loan, *Matrix Computations*, 3rd ed. The Johns Hopkins University Press, 1996.

[133] A. Pirkani, F. Norouzian, E. Hoare, M. Cherniakov, and M. Gashinova, "Automotive interference statistics and their effect on radar detector," *IET Radar, Sonar & Navigation*, vol. 16, no. 1, pp. 9–21, 2022.

[134] S. Xu and A. Yarovoy, "Doppler shifts mitigation for pmcw signals," in *2019 International Radar Conference (RADAR)*, 2019, pp. 1–5.

[135] M. Bauduin and A. Bourdoux, "Code diversity for range sidelobe attenuation in pmcw and ofdm radars," in *2021 IEEE Radar Conference (RadarConf21)*, 2021, pp. 1–5.

[136] O. Rabaste and L. Savy, "Mismatched filter optimization for radar applications using quadratically constrained quadratic programs," *IEEE Transactions on Aerospace and Electronic Systems*, vol. 51, no. 4, pp. 3107–3122, 2015.

[137] A. Hedayat and W. D. Wallis, "Hadamard Matrices and Their Applications," *The Annals of Statistics*, vol. 6, no. 6, pp. 1184 – 1238, 1978. [Online]. Available: https://doi.org/10.1214/aos/1176344370

[138] R. Gold, "Optimal binary sequences for spread spectrum multiplexing (corresp.)," *IEEE Transactions on Information Theory*, vol. 13, no. 4, pp. 619–621, 1967.

[139] J. E. Quirk, R. J. Chang, J. W. Owen, S. D. Blunt, and P. M. McCormick, "A simple yet effective metric for assessing doppler tolerance," *IEEE Transactions on Radar Systems*, vol. 1, pp. 12–20, 2023.

[140] K. V. Mishra, M. Bhavani Shankar, V. Koivunen, B. Ottersten, and S. A. Vorobyov, "Toward millimeter-wave joint radar communications: A signal processing perspective," *IEEE Signal Processing Magazine*, vol. 36, no. 5, pp. 100–114, 2019.

[141] G. Han, J. Choi, and R. W. Heath, "Radar imaging based on ieee 802.11ad waveform in v2i communications," *IEEE Transactions on Signal Processing*, vol. 70, pp. 4981–4996, 2022.

[142] Z. Xu and A. Petropulu, "A bandwidth efficient dual-function radar communication system based on a MIMO radar using OFDM waveforms," *IEEE Transactions on Signal Processing*, vol. 71, pp. 401–416, 2023.

[143] X. Fang, W. Feng, Y. Chen, N. Ge, and Y. Zhang, "Joint communication and sensing toward 6G: Models and potential of using MIMO," *IEEE Internet of Things Journal*, vol. 10, no. 5, pp. 4093–4116, 2023.

[144] Z. Gao, Z. Wan, D. Zheng, S. Tan, C. Masouros, D. W. K. Ng, and S. Chen, "Integrated sensing and communication with mmwave massive MIMO: A compressed sampling perspective," *IEEE Transactions on Wireless Communications*, vol. 22, no. 3, pp. 1745–1762, 2023.

[145] S. H. Dokhanchi, B. S. Mysore, K. V. Mishra, and B. Ottersten, "A mmwave automotive joint radar-communications system," *IEEE Transactions on Aerospace and Electronic Systems*, vol. 55, no. 3, pp. 1241–1260, 2019.

[146] J. Jin, J. Gubbi, S. Marusic, and M. Palaniswami, "An information framework for creating a smart city through internet of things," *IEEE Internet of Things journal*, vol. 1, no. 2, pp. 112–121, 2014.

[147] L. Mainetti, L. Patrono, and A. Vilei, "Evolution of wireless sensor networks towards the internet of things: A survey," in *SoftCOM 2011, 19th international conference on software, telecommunications and computer networks*. IEEE, 2011, pp. 1–6.

[148] J. A. Zhang, F. Liu, C. Masouros, R. W. Heath, Z. Feng, L. Zheng, and A. Petropulu, "An overview of signal processing techniques for joint communication and radar sensing," *IEEE Journal of Selected Topics in Signal Processing*, vol. 15, no. 6, pp. 1295–1315, 2021.

[149] Z. Cheng, L. Wu, B. Wang, M. R. Bhavani Shankar, and B. Ottersten, "Double-phase-shifter based hybrid beamforming for mmWave DFRC in the presence of extended target and clutters," *IEEE Transactions on Wireless Communications*, pp. 1–1, 2022.

[150] M. F. Keskin, V. Koivunen, and H. Wymeersch, "Limited feedforward waveform design for OFDM dual-functional radar-communications," *IEEE Transactions on Signal Processing*, vol. 69, pp. 2955–2970, 2021.

[151] Z. Xu and A. Petropulu, "A bandwidth efficient dual-function radar communication system based on a MIMO radar using OFDM waveforms," *IEEE Transactions on Signal Processing*, vol. 71, pp. 401–416, 2023.

[152] K. P. Rajput, M. F. Ahmed, N. K. Venkategowda, A. K. Jagannatham, G. Sharma, and L. Hanzo, "Robust decentralized and distributed estimation of a correlated parameter vector in MIMO-OFDM wireless sensor networks," *IEEE Transactions on Communications*, vol. 69, no. 10, pp. 6894–6908, 2021.

[153] T. Wei, L. Wu, K. V. Mishra, and B. Shankar M. R., "Ris-aided wideband holographic dfrc," *IEEE Transactions on Aerospace and Electronic Systems*, vol. 60, no. 4, pp. 4241–4256, 2024.

[154] W. Tang and L. Wang, "Cooperative OFDM for energy-efficient wireless sensor networks," in *2008 IEEE Workshop on Signal Processing Systems*. IEEE, 2008, pp. 77–82.

[155] Y. Iraqi and A. Al-Dweik, "Efficient information transmission using smart OFDM for IoT applications," *IEEE Internet of Things Journal*, vol. 7, no. 9, pp. 8397–8409, 2020.

[156] Y. Cui, F. Liu, X. Jing, and J. Mu, "Integrating sensing and communications for ubiquitous IoT: Applications, trends, and challenges," *IEEE Network*, vol. 35, no. 5, pp. 158–167, 2021.

[157] K. P. Rajput, L. Wu, and M. R. Bhavani Shankar, "Next-generation iot networks: Integrated sensing communication and computation," in *2023 IEEE International Conference on Acoustics, Speech, and Signal Processing Workshops (ICASSPW)*, 2023, pp. 1–4.

[158] U. Kumbul, N. Petrov, F. van der Zwan, C. S. Vaucher, and A. Yarovoy, "Experimental investigation of phase coded FMCW for sensing and communications," in *2021 15th European Conference on Antennas and Propagation (EuCAP)*, 2021, pp. 1–5.

[159] L. Wu, K. P. Rajput, Y. Liu, and B. Shankar, "Distributed sensing and centric computing via fmcw waveform in wireless sensor network," in *2023 IEEE 24th International Workshop on Signal Processing Advances in Wireless Communications (SPAWC)*, 2023, pp. 596–600.

[160] J. B. Lasserre, "Global optimization with polynomials and the problem of moments," *SIAM Journal on Optimization*, vol. 11, no. 3, pp. 796–817, 2001. [Online]. Available: https://doi.org/10.1137/S1052623400366802